Geosynthetic-Reinforced Retaining Walls with Flexible Facing Subjected to Footing Loading

BY

Seyed Mustapha Rahmaninezhad

Submitted to the graduate degree program in Civil, Environmental, and Architectural Engineering and the Graduate Faculty of the University of Kansas in partial fulfillment of the requirements for the degree of Doctor of Philosophy.

_____

Dr. Jie Han, Chairperson

_____

Dr. Hongyi Cai

_____

Dr. Shawn Keshmiri

_____

Dr. Robert L. Parsons

_____

Dr. Steven D. Schrock

Date Defended: 05/15/2019

The Dissertation Committee for Seyed Mustapha Rahmaninezhad

certifies that this is the approved version of the following dissertation:

Geosynthetic-Reinforced Retaining Walls with Flexible Facing Subjected to Footing Loading

_____

Dr. Jie Han, Chairperson

Date approved: 05/15/2019

Abstract

Geosynthetic-reinforced retaining (GRR) walls have been used as bridge abutments to support shallow foundations. This technology eliminates the need for traditional deep foundations, such as piles, to support bridges. However, limited studies have been conducted so far to evaluate the performance of GRR abutment walls constructed with flexible facing. The objectives of this study were: (1) to evaluate the performance of the GRR walls subjected to static footing loading and (2) to develop methods to predict facing lateral deflections and surface settlement of GRR walls under the footing loading. To fulfill the above research objectives, a comprehensive experimental study and analytical analysis were conducted.

In this study, pullout tests were conducted to evaluate the effect of the load application method using an airbag with and without stiff plates on the vertical stress distribution and the pullout capacities and deflections of extensible (geogrid) reinforcement in the soil in a large pullout box. The non-uniform pressure distribution resulting from the airbag with stiff plates reduced the pullout resistance of the reinforcement as compared with that without stiff plates. The test results also show that the displacements in the cross section of the same transverse bar were not equal when the normal load was applied through stiff plates.

This study investigated the combined effects of tension, bending, and friction on the measured strains on the upper and lower sides of uniaxial geogrid specimens by wrapping the specimen around a cylinder of different diameters. The test results show the combination of tension, bending, and friction reduced the average upper and lower strains by 28% as compared with the tension only. The cylinder diameter did not have any effect on the measured strains of the geogrid

on the cylinder.

The experimental study investigated eight reduced-scale GRR abutment walls with wrapped-around and modular concrete block facing subjected to static footing loading in a test box under a plane strain condition. The settlements of the footing, the lateral deflections of the facing, the vertical and lateral earth pressures, the tensile strains along reinforcement, and the failure mode were evaluated. The test results showed that the modular block facing acting as a relatively rigid structural element reduced the footing settlement as compared with the wrapped-around facing. Moreover, the maximum lateral deflection in the wrapped-around facing wall was much larger than that of the modular block facing wall under the same applied footing pressure. The measured maximum vertical stress was larger than the calculated stress from the Boussinesq equation and the 2:1 distribution method at the centerline of the footing. The maximum lateral earth pressure was recorded at the depth of 0.5H-0.7H and 0.9H (H is the wall height) from the top of the walls with modular block and wrapped facing, respectively. The Boussinesq equation was used to calculate the lateral earth pressure induced by footing loading, which approximately matched that measured for the wall with wrapped-around facing, but was quite different from that for the wall with modular block facing. Shallow, middle, and deep slip surfaces were observed in these test models at failure.

This study also investigated the effect of footing loading on global stability of GRR walls with wrapped-around and modular block facing. The limit equilibrium methods (i.e., the Bishop modified method and the Spencer method) included in the ReSSA program was used to determine critical slip surfaces and their corresponding factors of safety of the eight reduced-scale experimental models and ten case histories in the literature. Based on the limit equilibrium analyses, the critical slip surfaces identified by Bishop's modified method and Spencer's two-part wedge

method reasonably agreed with those observed in the walls under footing loading. The data analysis showed an exponential relationship between the calculated factor of safety using the Bishop method and the maximum lateral facing deflection or the surface settlement of the GRR walls under footing loading.

Dedication

The author dedicates this work to his parents.

Acknowledgements

I would like to express my sincere gratitude to my advisor and mentor, Professor. Jie Han, for providing me the opportunity to continue my study at the University of Kansas. His invaluable academic and personal guidance and support throughout my time as a student. He always tried his best to help me develop my strengths, overcome my weaknesses, and prepare for my future career. The time of my study under the guidance of Prof. Han was valuable, enjoyable, and memorable. I also would like to thank my Ph.D. committee members, Professors Robert L. Parsons, Hongyi Cai, Steven D. Schrock, and Shawn Keshmiri for their guidance and help in reviewing this dissertation.

I also want to thank the Geosynthetic Institute, Drs. Robert M. Koerner, and George R. Koerner for providing me the GSI fellowship during my Ph.D. study. Tensar International provided the geogrid samples used in this study. Dr. Hongyi Cai provided the photogrammetry equipment and guidance for the analysis of the images. The current and past laboratory managers and technicians, David Woody, Kent Dye, Matthew Maksimowicz, and Erick Nicholson provided their technical support. I also owe my thanks to Ms. Susan B. Scott, the graduate program coordinator, and Ms. Cathy Johnson, the former financial manager, for their valuable assistance.

I would like to thank the current and past members of the KU Geotechnical Society, Dr. Jamal Kakrasul, and Mr. Mehari Weldu, Ghaith Abdulrasool, Wessam Mohammed, Saif Jawad, Mahdi Al-Naddaf, and Dr. Yan Jiang, provided me their support during the experimental work.

Finally, I would love to appreciate my parents and my brother for their supports.

Contents

Table of Figures

List of Tables

Chapter 1. Introduction

1.1. Background

Geosynthetic-reinforced soil (GRS) is a composite soil mass that includes horizontal layers of geosynthetics as reinforcement in soil (Wu et al., 2006; Han, 2015). The concept of GRS has been employed in the construction of retaining walls, embankments, slopes, and shallow foundations (e.g., Badakhshan and Noorzad, 2017; Jiang et al., 2016; Wayne et al., 1998; Yasrobi et al., 2009b; Rahmaninezhad et al., 2009; Wu et al., 2006). The geosynthetic-reinforced retaining (GRR) walls have been extensively used in transportation systems to support self-weight of backfill soil, roadways and railways, bridges, and traffic loads (e.g., Viswanadham et al., 2017; Jiang et al., 2016; Tatsuoka et al., 2014; Yang et al., 2012; Zhu et al., 2008; Lee and Wu, 2004; Abu-Hejleh et al., 2001). The important factors for global acceptance of GRR walls are cost effectiveness, simple and fast construction, excellent seismic performance, and ability to tolerate large differential settlement (e.g., Leshchinsky, 2014; Lee and Wu, 2004; Sabermahani et al. 2009).

In recent years, there has been an increase in the use of GRR walls as abutments to support shallow foundations of bridges instead of traditional deep foundations, such as piles (Skinner and Rowe, 2005; Lee and Wu, 2004). In this technology, GRR walls support both bridge beams on spread footings constructed directly on the reinforced soil mass and approaching roadway embankments. Two obvious benefits of this technology are to reduce the overall cost of a project as compared with a traditional pile foundation option and minimize bumps at end of bridges (Skinner and Rowe,

2005; Helwany et al., 2003; Abu-Hejleh et al., 2001). Bridge bumps often occur due to the differential settlement between pile-supported abutments and approach embankments.

GRR walls can have rigid or flexible facing. One typical rigid facing is continuous reinforced concrete panels, either precast or cast-in-place (Yang et al., 2009; Lee and Wu, 2004; Tatsuoka et al., 1997). However, flexible facing can be geosynthetic wrapped-around facing, modular concrete blocks, natural rocks, or gabions (Wu et al., 2006; Lee and Wu, 2004). The wrapped-around facing is commonly used for: (1) temporary structures; (2) walls that will be subjected to significant post-construction settlement; (3) walls with low aesthetic requirements; and (4) walls where new facing will be added later for protection and aesthetic appearance to become permanent structures (commonly used in Japan) (Holtz and Lee, 1998).

Although several studies have been conducted to evaluate the behavior of the GRR walls with flexible facing under self-weight or surcharge (e.g., Jiang et al., 2016; Huang et al., 2009; Benjamin et al., 2007; Bathurst et al., 2006; Bathurst et al., 2001), limited experimental studies have been conducted to evaluate the behavior of the GRR walls with different facings under footings. Different from typical GRR walls, GRR abutment walls are generally subjected to high footing loading that are close to the wall facing (Rahmaninezhad et al., 2018; Xiao et al., 2016). Therefore, not only the stability of the GRR walls but also the bearing capacity and settlement of the bridge footing should be considered in design (Xiao et al., 2016). Although the GRR abutment walls with flexible facing have been the subject of a few studies, the interaction between the GRR wall and the footing is not well understood. In addition, very few studies have investigated the behavior of the GRR walls with wrapped-around facing (Rahmaninezhad et al., 2018; Benjamim et al., 2007).

Abu-Hejleh et al. (2001) monitored the performance of a 5.9-m-high GRR abutment wall with hollow-cored concrete block facing during construction and service. Yoo and Kim (2008) reported the behavior of a 5.6-m-high full-scale GRR wall in a tiered configuration under a square footing. Xiao et al. (2016) evaluated the relationship between the ultimate bearing capacity of the strip footing and its offset distance to the modular block facing, and identified failure modes of the GRR walls under footing loading. Kakrasul et al. (2016) studied the performance of GRR abutment walls with modular block facing and limited-space retained fill under a strip footing in the laboratory. In addition, a few numerical studies have been carried out on the GRR abutment walls (e.g., Leshchinsky, 2014; Fakharian and Attar 2007; Wu et al., 2006; Skinner and Rowe, 2005; Helwany et al., 2003).

1.2. Objective

The objectives of this study were: (1) to investigate stress distributions and pullout responses of geogrid in soil using different normal loading methods, (2) to evaluate the combined effects on measured strains of geogrid, (3) to evaluate the performance of GRR abutment walls with wrapped-around facing or modular concrete block facing subjected to footing loading, (4) to develop a method to predict the maximum lateral deflection of the GRR walls under footing loading, and (5) to develop a method to predict the settlement of the footing on the GRR walls.

1.3. Research Methodology

The research methodology adopted for this study includes: (1) a literature review of relevant

studies related to the GRR walls subjected to footing loading, including full-scale, reduced-scale tests and numerical modeling of these walls; (2) laboratory tests to determine the properties of a backfill material (i.e., the Kansas River Sand) and a reinforcement material (geogrid) used in the tests, (3) reduced-scale model tests of GRR abutment walls with wrapped-around or modular concrete block facing subjected to static footing loading in a test box under a plane strain condition, and (4) an analytical study on footing settlement and lateral facing deflection of GRR abutment walls with wrapped-around and modular concrete block facing.

Chapter 2. Literature Review

2.1. Introduction

Geosynthetic-reinforced retaining (GRR) walls are extensively used for highways, bridge abutments, and service roads throughout the world. This chapter presents a review of previous studies on the behavior of geosynthetic-reinforced retaining walls subjected to footing loading. The literature review of this study summarizes the following topics: (1) design methods; (2) reduced-scale model tests; (3) full-scale tests; (4) field tests; (5) numerical analysis; and (6) calculation methods for lateral deflection of wall facing.

2.2. Design Methods

2.2.1. Federal Highway Administration (FHWA) method (Berg et al., 2009)

According to the FHWA design guideline, the tensile force in reinforcement in mechanically-stabilized earth (MSE) walls is computed based on the lateral pressure, σ_h, and the tributary area of this pressure. For the MSE walls subjected to a spread footing loading, the FHWA guideline proposed the following equation to calculate the lateral earth pressure at each level:

$$\sigma_h = K\,(\gamma Z + \Delta\sigma_v) + \Delta\sigma_h \qquad \textbf{Eq. 2.1}$$

where σ_h = the lateral earth pressure, K = coefficient of the lateral pressure, γZ = vertical pressure due to the overburden pressure, $\Delta\sigma_v$ = induced vertical pressure due to the vertical surcharge

assuming a 2 (vertical):1 (horizontal) pyramidal distribution, $\Delta\sigma_h$ = induced lateral pressure due to the vertical surcharge. **Figure 2.1** shows the distribution of vertical stresses from footing loading on top of the MSE wall at a distribution angle of 2 (vertical):1 (horizontal), which is often referred to as a 2:1 distribution method.

Based on the FHWA guideline for an MSE wall with inextensible, steel reinforcements, there is a bi-linear failure plane starting from the edge of the footing as shown in Error! Reference s ource not found.**2.** The base width of the bridge support spread footing (b_f) and the location of the toe of the footing with respect to the back face of the walls panels (c_f) is usually such that $b_f + c_f$ is greater than one third of the height of the wall ($H/3$), as shown in Error! Reference source not f ound.**2**. The location the critical failure surface that occurred at the location of the maximum tensile force line has to be modified to extend to the back edge of the spread footing. The variation of K_r/K_a and F^* also should be modified (Error! Reference source not found.).

Similar shifts in the location of the critical failure surface to the back of the footing have been observed for the walls with extensible reinforcement under the footing loading. Therefore, the critical failure surface should also be modified for extensible reinforcement if the back edge of the footing extends beyond a distance of $H \times tan(45\text{-}\phi/2)$ from the wall face. These critical failure surfaces should be compared with the critical failure surface from compound stability analysis and the more conservative profile of the failure surface should be selected.

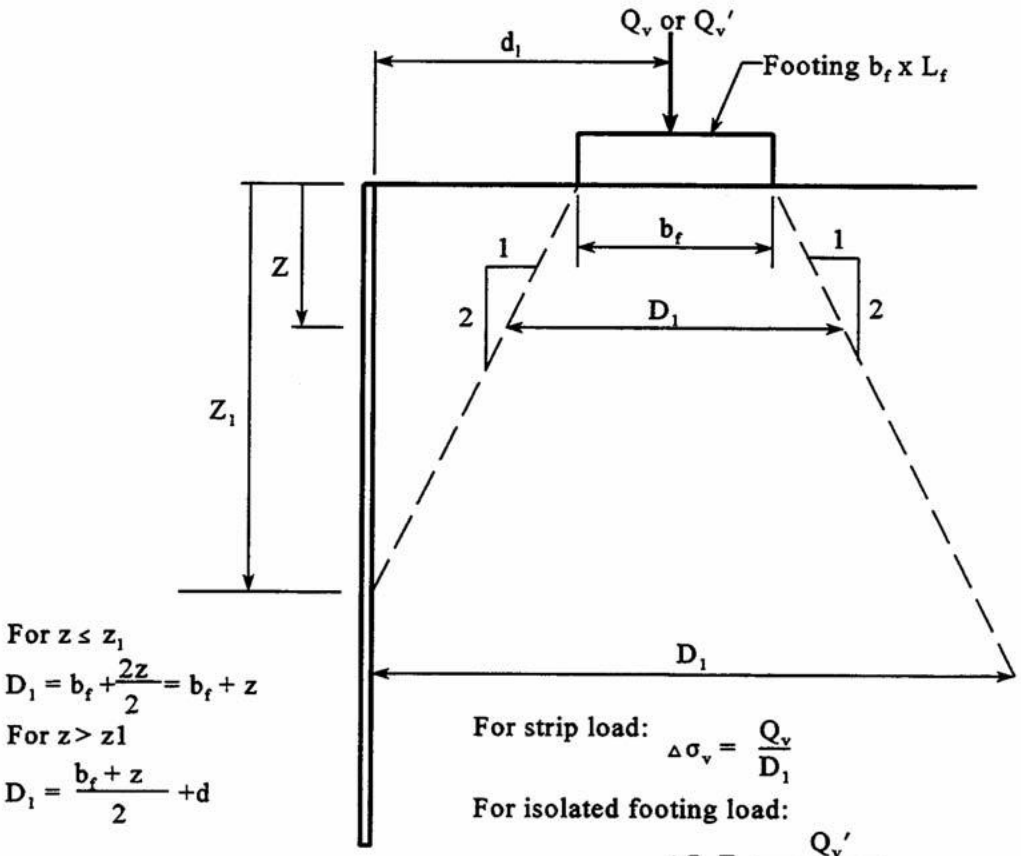

Where: D_1 = Effective width of applied load at any depth, calculated as shown above
b_f = Width of applied load. For footings which are eccentrically loaded (e.g., bridge abutment footings), set b_f equal to the equivalent footing width B′ by reducing it by 2e′, where e′ is the eccentricity of the footing load (i.e., b_f - 2e′).
L_f = Length of footing
Q_v = Load per linear meter of strip footing
Q_v' = Load on isolated rectangular footing or point load
z_1 = Depth where effective width intersects back of wall face = $2d_1 - b_f$

Assume the increased vertical stress due to the surcharge load has no influence on stresses used to evaluate internal stability if the surcharge load is located behind the reinforced soil mass. For external stability, assume the surcharge has no influence if it is located outside the active zone behind the wall.

Figure 2.1. Distribution of stresses from a concentrated vertical load (after Berg et al. 2009)

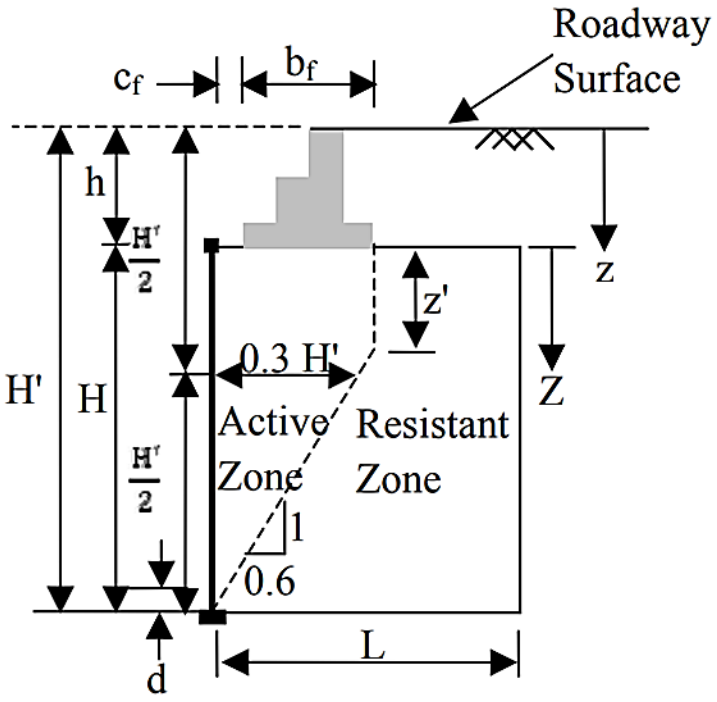

Figure 2.2. Geometry definition, location of critical failure surface (after Berg et al. 2009)

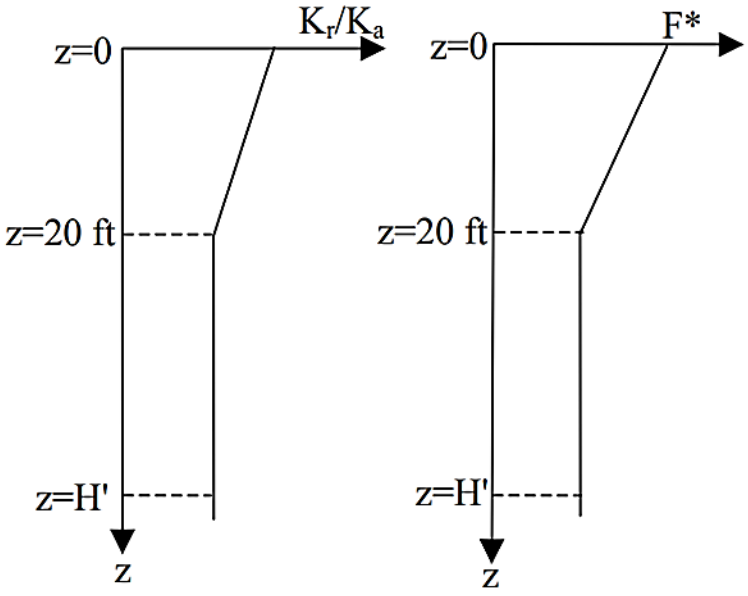

Figure 2.3. Variation of K_r and F* parameters for analysis of a MSEW abutment on spread footing (after Berg et al. 2009)

2.3. Reduced-scale model tests

2.3.1. Xiao et al. (2016)

Xiao et al. (2016) presented the results of a series of reduced-scale model tests on the GRS walls with modular block facing subjected to static loading to investigate the effects of the offset distance of a strip footing, the width of the strip footing, the length of geogrid reinforcement, and the connection mode between geogrid and facing, on the ultimate bearing capacities of the strip footings on the GRS walls. The model walls were designed at a scale factor of 1/5 to typical field walls. Xiao et al. (2016) found that the footings on the GRS walls with 0.7H (H is the wall height) long reinforcement reached the maximum bearing capacities at the offset distances of 0.3H and 0.4H in the wall tests with mechanical and frictional connections, respectively. Moreover, when these walls had the geogrids with longer reinforcement length (2H), the ultimate bearing capacity increased with the offset distance of the footing and became constant when the offset was larger than 0.4H.

2.3.2. Kakrasul (2018)

Kakrasul (2018) conducted a series of laboratory model tests to investigate the performance of geosynthetic reinforced retaining (GRR) walls with modular block facing constructed with limited fill space subjected to strip footing loading. Kakrasul (2018) constructed and tested the model tests under a plane strain condition. The model walls were 1.0 m high and 0.45 m wide. In each model test, a load was applied on the top of the wall through a 200 mm wide rigid plate to simulate a strip footing. Earth pressure distributions, wall facing deflections, and footing settlements were

measured during the footing loading tests. Kakrasul (2018) found the limited widths of the retained and the reinforced fill affected the internal stability of the wall, the lateral deflection of wall facing, and the settlement of the footing. **Figure 2.4** shows the cross-section of one model wall. This wall had a height of 1.0 m, vertical spacing between geogrid layers of 0.2 m, an offset distance of the footing to the back of the wall facing of 0.05 m, a geogrid length of 0.5 m. Error! Reference source n ot found.shows the pressure-settlement curves of the footing on the model wall. **Figure 2.6** shows the lateral deflections along the height of the wall with modular block facing, under the applied footing pressures.

Kakrasul (2018) reported that reduction of the wall width from 0.5H to 0.3H (H is the wall height) resulted in excessive wall deflection and footing settlement, and even sudden failure of the model wall. On the other hand, the test results revealed that connecting geosynthetic reinforcement to the stable retained medium resulted in substantial reduction in the lateral deflection of the wall facing and the settlement of the footing. In addition, Kakrasul (2018) found that the vertical earth pressures along the depth of the model tests increased with the increase of the depth in the model and the applied footing load. Likewise, the lateral earth pressures on the wall facing along the depth in the model test increased with the applied footing load.

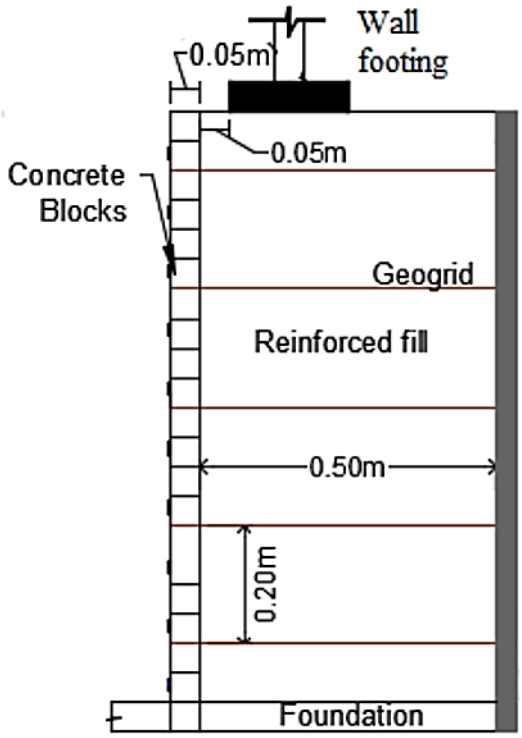

Figure 2. 4. Cross-section of one model wall (after Kakrasul 2018)

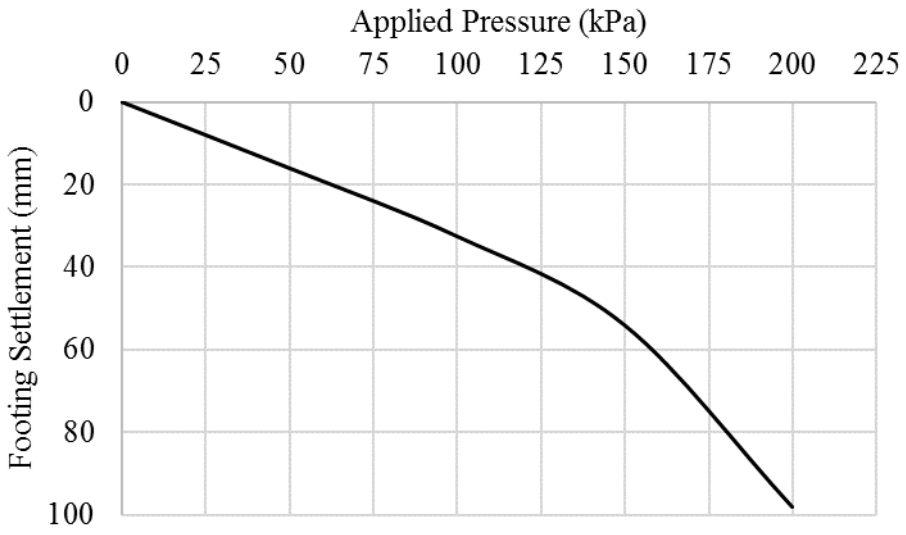

Figure 2. 5. Pressure-settlement curve of footing on model wall (after Kakrasul 2018)

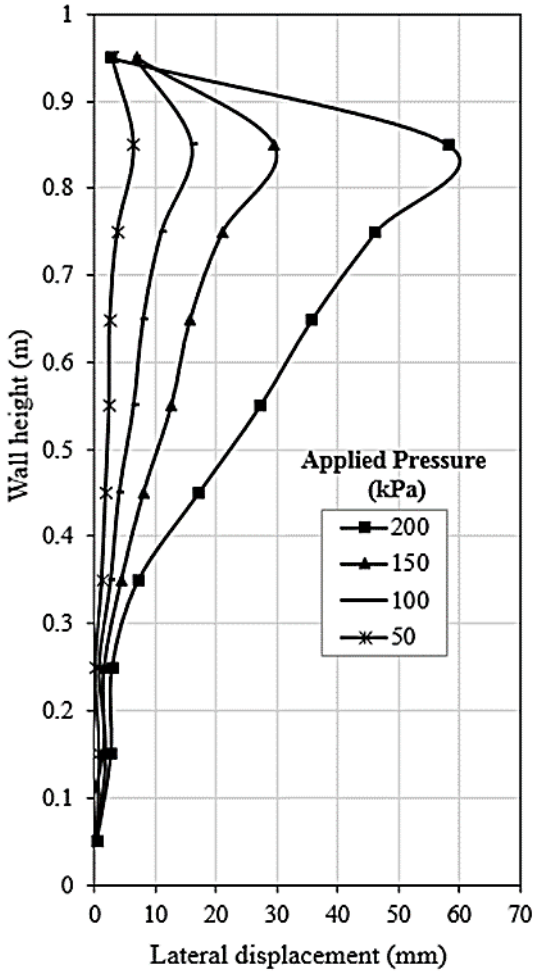

Figure 2.6. Deflections of the model wall with modular block facing under the applied pressures (after Kakrasul 2018)

2.4. Full-scale model tests

2.4.1 Werner and Resl (1986)

Werner and Resl (1986) evaluated the performance of a 2.4-m-high full-scale field geotextile-reinforced wall with wrapped around facing under static footing loading. **Figure 2.7** shows the front view and the cross-section of the wall. A polypropylene needle-punched nonwoven geotextile with the ultimate tensile strength of 16 kN/m was used as reinforcement. This wall was subjected to climatic fluctuations and environmental influences for three years until loading in 1984. The settlement of the footing and the maximum lateral deflection of the facing induced by footing loading of 130 kPa were 160 and 110 mm, respectively.

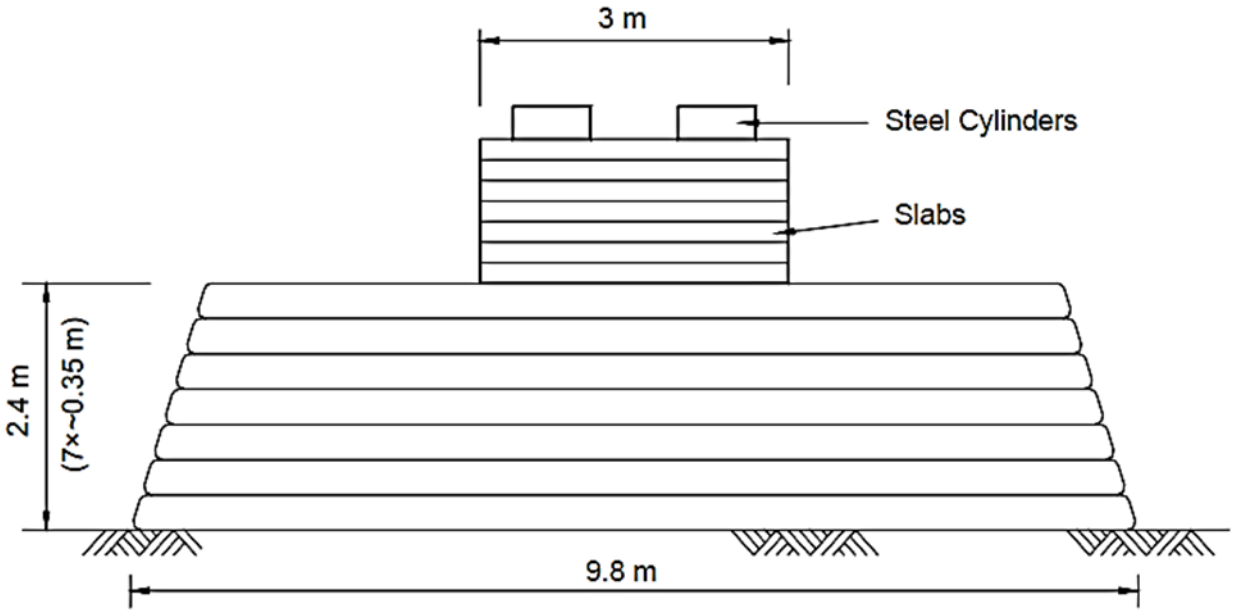

(a)

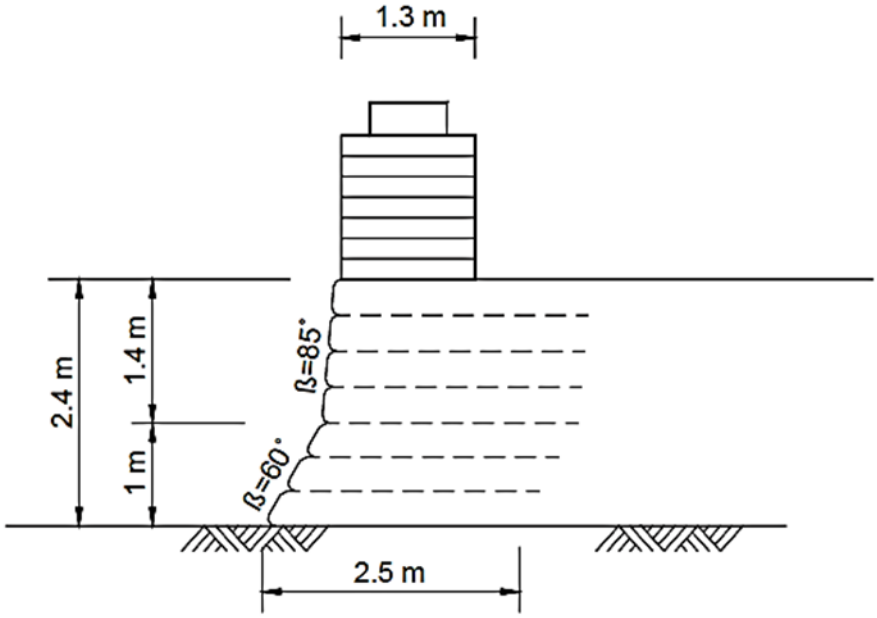

(b)

Figure 2. 7. Wall: (a) front view and (b) cross-section (after Werner and Resl 1986)

2.4.2 Benigni et al. (1996)

Benigni et al. (1996) conducted a footing loading test on a 5-m high test wall, referred to as the Trento test wall, with wrapped-around facing in Northern Italy. During the construction, the wall face was supported by high wooden support. The length of the geosynthetic reinforcement layers was 2 m. The underlying geosynthetic reinforcements were wrapped around at the face and extended 2 m inside the backfill, as shown in **Figure 2.8**. The vertical spacing between the reinforcement layers was 0.5 m. Reinforcements were not anchored in the backfill. The maximum footing settlement under the footing pressure of 84 kPa was 50 mm. Benigni et al. (1996) reported that the wall did not collapse under the applied load, although large movements were recorded. Despite the lateral and vertical deflections were not recovered upon unloading, it appeared that the wall had sustained almost no damage.

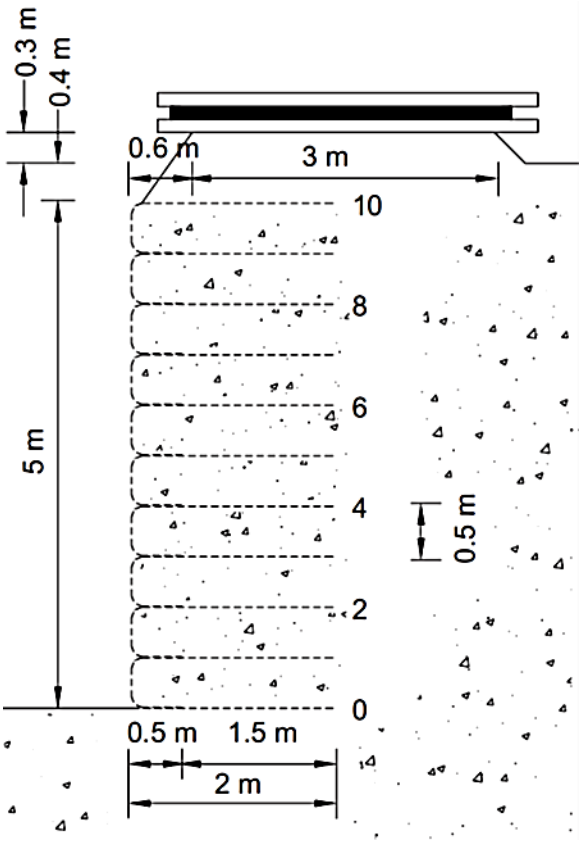

Figure 2. 8. Trento test wall (after Benigni et al. 1996)

2.4.3 Gotteland et al. (1997)

Gotteland et al. (1997) studied the failure behavior of two top-loaded reinforced walls with cellular facing, referred to as the ‘‘Garden’’ program. One of the walls was reinforced with a low strength nonwoven geotextile (NW). However, a high strength woven geotextile (W) was used in the other wall. The model walls had a height of 4.35 m, vertical spacing between geogrid layers of 0.29 m, a offset distance of the footing to the back of the wall facing of 1.5 m, and a footing width of 1.0 m. **Figure 2.9** shows the test walls. Gotteland et al. (1997) reported that the critical loads at the break point for the NW wall and the W wall were 140 and 123 kN/m, respectively. The corresponding settlements of the NW wall and the W wall were 36 and 33 mm, respectively. **Figure**

2.10 shows the pressure-settlement curves of the footing on the NW wall and W wall. **Figure 2.11** also shows the lateral deflections of the NW wall and W wall under the applied load of 190 kN/m. The results show the maximum lateral deflections in the NW wall and W wall occurred at the level of 3.0 and 4.2 m from the toe of the walls.

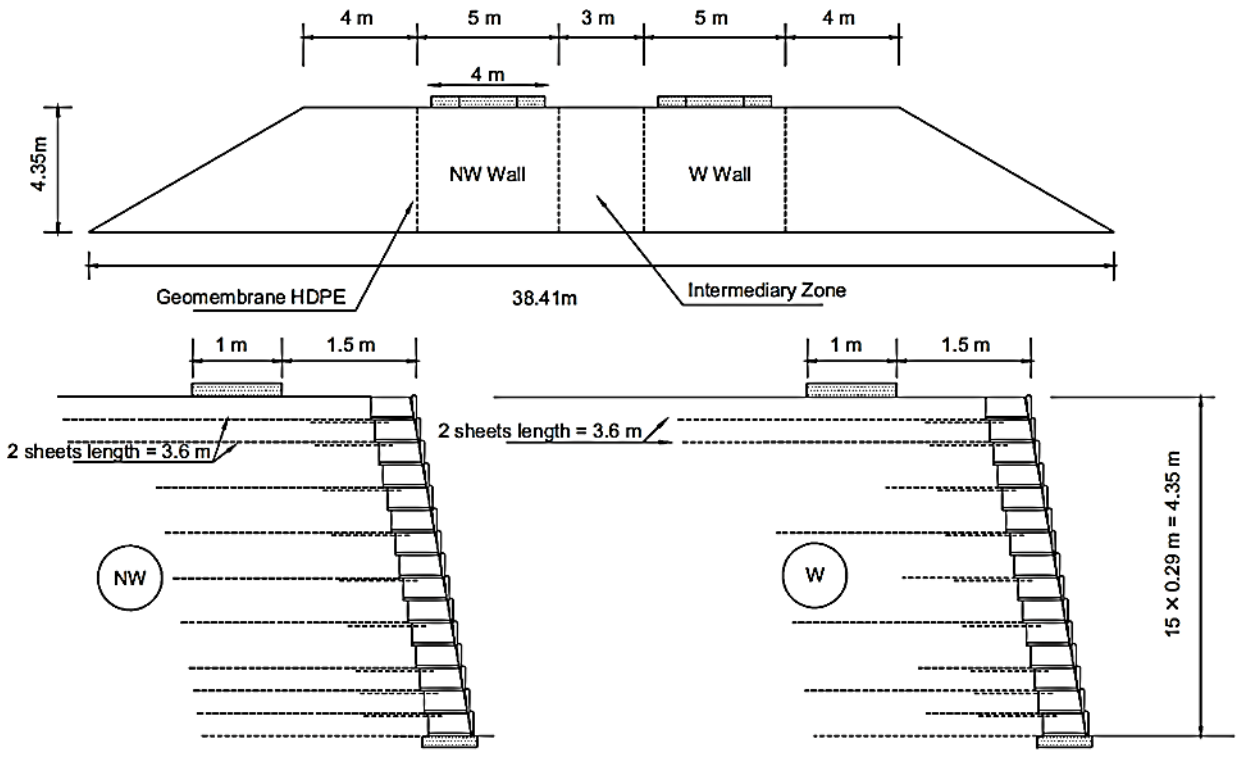

Figure 2.9. Garden test walls (after Gotteland et al. 1997)

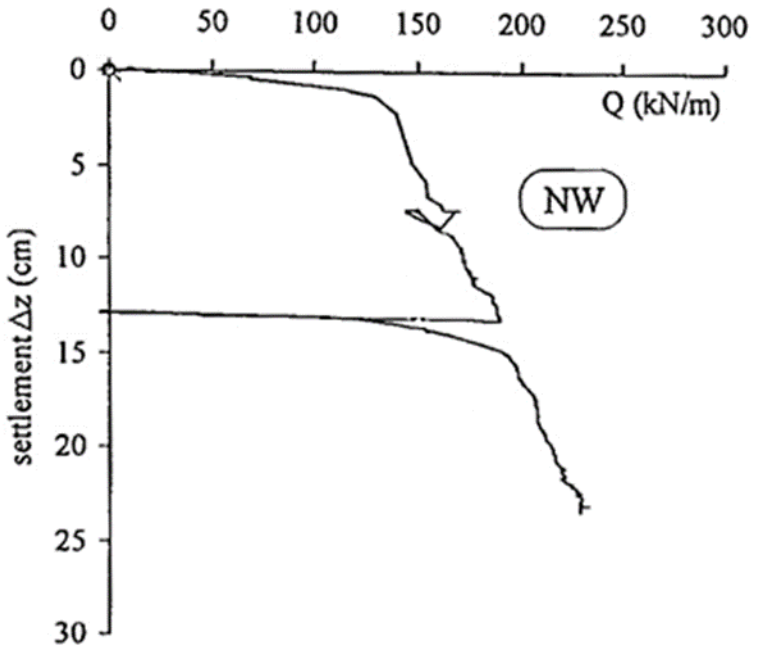

(a)

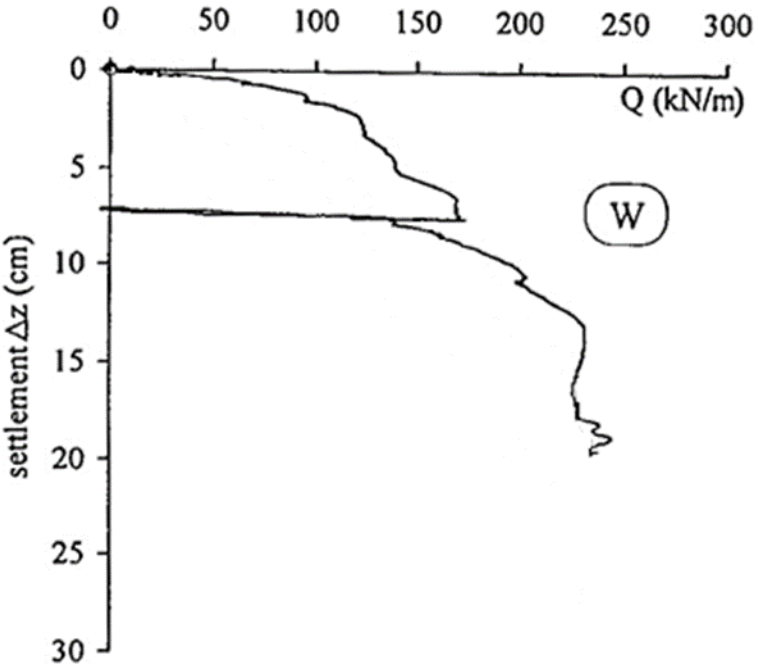

(b)

Figure 2.10. Pressure-settlement curves: (a) NW wall and (b) W wall (after Gotteland et al. 1997)

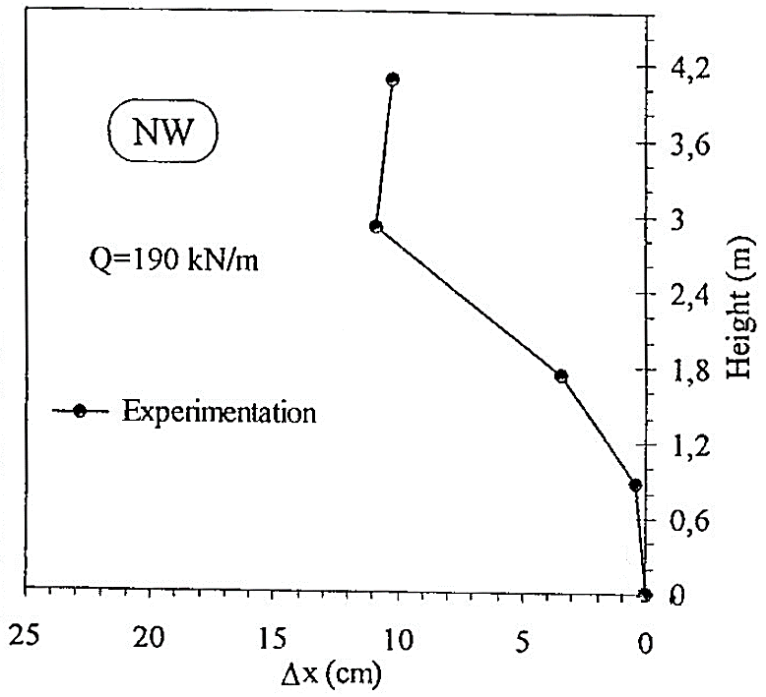

(a)

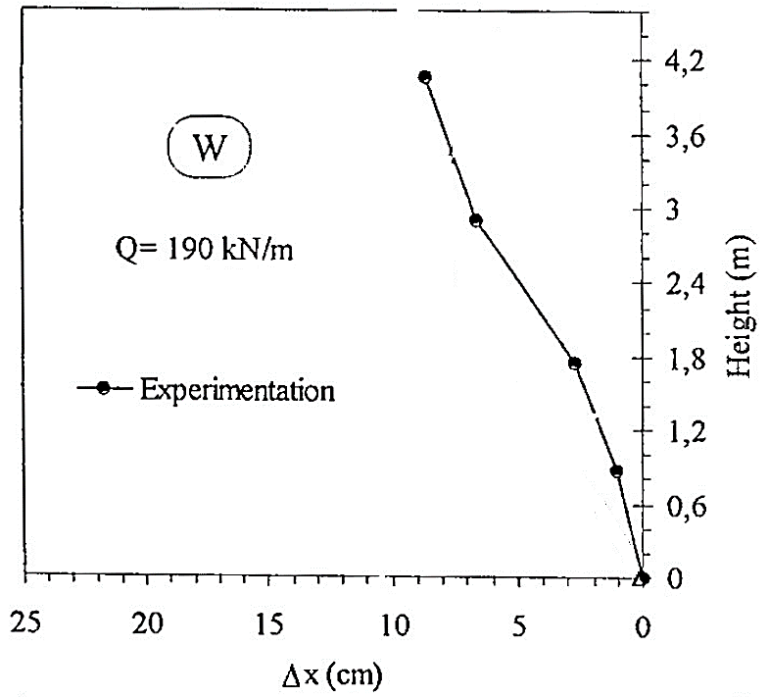

(b)

Figure 2.11. Measured lateral deflections for: (a) NW wall and (b) W wall (after Gotteland et al. 1997)

2.4.4. Yoo and Kim (2008)

Yoo and Kim (2008) investigated the performance of a 5-m-high full-scale two-tier geogrid-reinforced retaining wall with modular block facing subjected to various levels of surface load (**Figure 2.12**). Yoo and Kim (2008) evaluated the performance of the wall under the surcharge load in terms of the lateral facing deflections and the strains in geogrid. They found that the surcharge load-induced reinforcement strains exponentially decreased with depth, which is in a good agreement in qualitative terms with that assumed in the FHWA design guideline. Yoo and Kim (2008) also reported the measured lateral deflections along the height of the wall, as shown in **Figure 2.13**. The maximum deflection of 1.7 mm was reported at the top of the upper tier while the deflections were smaller than 0.5 mm in the lower tier under the surcharge load of 60.5 kPa (384 kN).

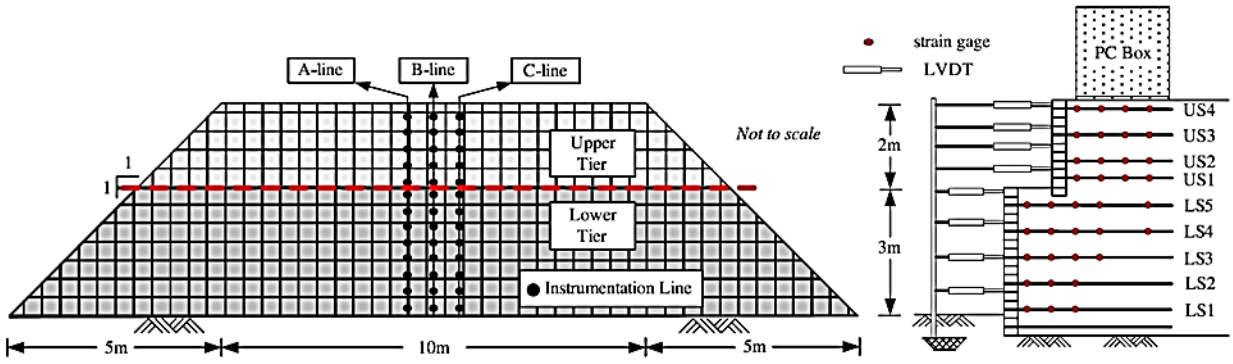

Figure 2. 12. Instrumentation layout (after Yoo and Kim, 2008)

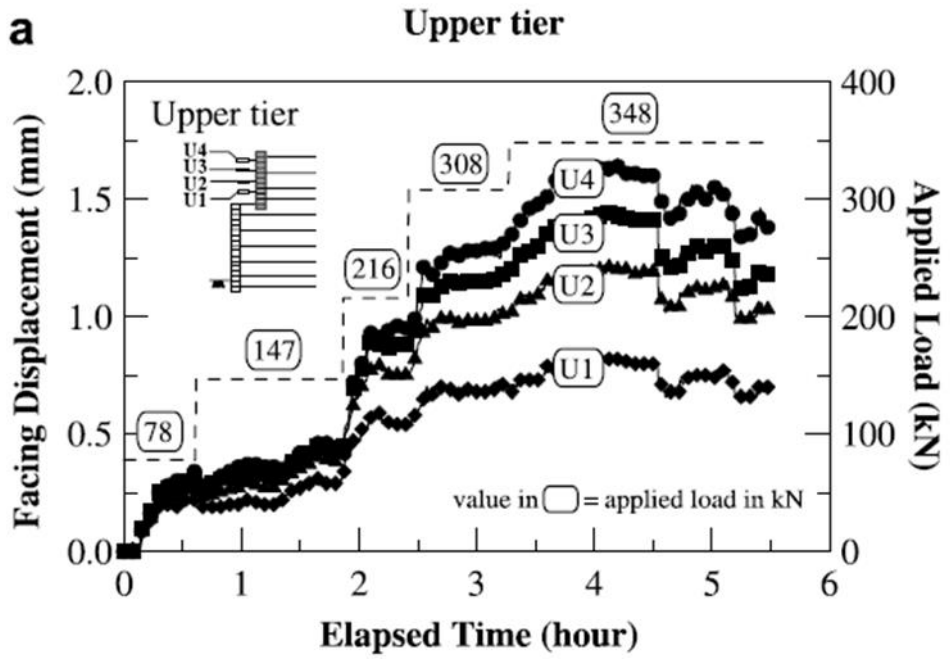

(a)

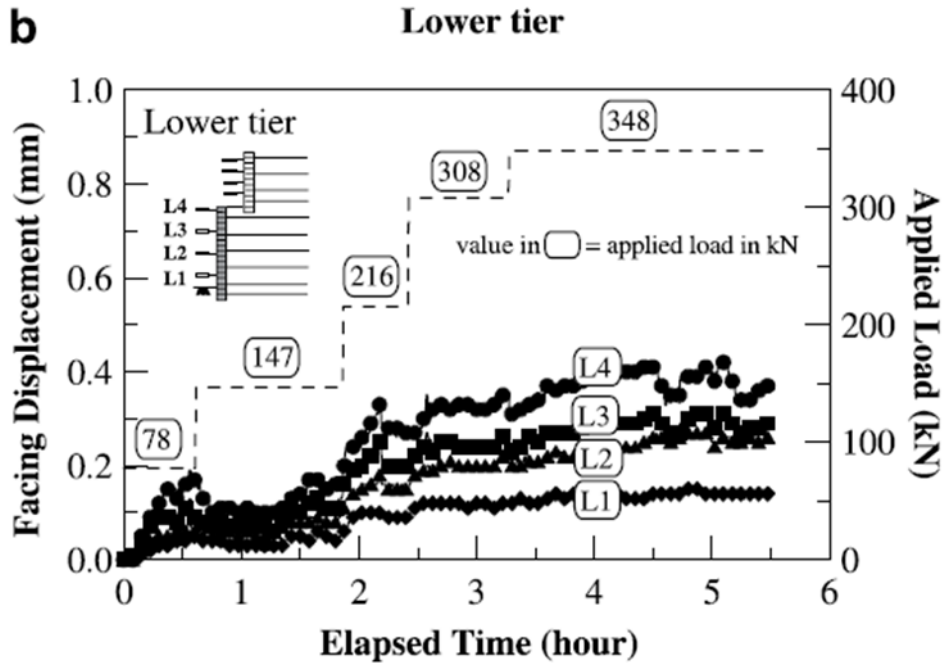

(b)

Figure 2. 13. Lateral deflection of the wall in: (a) upper tier and (b) lower tier (after Yoo and Kim, 2008)

2.4.5. Ahmadi and Bezuijen (2018)

Ahmadi and Bezuijen (2018) carried out a footing loading test on a full-scale MSE wall with a plywood face. In this study, Ahmadi and Bezuijen (2018) considered the plywood face as flexible facing. The full-scale model had a height of 4 m, a width of 4 m, vertical spacing between geogrid layers of 0.5 m, an offset distance of the footing to the back of the wall facing of 0.5 m, and a footing width of 1 m. A poorly-graded sand (SP) without fines, according to the Unified Soil Classification System (USCS), was used as a backfill material. A polyester geogrid (PET) had a maximum tensile strength of 40 kN/m (at the break strain of less than 6.6%). Error! Reference s ource not found.**2.14** shows the configuration of the MSE walls. Ahmadi and Bezuijen (2018) reported the lateral wall deflection under a strip footing load as shown in **Figure 2.15**. The results shows the maximum lateral deflections occurred at 0.2H from the top of the wall. The strains in the reinforcement were measured to evaluate the behavior of the geogrids during the construction and under strip footing loading. They found that the maximum strains in the reinforcement occurred in the upper layers under the strip footing load.

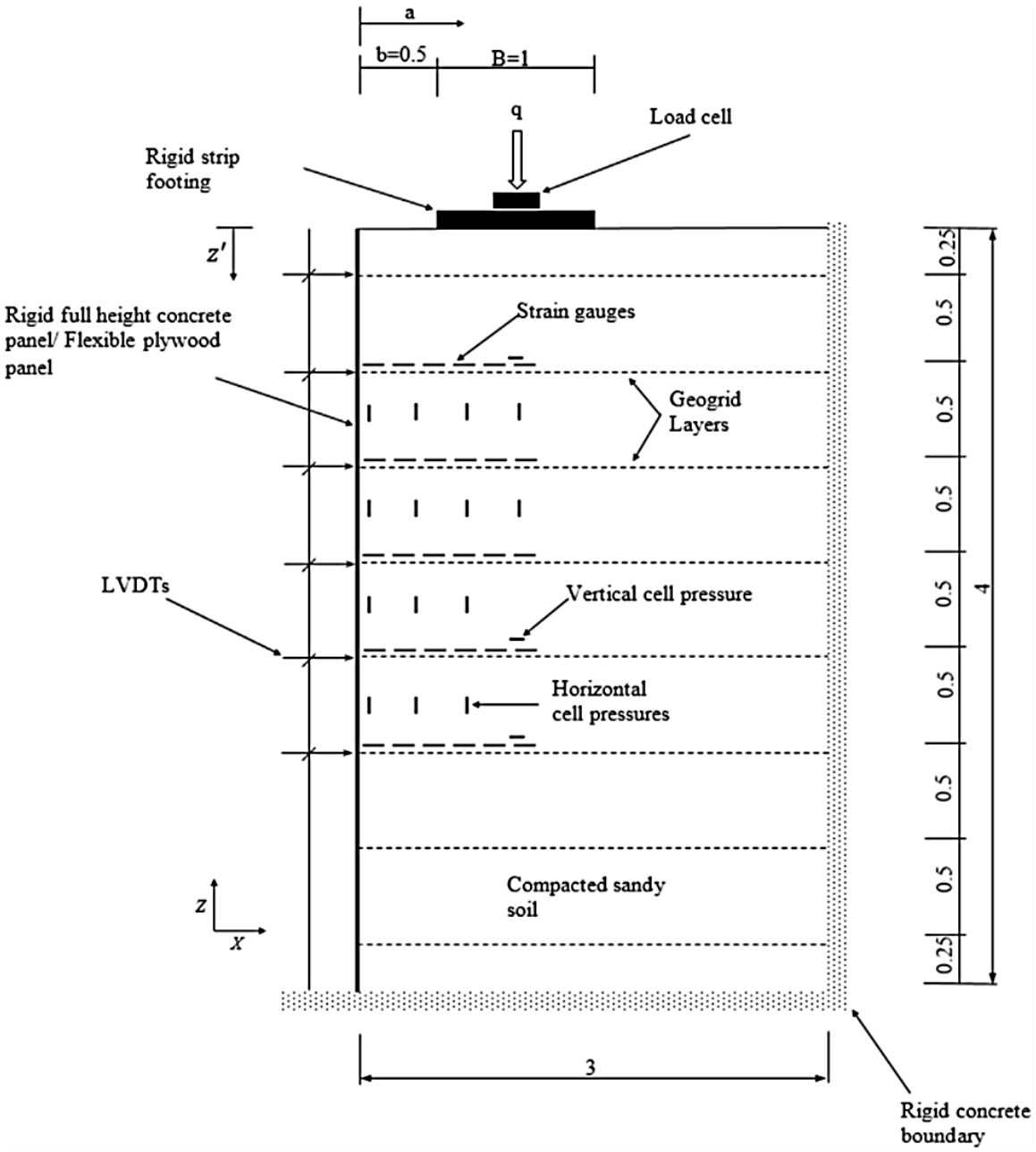

Figure 2.14. Test layout for full-scale models and instruments (all dimensions in meters) (after Ahmadi and Bezuijen 2018)

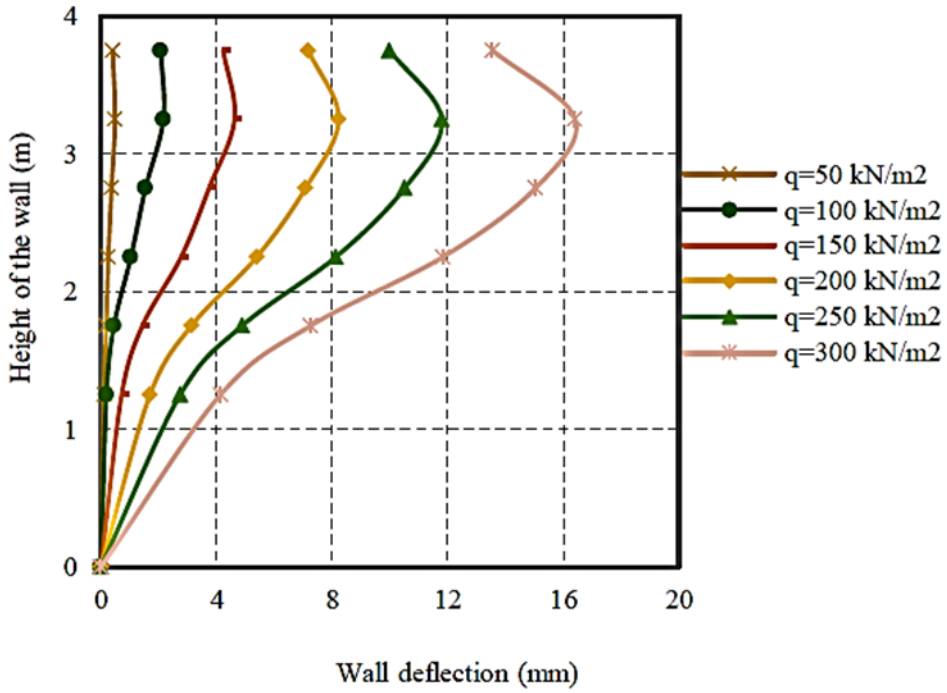

Figure 2.15. Lateral wall deflection under the strip footing load (after Ahmadi and Bezuijen 2018)

2.5. Field studies

2.5.1. Abu-Hejleh et al. (2001)

The Founders/Meadows bridge was the first major bridge in the United States supported by spread footings on GRS walls with modular block facing. Abu-Hejleh et al. (2001) evaluated the performance of these GRS walls by measuring the movements of the wall facing, settlement of the bridge footing, distributions of the vertical and lateral earth pressures during the construction and while in service as shown in Error! Reference source not found.**2.16**. The reinforced soil zone b ehind and below the bridge abutment had a trapezoid-shaped reinforcement layout, in which reinforcement length increased linearly from 8.0 m at the bottom with a 1:1 slope toward the top. The reinforcement lengths for the abutment wall were 11–13 m. The centerline of the bridge abutment wall and the edge of the foundation were placed 3.1 and 1.35 m from the front of wall face, respectively. The reinforcement spacing was 0.4 m. The backfill soil was a mixture of gravel (35%), sand (54%), and fines (11%). Abu-Hejleh et al. (2001) did not find any potential for overturning of the structure (due to the flexibility of the GRS wall system and the reduction of loads behind and against the wall facing). Moreover, they found that the measured bearing pressures were well below the allowable soil bearing capacity. **Figure 2.17** shows that the maximum outward movements experienced during the placement of the bridge superstructure were approximately 7–9 mm.

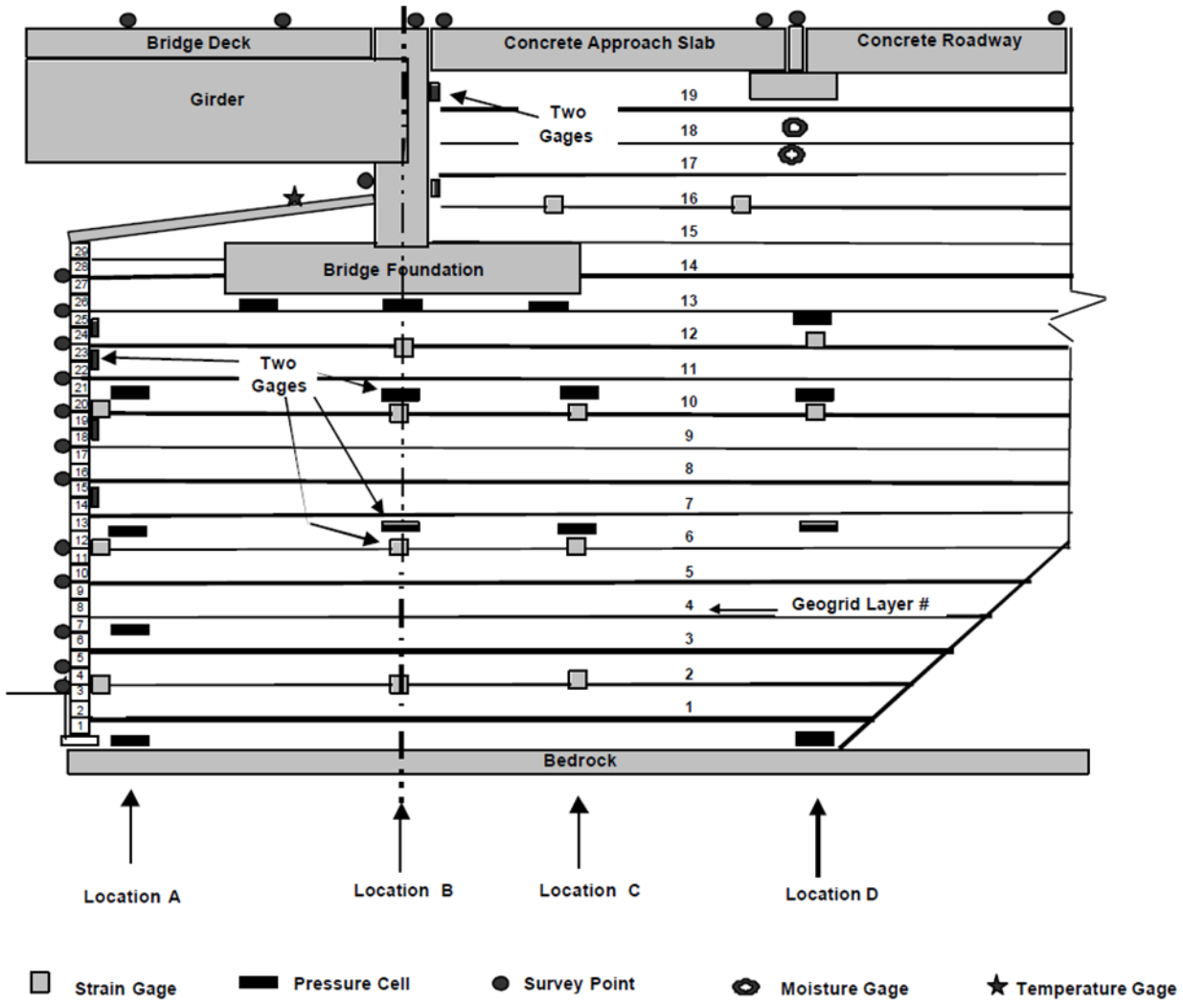

Figure 2.16. Instrumentation layout (after Abu-Hejleh et al. 2001)

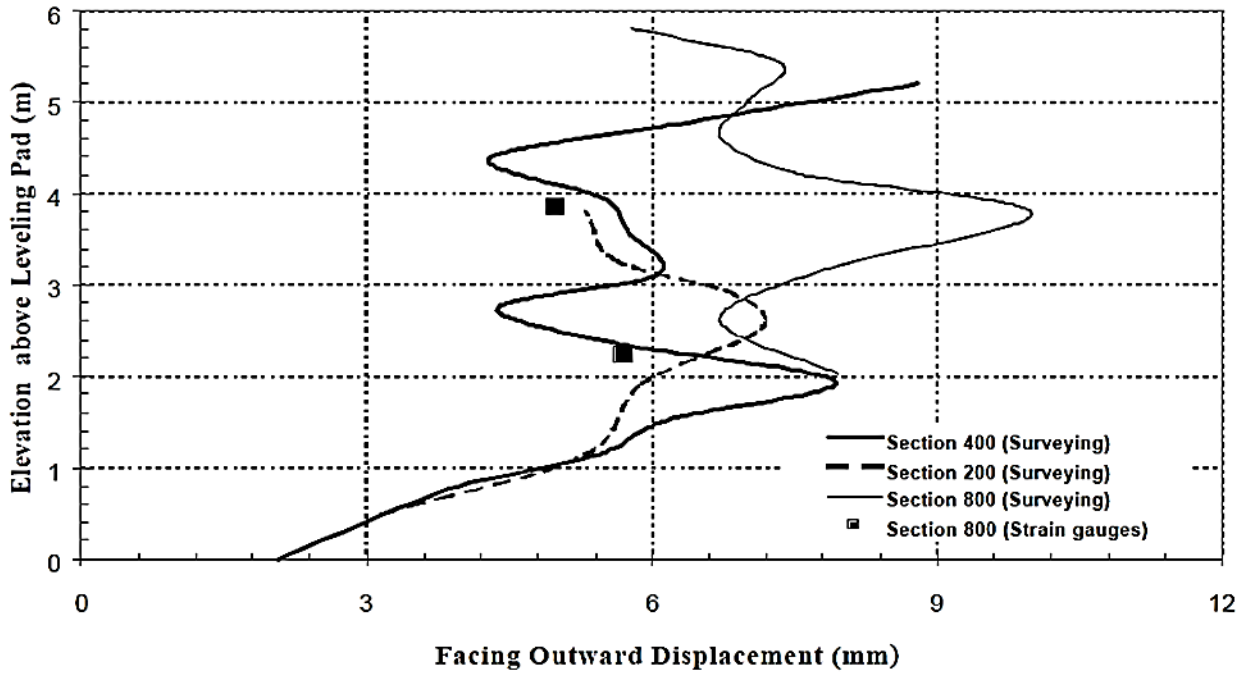

Figure 2. 17. Facing deflection (after Abu-Hejleh et al. 2001)

2.5.2. Lindsey (2015)

Lindsey (2015) monitored the performance of a Geosynthetic Reinforced Soil – Integrated Bridge System (GRS-IBS) for the Rustic Road Bridge as shown in **Figure 2.18**. The GRS-IBS wall was a mechanically stabilized earth (MSE) wall used as the abutment with a bridge deck placed on top. Lindsey (2015) used inclinometers, settlement plates, crack gages, and surface survey points for field monitoring. Lindsey (2015) reported that the maximum lateral deflection of the wall facing under the footing pressure of 85 kPa was 7.62 mm.

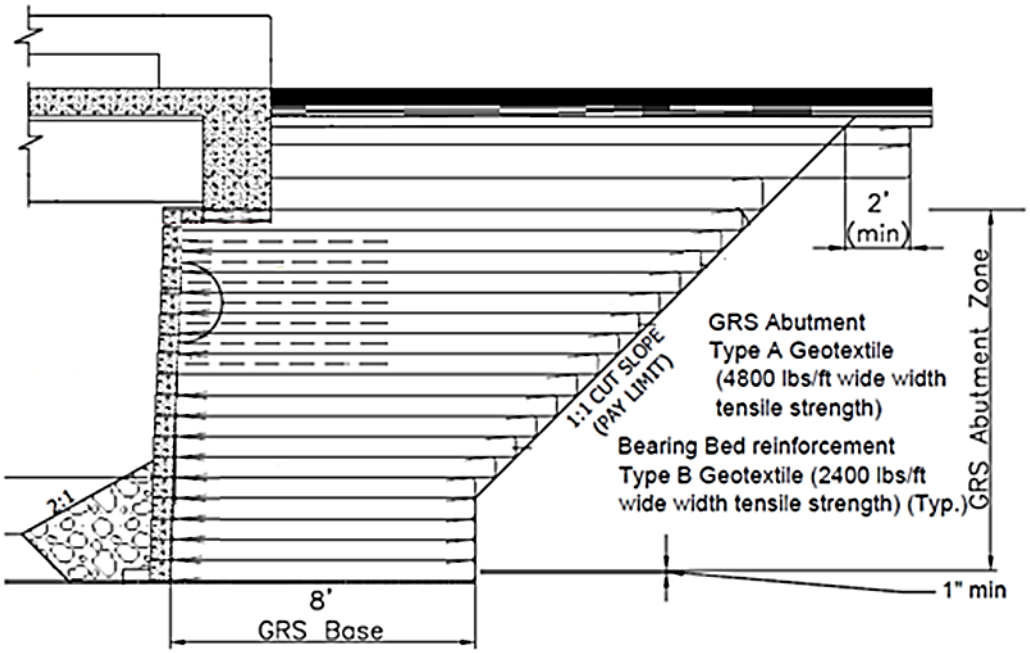

Figure 2. 18. GRS-IBS (after Lindsey 2015)

2.5.3. Saghebfar et al. (2017)

Saghebfar et al. (2017) monitored the performance of a GRS-IBS by measuring bridge deflections, settlements, strains along the reinforcement, vertical and lateral stresses within the abutment, and pore water pressures. **Figure 2.19** shows the cross-section of the GRS-IBS. Saghebfar et al. (2017) reported that the maximum lateral movement occurred near the top of the wall. Following the construction of the bridge abutment, the facing wall experienced some appreciable outward (away from backfill) lateral deflection, as shown in **Figure 2.20**. **Figure 2.20** also shows that after placing the girders, the lateral movement close to the wall significantly increased.

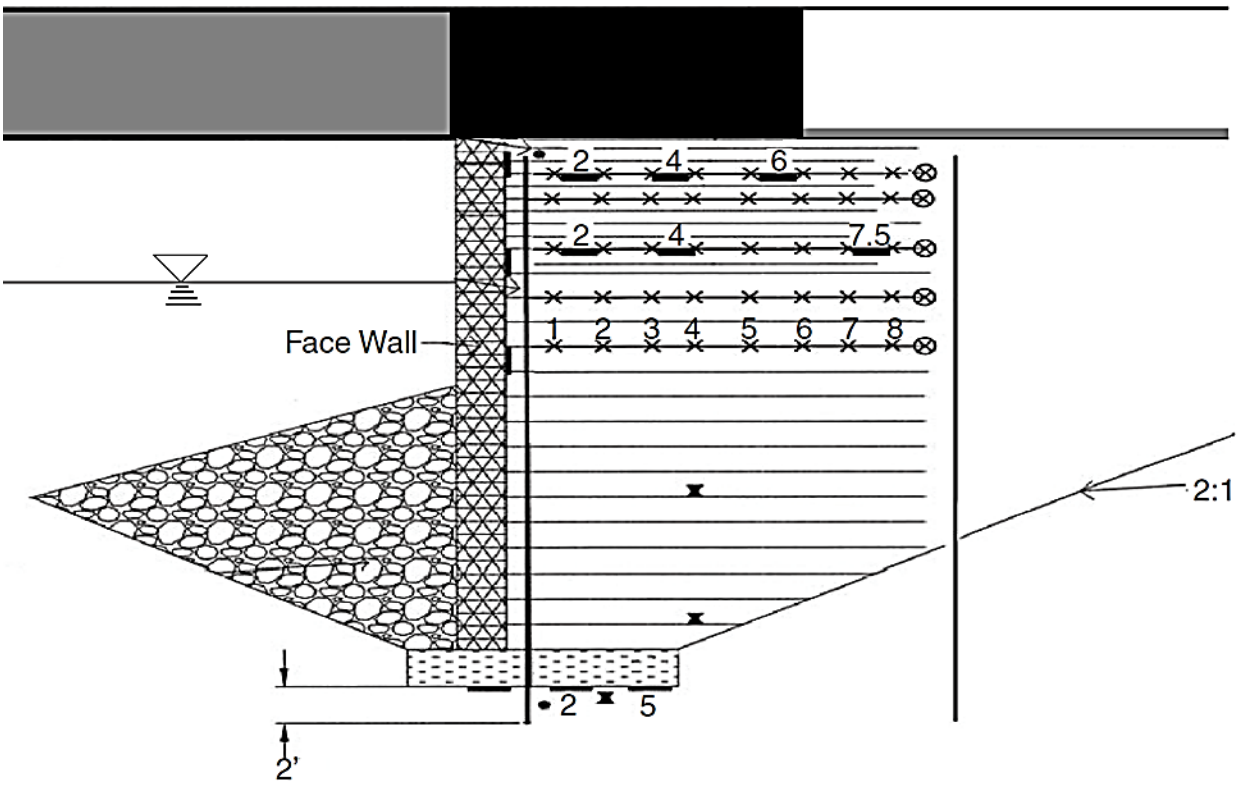

Figure 2. 19. GRS-IBS (after Saghebfar et al. 2017)

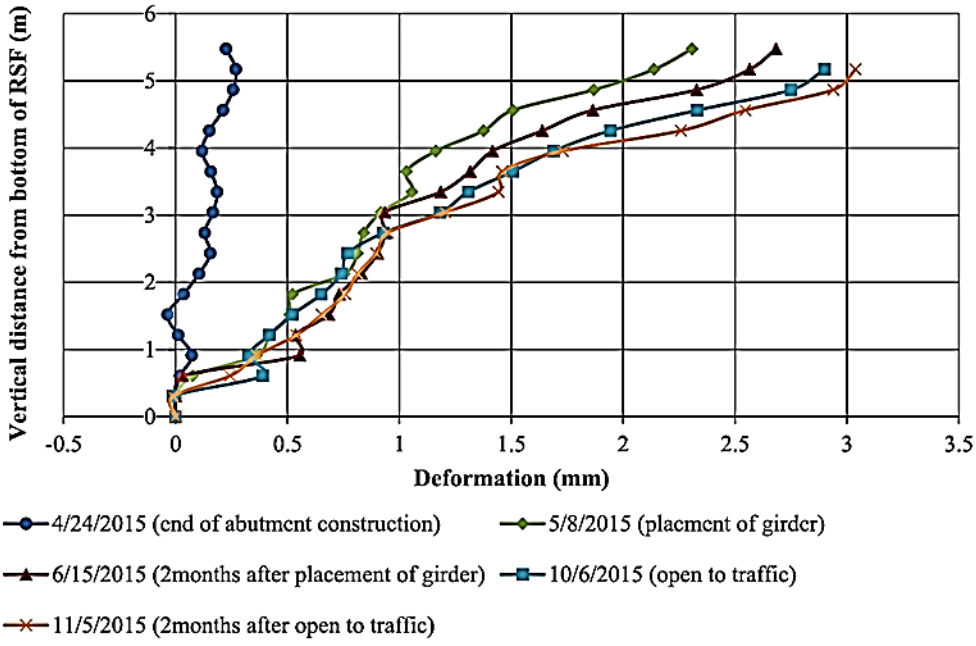

Figure 2. 20. Facing deflection (after Saghebfar et al. 2017)

2.6. Numerical Studies

2.6.1. Gotteland et al. (1997)

Gotteland et al. (1997) conducted a finite different analysis (FDA) and a finite element analysis (FEA) on the walls with nonwoven geotextile (NW) and woven geotextile (W) reinforcements described in **Section 2.4.2**. **Figure 2.21** shows the central slab load-settlement curves. Gotteland et al. (1997) stated that the difficulty to simulate the construction of the walls and particularly the effect of compaction during the construction gradually resulted the differences between the FDA and FEA, as shown in **Figure 2.21**.

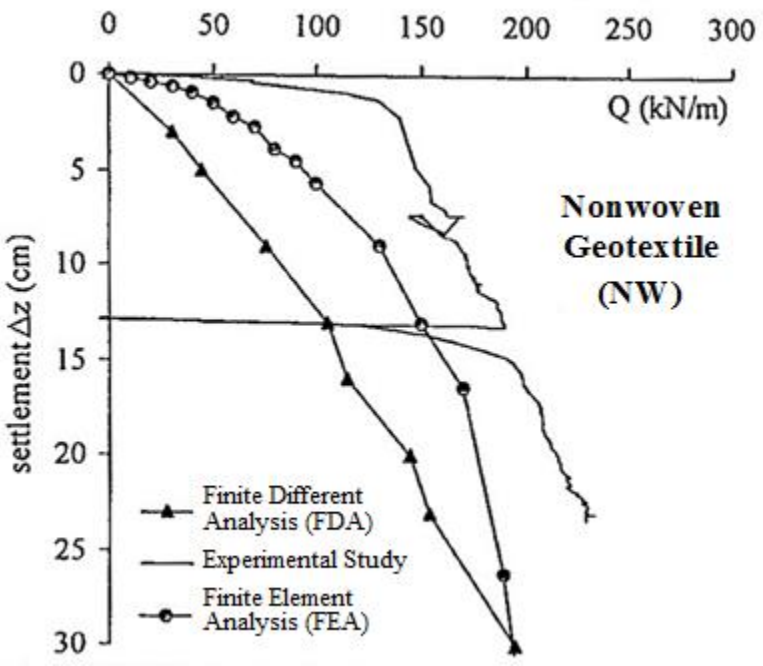

(a)

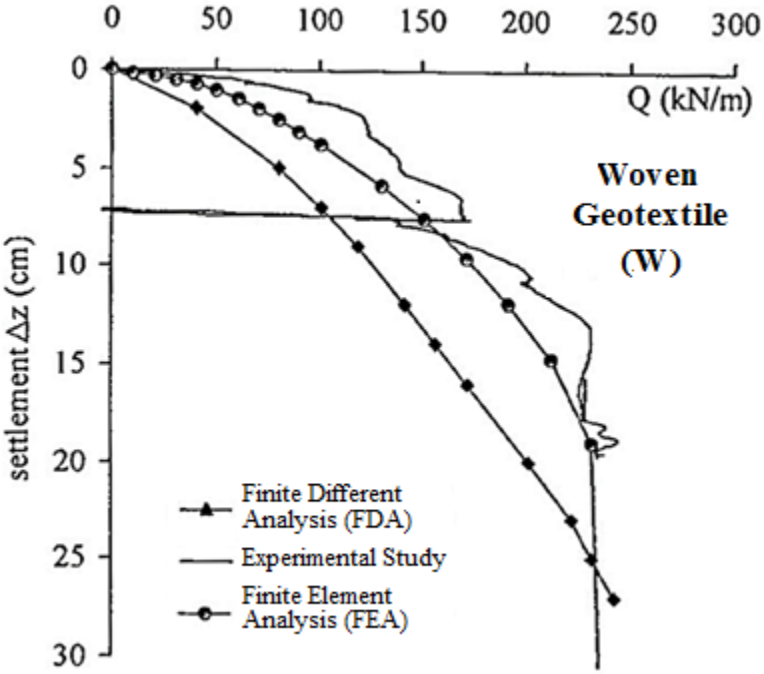

(b)

Figure 2.21. Load-settlement curves: (a) wall with nonwoven geotextile (NW) and (b) wall with woven geotextile (after Gotteland et al. 1997)

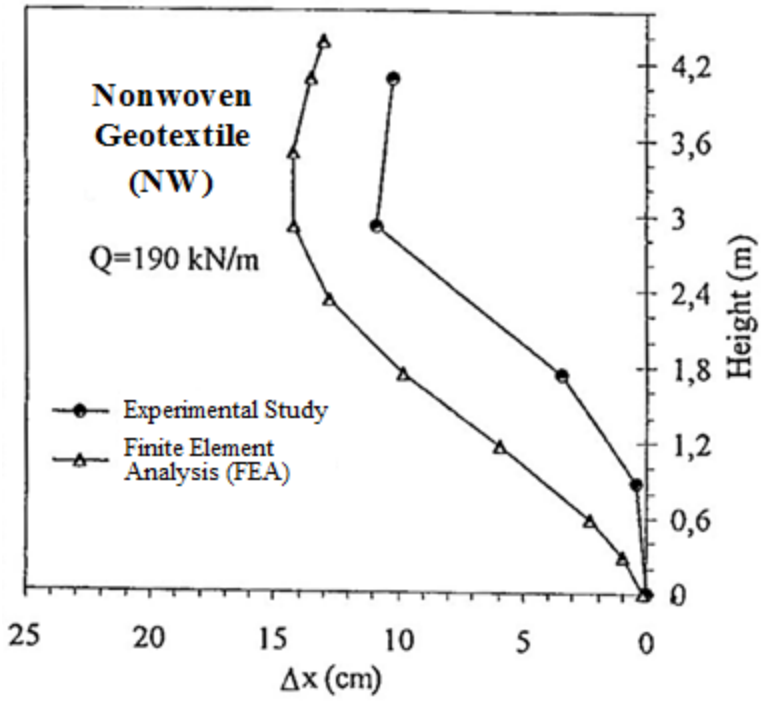

(a)

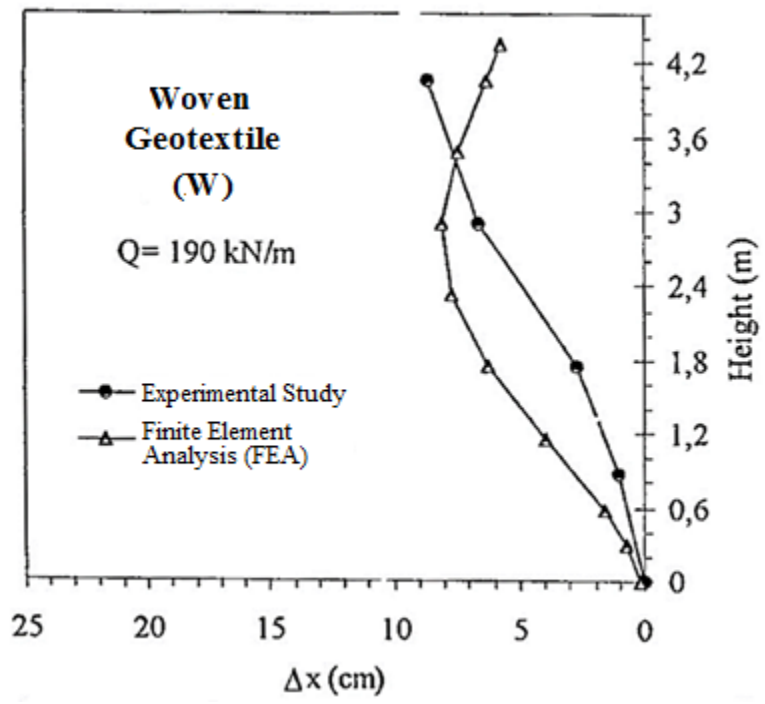

(b)

Figure 2. 22. Lateral deflection: (a) NW wall and (b) W wall (after Gotteland et al. 1997)

2.6.2. Helwani et al. (2003)

Helwani et al. (2003) investigated the potential of GRS bridge abutments to alleviate bridge approach settlements. The finite element method incorporated in the computer program DACSAR was used in this study. This program was first calibrated by comparing its results with the measured data from the Founders/Meadows bridge abutment. Moreover, a parametric study was conducted to evaluate the effects of different foundation soils, ranging from loose sand to stiff clay, on the performance of a GRS abutment.

2.6.3. Wu et al. (2006)

Wu et al. (2006) used the finite element method to investigate the allowable bearing pressures of bridge sills over GRS abutments with flexible facing. A finite element parametric study was conducted to examine the effect of sill type, sill width, soil stiffness/strength, reinforcement spacing, and foundation stiffness on the load-carrying capacity of GRS abutment sills. Wu et al. (2006) determined the allowable bearing pressures of GRS abutments based on two performance criteria: (1) a limiting displacement criterion and (2) a limiting shear strain criterion.

2.6.4. Fakharian and Attar (2007)

Fakharian and Attar (2007) conducted a numerical analysis of a GRS bridge abutment with modular block facing subjected to construction-induced loads and seismic loads. The static performance of the Founders/Meadow bridge abutment during construction and in-service was used for numerical modeling verification purposes. The finite-difference FLAC 2-D program was

used for model verification and parametric studies. They found that the current active earth pressure theories applied to reinforced soil walls significantly overestimate the horizontal reinforcement forces as compared with the measurements and the numerical model predictions.

2.6.5. Helwani et al. (2007)

Helwani et al. (2007) conducted a finite element analysis of two full-scale loading tests of GRS bridge abutments with modular block facing using the computer program Dyna3d. The effects of the backfill properties, reinforcement stiffness properties, and reinforcement vertical spacing were investigated on the performance of these bridge abutments subjected to live and dead loads from a bridge superstructure.

2.6.6. Xie and Leshchinsky (2015)

Xie and Leshchinsky (2015) conducted a parametric analysis study on the effects of reinforcement spacing, reinforcement strength, and footing location on the bearing capacity and factor of safety of footing placed upon the reinforced soil of MSE walls. Xie and Leshchinsky (2015) found that increasing the reinforcement strength provided increased stability and bearing capacity in context of constant surcharge or increasing surcharge, respectively. Moreover, Xie and Leshchinsky (2015) found increased distance between the footing and the wall facing allows for increased bearing capacity of factor of safety as it reduces the influence of the wall, transitioning the critical collapse mechanism to a bearing capacity failure. In addition, they stated that the non-uniform reinforcement spacing produced an efficient design of surcharged MSE walls.

2.6.7. Fakharian and Kashkooli (2018)

Fakharian and Kashkooli (2018) conducted a finite different analysis on the behavior of a reinforced soil abutment wall of a single-span bridge under seismic excitations. The abutment wall had a height of 7 m as shown in **Figure 2.23**. The foundation soil type was soft to medium stiff clayey deposit with a high groundwater level. Fakharian and Kashkooli (2018) reported the post-cyclic facing lateral deflections and bridge deck footing settlements, and the seismic behavior of the wall. **Figure 2.24** shows that at the end of construction, the maximum lateral facing deflection occurred at the mid-height. Due to the eccentricity of the deck load under a static condition, the bridge deck footing had a clockwise rotation at the end of construction, as shown in **Figure 2.25**.

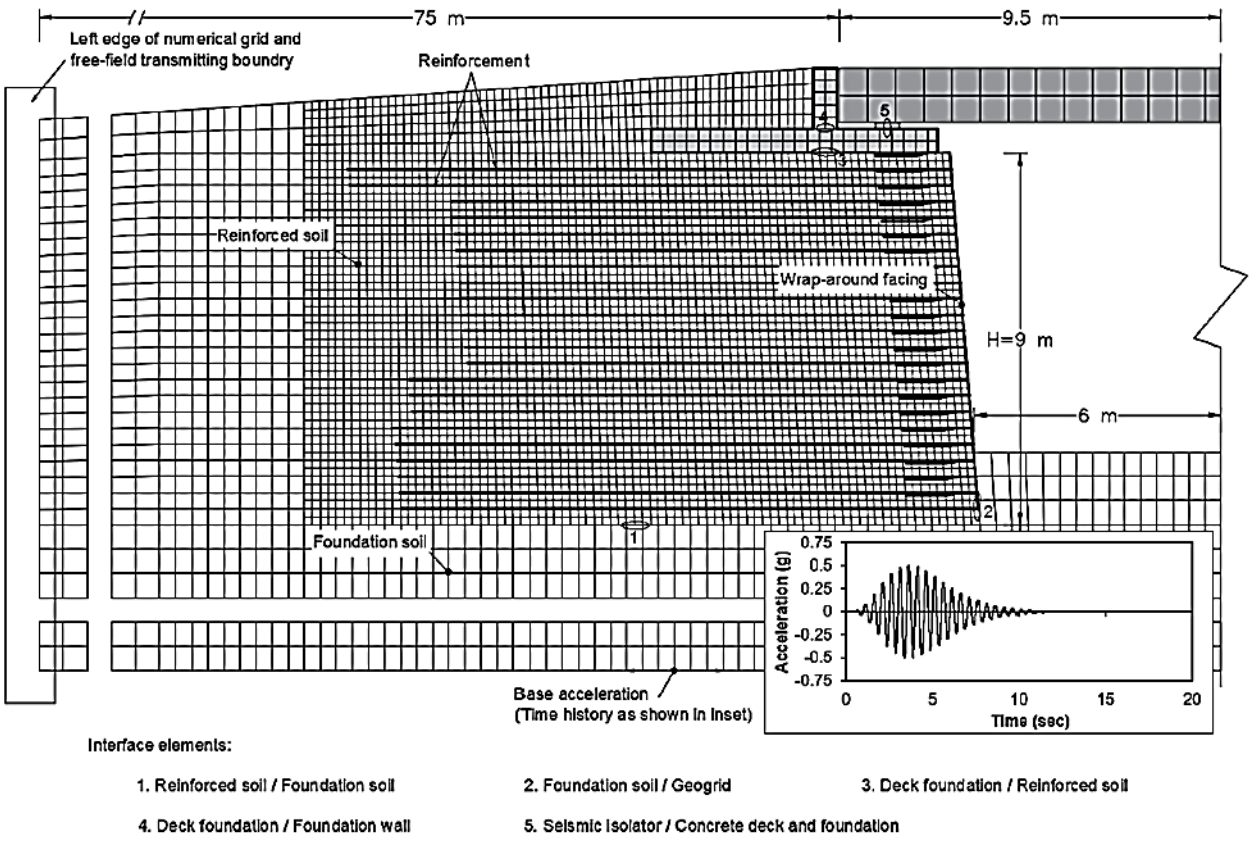

Figure 2.23. Grid, interface elements, boundary conditions, and seismic loading of the numerical model (after Fakharian and Kashkooli 2018)

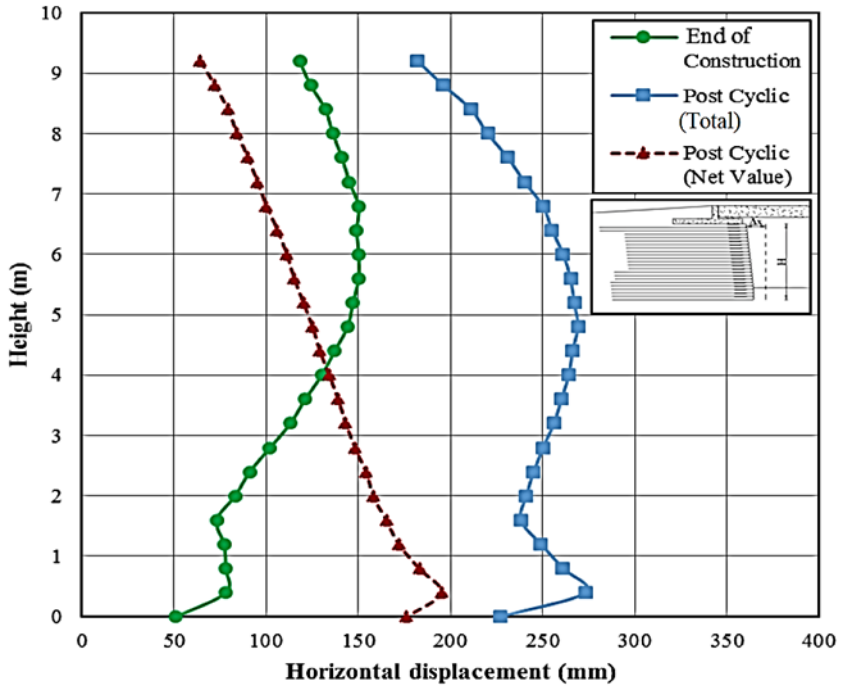

Figure 2.24. Facing deflection profile before and after seismic excitations (after Fakharian and Kashkooli 2018)

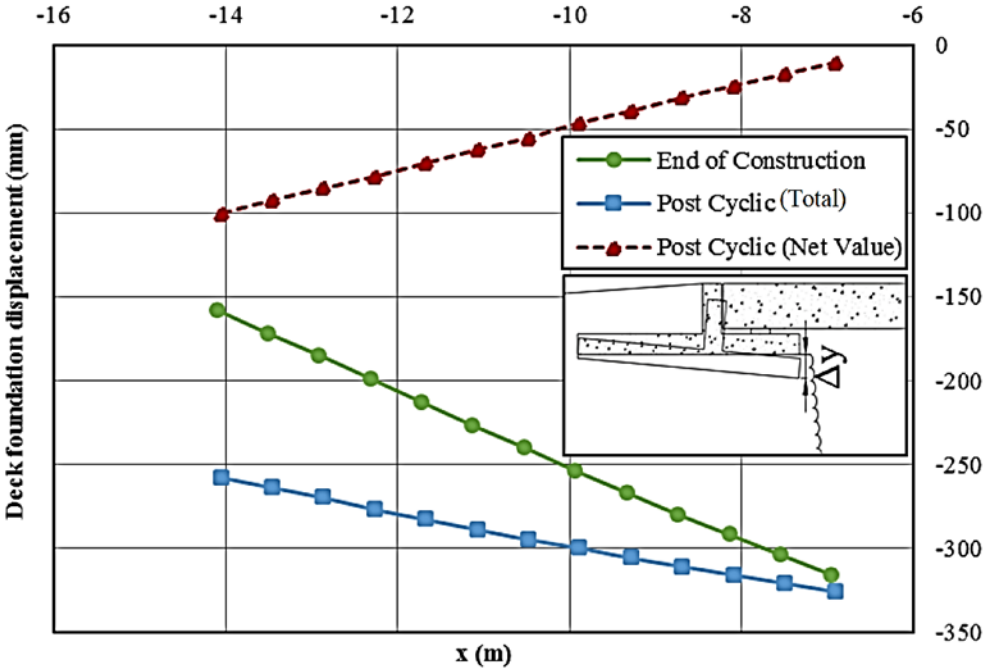

Figure 2.25. Settlements and rotation of bridge deck footing (after Fakharian and Kashkooli 2018)

2.7. Methods for Predicting Lateral Deflection of Wall Facing

2.7.1. Jewell-Milligan method (Jewell, 1988; Jewell and Milligan, 1989)

Jewell (1988) and Jewell and Milligan (1989) proposed design charts for estimating lateral facing deflections of walls based on the analysis of stresses and displacements in a reinforced soil mass. The design charts show the graphical relationships between a normalized deflection factor, $\delta_h K_r / H P_b$, and the normalized depth, *Z/H*, where δ_h = lateral deflection of the facing, K_r = stiffness of the reinforcement, P_b = calculated reinforcement tensile force at the base of the wall, Z = depth from the top of the wall, and H = height of the wall.

2.7.2. Geoservice method (Giroud, 1989)

Giroud (1989) developed the Geoservice method based on a limit equilibrium analysis to calculate lateral deflections of reinforced retaining walls or abutments by using the maximum strain generated in reinforcement layers and assuming a triangular distribution of strain in the reinforcements. Error! Reference source not found.**2.26** shows the assumed strain distribution for c alculating wall lateral movement as follows:

$$\delta_h = \frac{\varepsilon_d L}{2} \qquad \textbf{Eq. 2.2}$$

where δ_h = lateral deflection, and ε_d = strain limit or maximum strain in each layer of reinforcement (ε_{max}), and L = length of reinforcement. Giroud (1989) suggested that when the

reinforcement strain is unknown, the lateral deflection can be determined by first choosing a strain limit for the reinforcement that is usually less than 10%. The limit of strain depends on the type of wall facing, the deflection tolerance, and the type of reinforcement.

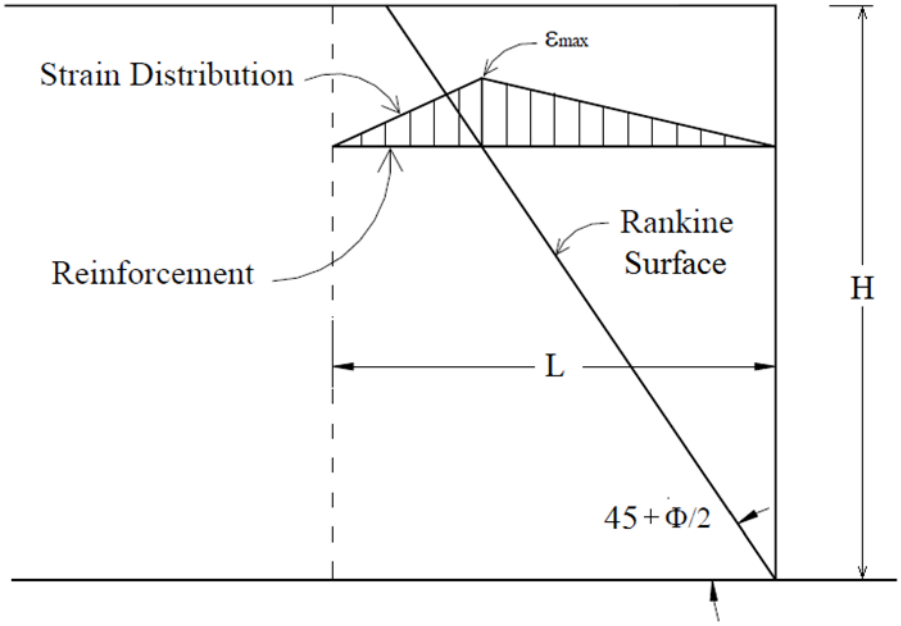

Figure 2.26. Strain distribution assumption in the Geoservices Method

2.7.3. FHWA Method (Christopher et al., 1990)

Christopher et al. (1990) suggested an empirical method for calculating the maximum lateral deflection of a reinforced retaining wall during construction. This method correlates the ratio of the reinforcement length (L) to the height of the wall (H) with deflection coefficient of reinforced soil wall (δ_R). Error! Reference source not found.**2.27** presents the relationship between L/H and

δR, the empirically derived relative displacement coefficient. The curve in Error! Reference source not found.**2.27** has been approximated by a fourth-order polynomial equation:

$$\delta_R = 11.81\left(\frac{L}{H}\right)^4 - 42.25\left(\frac{L}{H}\right)^3 + 57.16\left(\frac{L}{H}\right)^2 - 35.45\left(\frac{L}{H}\right) + 9.47 \qquad \textbf{Eq. 2.3}$$

where δ_R = deflection coefficient of reinforced retaining wall; *L* = length of reinforcement; *H* = height of wall. The value of *L/H* should be between 0.30 and 1.17. The maximum lateral wall displacement, δ_{max} can be estimated from by the following equation:

$$\delta_{max} = \delta_R\left(\frac{H}{75}\right) \qquad for\ extensible\ reinforcement \qquad \textbf{Eq. 2.4}$$

$$\delta_{max} = \delta_R\left(\frac{H}{250}\right) \qquad for\ inextensible\ reinforcement \qquad \textbf{Eq. 2.5}$$

Christopher et al. (1990) suggested that for a 6.1 m high wall, each extra 19.15 kPa of surcharge load increases the relative deflection by approximately 25%; however, the surcharge effect may be greater for higher walls.

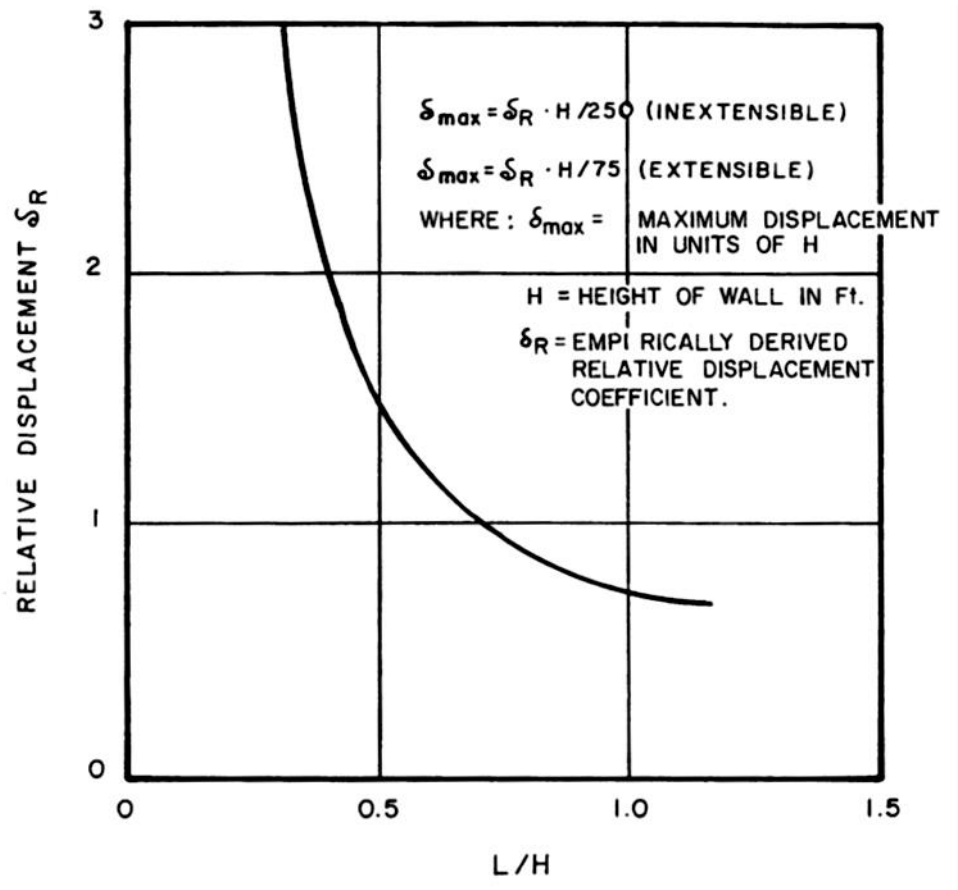

Figure 2. 27. Empirical curve for estimating maximum wall movement during construction in the FHWA method (after Christopher et al., 1990)

2.7.4. CTI Method (Wu, 1994)

Wu (1994) developed a semi-empirical relationship for calculating the lateral deflections of reinforced retaining walls and abutments for the Colorado Transportation Institute (CTI). The CTI method is a service load-based design method. The maximum lateral displacement of a wall can be calculated by the following equation:

$$\delta_{max} = \frac{\varepsilon_d H}{1.25} \qquad \textbf{Eq. 2.6}$$

where δ_{max} = maximum lateral deflection; and ε_d = strain limit or maximum strain in each layer of reinforcement; and *H* = height of the wall. For a reasonable estimation, the strain limit should be between 1 to 3% for permanent walls and up to 10% for temporary walls. This method can be applied to walls of less than 6.1 m high with flexible facing, such as walls with wrapped-around facing. For walls with modular block facing, however, the maximum lateral deflection is approximately 15% smaller than the calculated deflection.

2.7.5. FHWA Method for Geosynthetic Reinforced Soil Integrated Bridge System (GRS-IBS)

Adams et al. (2011) considers a zero volume change in the geosynthetic-reinforced abutment walls to predict the lateral facing deflections of the walls. FHWA provides the following equation to estimate the maximum lateral deflection by assuming the volume loss at the top of the abutment due to the settlement equal to the volume gain at the face due to lateral deflection:

$$D_L = \frac{2\, b_q\, D_v}{H} \qquad \textbf{Eq. 2.7}$$

where *bq* is the width of the load along the top of the wall, D_v is the vertical settlement above the wall, and H is the wall height.

Chapter 3: Geogrid Properties Evaluation

3.1. Introduction

This chapter includes: (1) stress distributions and pullout responses of geogrid in soil using different normal loading methods and (2) investigation of combined effects on measured strains of geogrid.

In design of reinforced soil structures (i.e., GRR walls), pullout capacity of reinforcement in an anchorage zone is an important parameter for stability analysis. This parameter is generally quantified by conducting laboratory or field pullout tests. In the laboratory pullout test, the reinforcement is embedded in the soil mass at a normal stress, which is commonly applied by a pressurized airbag or a hydraulic jack through a rigid plate, and then a horizontal tensile force is applied to the reinforcement. The first part of this chapter reports an experimental study conducted to evaluate the effect of the load application method using an airbag with and without stiff wooden plates on the vertical stress distribution and the pullout capacities and deflections of extensible (geogrid) reinforcement (steel strip) in the soil in a large pullout box. This part of the study monitored the distributions of the vertical earth pressures at the top and bottom of the soil mass in the pullout box, and at the level of reinforcement using earth pressure cells.

To determine tension in the geosynthetic, strain gauges are often attached on the geosynthetic. In many studies, foil electrical resistance strain gauges have been attached on one

side of the geosynthetics to measure their strains. Such attachment of strain gauges is acceptable if only pure tension develops in the geosynthetics. However, in some applications, such as geosynthetic-reinforced column-supported (GRCS) embankments and geosynthetic-reinforced retaining (GRR) walls, the geosynthetic is subjected to bending and friction in addition to tension. Bending and friction may happen locally during construction, especially around aggregates. To address this issue, two strain gauges attached on the upper and lower sides of the geosynthetic at the same location have been suggested and used in the practice. The second part of this chapter reports the combined effects of tension, bending, and friction on the measured strains on the upper and lower sides of uniaxial geogrid specimens. The specimens were instrumented with resistance strain gauges and subjected to tension, bending, and friction at the same time, which were simulated by wrapping the specimen around three cylinders of different diameters. Moreover, the effect of the confined pressure induced by applied normal stress on the calculated CF was investigated by using pullout box.

3.2. Stress Distributions and Pullout Responses Using Different Normal Loading Methods

3.2.1. Test Device and Materials

Pullout box

In this study, a newly developed pullout box designated as "RJH Box"[1] was used. This box was designed and fabricated in the Geotechnical Laboratory at the University of Kansas in accordance

1 The RJH represents the initials of last names of the people who developed and fabricated this box: S.M. Rahmaninezhad, Y. Jiang, and J. Han.

with ASTM D6706-01 recommendations. The box was made of steel and has inner dimensions measuring 1.5 m long, 0.6 m wide, and 0.6 m high, which exceeds the minimum dimensions recommended by ASTM D6706-01. The pullout box has a 0.045-m-high by 0.5-m-long slot on the front wall. To minimize the arching effect during pullout tests, a 0.15-m-wide sleeve was fixed on the inner side of the front wall, right above the slot. In addition, the sleeve may reduce the influence of the box front face (Palmeira 2009). **Figure 3.1** shows the pullout box after the fabrication.

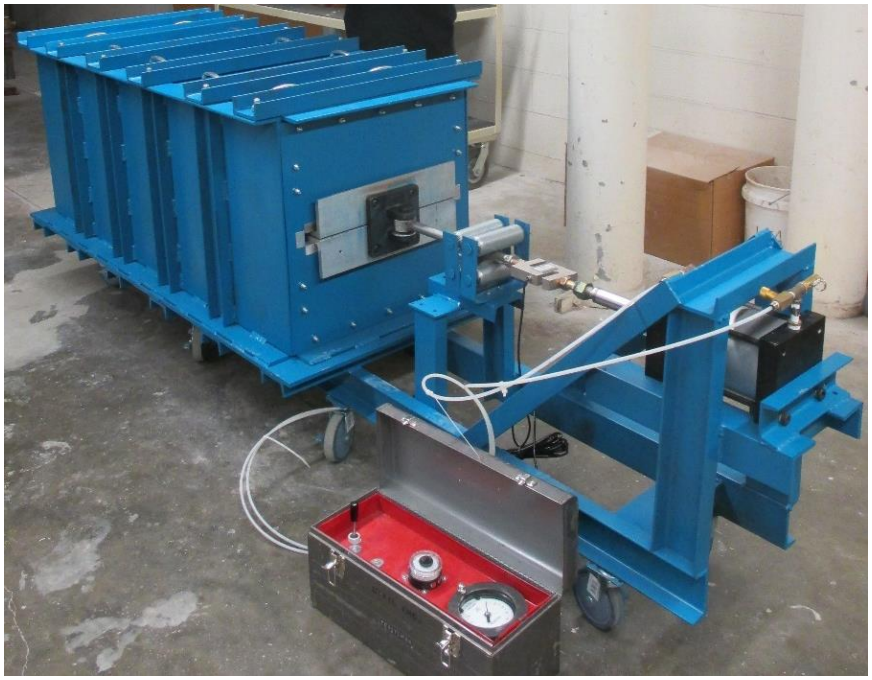

Figure 3. 1. RJH box

Materials

The laboratory pullout tests were carried out on extensible reinforcement (polypropylene punched-drawn uniaxial geogrid) embedded in Kansas River sand. Particle size distribution test was conducted using the ASTM D422 (2007), *Standard Test Method for Particle-Size Analysis of Soils*. A standard direct shear test was used to determine the friction angle for the sand compacted at 70% relative density. That test was according to ASTM D3080 (2011), *Standard Test Method for Direct Shear Test of Soils under Consolidated Drained Conditions.* The minimum and maximum dry densities for both backfill materials were obtained by the index density methods according to ASTM D4254 (2016), *Standard Test Methods for Minimum Index Density and Unit Weight of Soils and Calculation of Relative Density*, and ASTM D4253 (2016), *Standard Test Methods for Maximum Index Density and Unit Weight of Soils Using a Vibratory Table*, respectively. **Table 3.1** summarizes the physical properties, the Unified Soil Classification System (USCS) classification, and the angle of friction of the backfill material used in the pullout tests.

A uniaxial geogrid modified from a punched-drawn biaxial PP geogrid, as an extensible reinforcement, was used in this experimental study. This geogrid was selected because it has been adopted in our model tests and its in-air load-strain properties were determined by a previous study (Xiao, Han, and Zhang 2016). Considering the fact that uniaxial geogrid is commonly used in reinforced walls or slopes, three transverse ribs (i.e., the crossmachine direction ribs) of the biaxial geogrid were removed in every four ribs to create a shape of uniaxial geogrid. Xiao, Han, and Zhang (2016) first adopted this modification, and then Rahmaninezhad et al. (2016), Kakrasul et al. (2016), and Rahmaninezhad et al. (2018) used it in their model studies. The longitudinal ribs (i.e., the machine direction ribs) and the transverse members of the geogrid contribute to the total pullout resistance. In other words, the total pullout resistance is the sum of the frictional resistance

on the geogrid surface and the bearing resistance of the transverse members (Tran, Meguid, and Chouinard 2013). Alagiyawanna et al. (2001) found that removal of 75 % of the transverse ribs reduced the reinforcing effect of the geogrid on the sand movement. **Table 3.2** provides the properties of the biaxial geogrid. In this study, one uniaxial geogrid that was 300 mm wide and 600 mm long was used in the evaluation of vertical pressure distribution while another uniaxial geogrid specimen that was 370 mm wide and 765 mm long was used in the evaluation of pullout behavior. These geogrid samples before the removal of transverse ribs had an ultimate tensile strength of 12.4 kN/m in the machine direction and 19 kN/m in the cross-machine direction.

Table 3.1. Properties of backfill materials

Property	**Kansas River sand**
Coefficient of uniformity, C_u	3.18
Coefficient of curvature, C_c	0.93
USCS classification	SP
Mean particle size, D_{50}, mm	0.56
Minimum dry unit weight, kN/m^3	16.0
Maximum dry unit weight, kN/m^3	18.8
Angle of friction, deg.	37

Table 3.2. Properties of the biaxial geogrid (provided by the manufacturer)

Index properties	MD	XMD
Aperture dimensions, mm	25	33
Minimum rib thickness, mm	0.76	0.76
Tensile strength at 2% strain, kN/m	4.1	6.6
Tensile strength at 5% strain, kN/m	8.5	13.4
Ultimate tensile strength, kN/m	12.4	19

Note: MD= machine direction; XMD = cross-machine direction.

Instrumentation

The instrumentation included a load cell, displacement transducers, pressure cells, a pressure gauge, and a data acquisition system. An S-shaped load cell with a capacity of 50 kN was used to measure the pullout force. Five displacement transducers were used to measure the displacements at the junctions of the geogrid. These transducers were connected to the geogrid by steel rods that were extended from junctions out to the rear side of the box. Strain gauge–type earth pressure cells 25 mm in diameter were installed to evaluate the normal stresses at different levels of the soil mass. The capacities of these earth pressure cells were 200 and 500 kPa, respectively. A pressure gauge was used to control the pressure applied to the airbag.

3.2.2. Test Procedure

The procedure for preparing a pullout test included filling half of the box with the backfill material and compaction, placement of the reinforcement, installation of sensors and connection to the data acquisition system, and continuous filling of the box with the remaining backfill. The backfill material was placed into the box in two layers, and each layer was compacted until the minimum relative density of 70 % was achieved. The effect of compaction on the reinforced sand for reduced-scale models was discussed in Rahmaninezhad, Yasrobi, and Eftekharzadeh (2009). The geogrid was embedded in the middle of the backfill height (i.e., at the same elevation of the clamp), and attached to the pullout load assembly. Because the connection between the hydraulic jack and the clamp was relatively rigid, the pullout force was applied horizontally. Moreover, the clamp was placed between the sleeves, which prevented the rotation of the clamp. Finally, all the sensors, including the displacement transducers, the earth pressure cells, the load cell, and the pressure gauge, were installed at their desired locations. Normal stress was applied with a pressurized airbag placed on the top of the compacted backfill. This airbag allowed soil dilation or contraction during pullout testing and maintained a constant normal stress. To simulate the reinforcement at different elevations of a wall in the field, three normal stresses were selected. In some tests, five wood plates that were 0.58 m long, 0.29 m wide, and 0.05 m thick were placed on top of the compacted backfill, one next to another, before the placement of the airbag. Once the whole pullout test setup was completed, all sensors were activated to allow the data acquisition system to start recording. After the normal stress distribution throughout the soil mass became stable, the pullout load was applied using a double-acting hydraulic jack. **Figure 3.2** shows the schematic view of the cross sections of the pullout box, in which one did not have stiff wood plates and the other did.

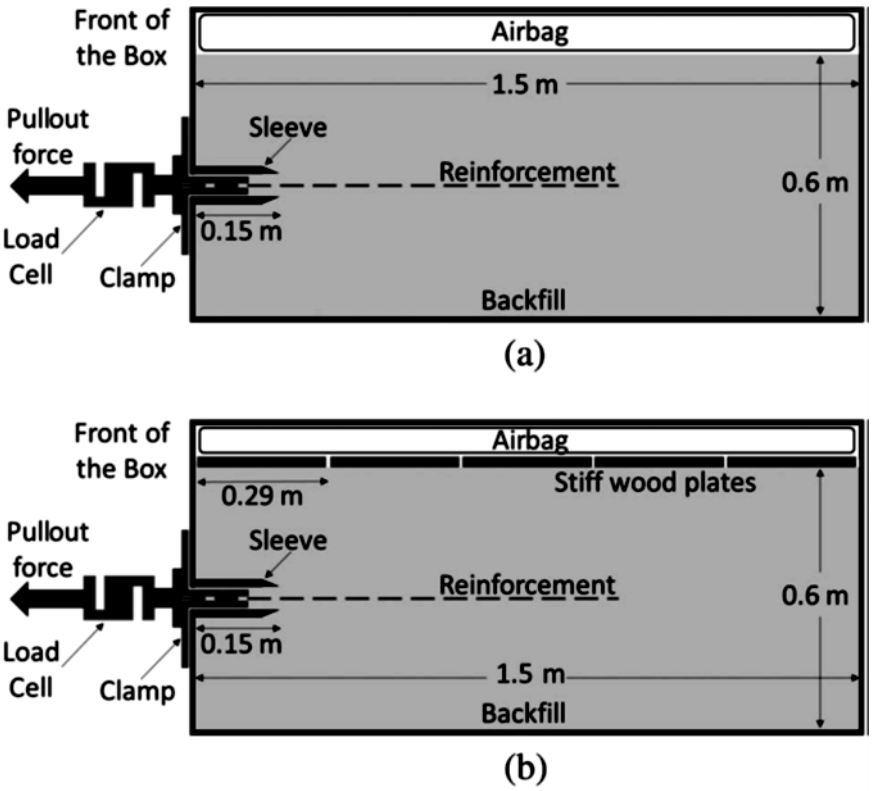

Figure 3. 2. Schematic view of the cross sections of the pullout box with: (a) the air bag on the soil; (b) the air bag on the stiff wood plates

3.2.3. Test Results

Distribution of normal stress

In this study, 21 earth pressure cells were used to examine the distributions of the vertical pressures at the top and the bottom of the soil mass and at the level of the reinforcement in the pullout box. **Figure 3.3** illustrates the arrangement of the earth pressure cells on the top of the reinforced soil

mass. The variations of the measured vertical pressures under different normal stresses across the box width (axis A-A) and the box length (axis B-B) are shown in Figs. 4 and 5, respectively. The measured vertical pressures presented in these figures are the additional vertical stresses induced by the applied normal pressures. In these two figures, it was assumed that the distributions of the vertical pressures across the box width (i.e., the transversal section) were symmetric. Fig. 4a shows that when the airbag was used without stiff plates, the vertical pressure concentrated in the middle of the box. On the other hand, when the normal stress was applied by the airbag with stiff plates, the maximum measured vertical pressures were close to the sides of the box (**Figure 3.4 (b)**). Likewise, on the longitudinal section of the box (i.e., the axis B-B), when the airbag was used without any stiff plates, the measured maximum vertical pressures were higher than those using the stiff plates as shown in **Figure 3.5 (a)** and b. However, **Figure 3.4 and 3.5** imply that the application of the normal load by the airbag without any stiff plates (as a flexible diaphragm) resulted in a more uniform pressure distribution than that by the airbag with stiff plates.

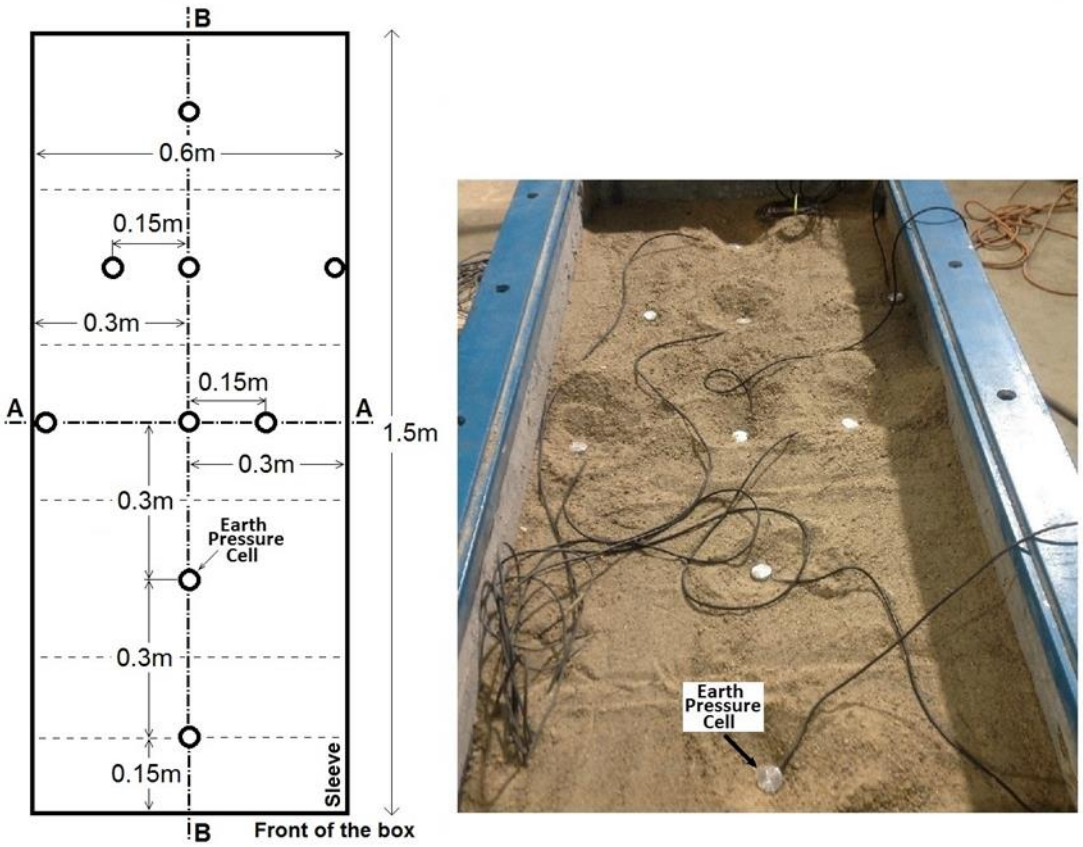

Figure 3. 3. The arrangement of the earth pressure cells on the top of the soil mass

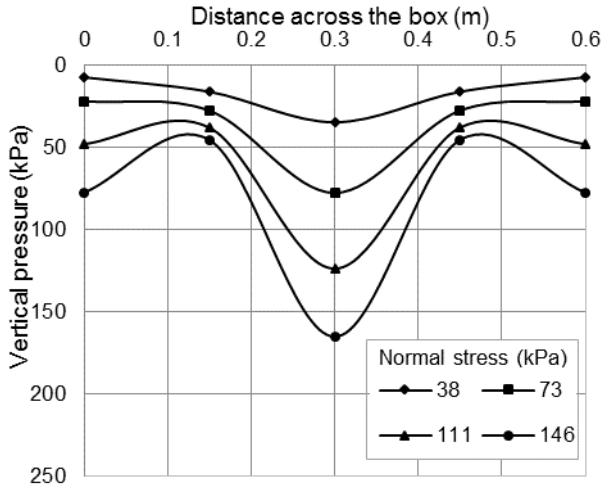

(a)

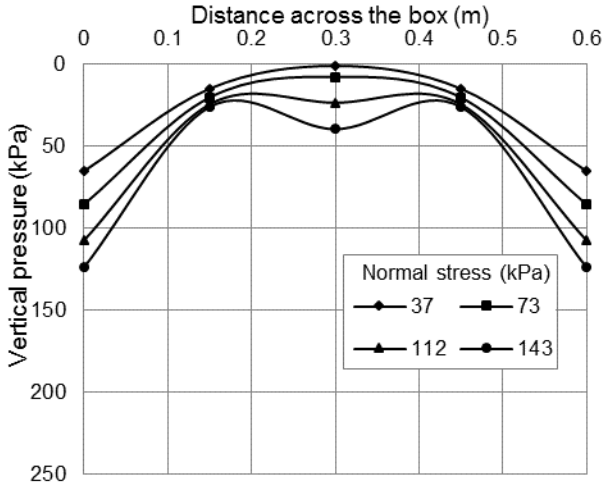

(b)

Figure 3. 4. Variations of the measured vertical pressures on the top of the soil and across the box width (axis A-A) under different normal stresses applied by: (a) the air bag without stiff plates; (b) the air bag with stiff plates

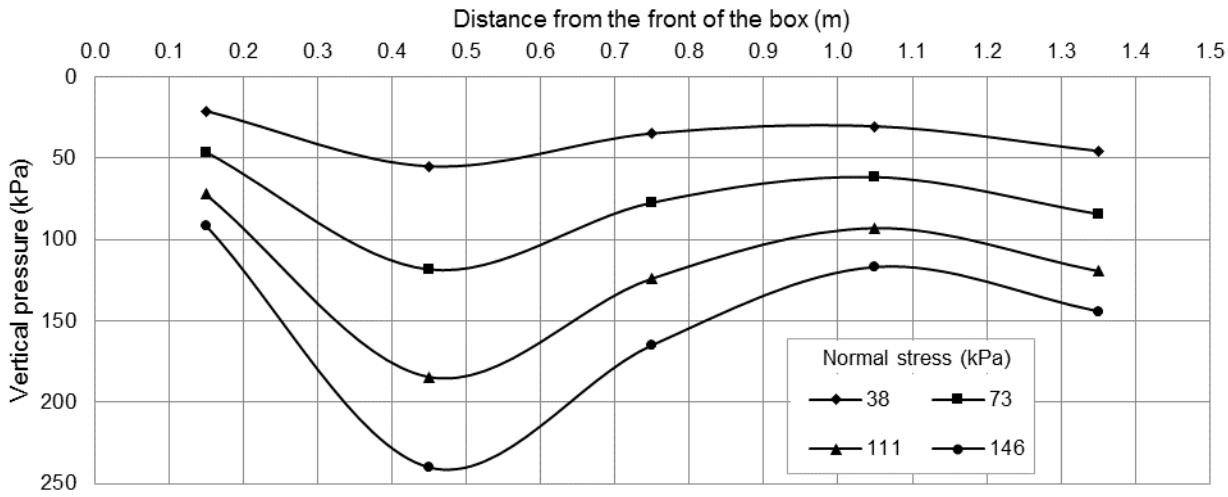

(a)

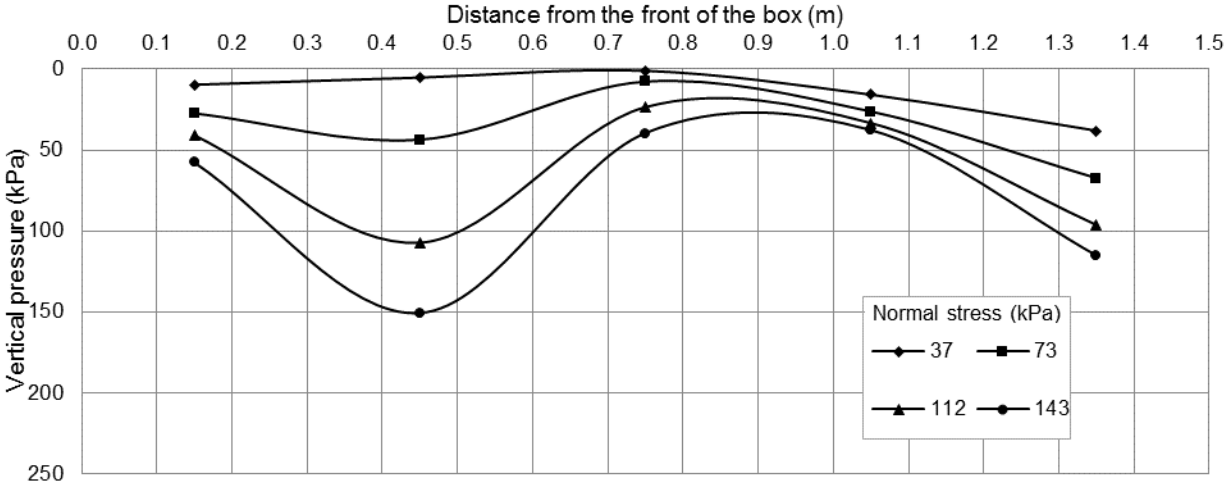

(b)

Figure 3. 5. Variations of the measured vertical pressures on the top of the soil and across the box length (axis B-B) under the normal stresses applied by: (a) the air bag without stiff plates; (b) the air bag with stiff plates

Sugimoto, Alagiyawanna, and Kadoguchi (2001) and Palmeira (2009) found that the conditions of the frontal face of the pullout box might have a noticeable effect on the pullout behavior of the reinforcement. Researchers suggested using a lubricated frontal or movable/flexible frontal face, or both, with a sleeve, to keep the reinforcement distant from the front wall of the pullout box (e.g., Wilson-Fahmy, Koerner, and Sansone 1994; Perkins and Cuelho 1999; Sugimoto, Alagiyawanna, and Kadoguchi 2001; Palmeira 2009). Palmeira (2009) found that the use of a sleeve yielded the maximum pullout resistance that was higher than that observed in the case of using a lubricated frontal face. It appears that the sleeve had less influence on the pullout test result than the box frontal wall; however, the sleeve still changed the uniformity of the distribution of the vertical pressure near the front of the box as shown in **Figure 3.5 (a)**. The result indicates that the measured vertical pressure behind the sleeve was consistently lower than the applied normal stress. This finding is consistent with that by Bathurst et al. (2001) on the vertical load transfer from the soil to the rigid sleeve.

Figure 3.6 shows the layout of the earth pressure cells on the bottom of the box. **Figure 3.7 (a) and (b)** shows the variations of the measured vertical pressures along the box width (i.e., the axis C-C) and length (i.e., the axis D-D), respectively, under different normal stresses applied by the airbag without any stiff plates. The maximum measured normal pressures on the bottom of the box happened in the center of the transverse section of the box. In the longitudinal section, the maximum vertical pressures were also in the center (**Figure 3.7 (b)**). On the top of the soil mass, however, the maximum vertical pressures happened near the front of the box (**Figure 3.5 (b)**).

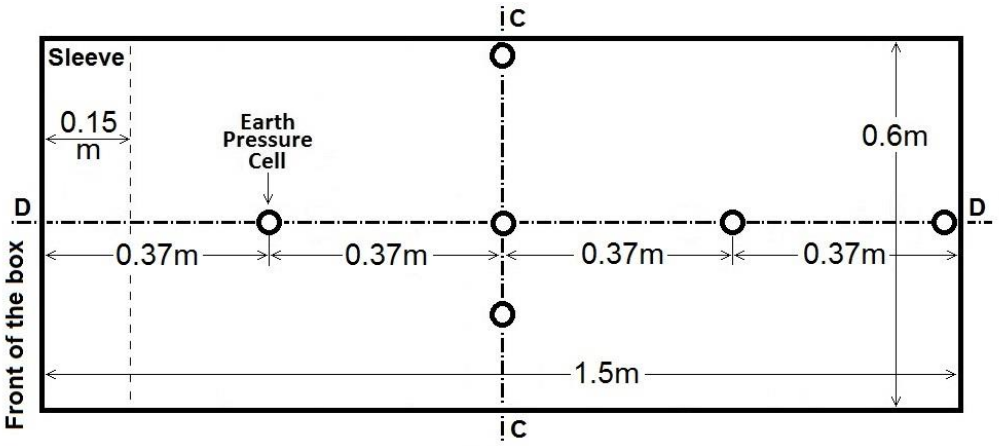

Figure 3. 6. The layout of the earth pressure cells on the bottom of the soil mass

Figure 3.8 shows the layout of the earth pressure cells and the telltales on the level of the geogrid that was 300 mm wide and 600 mm long. The earth pressure cells were placed to determine the distribution of vertical pressures, while the telltales were fixed on the junctions of the geogrid following ASTM D6706-01 to determine the displacements of the geogrid along its length. The detail of the telltale measurements will be discussed later in this article. **Figure 3.9 (a)** shows the variations of the vertical pressures along the F-F section under different normal stresses applied by the airbag without any stiff plates. The concentration of the vertical pressures was on the center of the transverse section of the box, on the level of the reinforcement. **Figure 3.9 (b)** displays the variations of the measured vertical pressures along the E-E section under different normal stresses applied by the airbag without any stiff plates. These distributions were measured just along the length of the geogrid. In some research (e.g., Jayawickrama et al. 2014; Wang, Jacobs, and Ziegler 2016), one or two earth pressure cells were placed along the central line of the pullout box under the airbag or stiff plates. Based on this study, the distribution of the vertical pressures along the centerline may not reflect the actual distribution of the vertical pressures.

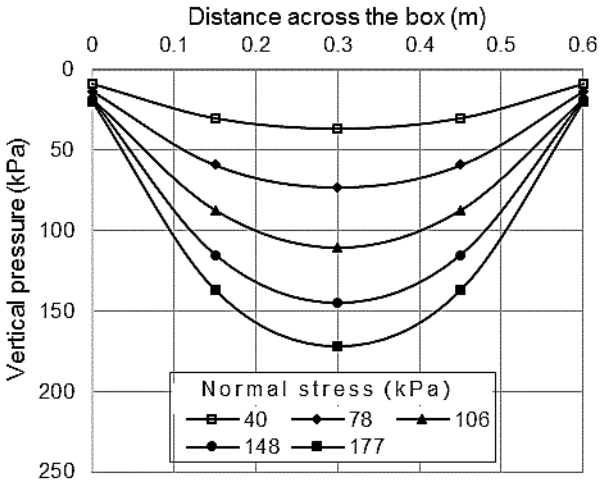

(a)

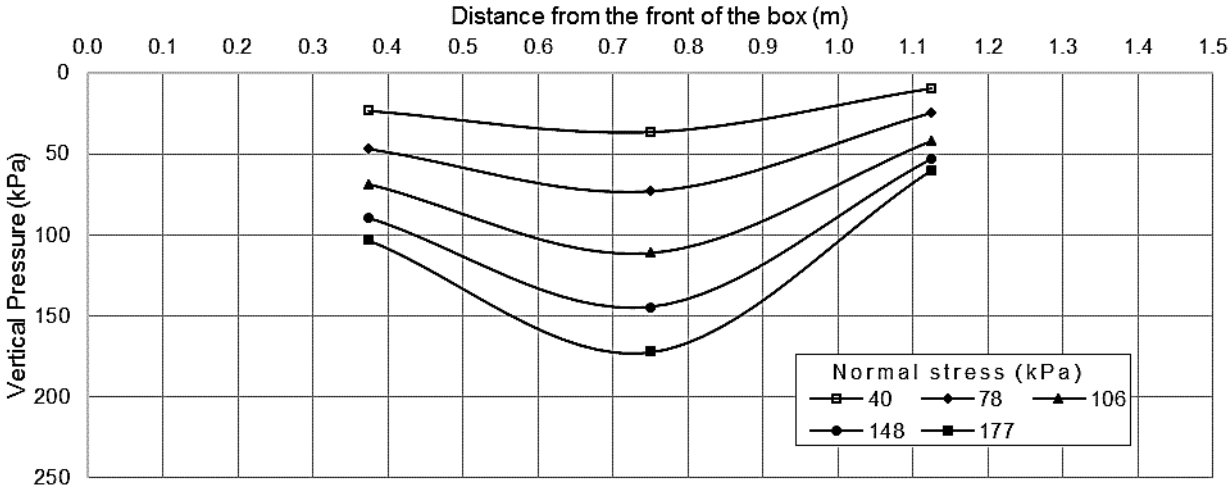

(b)

Figure 3. 7. Variations of the measured vertical pressures on the bottom of the box under different normal stresses applied by the air bag without any stiff plates along: (a) the axis C-C; (b) the axis D-D

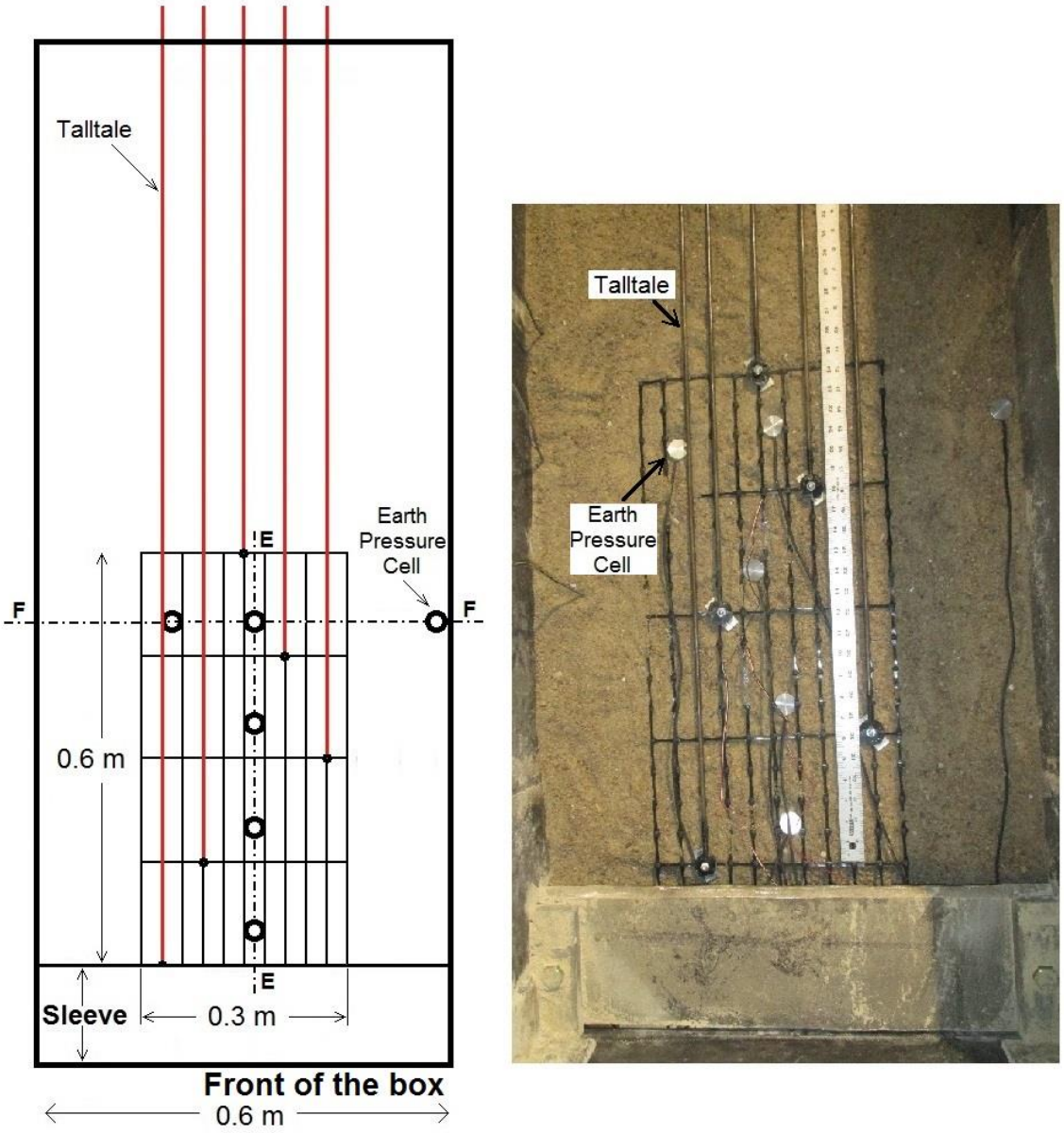

Figure 3. 8. Layout of the geogrid, the earth pressure cells, and the telltales

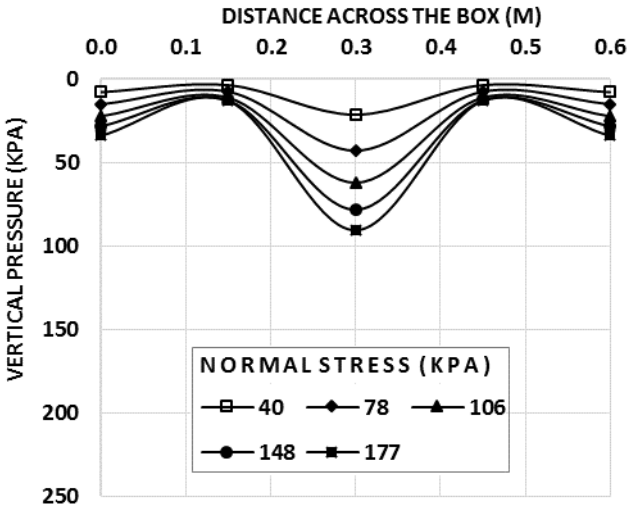

(a)

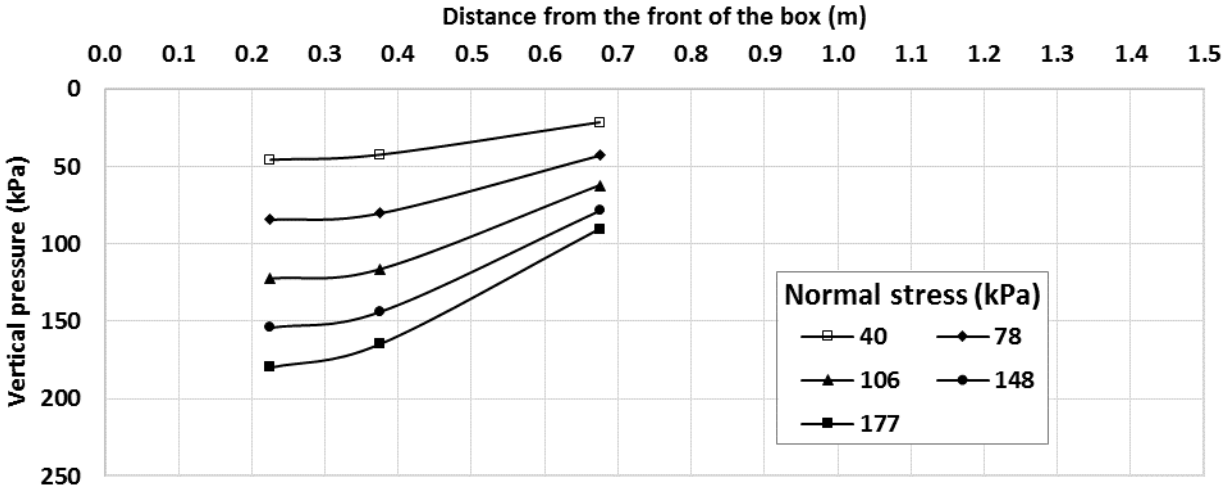

(b)

Figure 3.9. Variations of the measured vertical pressures along the geogrid under different normal stresses applied by the air bag without any stiff plates along: (a) the axis F-F; (b) the axis E-E

Pullout resistance of reinforcement

Pullout tests were carried out in this study to evaluate the effects of two different methods of applying the normal stress on the pullout resistance of the uniaxial geogrid embedded in the soil. In the geogrid tests, 370-mm-wide and 765-mm-long geogrids were used.

Figure 3.10 presents the pullout test results of the geogrids with two different methods of applying the normal stress. These figures show that at the normal stress of 10 kPa applied by the airbag without and with stiff plates, the pullout forces were 15.87 and 11.11 kN/m, respectively, at the front displacement of 20 mm. Also, at the normal stress of 7 kPa applied by the airbag without and with stiff plates, the pullout forces were 9.32 and 7.47 kN/m, respectively, at the same front displacement (20 mm). Therefore, the pullout resistance of the geogrid under the airbag without any stiff plates was higher than that under the airbag with stiff plates. Under the normal stresses of 10, 7, and 3.5 kPa, the pullout resistance values of the geogrid when the airbag was used with stiff plates were 30, 20, and 3 %, respectively, lower than those measured without stiff plates. Evidently, at the low normal stress, there was a minor difference between the pullout resistances using these two different loading methods.

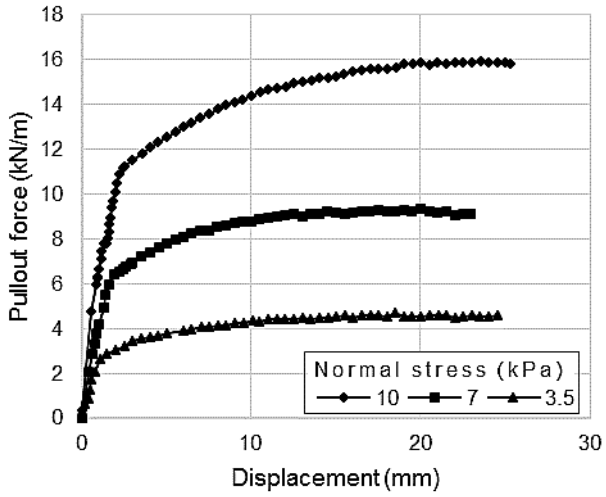

(a)

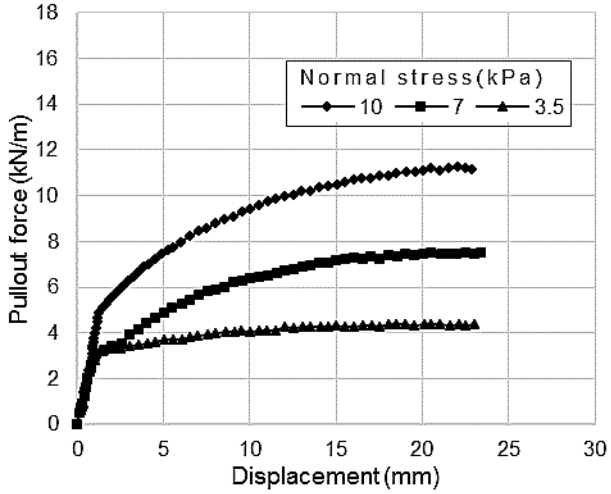

(b)

Figure 3. 10. Pullout force versus displacement of the geogrid under normal stresses applied by:

(a) the air bag without stiff plates; (b) the air bag with stiff plates

Displacement and strain of geogrid

To investigate the effect of these two different methods of applying the normal stress on the deflection of the geogrid, two tests were conducted by attaching five telltale rods on the junctions of one transverse rib as shown in **Figure 3.11**. **Figure 3.12** shows the measured displacements at these junctions under different pullout forces when a normal stress of 10 kPa was applied using the airbag without and with stiff plates. **Figure 3.12 (a)** shows that the displacements of the geogrid at the junctions were nearly uniform because the airbag without stiff plates generated the nearly uniform distribution of the vertical pressures in the center of the box as shown in **Figure 3.12 (a)** and **Figure 3.9 (a)**.

Figure 3.12 (b) shows that when the stiff plates were used, the maximum displacement at the junctions of the geogrid occurred in the middle of the longitudinal ribs, and the minimum displacements at the junctions occurred near the sides of the box. This result can be explained based on the distribution of the vertical pressures in the transverse section of the box as shown in **Figure 3.4 (b)**, i.e., the lowest vertical pressure at the center and the highest vertical pressure at the edges of the box. **Figure 3.12** shows that the measured displacements along the transverse bar of the geogrid were different. However, most researchers have placed the telltales on the junctions of

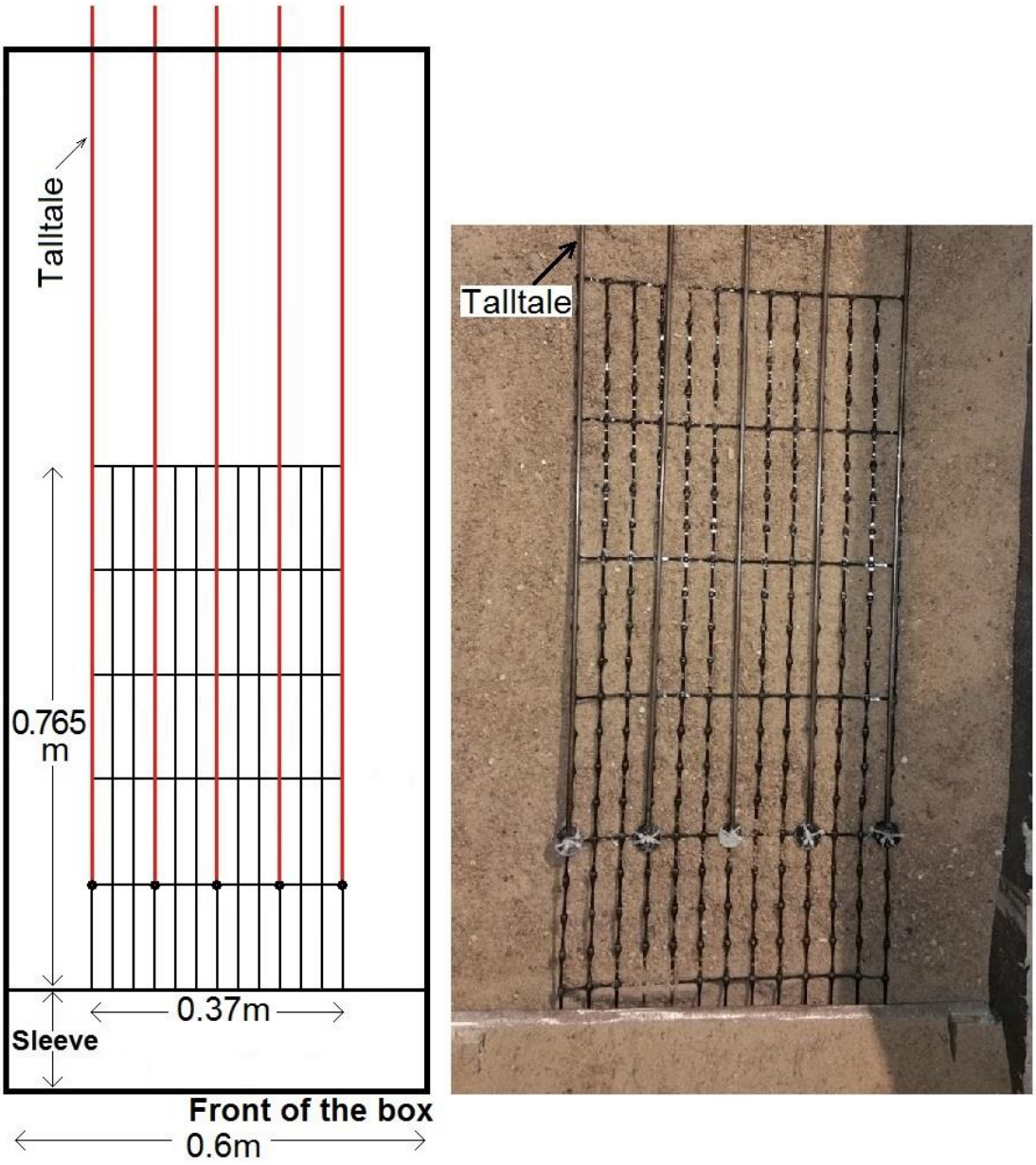

Figure 3. 11. Telltale rods attached on the junctions of the transverse rib

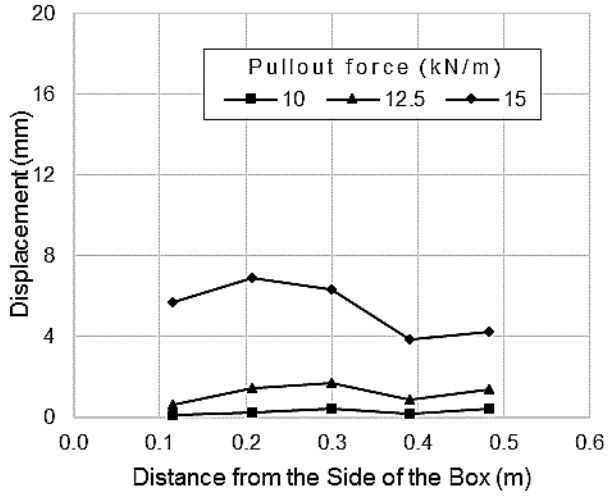

(a)

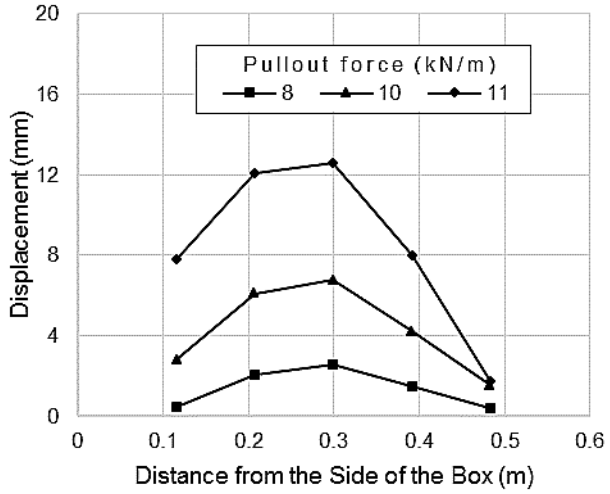

(b)

Figure 3. 12. Displacements of the junctions on the transverse rib under different applied pullout forces under the normal stress of 10 kPa by: (a) the air bag without stiff plates; (b) the air bag with stiff plates

3.3. Combined Effects on Measured Strains of Geogrid

3.3.1. Adopted tensile tests, results, and discussion

Test apparatus

Figure 3.13 shows the setup of the tensile test of a geogrid specimen. The ASTM D6637 standard (ASTM, 2015) for measuring tensile strength of a geogrid was adopted for this test. Bending and friction on a geogrid were simulated by wrapping the geogrid specimen around a cylindrical pipe. Three cylindrical pipes were used and had nominal outside diameters of approximately 65, 100, and 160 mm. One end of the geogrid was connected to the frame using a metal bar clamp like a bodkin connector. Another end of the geogrid was connected to a load cell. Loads were applied using placing weights in a bucket hanging under one end of the geogrid. One load cell was used to measure the actual load.

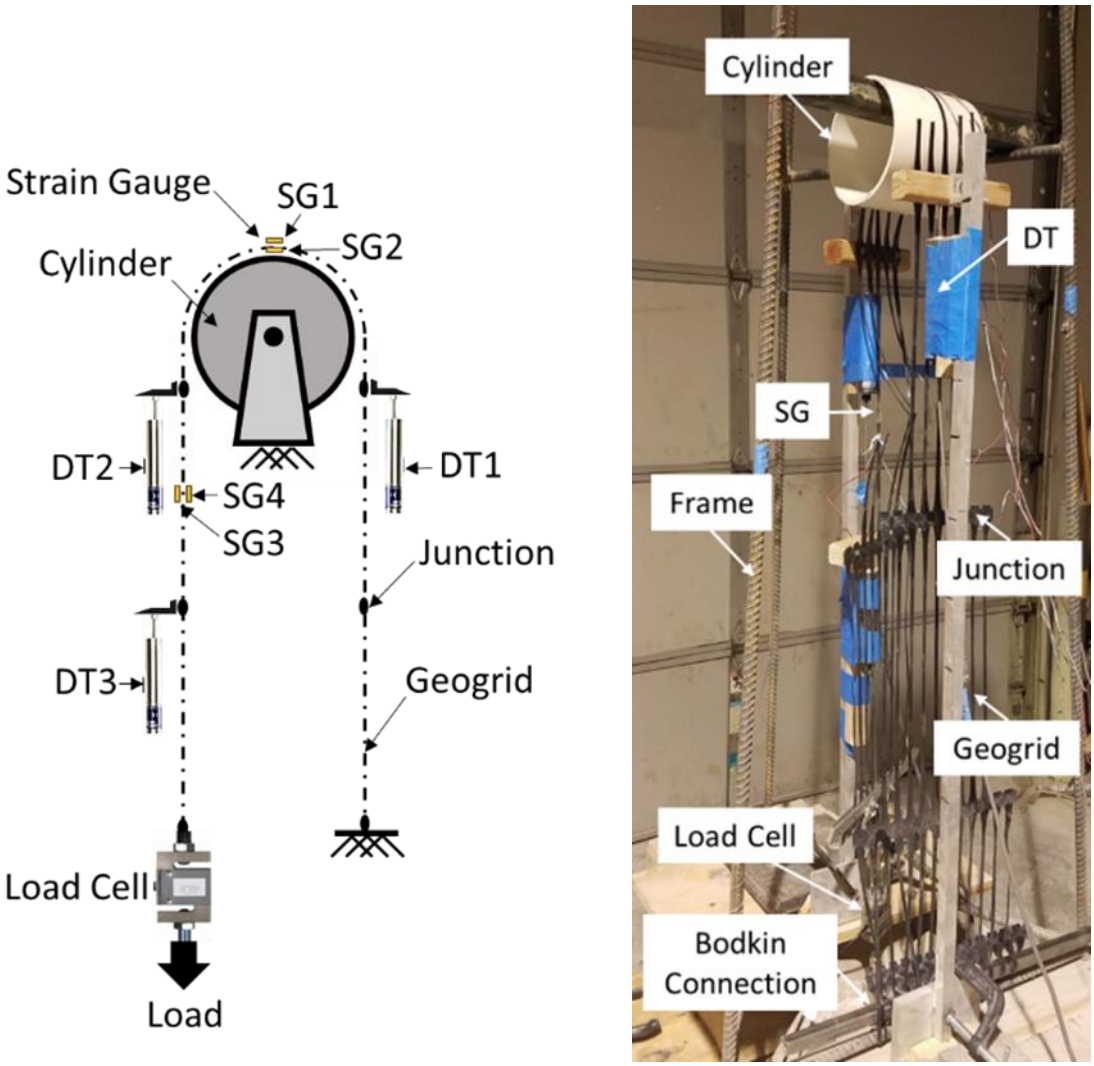

(a) (b)

Figure 3. 13. Test Setup: (a) schematic cross-section and (b) picture of the test setup

Geogrid

One type of uniaxial (UX) HDPE geogrid was used in these tests. Since the UX geogrid is thicker than biaxial (BX) HDPE geogrids, the tension that induced by bending on the upper and lower sides of the UX geogrids might be higher than BX geogrids. Therefore, the UX geogrid was used for this part of the study. The physical and mechanical properties of the geogrid provided by the manufacturer are shown in **Table 3.3**. To avoid possible property variability of different ribs, only one rib was used for loading and measurements.

Table 3.3. Properties of Geogrids (Provided by the Manufacturer)

Geogrid Properties	
Tensile Strength @ 5% Strain (kN/m)	27.0
Ultimate Tensile Strength (kN/m)	58.0
Junction Strength (kN/m)	54.0
Flexural Stiffness (mg-cm)	500,000
Minimum Reduction Factor for Installation Damage (RF_{ID})	1.05
Reduction Factor for Creep for 120 yr design life (RF_{CR})	2.60
Minimum Reduction Factor for Durability (RF_{D})	1.00

Measurements

The applied load was measured using an S-shape load cell with a capacity of 10 kN. The elongations of the rib of the geogrid at two locations were measured using three displacement transducers (DTs) with a displacement limit of 50 mm. The global strains were calculated using the elongations in the ribs of the geogrid measured by DTs. Furthermore, the geogrid was instrumented with four strain gauges: SG1, SG2, SG3, and SG4, as shown in **Figure 3.13**. The strain gauges were attached on both sides of the geogrid rib in the middle of the aperture (**Figure 3.14**). The strain gauges had a gauge length of 5 mm and a resistance of 120 Ω. The measured strains from these strain gauges s represent the local strains.

(a) (b)

Figure 3. 14. (a) Location of strain gauge on the middle of the geogrid rib; (b) arrangement of the geogrid and strain gauges on one cylinder

Global strain

Figure 3.15 shows the relationships of the applied load versus the global strain of the geogrids. The rib with DT2 and DT3 was under tension only. Therefore, the slope of the trend-line for the rib with DT2 and DT3 represents the tensile stiffness of the geogrids. With different cylinder diameters, the tensile stiffness of the rib was similar (i.e., 12-13 kN/rib). However, the global strains calculated from DT1 and DT2 were affected by the combination of tension, bending, and friction. The results show that at the same applied load, the global strain in the rib induced by tension only was higher than the one induced by tension, bending, and friction. In addition, Figure 3 shows that at the same global strain, the load carried by the geogrid rib induced by tension only was less than that induced by tension, bending, and friction because the friction was in the opposite direction to the tension and additional load was required to overcome the friction to induce the same strain on the geosynthetic. For example in **Figure 3.15 (a)**, at the global strains of 0.5%, 1%, and 1.5%, the differences between the loads carried by the geogrid rib under tension only and the rib under tension, bending, and friction were approximately 0.03, 0.04, 0.03 kN, respectively. Since bending does not induce any tensile resistance, this difference is the load carried by friction between the geogrid and the cylinder. The average loads carried by friction on the cylinders with diameters of 65, 100, and 160 mm were approximately 0.025, 0.020, and 0.016 kN, respectively, from the beginning to the end of the tests.

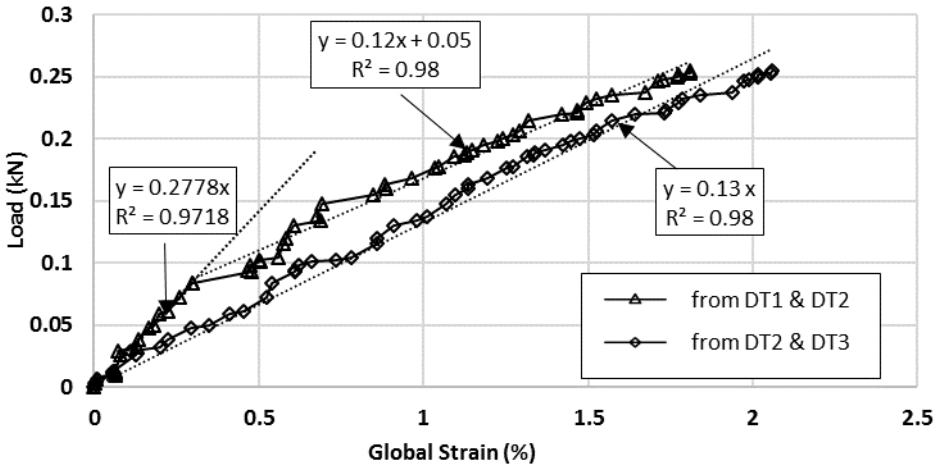

(a)

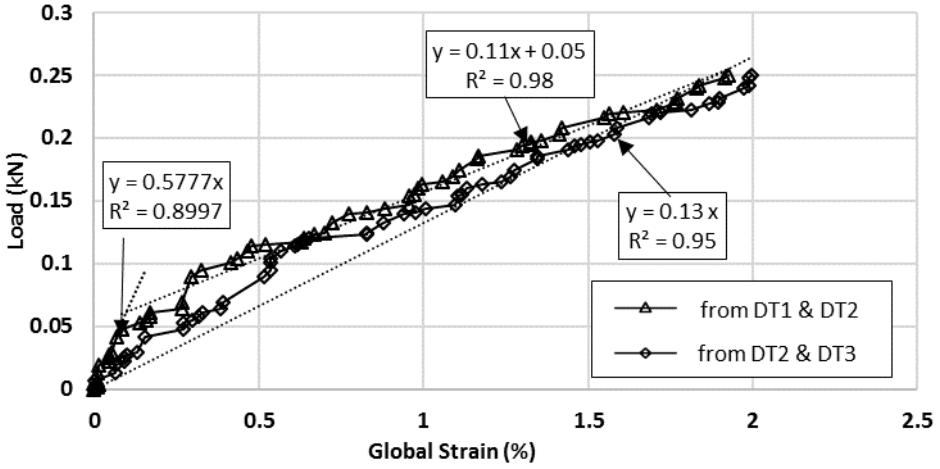

(b)

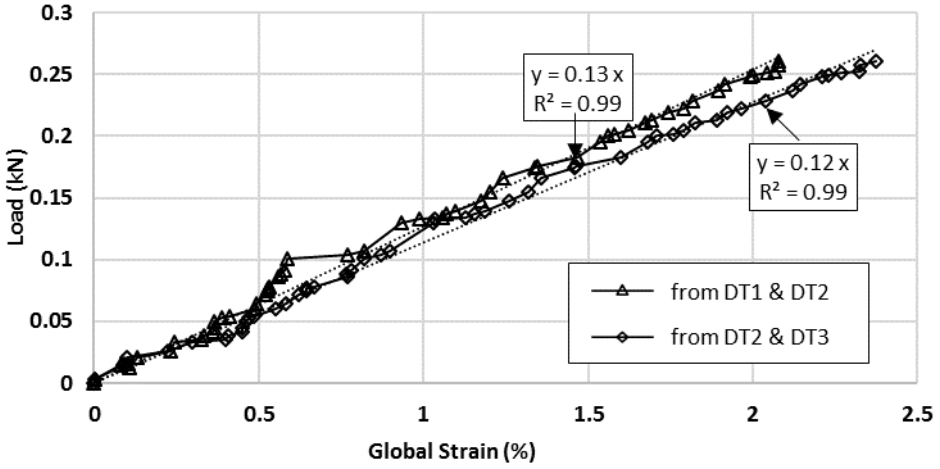

(c)

Figure 3. 15. Applied load versus global strain with the cylinder diameter of: (a) 65 mm; (b) 100 mm; and (c) 160 mm

Global strain and average local strain

The calibration factor, CF, is the ratio of the measured global strain by the displacement transducers to the local strain by the strain gauge. The CF can be estimated using the following equation:

$$CF = \frac{Global\ Strain}{Local\ Strain} \qquad \textbf{Eq. 3.1}$$

Figure 3.16 shows the relationship of the global strain versus the average local strain of the geogrids. The average local strain represents the average of the measured strains from strain gauges attached on the upper and lower sides of the geogrid and can be estimated using the following equation:

$$Average\ Local\ Strain = \frac{\varepsilon_{upper} + \varepsilon_{lower}}{2} \qquad \textbf{Eq. 3.2}$$

where ε_{upper} = the measured local strain from the strain gauge attached on the upper side of the geogrid; ε_{lower} = the measured local strain from the strain gauges attached on the lower side of the geogrid. The calculated CFs from SG1 (ε_{upper}) and SG2 (ε_{lower}) placed on the cylinders with diameters of 65, 100, and 160 mm were 2.15, 1.77, and 2.65, respectively, with an average of 2.19. However, the calculated CFs from SG3 (ε_{upper}) and SG4 (ε_{lower}) using the cylinders with diameters of 65, 100, and 160 mm were 1.44, 1.53, and 1.78, respectively, with an average of 1.58. Therefore, the friction increased the CF by 39%.

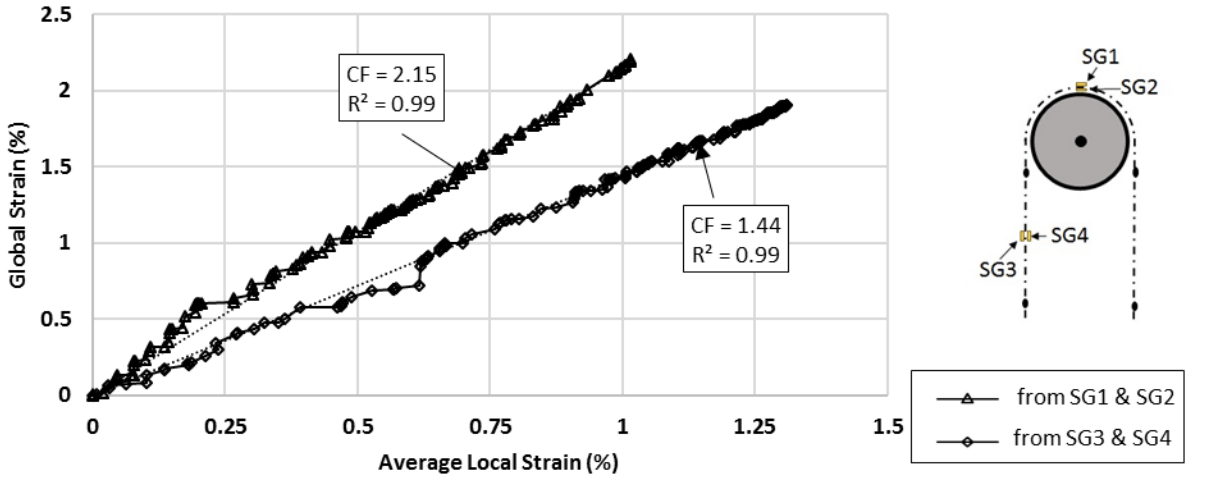

(a)

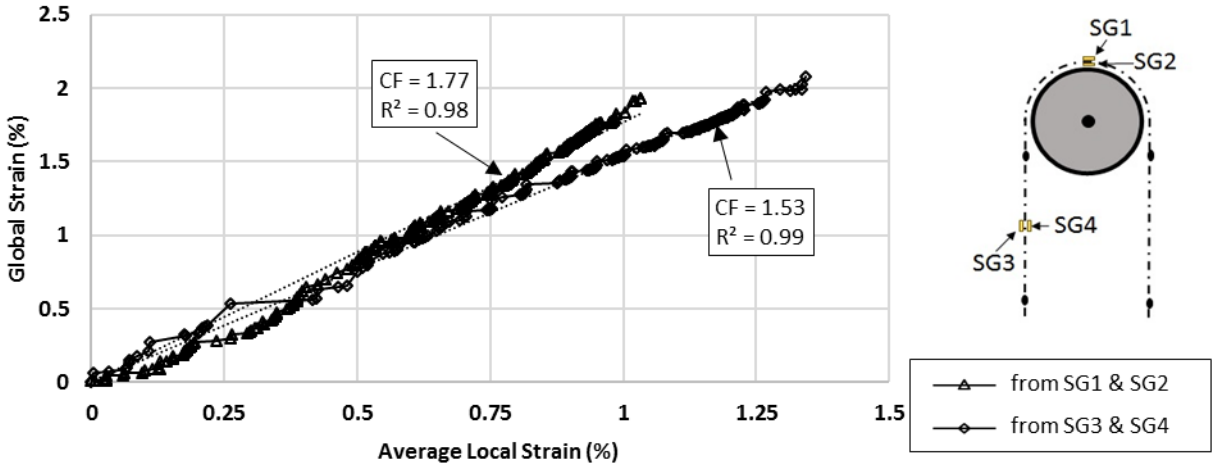

(b)

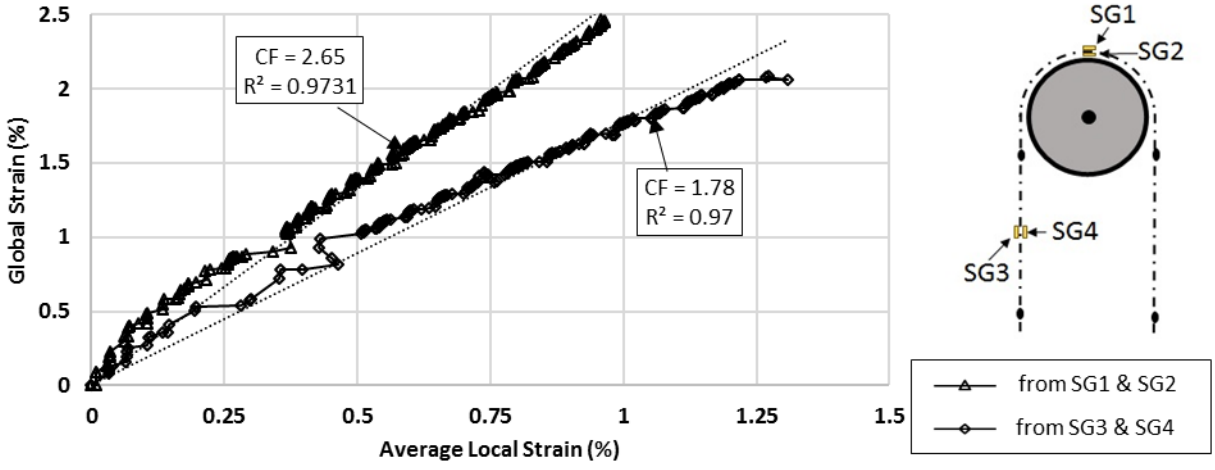

(c)

Figure 3. 16. Global strain versus average local strain with the cylinder diameters of: (a) 65 mm; (b) 100 mm; and (c) 160 mm

Average local strain ratio

Since the friction is in the opposite direction to the tensile load, the measured strains on the rib on top of the cylinder were lower than those on the vertical rib. Their differences could be calculated and are the indication of the friction effect. **Figure 3.17** shows the differences between the average local strains induced by tension (SG3 and SG4) and those induced by tension, bending, and friction (SG1 and SG2) versus their global strains. The results indicate that the diameter of the cylinder had no effect on the differences between the average local strains. In other words, the cylinders of different diameters had the same friction effect on the measured strains.

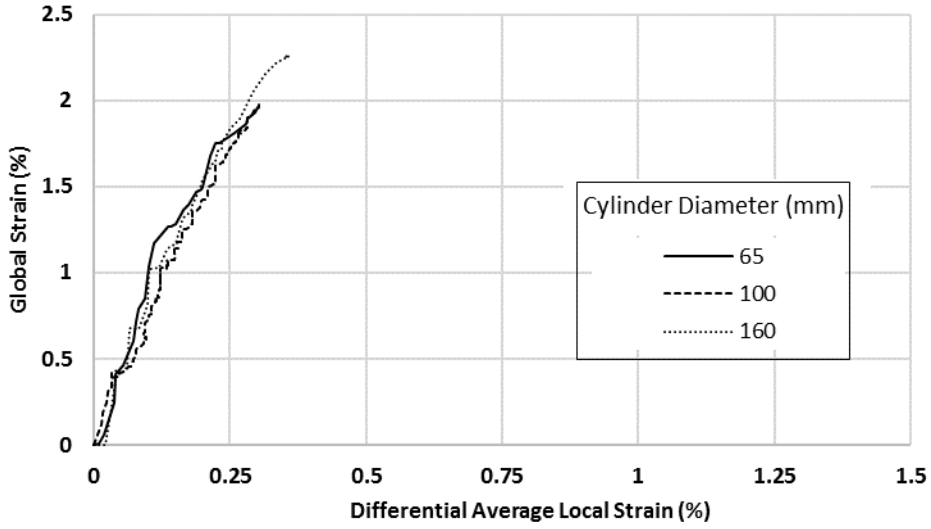

Figure 3. 17. Global strain versus the differential average local strain ratio

The local strain ratio is the ratio of the average local strain induced by tension only to the average local strain induced by tension, bending, and friction.

$$Local\ Strain\ Ratio = \frac{Average\ Local\ Strain\ (tension\ only)}{Average\ Local\ Strain\ (combined)} \qquad \textbf{Eq. 3.3}$$

Figure 3.18 shows the average local strain ratio versus the applied load. At a small load (<0.025 kN), the effect of friction was significant. With an increase of the tensile load, this effect became smaller and stable. The result shows that the local strain ratios in the tests with the geogrids wrapped around the cylinders with diameters of 65, 100, and 160 mm were 1.23, 1.22, and 1.38, respectively, with an average of 1.28, after the applied load was higher than 0.025 kN. Figure 6 also shows that regardless of the cylinder diameter, the measured strains induced by tension were approximately 28% higher than the average strains of the upper and lower strains induced by the combination of tension, bending, and friction.

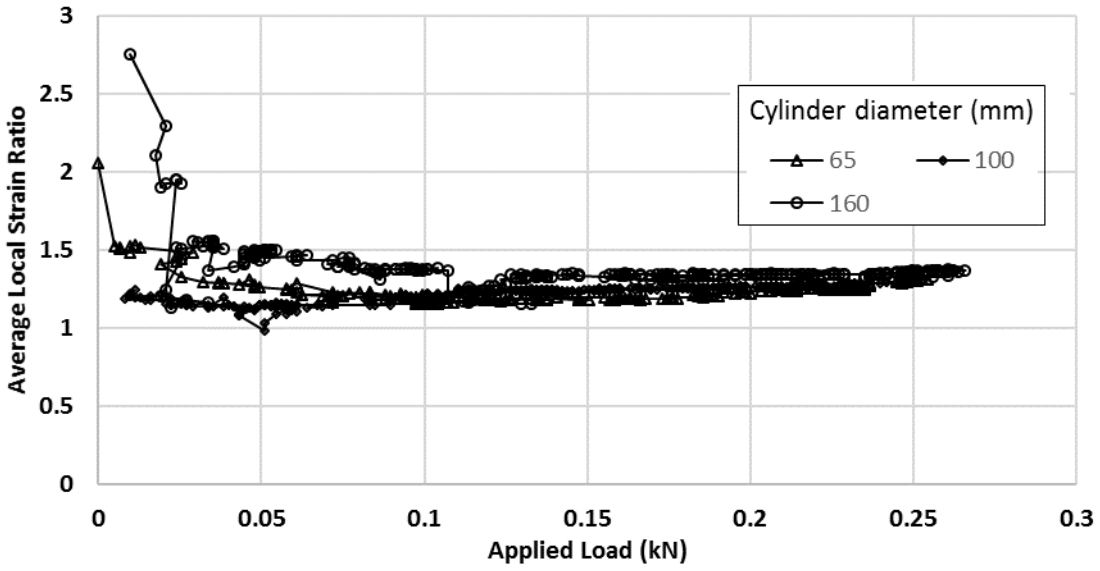

Figure 3. 18. The average local strain ratio versus the applied load

3.3.2. Tensile tests in soil

A set of pullout tests were carried out to evaluate the CF of the embedded geogrid in soil.

Test aperture

The local and global strains on the embedded geogrid were evaluated using pullout tests. The RJH Box was used to conduct pullout tests. The specification of the RJH Box was presented on Section 3.2.1. **Figure 3.19** shows the setup of the tensile test of a geogrid specimen inside the pullout box.

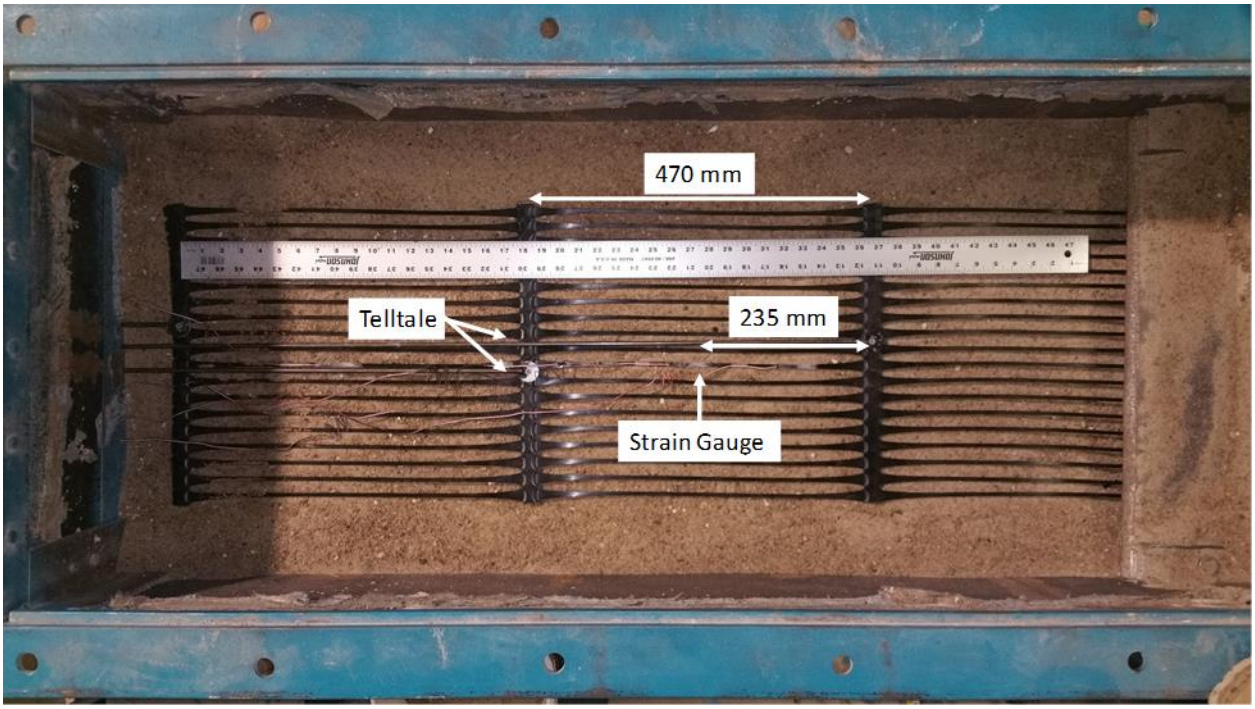

Figure 3. 19. Setup of the tensile test inside the pullout box

Materials

The UX HDPE geogrid as discussed in Section 3.3.1 was used in these tests. The geogrid was embedded in Kansas River sand. **Table 3.1** summarizes the physical properties, the Unified Soil Classification System (USCS) classification, and the friction angle of the backfill material used in the pullout tests.

Instrumentation

The instrumentation included DTs and strain gauges. Four displacement transducers were used to measure the displacements at the junctions of the geogrid. These transducers were connected to the geogrid by steel rods that were extended from junctions out to the rear side of the box. The results from the DTs were used to calculate global strains. Two strain gauges were installed on the upper and lower sides of the geogrid specimens in the middle of the aperture.

Test procedure

The procedure for preparing a pullout test was similar to that explained in Section 3.2.2. Each backfill layer was compacted to the relative density of 70 %. A normal stress was applied with a pressurized airbag placed directly on the top of the compacted backfill. To simulate the reinforcement at different elevations of a wall in the field, two normal stresses were selected. Once the whole pullout test setup was completed, all sensors were activated to allow the data acquisition system to start recording. After the normal stress distribution throughout the soil mass became stable, the pullout load was applied using a double-acting hydraulic jack.

Results and discussions

Figure 3.20 presents the relationship of the global strain versus the average local strain of the geogrid. The average local strains were calculated using **Eq. 3.2**. The calculated CFs from the strain gauges (ε_{upper} and ε_{lower}) and the telltales placed on the geogrid under the applied normal

stresses of 35 and 70 kPa were 0.84 and 0.86, respectively, with an average of 0.85. Comparing the average CF, obtained from the pullout test, with the average CF from the strain gauges subjected to tension only in air, as discussed in Section 3.3.1, shows that the normal stress had a significant effect on the calculated CF.

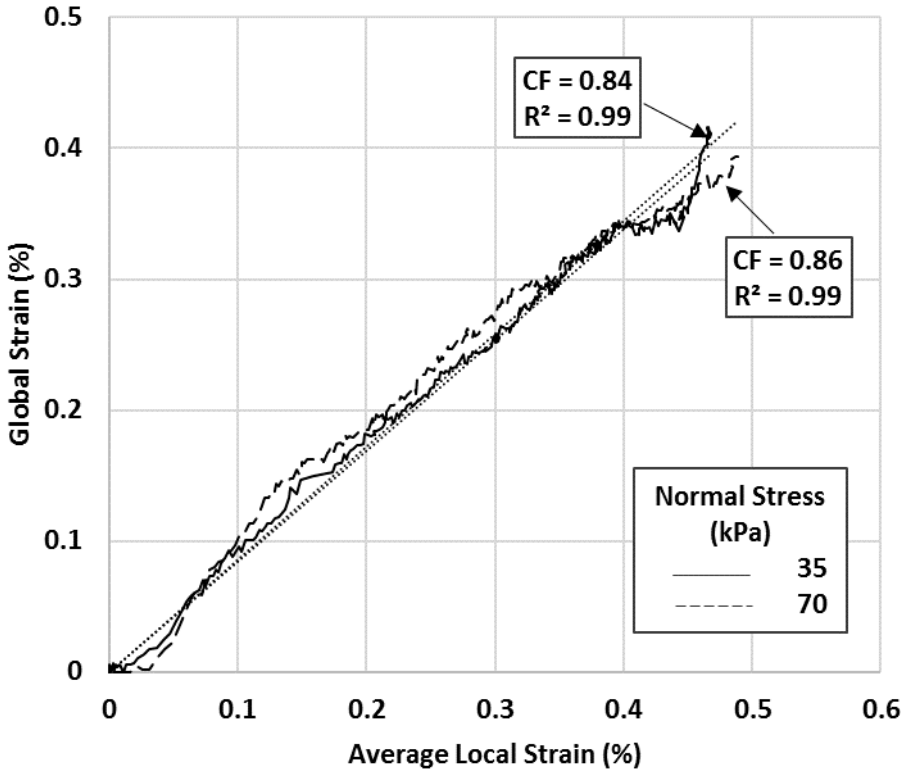

Figure 3.20. Global strain versus average local strain of the geogrid embedded in soil

3.4. Summary

The first objective of this study was to evaluate the effects of stiff plates under an airbag on the distributions of the vertical stresses, the pullout resistance, and the displacements of the reinforcement in the pullout tests. To achieve this objective, six large-scale pullout tests were conducted, in which the geogrid was placed within the soil mass. The following findings can be summarized based on this study:

(1) When the normal stresses were applied by the airbag without any stiff plates, the measured maximum vertical pressures in the transverse direction on top of the soil mass occurred in the middle of the pullout box. However, in the case of the airbag with stiff plates, the maximum vertical pressures in the transverse direction were measured near the edges of the box.

(2) When the normal stress was applied by the airbag without any stiff plates, the displacements at the transverse bar of the geogrid were approximately uniform. When the stiff plates were used, however, the low vertical pressures in the central zone of the box led to the maximum displacement of the geogrid at that location.

The second objective of this study was to evaluate the combined effects of tension, bending, and friction on the relationship between local and global strains in the geogrid and on the measured local strains from the upper and lower sides of uniaxial geogrid specimens subjected to tensile force. Moreover, the effect of the confined pressure induced by applied normal stress on the calculated CF was investigated by using pullout box. The following conclusions can be made based on this experimental study:

(1) The effect of friction on the strains in the geogrid could not eliminated by averaging the strains measured by the strain gauges on upper and lower sides of the geogrid.

(2) The calibration factors (CFs) calculated from the strain gauges subjected to tension, bending, and friction were approximately 39% higher than those calculated from the strain gauges subjected to tension only in the test in air.

(3) In the tests using pullout box for evaluation the CF, the normal stress had a significant effect on the calculated CF comparing with that from the test in air.

Chapter 4: Experimental Study on GRR Walls

4.1. Introduction

The main objective of this study was to evaluate and compare the performance of GRR abutment walls with wrapped-around facing with that with modular concrete block facing. The physical models were constructed in a test box with a rigid base and subjected to static footing loading. This paper evaluates the settlement of the footing, the vertical deflections of the backfill, the lateral displacements of the facing, the vertical and lateral pressure distributions, the strains and tensile forces along the reinforcement, and the failure surfaces through the GRR abutment fill.

4.2. Model Tests

4.2.1. Test apparatus

Eight model tests were carried out to investigate the behavior of the GRR abutment walls with wrapped-around and modular block facing subjected to static loading on a rigid footing up to the failure under a plane strain condition. This experimental study investigated the effect of the facing type (also stiffness) on the performance of GRR abutment walls. The model tests were conducted in a test box with an inside dimension of 2.4 m long, 0.45 m wide, and 1.1 m high as shown in Error! Reference source not found.**4.1**. The frame of the box was made of structural steel profiles. T he two sides of the box were made of 20 mm thick plexiglass. The plexiglass sides allowed visual observation and photogrammetry of the failure modes, the footing settlement, and the deflections

of the GRR walls during construction and loading. To reduce the boundary effect due to the friction of the sides of the box, lubricant was applied onto the plexiglass inside. The loading system consisted of a long-stroke hydraulic jack, which was controlled by a hand-operated regulator, a check valve, and a high-precision pressure gauge to apply the load.

Figure 4. 1. View of the geotechnical test box

4.2.2. Strip footing

Two rigid strip footings were made from a 25-mm thick steel plate. The steel plate was reinforced by two steel profiles to minimize its bending under loading. The smaller footing was 0.20 m wide and 0.45 m long. However, the larger footing was 0.75 m wide and 0.45 m long. To ensure a plane strain condition, the length of the footing was equal to the internal width of the test box.

4.2.3. Backfill

The poorly-graded dry Kansas River sand that was used in pullout tests in chapter 3 was used in this study as the backfill. The mean grain size (D_{50}) was 0.56 mm. The uniformity coefficient (C_u) and the coefficient of curvature (C_c) of the sand were 3.18 and 0.93, respectively. The maximum and minimum dry unit weights of the sand were 18.9 and 16 kN/m^3, respectively. The effect of compaction on the reinforced sand for reduced-scale models was discussed in Rahmaninezhad et al. (2009). A standard direct shear test (ASTM D3080) was used to determine the friction angle of the sand compacted at 70% relative density. The measured peak friction angle of the sand was 37^o.

4.2.4. Geogrid reinforcement

As discussed in the section 3.3.1.2, considering the scale effect in this study, uniaxial geogrid was prepared by modifying punched-drawn biaxial polypropylene (PP) geogrid. The selection of this type of geogrid for reduced-scale model walls was discussed in Xiao et al. (2016). Three transverse ribs of the biaxial geogrid were removed in every four ribs on the machine direction in order to achieve a form of a uniaxial geogrid. Xiao et al. (2016) first adopted this modification and then Rahmaninezhad et al. (2016) and Kakrasul et al. (2018) used it for their studies. The provided

properties of this biaxial geogrid by the manufacturer had the ultimate tensile strength of 12.4 kN/m in the machine direction and 19 kN/m in the cross-machine direction. The cross-machine direction of the biaxial was the same as the longitudinal direction of the uniaxial geogrid. Xiao et al. (2016) showed that the removal of the transverse ribs reduced the ultimate tensile strength of the geogrid in the longitudinal direction by 4%.

Three tests with a tensile testing machine were conducted for determining the tensile properties of single rib of the geogrid in accordance with ASTM D6637/D6637M. Error! Reference source not f ound.**4.2** shows the tensile properties of the geogrid in the cross-machine direction. In Error! Reference source not found.**4.2**, the global strain refers a strain that determined by instruments (e.g., by pairs of extensometers) that are capable of measuring the distance between two reference points such as the tensile testing machine clamps. **Table 3.2** shows the properties of the geogrid obtained from the manufacturer. As discussed in Chapter 3, a set of the pullout tests in accordance with ASTM D6706-01 were carried out using the RJH box to determine the pullout resistance of the modified geogrid that was embedded in the sand. From the pullout test, the coefficient of interaction (μ) was determined as 0.75.

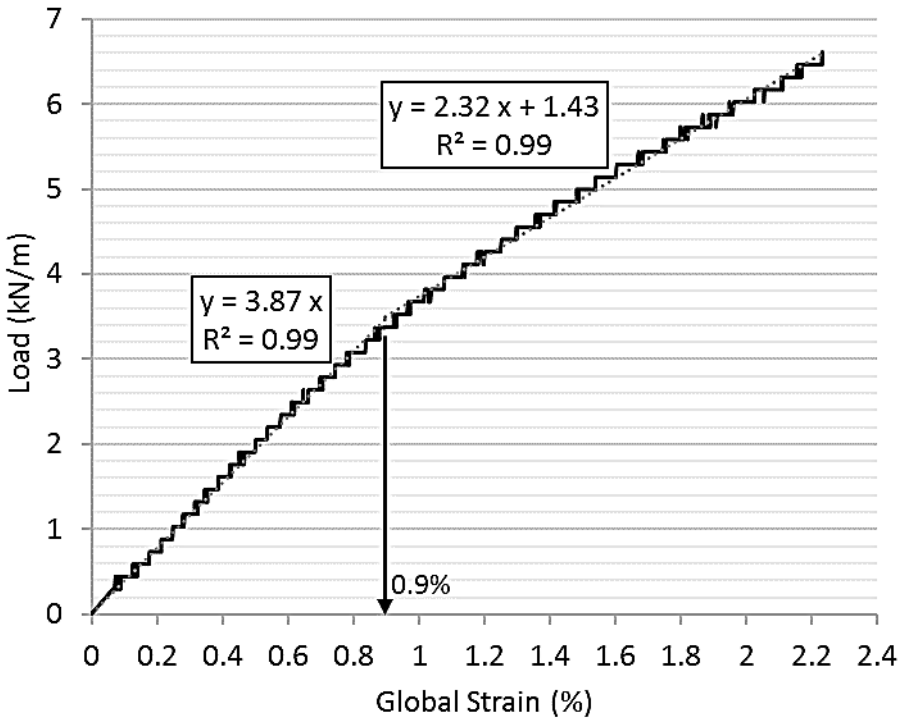

Figure 4. 2. Tensile properties of geogrid in the cross-machine direction

4.2.5. Facing

Two types of wall facing were evaluated in this study: wrapped-around facing and modular block facing. In the wrapped-around faced GRR wall, the uniaxial geogrid sheets were placed with the machine direction perpendicular to the facing of the wall. Christopher and Holtz (1985) suggested that the geosynthetic sheet should be secured in place to prevent movement during fill placement. The wall with the wrapped-around facing was constructed by folding the extended geogrid sheet through 180° at the face over the current fill, anchoring it back into the backfill, and having it tied to another geogrid sheet at a higher elevation. Thin and low-strength gardening sheets were used between the wrapped geogrid and the backfill to keep the sand behind the facing and prevent it

from flowing out. In the block facing models, the wall facing was made with individual modular concrete blocks, which were prepared by cutting plain concrete blocks available in the market. Each block was 150 mm long, 50 mm high, 50 mm wide and had a mass of about 0.85 kg. The concrete blocks were placed one above another. The geogrid layers were placed at 200 mm vertical spacing and connected mechanically to the facing units. All models were vertical with a zero-degree facing batter during the construction.

4.2.6. Instrumentation

Pressure cells were used to measure vertical and lateral pressures. The capacities of the pressure cells were 200 or 500 kPa. A pressure gauge was used to control the hydraulic pressure applied to the footing. Survey targets and colored sand were used for measuring the wall displacements and footing settlements, and photos were taken to evaluate slip surfaces in the backfill. A laser tape with the accuracy of 0.1 mm was used to measure displacements and settlements.

The strains of the geogrids were measured by foil-type strain gauges that attached on both upper and lower sides of the geogrid. This type of strain gauge had a matrix length of 0.32 inches and a matrix width of 0.17 inches, and could measure a tensile strain up to 3%. For the geogrid, the strain gauge length lead to measure localized strain. The shape of the geogrid ribs and junctions produces stress concentration in the special zones (Min et al., 1995; Allen and Bathurst, 2003). Therefore, the measured local strains from the strain gauges glued to the geogrid were correlated with global strains. The global strain can refer to an averaged strain over a length (in the case of a geogrid, one or more aperture lengths) that is larger than the length of the strain gauge (Bathurst et al., 2002).

The calibration factor, *CF*, presents the ratio between the measured local strain of the strain gauge and global strain.

In-isolation laboratory tests were carried out to determine the calibration between local and global strains of the geogrids used in this study. Error! Reference source not found.**4.3 (a)** shows t he location of a strain gauge on the geogrid and the setup of the test using universal tensile machine. **Figure 4.3 (b)** shows the setup of the tensile test of a geogrid specimen inside the pullout box as discussed in section 3.3.2.1. Error! Reference source not found.**4.4 (a)** shows the local strain from strain gauges versus to the global strain of the geogrid in air. A single-value *CF* is approximately *CF* = 1.04. However, the calculated *CFs* from strain gauges (ε_{upper} and ε_{lower}) and telltale system placed on the geogrid under applied normal stress of 3.5, 7.0, and 10.0 kPa were 1.00, 0.96, and 0.97, respectively, with an average of 0.98. The average *CF* calculated from the test in the air was approximately equal with that from the tests in soil.

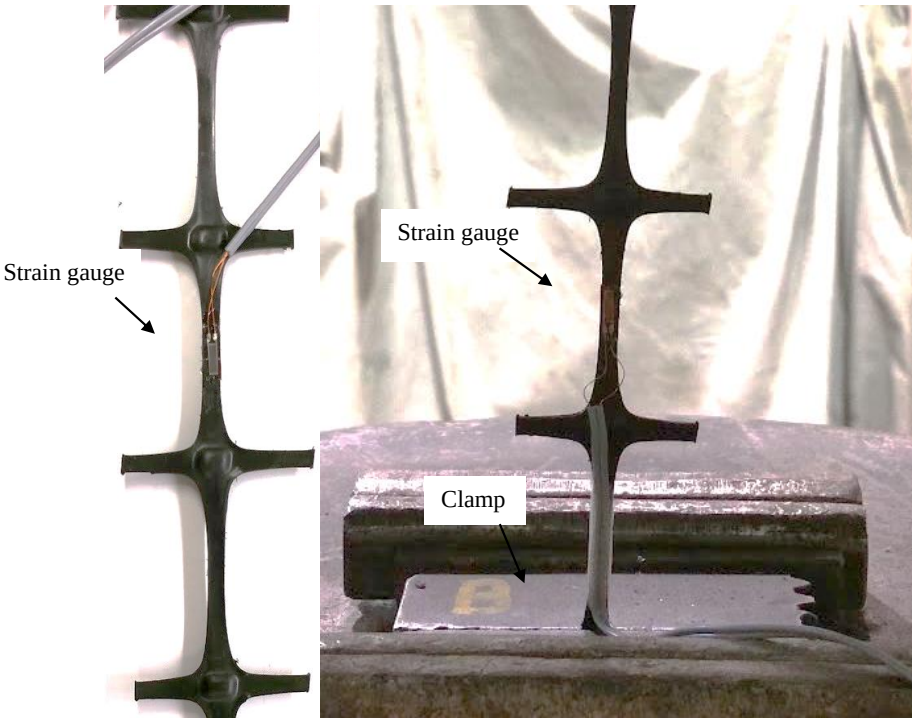

(a)

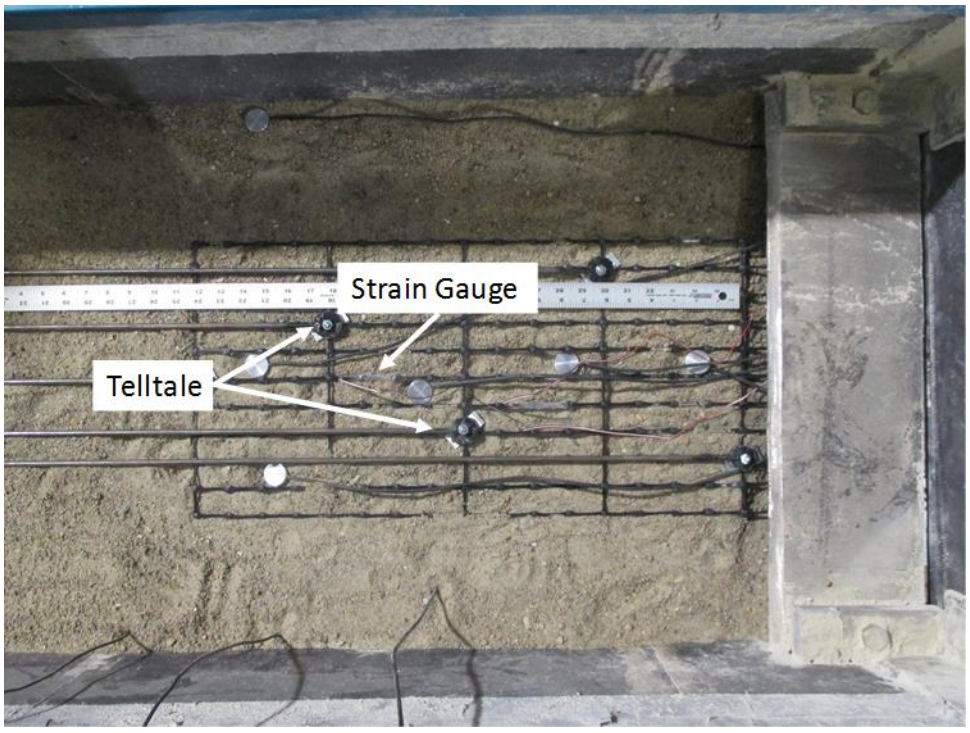

(b)

Figure 4. 3. Location of strain gauge and the setup of the test: (a) in air; (b) in soil

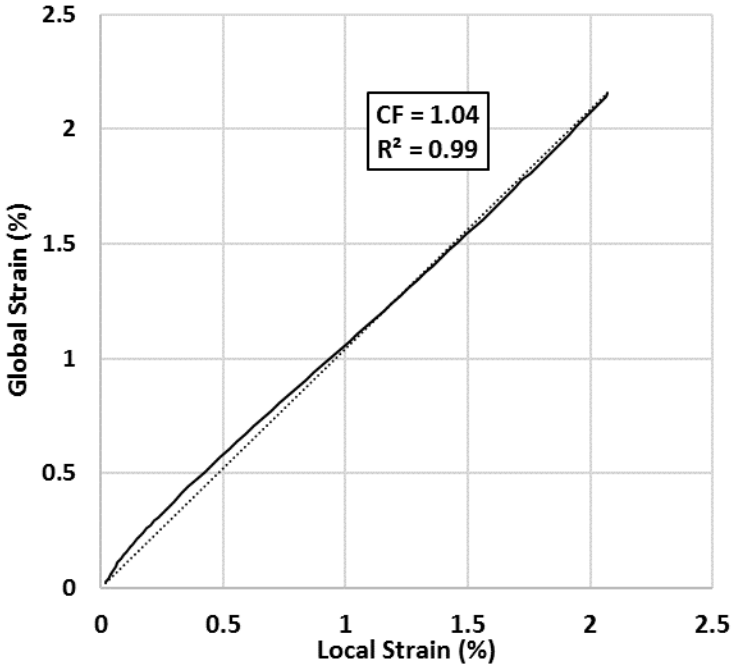

(a)

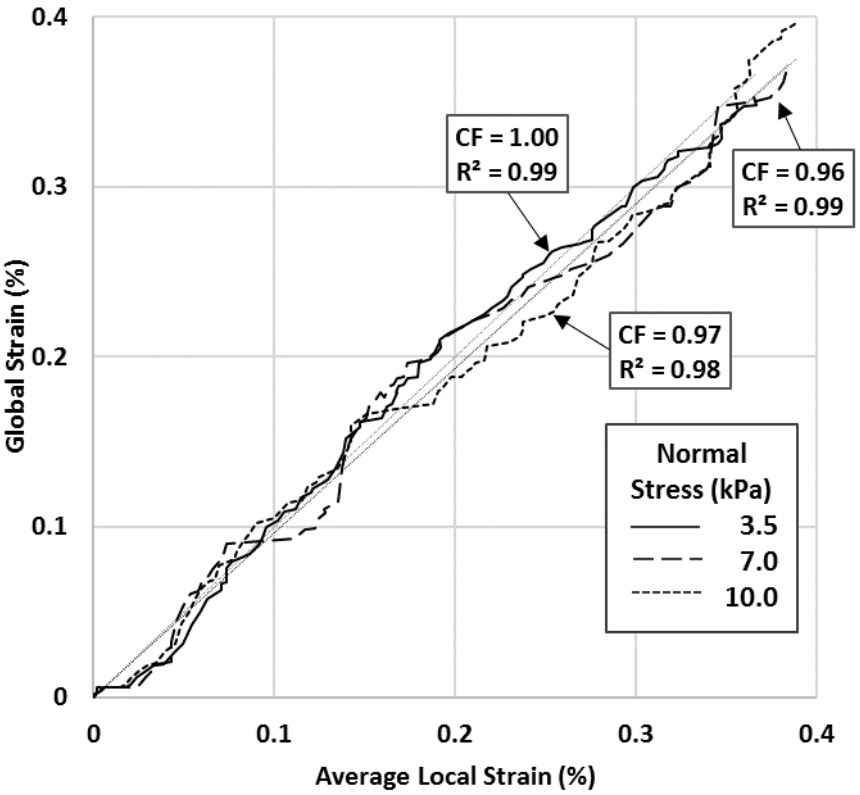

(b)

Figure 4. 4. Global strain versus local strain gauges: (a) in air; (b) in soil

Figure 4.5 presents the pullout test results of the geogrid. These figures show that at the normal stress of 10 kPa applied by the airbag without and with stiff plates, the pullout forces were 15.87 and 11.11 kN/m, respectively, at the front displacement of 20 mm.

Also, at the normal stress of 7 kPa applied by the airbag without and with stiff plates, the pullout forces were 9.32 and 7.47 kN/m, respectively, at the same front displacement (20 mm). Therefore, the pullout resistance of the geogrid under the airbag without any stiff plates was higher than that under the airbag with stiff plates. Under the normal stresses of 10, 7, and 3.5 kPa, the pullout resistance values of the geogrid when the airbag was used with stiff plates were 30, 20, and 3 %, respectively, lower than those measured without stiff plates. Evidently, at the low normal stress, there was a minor difference between the pullout resistances using these two different loading methods.

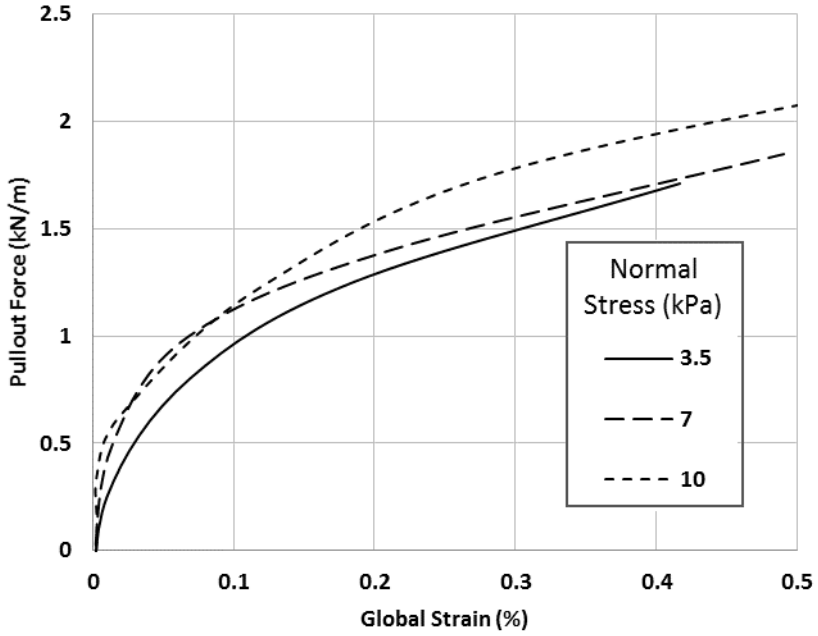

Figure 4. 5. Pullout resistance of geogrid versus global strain

4.2.7. Test configurations

The GRR model walls were constructed to investigate the effect of two types of wall facing on the performance of the GRR walls subjected to footing loading. The walls were constructed on 50 mm sand above a rigid base and subjected to static strip loading. Regarding the type of the facing, the models walls were categorized into two series including: (1) series W and (2) series B. The walls series W represented the walls with a wrapped-around facing. The walls series B represented the walls with a modular block facing. **Figure 4.6 and 4.7** show the cross sections of the model walls, which had the height, H, of 1 m, the vertical spacing between geogrid layers, S_v, of 0.2 m, and the offset distance of the footing to the back of the wall facing, D, of 0.2 m. However, in these model walls the geogrid length, L, and the retained zone length, l, were variable. **Table 4.1** shows the details of the model walls.

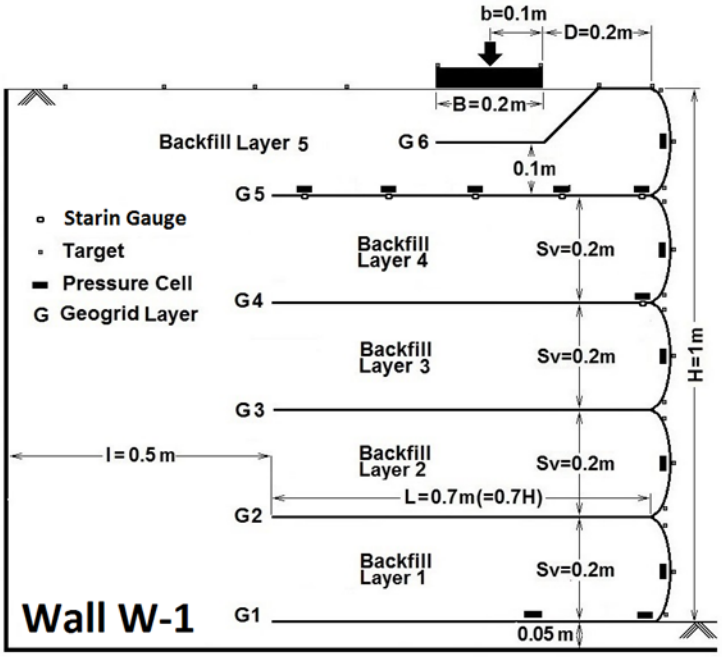

(a)

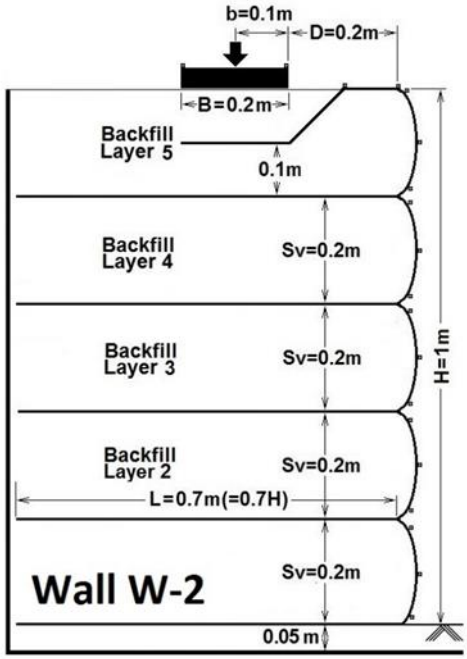

(b)

Figure 4. 6. Schematic view of model walls with wrapped-around facing: (a) Wall W-1; (b) Wall W-2, (c) Wall W-3, and (d) Wall W-4 (continued)

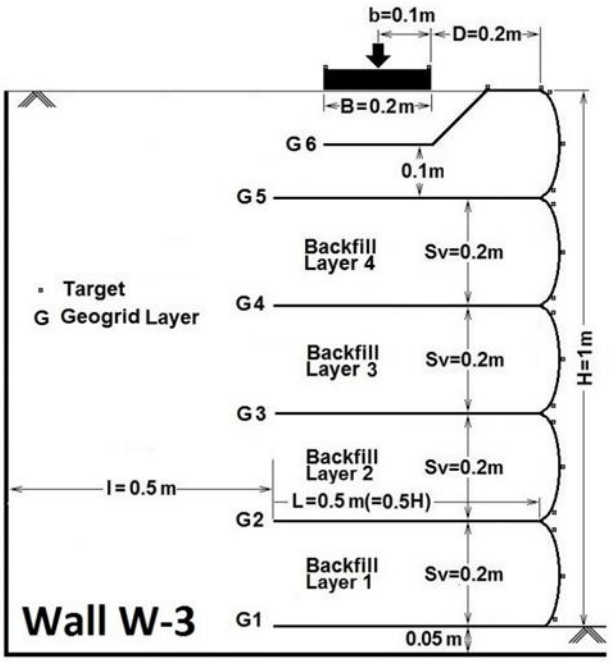

(c)

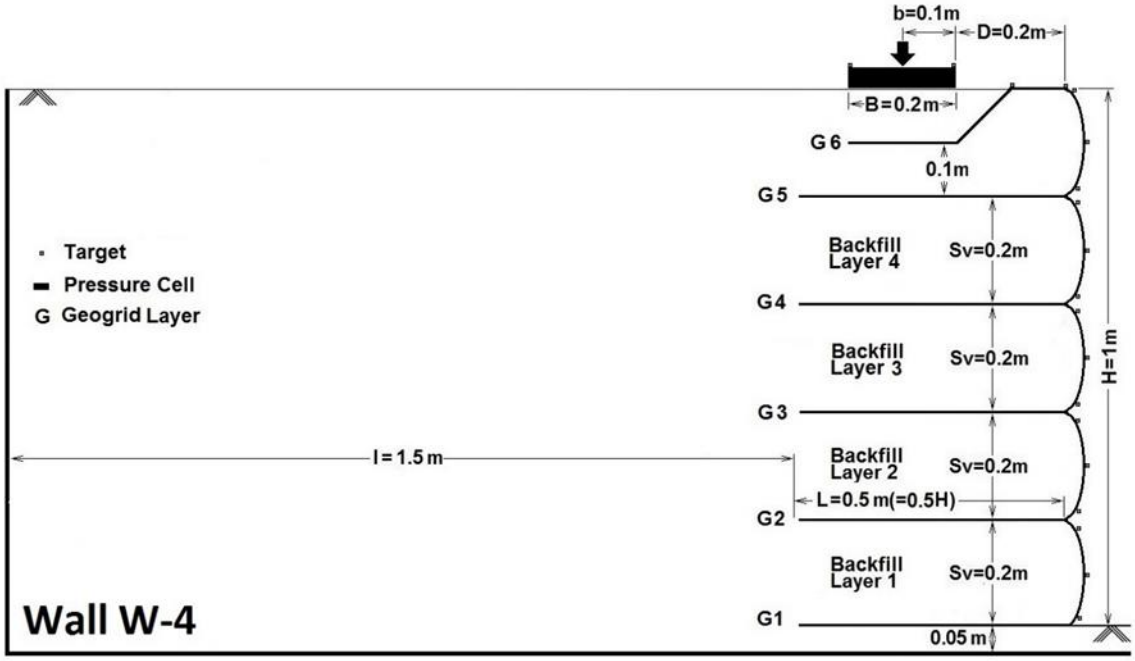

(d)

Figure 4.6. Schematic view of model walls with wrapped-around facing: (a) Wall W-1; (b) Wall W-2, (c) Wall W-3, and (d) Wall W-4

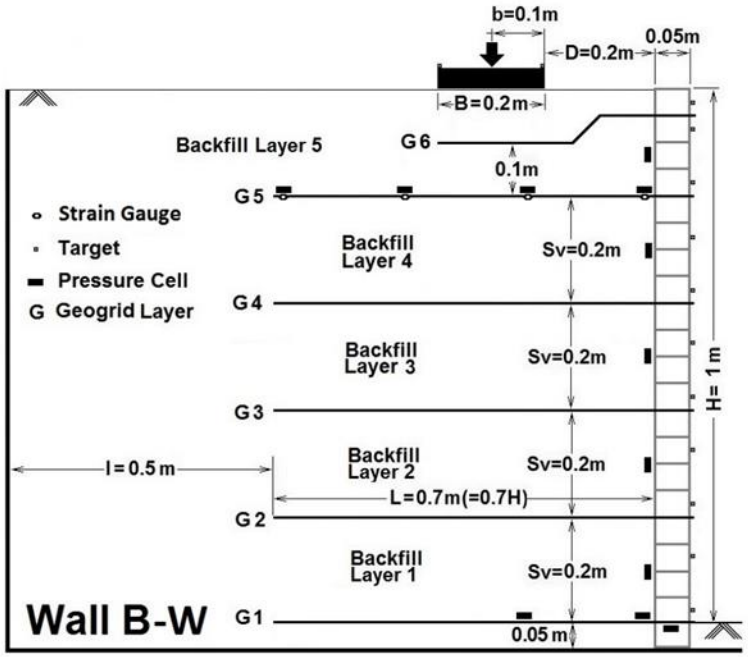

(a)

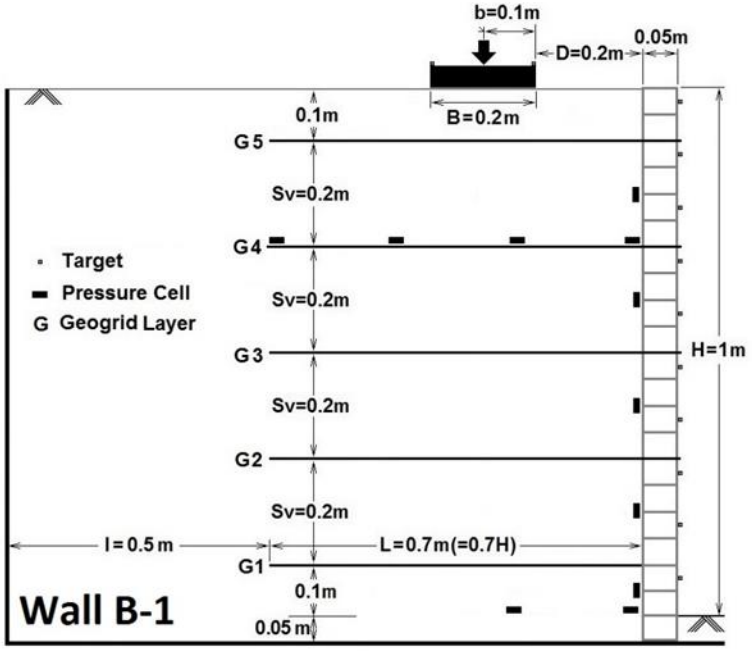

(b)

Figure 4. 7. Schematic view of model walls with modular block facing: (a) Wall B-W; (b) Wall B-1, (c) Wall B-2, (d) Wall B-3, and (e) Wall B-4 (continued)

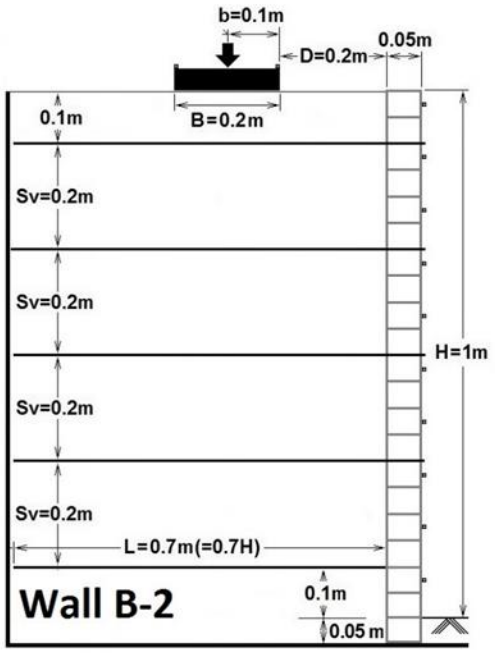

(c)

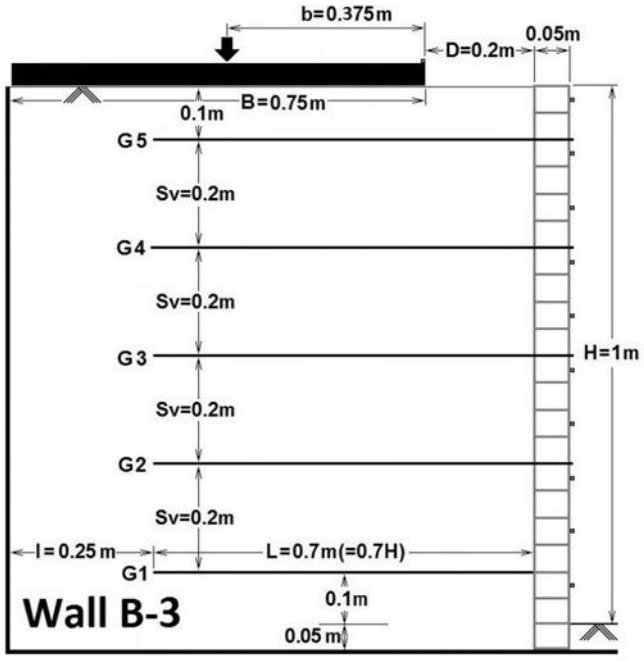

(d)

Figure 4.7. Schematic view of model walls with modular block facing: (a) Wall B-W; (b) Wall B-1, (c) Wall B-2, and (d) Wall B-3

Table 4.1. Details of the model walls

No.	Wall	Type of Facing	Height, H (m)	Vertical Spacing, Sv (m)	Geogrid Length, L (m)	Offset, D (m)	Retained Zone Length, l (m)	Footing Width, B (m)
1	W-1	wrapped-around	1	0.2	0.7	0.2	0.5	0.2
2	W-2	wrapped-around	1	0.2	0.7	0.2	0	0.2
3	W-3	wrapped-around	1	0.2	0.5	0.2	0.5	0.2
4	W-4	wrapped-around	1	0.2	0.5	0.2	1.5	0.2
5	B-W	modular block	1	0.2	0.7	0.2	0.5	0.2
6	B-1	modular block	1	0.2	0.7	0.2	0.5	0.2
7	B-2	modular block	1	0.2	0.7	0.2	0	0.2
8	B-3	modular block	1	0.2	0.7	0.2	0.25	0.75

Walls W-1, W-2, W-3, and W-4 were constructed with six layers of the uniaxial geogrid but without the hard facing. In these walls, the sixth geogrid layer was extended back from the facing wrap of the fifth layer into the reinforced zone. During the construction, wooden plates were placed to temporarily support the wall facing at zero facing batter. Each facing wrap was connected to the geogrid layer above using zip ties instead of metal bar clamp like bodkin connection. Except for of the top layer, the facing wrapped geogrids were not extended back into the reinforced zone.

Wall B-W was constructed with six layers of the uniaxial geogrid in an identical manner to Wall W-1 but with modular blocks for the facing. This wall was designed to evaluate the effect of facing rigidity as compared with Wall W-1. Hence, the layout of geogrids may not resemble those in typical walls with block facing (i.e., the bottom layer may not be placed at such a location in the field). Mechanical connections were used to connect the geogrid to the blocks.

Walls B-1, B-2, and B-3 were constructed with five layers of the uniaxial geogrid. This wall was designed to represent a typical GRR wall with modular block facing in the practice.

4.3. Measured Data and Discussion

4.3.1. Settlement

The settlement of the center of the footing at each applied pressure was measured using the laser tape. Error! Reference source not found.**4.8(a)** shows the pressure-settlement curves of the footing o n the GRR walls with wrapped-around facing. Under the same applied footing pressure, Wall W-1, with the retained zone, had a lower settlement than Wall W-2, without the retained zone (Error! R eference source not found.**4.8(a)**). Wall W-1, with longer geogrid reinforcement layers, had a lower settlement than Wall W-3, with shorter geogrid reinforcement layers under the same applied footing pressure. Error! Reference source not found.**4.8(a)** also shows Wall W-4 with short geogrid r einforcement layers and larger retained zone had larger settlement than Wall-3 with short geogrid reinforcement layers and smaller retained zone.

Error! Reference source not found.**4.8(b)** shows that the pressure-settlement curves of the footing o n the GRR walls with modular block facing. When the applied pressure was lower than 200 kPa, Wall B-W had larger settlements than Walls B-1, under the same applied footing pressure (Error! R eference source not found.**4.8(b)**). However, after 200 kPa, Walls B-W and B-1 behaved similarly. Wall B-1, with the retained zone, and Wall B-3, without the retained zone, also behaved similarly as shown in Error! Reference source not found.**4.8(b)**. Error! Reference source not found.**4.8(b)** also shows Wall B-3 with a larger footing had a less settlement than other walls.

Error! Reference source not found.**4.9** shows that the pressure-settlement curves of the footing on W alls W-1, W-B, and B-1 together. When the applied pressure was lower than 175 kPa, all three walls behaved similarly. However, after 175 kPa, Wall W-1 with wrapped-around facing had larger

settlements than Walls B-W and B-1. For instance, under the applied pressure of 230 kPa, the settlements of the footing on Walls W-1, B-W and B-1 were approximately 138, 87, and 86 mm, respectively.

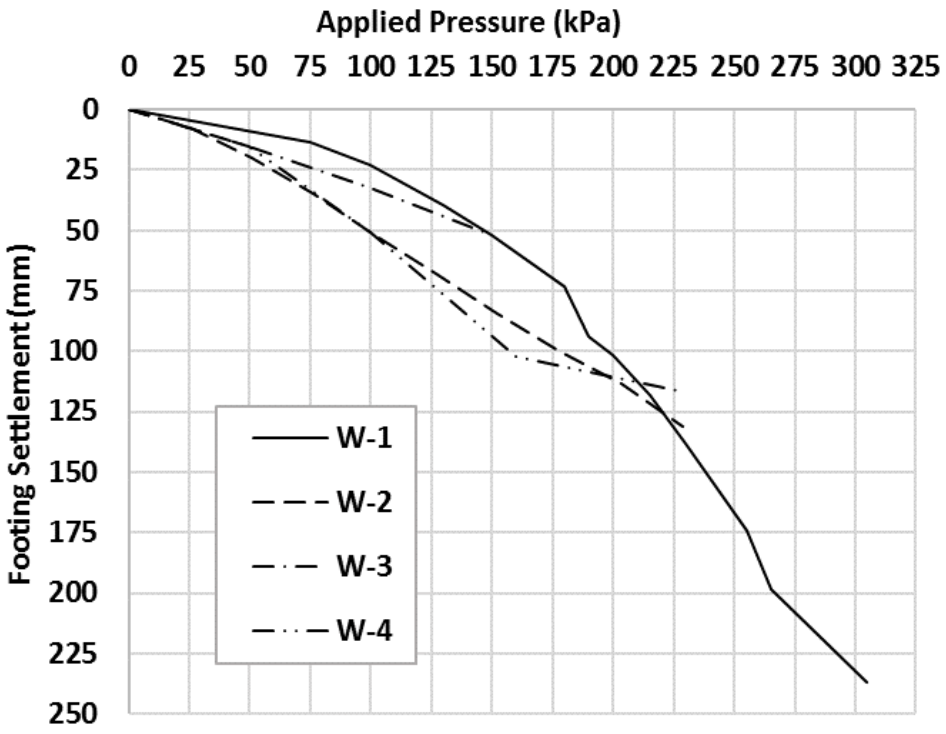

(a)

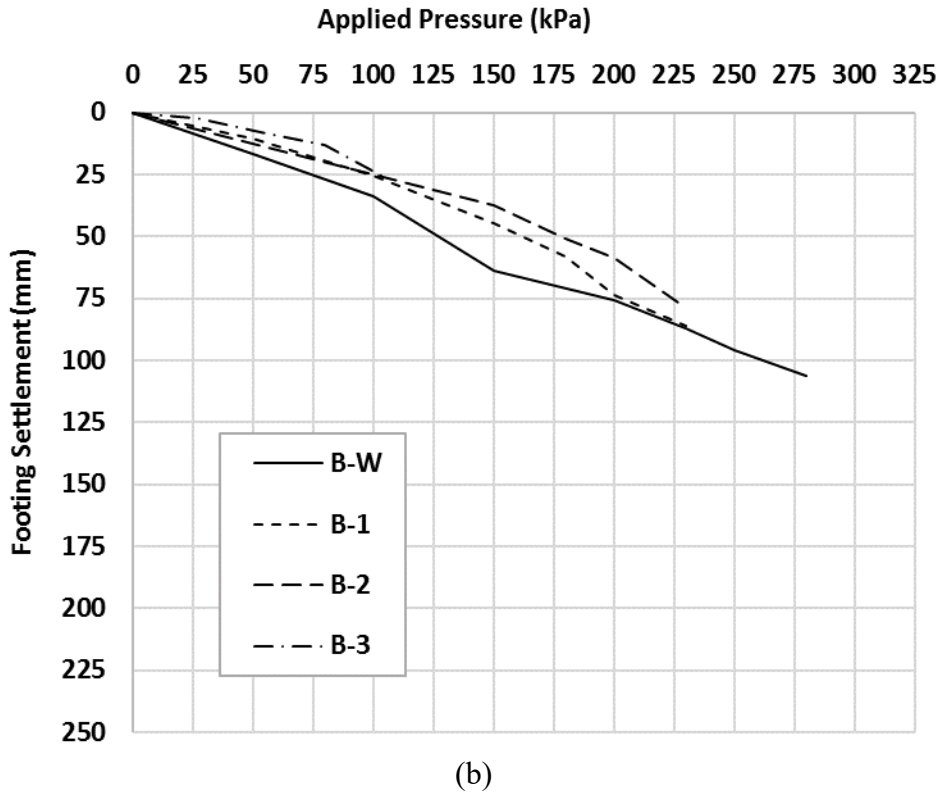

(b)

Figure 4. 8. Pressure-settlement curves of footings on GRR walls: (a) model walls with

wrapped-around facing and (b) model walls with modular block facing

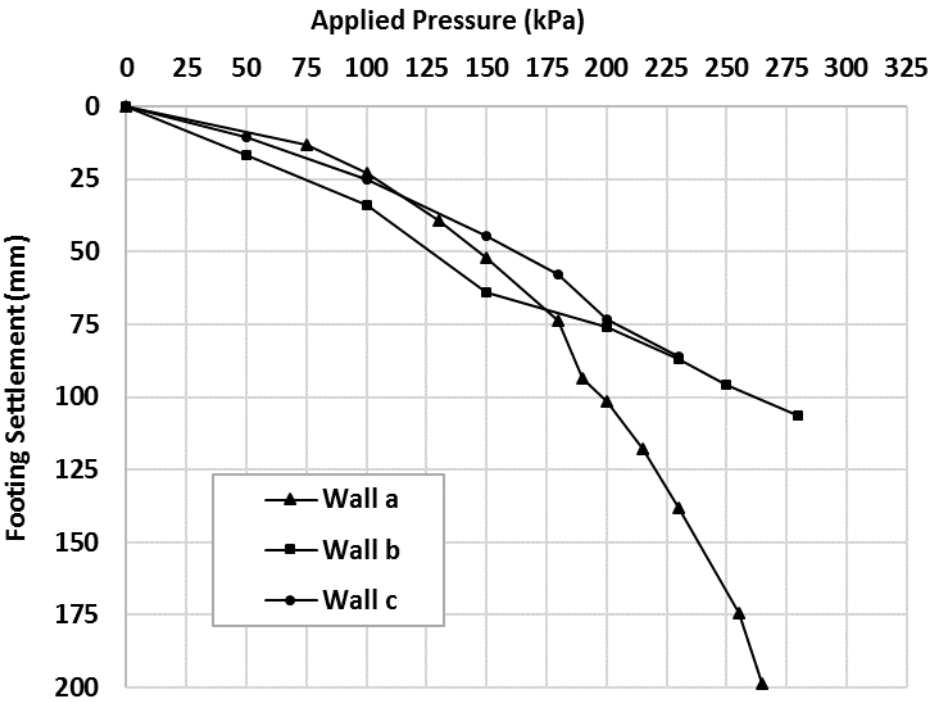

Figure 4. 9. Pressure-settlement curves of footings on GRR walls

Error! Reference source not found.**4.10** presents the settlements at different elevations of Walls W-1 , W-B, and B-1 under the applied footing pressure of 230 kPa using the photogrammetry method. Error! Reference source not found.**4.10** also shows that the settlements in Wall W-1 were much l arger than Walls B-W and B-1. Furthermore, Wall W-1 started to tilt toward the facing. However, in Walls B-W and B-1, the maximum settlements were localized under the footing. In Wall W-1, large compression occurred in the backfill under the footing. The large deflections happened between the wall facing and the centerline of the footing. The compressions of the upper three wraps at the facing were 21, 23, and 28 mm, respectively. Small compressions were observed in the lower two wraps. Since the facing units of Walls B-W and B-1 were relatively rigid, no facing compression was observed during and after the construction and loading. The 2:1 distribution lines (AASHTO, 2012; Berg et al., 2009) are also plotted in **Figure 4.10**, which shows most of compressions happening within the distributed areas. Clearly, the settlements under the footing in Walls B-W and B-1 are approximately symmetric to the centerline of the footing due to the existence of the relative rigid facing. On the other hand, the settlements under the footing in Wall W-1 are not symmetric to the centerline of the footing due to the existence of the flexible facing (i.e., larger settlements toward the facing).

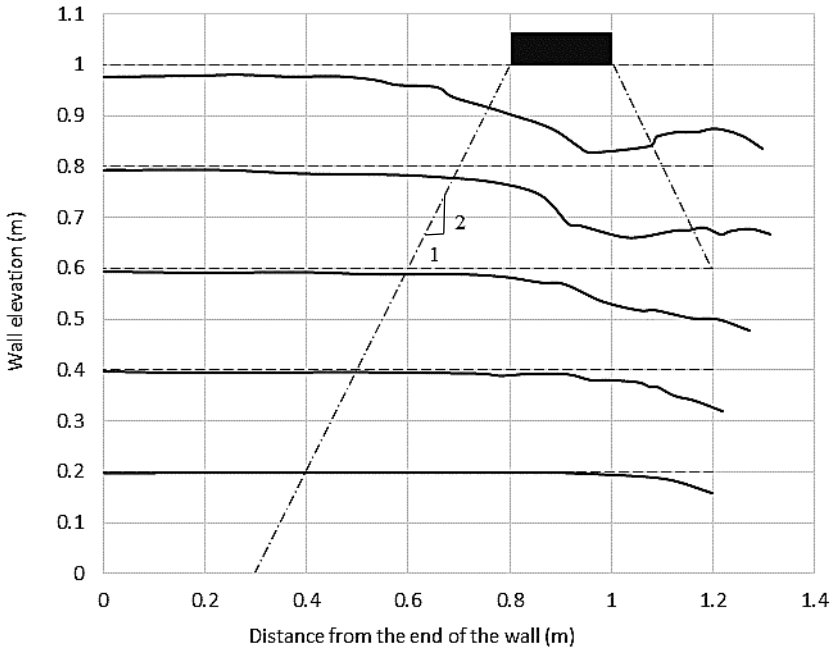

(a)

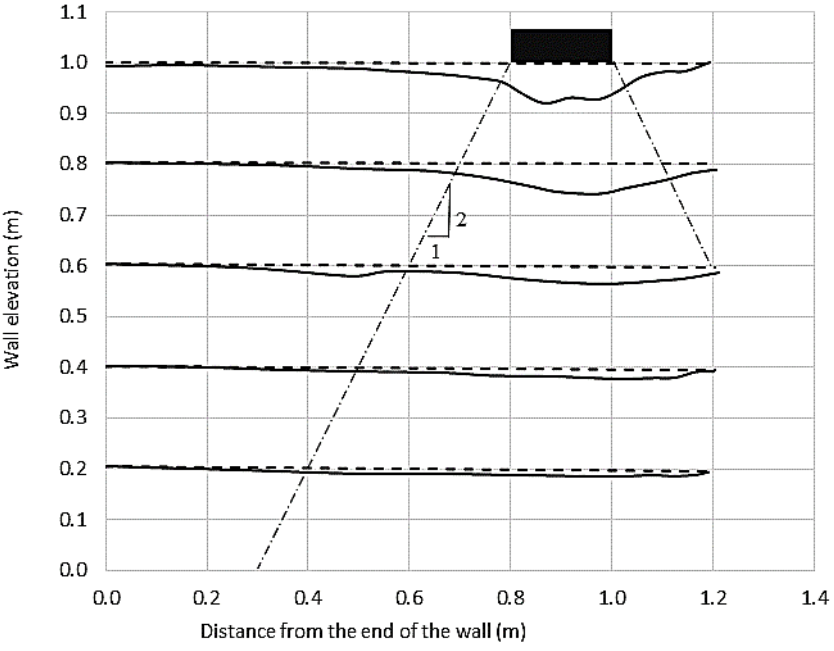

(b)

Figure 4. 10. Settlements at different elevations under the applied footing pressure of 230 kPa: (a) Wall W-1, (b) Wall B-W, and (c) Wall B-1 (continued)

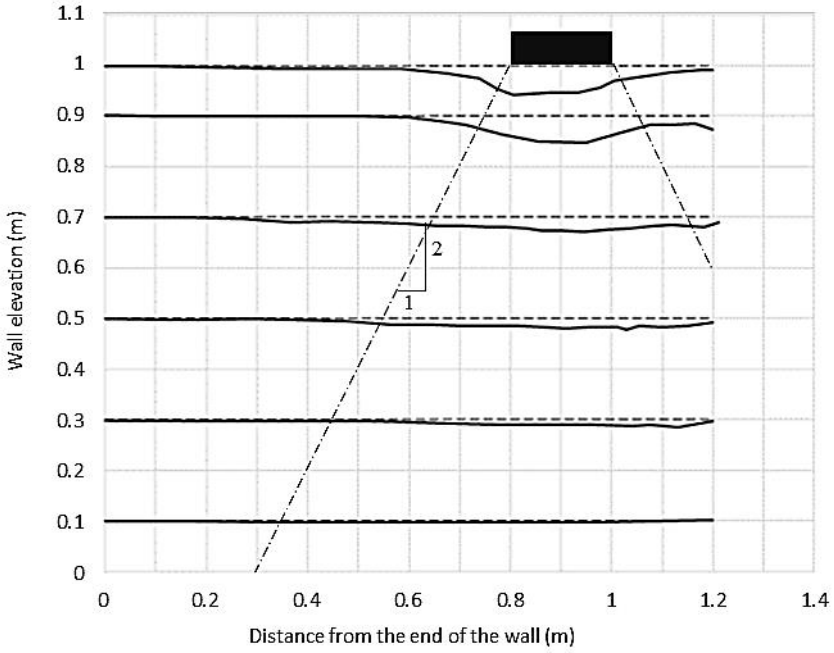

(c)

Figure 4.10. Settlements at different elevations under the applied footing pressure of 230 kPa: (a) Wall W-1, (b) Wall B-W, and (c) Wall B-1

4.3.2. Facing deflection

After the construction, the temporary supporting wooden plates were removed. In the walls with wrapped- around facing, the wrapped face of each layer was allowed for lateral movement. This movement caused backfill settlement of approximately 23 mm at the back of the wrapped facing. Moreover, an outward inclination of approximately 3° was observed after removal of the temporary support. In the walls with block facing after the construction, the photogrammetry showed an outward inclination of approximately 1.5°.

In addition to the photogrammetry method, targets were placed along the centerline of the wall facing to measure its lateral displacements by a laser tape. **Figure 4.11** shows the lateral displacements of the targets along the height of the walls with wrapped- around facing, under the applied footing pressures, without considering the facing settlements. The measurement of the photogrammetry was taken from sides of the wall while that of the laser tape was taken along the centerline of the walls. Even though they measured different magnitudes of wall facing movement, they showed similar patterns of the wall facing deflections. The maximum lateral displacements for Walls W-1, W-2, W-3, and W-4 occurred at 0.3H, 0.22H, 0.42H, and 0.4H from the top of the walls, respectively (**Figure 4.11**). These results indicate that in the walls with longer geogrid reinforcement layers (Walls W-1 and W-2) the maximum lateral displacements occurred within the upper third of the wall height. However, in the walls with shorter geogrid reinforcement layers (Walls W-3 and W-4) the maximum lateral displacements occurred within the middle third of the wall height as shown in Error! Reference source not found.**4.11(c) and (d)**. **Figure 4.11** also shows t hat the maximum lateral displacement of Walls W-1, W-2, W-3, and W-4 were 80, 59, 94, and 78 mm, respectively, under the applied footing pressure of 230 kPa.

Figure 4.12 shows the lateral displacements of the targets along the height of the walls with modular block facing, under the applied footing pressures. The maximum lateral displacements for Walls B-W, B-1, B-2, and B-3 occurred at 0.37H, 0.13H, 0.15H, and 0.25 H from the top of the walls, respectively. The short reinforcement layer on the top of Wall B-W affected the deflection of the wall under the footing loading. With an increase of the applied pressure, the top reinforcement dragged the top of the facing inward as shown in **Figure 4.12 (a)**. However, in Wall W-1, because of the flexibility of the facing, there was no inward deflection (**Figure 4.12 (a)**). The maximum lateral displacement of Walls B-W, B-1, and B-2 were 22, 36, and 33 mm, respectively,

under the applied footing pressure of 230 kPa. Since the footing of Wall B-3 was longer than other walls, the capacity of the loading system was not enough to apply more than 100 kPa. The maximum lateral displacement of the Wall W-1 was 3.5 times larger than that of the Wall B-W and 2.2 times larger than that of the Wall B-1 under the applied footing pressure of 230 kPa. Abu-Hejleh et al. (2001) reported the maximum displacement of a 6 m high modular block facing wall Induced by placement of bridge superstructure (estimated as 115 kPa) was about 10 mm occurred within the upper third of the wall height. Bathurst et al. (2006) reported that under a surcharge pressure of 80 kPa, the maximum post-construction facing displacement of the wrapped-around facing wall was three times larger than that of the stiff facing wall.

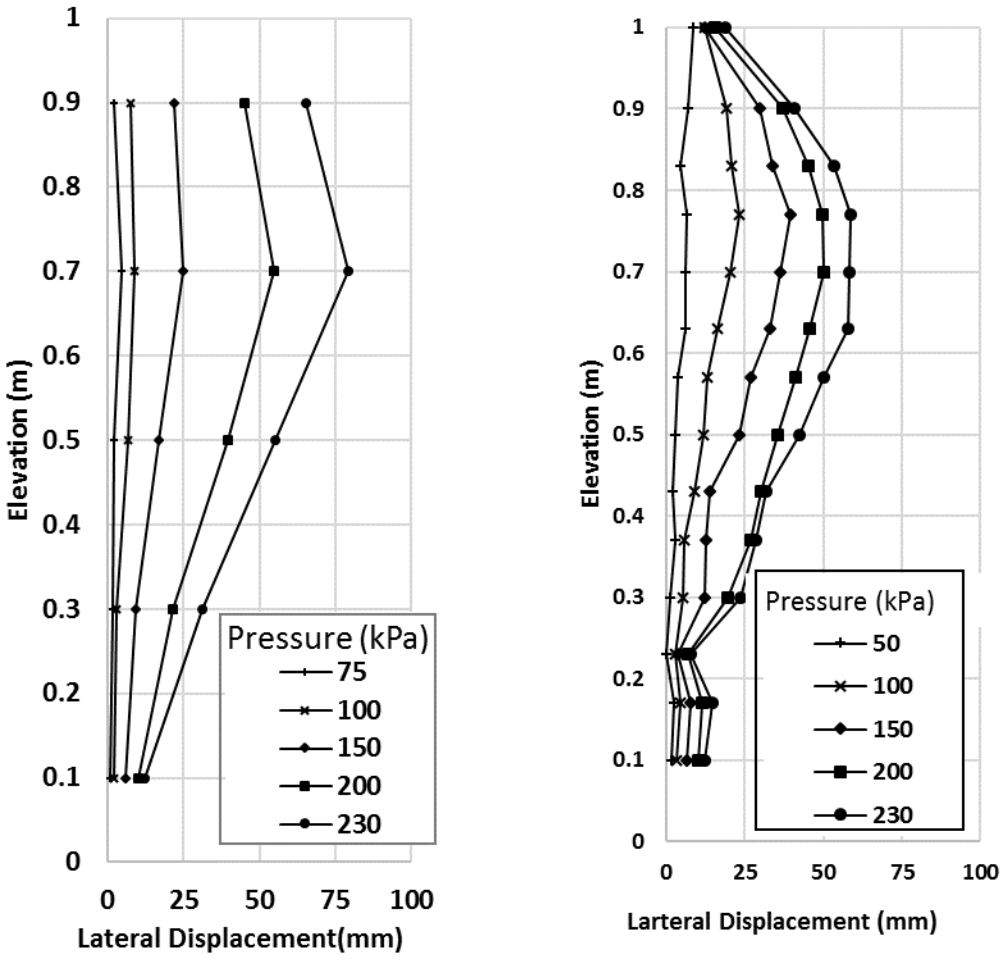

(a) (b)

Figure 4. 11. Deflections of the model walls with wrapped-around facing under the applied pressures: (a) Wall W-1, (b) Wall W-2, (c) Wall W-3, and (d) Wall W-4 (continued)

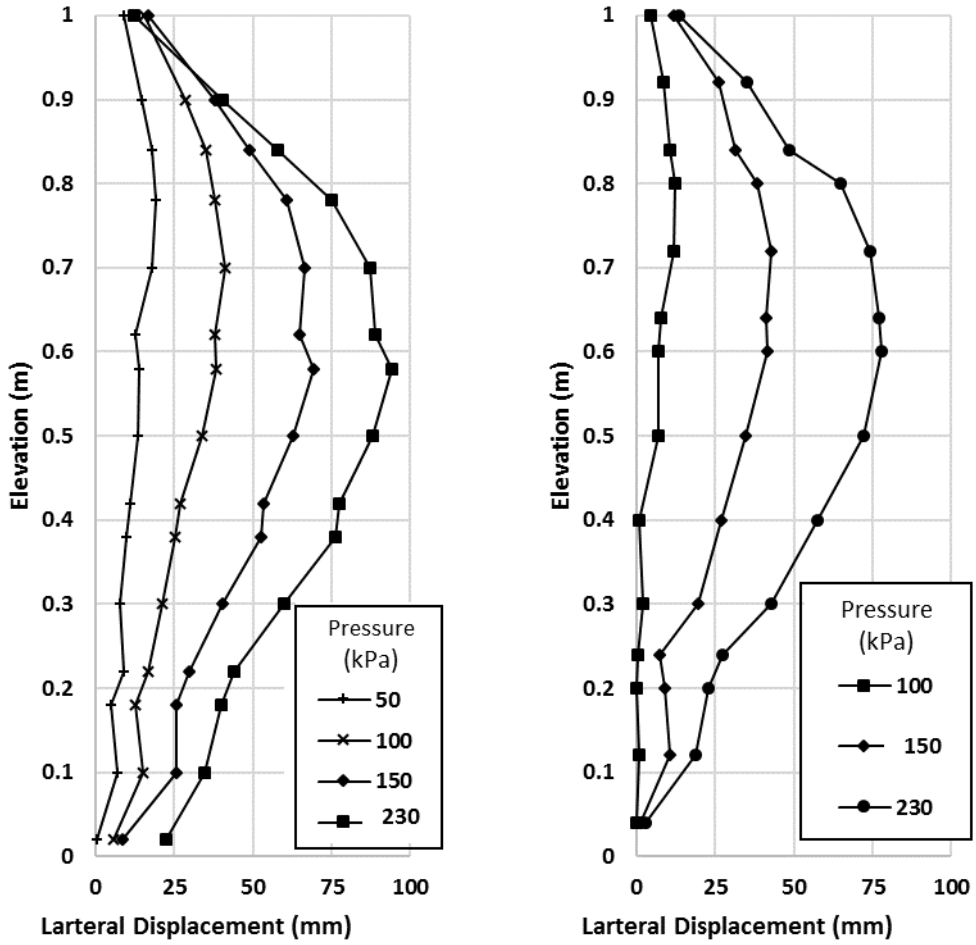

(c) (d)

Figure 4.11. Deflections of the model walls with wrapped-around facing under the applied pressures: (a) Wall W-1, (b) Wall W-2, (c) Wall W-3, and (d) Wall W-4

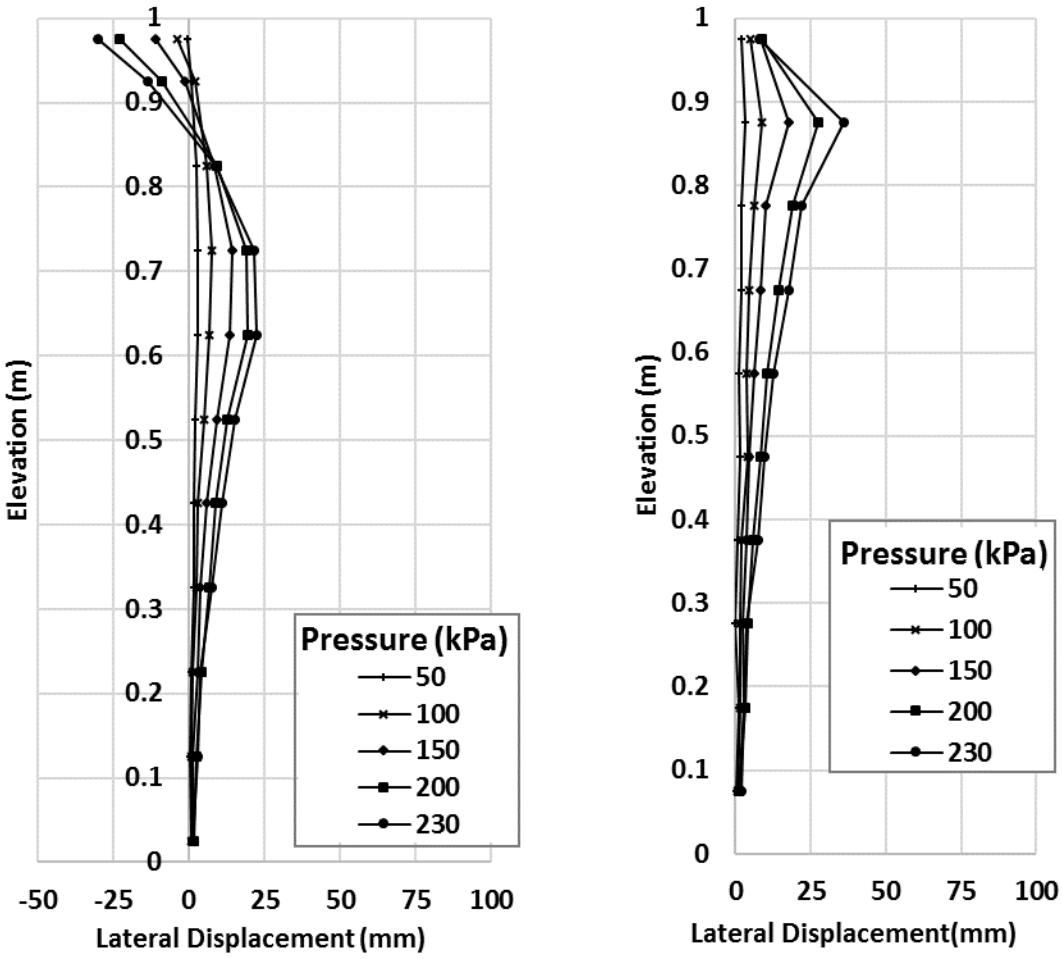

(a) (b)

Figure 4. 12. Deflections of the model walls with modular block facing under the applied pressures: (a) Wall B-W, (b) Wall B-1, (c) Wall B-2, and (d) Wall B-3 (continued)

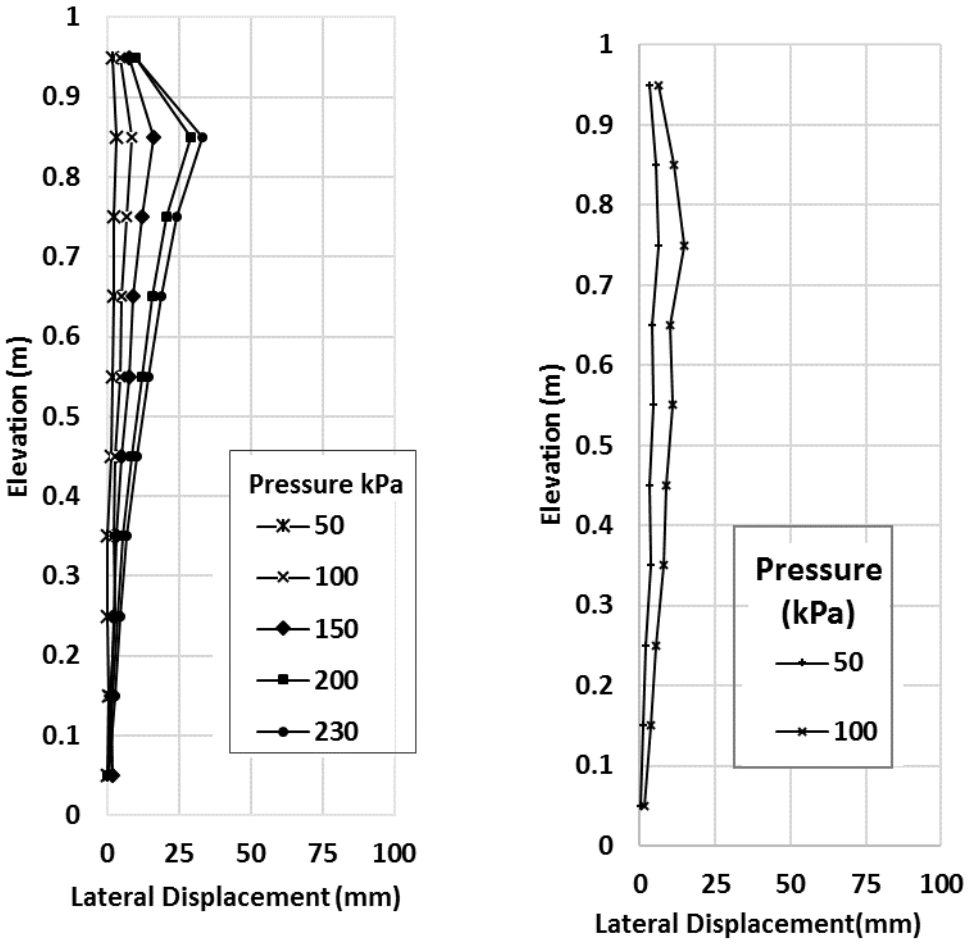

(c) (d)

Figure 4.12. Deflections of the model walls with modular block facing under the applied pressures: (a) Wall B-W, (b) Wall B-1, (c) Wall B-2, and (d) Wall B-3

4.3.3. Vertical earth pressure

Figure 4.13 presents the vertical earth pressures ($\Delta\sigma_v$) induced by footing loading along the distance to the wall facing at the wall height of 0.8 m (i.e. Layer 5) for Walls W-1 and B-W, and at the wall height of 0.7 m for Wall B-1. The vertical pressures calculated by the Boussinesq's equation and the 2:1 distribution method proposed by FHWA (Berg et al., 2009), AASHTO (AASHTO, 2012), and Holtz and Kovacs (1981) are also plotted with the measured vertical pressures for comparison. The Boussnisq's solution based on the theory of elasticity is commonly used to compute the vertical and lateral pressure profile against walls from the surface surcharge (Point, line, or strip) loading (Bowles, 1996). It should be noted that the measured and the calculated earth pressures presented in this paper are the additional pressures induced by the footing loading and do not include the pressure due to self-weight of the wall.

The measured vertical earth pressures generally increased with the increase of the applied footing pressure for Walls B-W and B-1. However, the pressure cells installed in the Wall W-1 model behaved somewhat differently. In the Wall W-1 and B-W, the pressure cells placed at the distances of 0.62 and 0.47 m from the wall facing measured very low pressures during the loading. The maximum vertical earth pressures in Walls W-1, B-W, and B-1 were measured from the pressure cells that placed at 0.17 m, 0.17 m, and 0.25 m from the wall facing, respectively which approximately were located under the outer edge of footing. In all three walls, the maximum measured vertical earth pressures had higher magnitudes as the calculated vertical pressures. The maximum measured vertical earth pressures in Walls W-1, B-W, and B-1 at the applied pressure of 230 kPa were 1.46, 1.41, and 1.72 times higher than the calculated maximum vertical pressure magnitudes by 2:1 method.

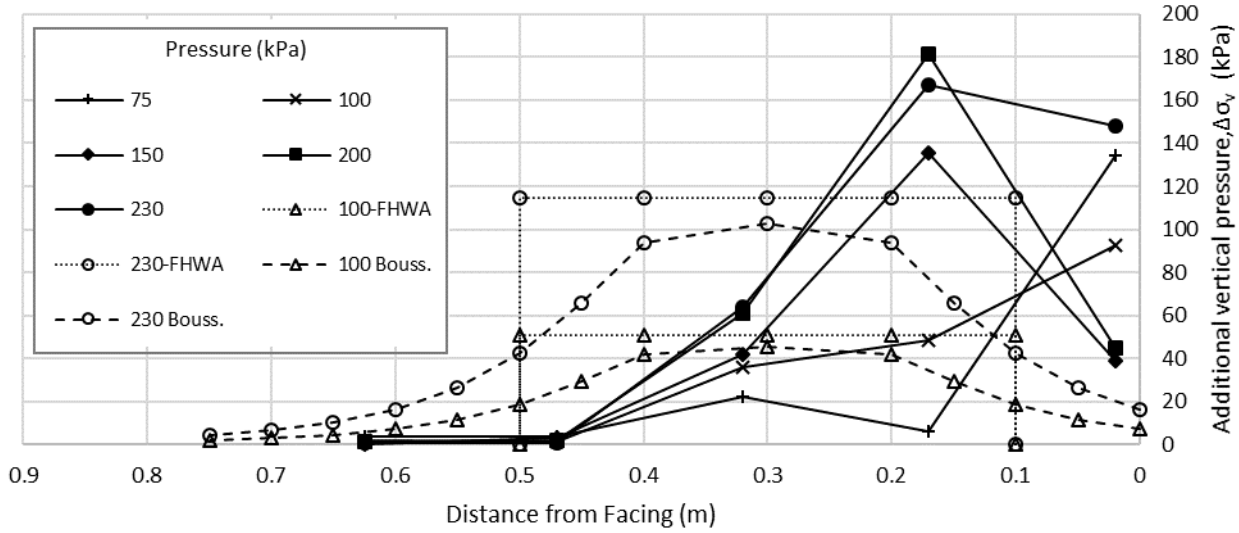

(a)

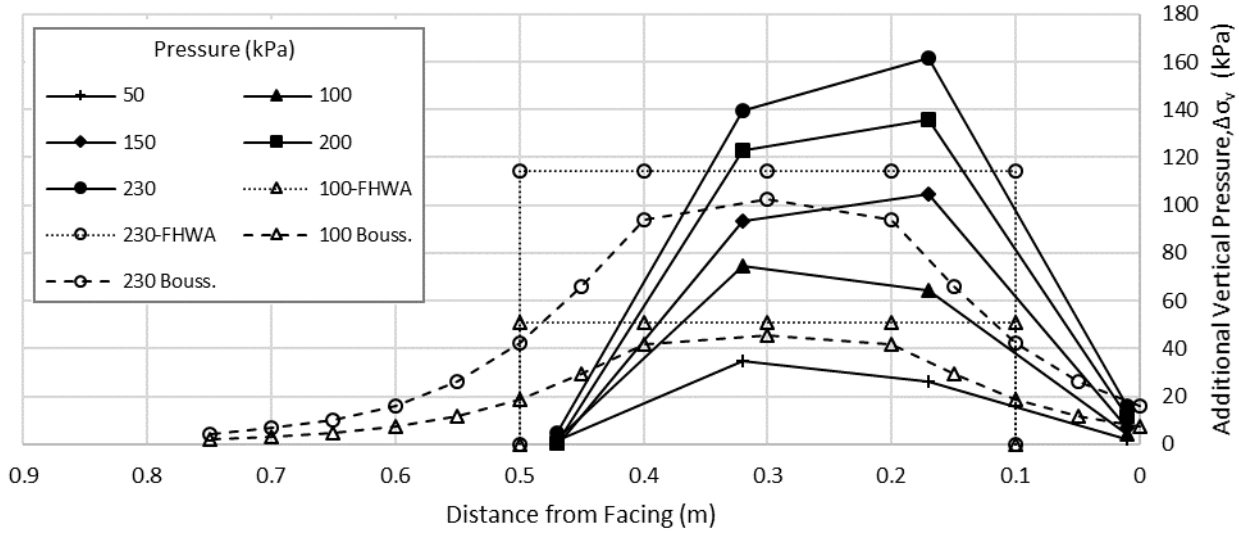

(b)

Figure 4. 13. Additional vertical earth pressure distribution: (a) Wall W-1, (b) Wall B-W, and (c) Wall B-1 (continued)

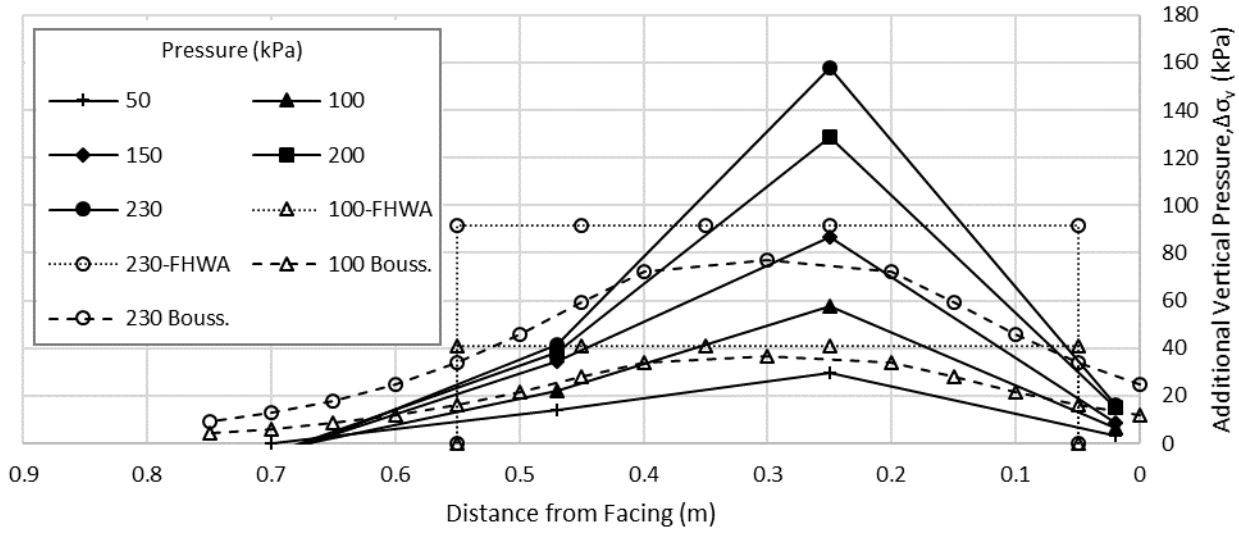

(c)

Figure 4.13. Additional vertical earth pressure distribution: (a) Wall W-1, (b) Wall B-W, and (c) Wall B-1

Figure 4.14 shows the measured vertical earth pressure ($\Delta\sigma_v$) versus the applied vertical pressure by footing at two locations (i.e., EPC1 and EPC2) at the base of Walls W-1, B-W, and B-1, which were located at the distances of 0.02 and 0.2 m from the facing wall, respectively. The vertical pressures calculated using the 2:1 distribution method are also plotted with the measured vertical pressure for comparison. **Figure 4.14** shows that the measured vertical pressures increased with the applied pressures at the both locations for Walls W-1, B-W, and B-1. At the same applied pressure, the pressure cells close to the centerline of the footing measured higher pressures than those close to the toe. This pressure distribution may result from the Boussinesq's stress distribution and the soil arching effect behind the wall facing. The calculated pressures using the 2:1 distribution method proposed by FHWA and AASHTO (Berg et al., 2009; AASHTO, 2012) were less than the measured ones close to the centerline of the footing in all three walls. However, in the Walls W-1 and B-W, the calculated pressures were higher than the measured ones close to the facing.

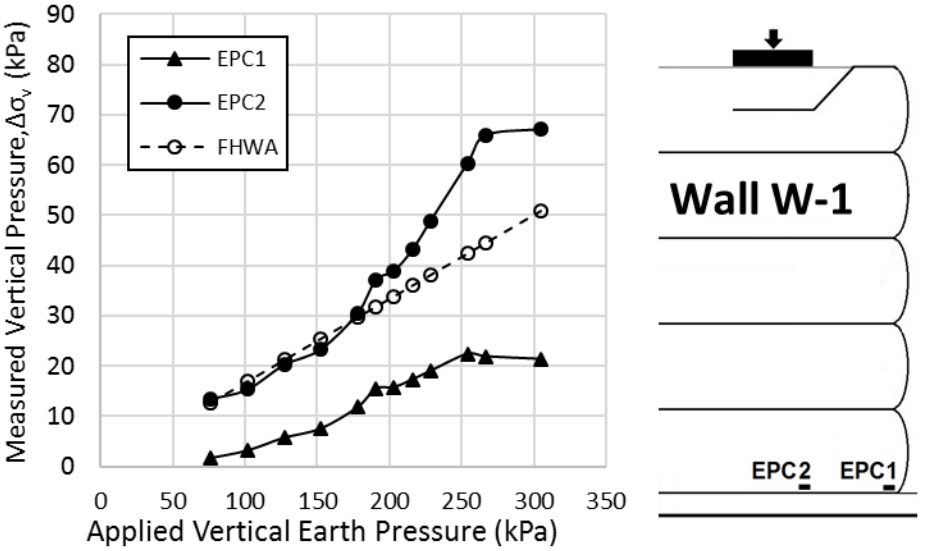

(a)

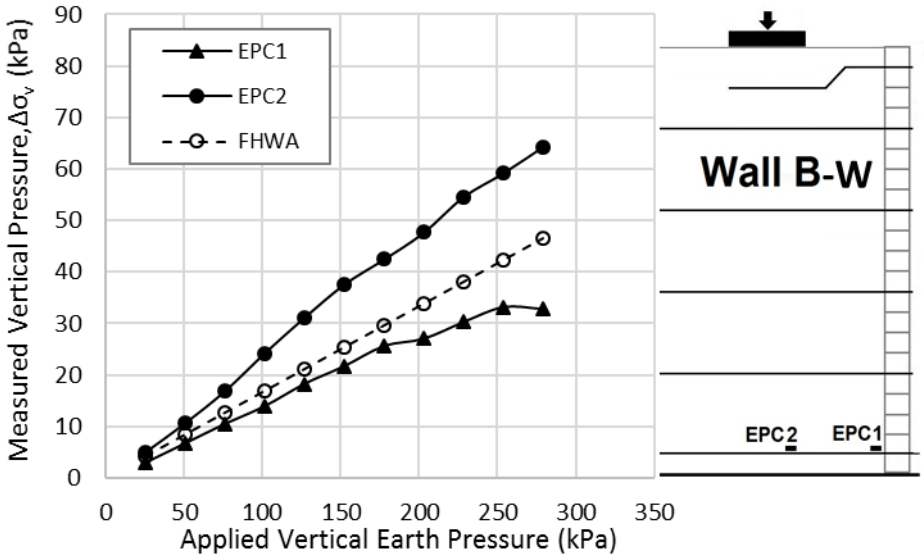

(b)

Figure 4. 14. Vertical earth pressure distribution at the base of the wall: (a) Wall W-1, (b) Wall B-W, and (c) Wall B-1 (continued)

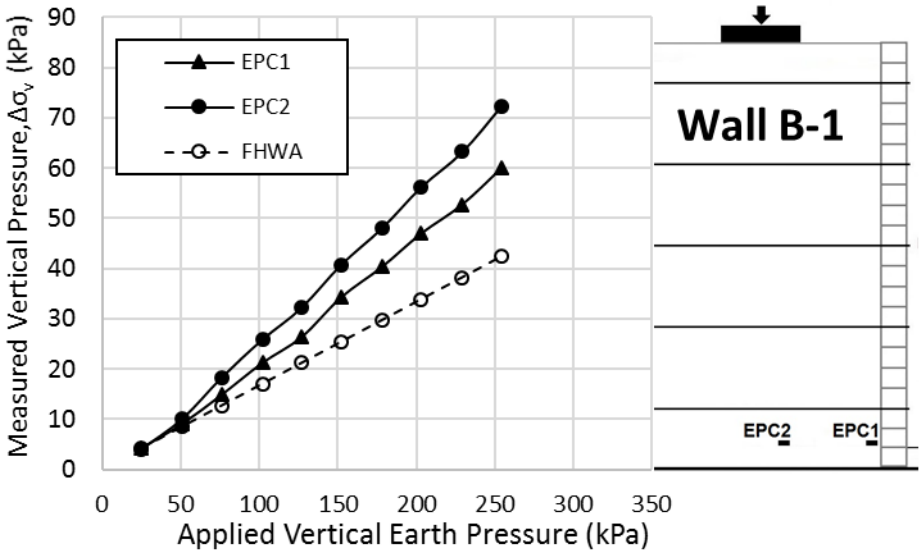

(c)

Figure 4.14. Vertical earth pressure distribution at the base of the wall: (a) Wall W-1, (b) Wall B-W, and (c) Wall B-1

4.3.4. Lateral earth pressure

Figure 4.15 shows the measured lateral earth pressures ($\Delta\sigma_h$) induced by footing loading from the pressure cells installed along the height of wall facing for the Walls W-1, B-W, and B-1. The lateral earth pressures estimated based on a theoretical method (i.e. Boussinesq's solution) are also plotted with the measured lateral earth pressures for comparison.

The measured lateral earth pressures generally increased with the increase of the applied pressure in both walls. The maximum lateral earth pressure was recorded at the top-height of the wall (i.e. at the height of 0.9 m) for Wall W-1, at the height of 0.7 m for Wall B-W, and about the height of 0.6 m for Wall B-1 under the entire application of loads. The theoretical method suggested by Boussinesq was based on unyielding wall facing (i.e., rigid facing). However, Wall W-1 had flexible facing, the measured lateral earth pressures generally agreed with the calculated ones by the theoretical method. For Walls B-W and B-1 with relatively rigid facings, the calculated lateral earth pressure distributions by the theoretical method were quietly different from the measured distributions because of the rigidity of the walls facing.

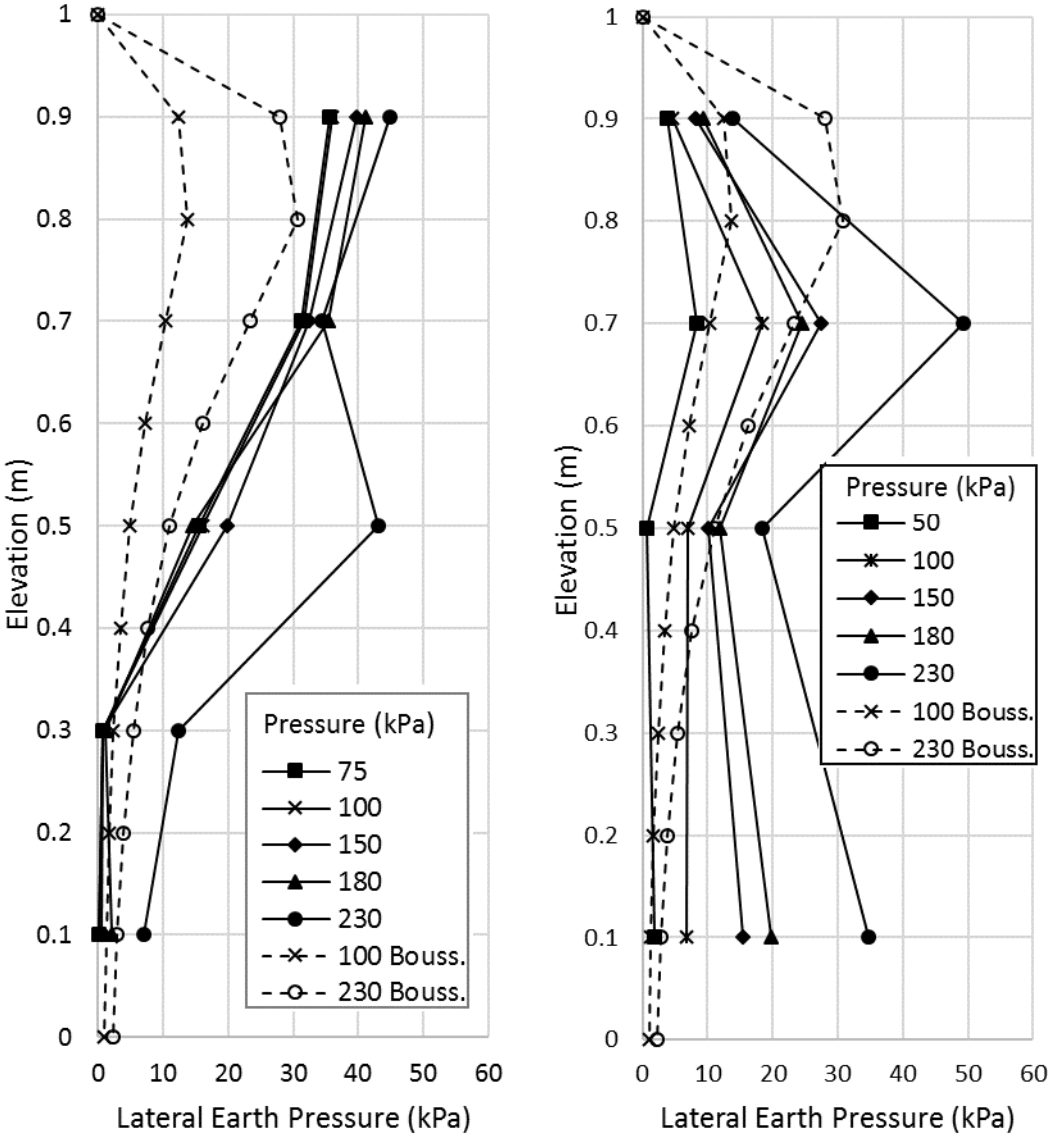

(a) (b)

Figure 4. 15. Lateral earth pressure distribution: (a) Wall W-1, (b) Wall B-W, and (c) Wall B-1

(continued)

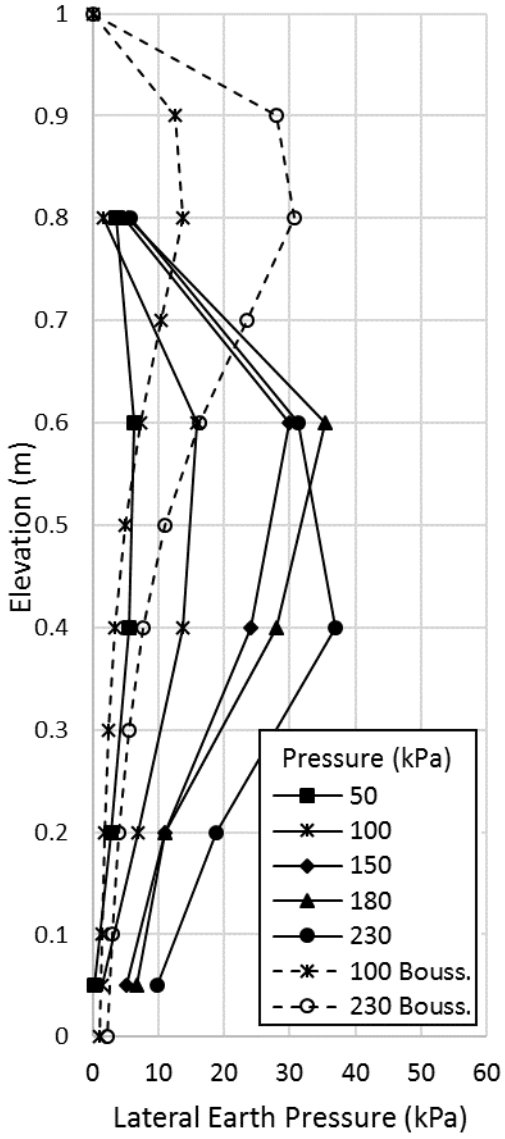

(c)

Figure 4.15. Lateral earth pressure distribution: (a) Wall W-1, (b) Wall B-W, and (c) Wall B-1

4.3.5. Strain

Figure 4.16 shows the average measured local strains induced by footing loading from the strain gauges installed along the geogrid at layer 5 (G5) of the Walls W-1 and B-W as shown in **Figures 4.6(a) and 4.7(b)**. The average local strain calculated from the strain gauges attached on the upper and lower sides of the geogrid using **Eq. 3.2**. The average measured local strains generally increased with the increase of the applied footing pressure for Walls W-1 and B-W. The maximum measured local strains in Walls W-1 and B-W were measured from the strain gauges that placed at 0.17 m from the wall facing which approximately were located under the outer edge of footing. The maximum average measured local strains in Walls W-1 and B-W at the applied pressure of 230 kPa were 6.6% and 7.7%, respectively.

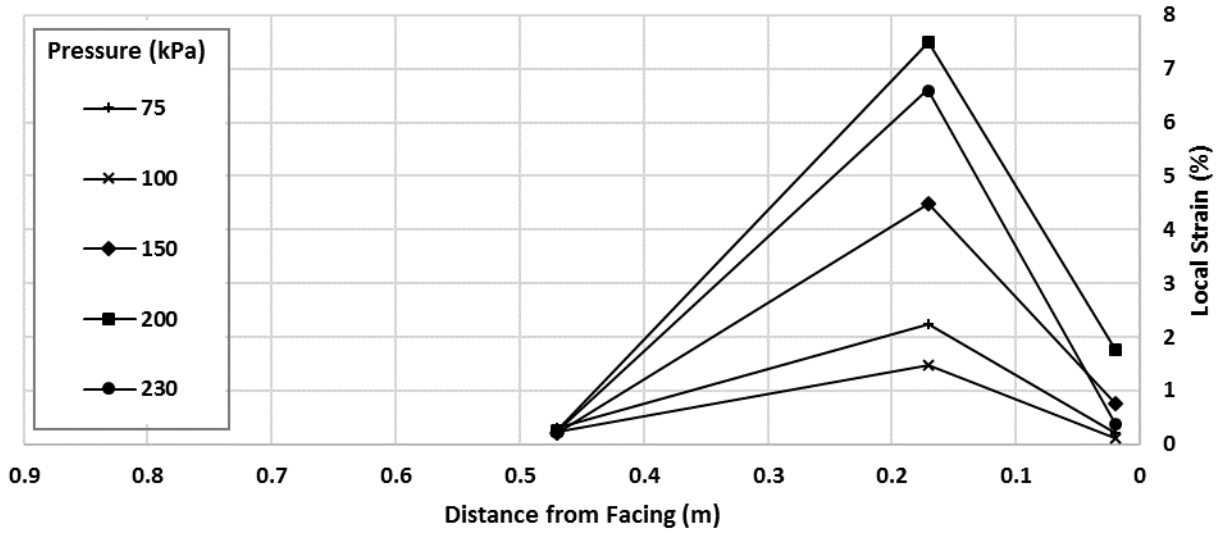

(a)

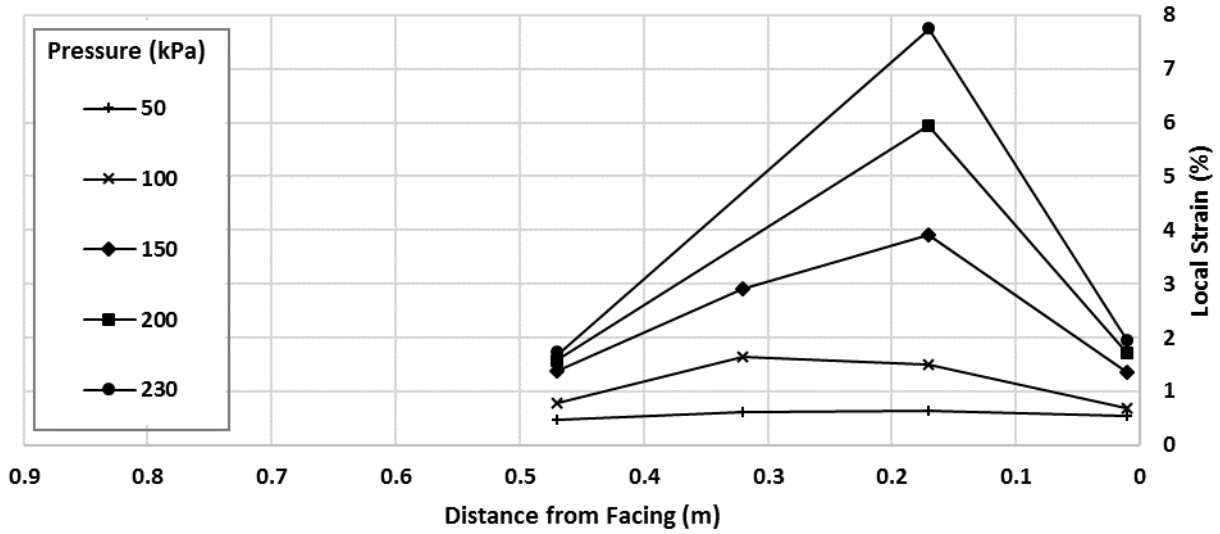

(b)

Figure 4. 16. Lateral earth pressure distribution: (a) Wall W-1 and (b) Wall B-W

4.3.6. Coefficient of earth pressure

Figure 4.17 shows the lateral earth pressure versus measured vertical pressure induced by footing loading at three locations (i.e., Toe, Layer 4, and Layer 5) of Walls W-1, B-W, and B-1. The lateral earth pressure was measured from the earth pressure cells, and calculated from the measured tension in the reinforcement per unit width of wall using the following equation:

$$\sigma_h = \frac{T}{S_v} \qquad \textbf{Eq. 4.1}$$

where T = measured tension in the reinforcement; S_v = vertical spacing of reinforcement. The tension in the reinforcement was estimated by using the measured local strain of the geogrid (from strain gauges) multiplied by *CF* and the geogrid tensile stiffness. In additional, the measured lateral and vertical earth pressure, and the measured maximum tension in the reinforcement were used for determining K_r behind the wall (Jiang et al. 2016; AASHTO, 2012; Berg et al., 2009). The K_r was calculated from the maximum tension in the reinforcement per a defined unit width of wall using the following equation:

$$K_r = \frac{T_{max}}{S_v \times \sigma_v} \qquad \textbf{Eq. 4.2}$$

where T_{max} = measured maximum tension in the reinforcement; σ_v is the vertical earth pressure. Therefore, **Figure 4.17** essentially represents the K_r induced by footing loading at different elevations (i.e., Toe, Layer 4, and Layer 5). Based on the findings of this study the maximum vertical pressure ($\Delta\sigma_{v,\ max}$) and maximum tension in the reinforcement (ΔT_{max}) induced by the footing loading occurred close to the center line of the applied footing (i.e., **Figure 4.13**). Thus, the measured $\Delta\sigma_{v,\ max}$ and ΔT_{max} were used for calculating the coefficient of lateral earth pressure (K_r). In addition, the coefficient of lateral earth pressure (K_r) was also calculated based on the measured tension (ΔT) in the reinforcement and measured vertical earth pressure ($\Delta\sigma_v$) behind the wall facing induced by the footing loading, and the results are presented in **Figure 4.17**. For comparison purpose, the calculated coefficient of active (K_a), at rest (K_o), and passive (K_p) earth pressure (using the peak friction angle of 37°) are also plotted in this figure. The K_a, K_o, and K_p were about 0.25, 0.4, and 4.02, respectively.

In the Wall W-1, the K_r values calculated from the earth pressure cells placed behind the facing at layer 5, layer 4, and toe were about 1, 0.75, and 0.38, respectively (**Figure 4.17(a)**). The K_r values at layer 5 and layer 4 were higher than K_o. However, at the toe of this wall, the K_r value was close to the K_o (i.e., 0.4) value. Moreover, at layer 5, the K_r values calculated based on the ΔT_{max} and $\Delta\sigma_{v,\ max}$ was 0.41 which was almost the same as K_o value. The K_r value calculated based on the ΔT and $\Delta\sigma_v$ was 0.46 that was also close to the K_o. However, the K_r value calculated based on ΔT_{max} and $\Delta\sigma_v$ was higher than the other K_r values. In other words, the K_r values calculated based on the measured data from the experimental tests were higher than the K_a value.

In the Wall B-W, the K_r values calculated from the earth pressure cells placed behind the facing at layer 5, layer 4, and toe were 0.65, 0.75, and 0.85, respectively (**Figure 4.17(b)**). The K_r values calculated based on the ΔT and $\Delta\sigma_v$ at layer 5 and layer 4 were 1 and 0.7, respectively. The K_r value

calculated based on the ΔT_{max} and $\Delta \sigma_{v,\,max}$ (close to the centerline of the footing) at layer 5, was 0.46 that was close to the K_o value. However, the K_r value calculated based on the ΔT_{max} and $\Delta \sigma_v$ was close to the K_p value and higher than the other K_r values.

In the Wall B-1, the K_r values calculated from the earth pressure cells placed behind the facing at layer 5, layer 4, and toe were about 0.75, 0.43 and 0.16, respectively (**Figure 4.17(c)**). At the layer 4 of this wall, the K_r value was close to the K_o value. However, the K_r value of the layer 5 was higher than the K_o, and at toe, the K_r value was lower than K_a.

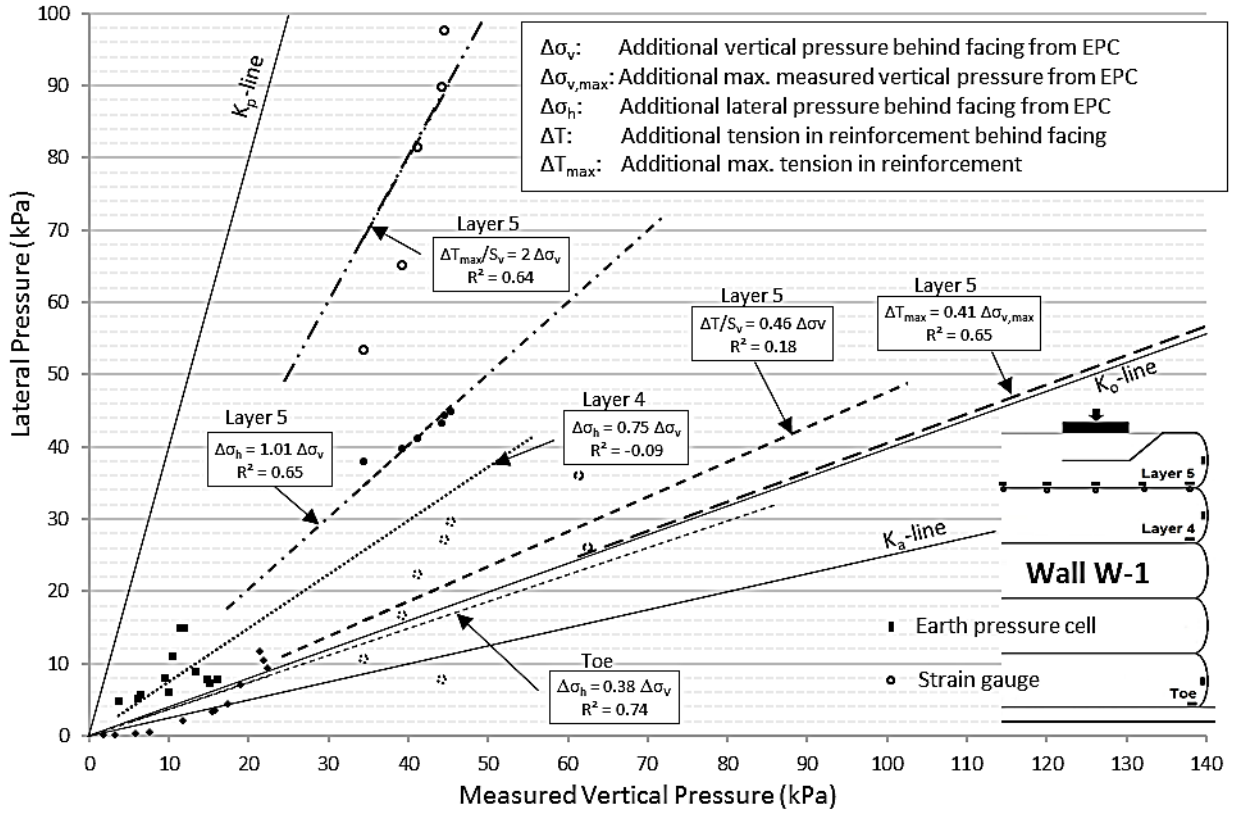

(a)

Figure 4. 17. Measured lateral earth pressure versus the measured vertical pressure: (a) Wall W-1, (b) Wall B-W, and (c) Wall B-1 (continued)

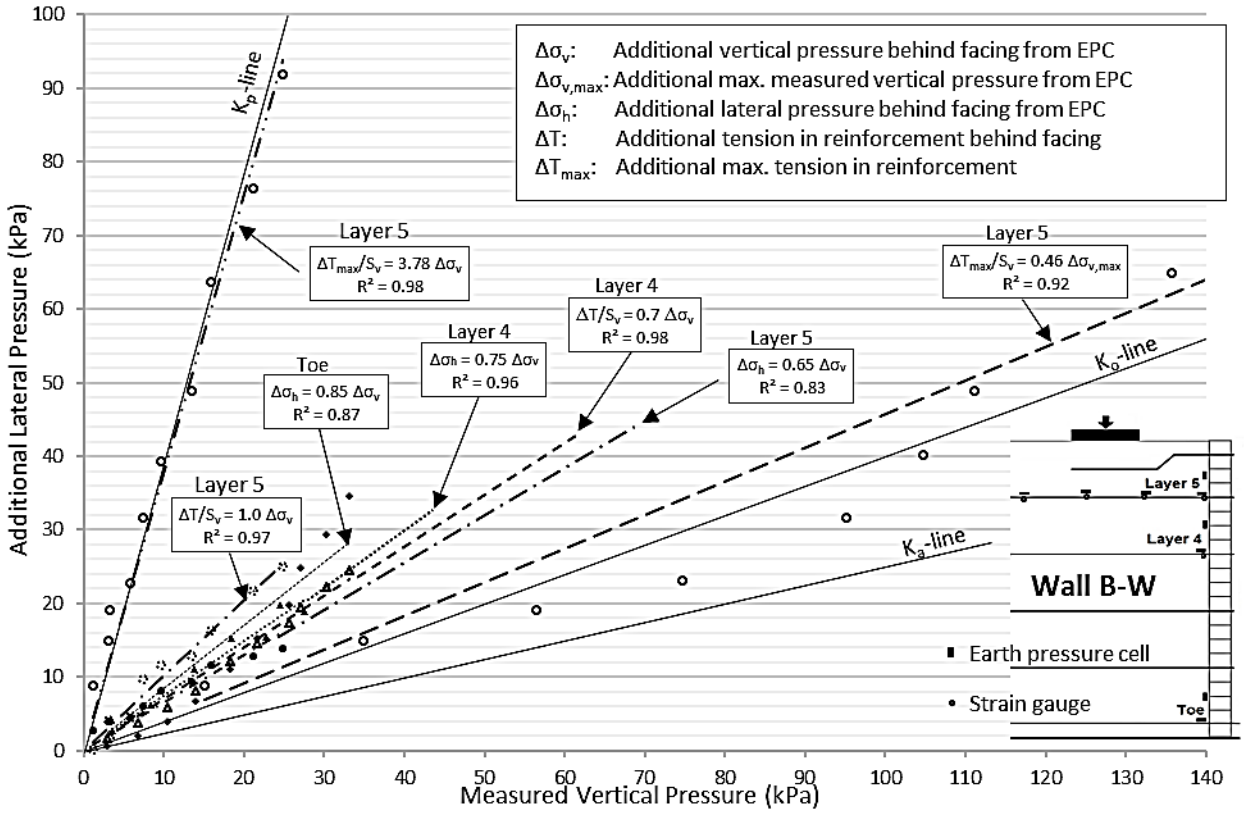

(b)

Figure 4.17. Measured lateral earth pressure versus the measured vertical pressure: (a) Wall W-1, (b) Wall B-W, and (c) Wall B-1 (continued)

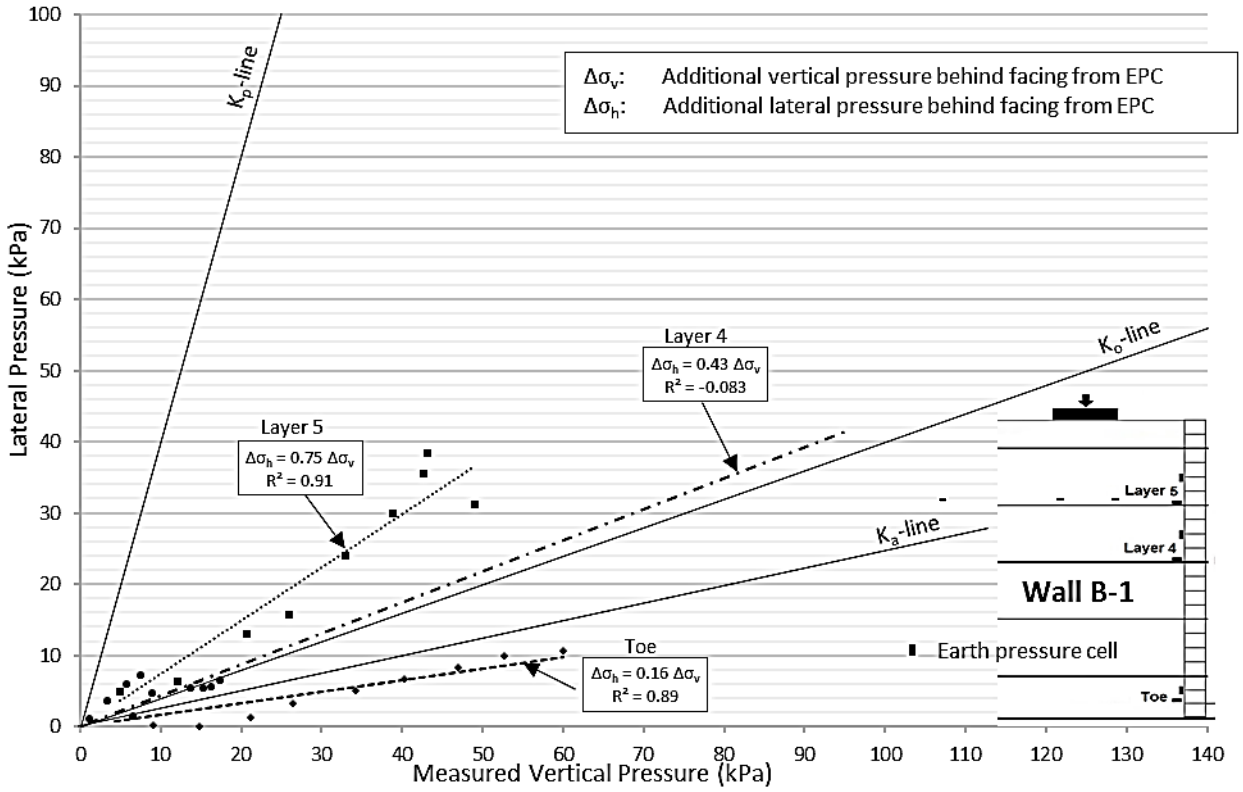

(c)

Figure 4.17. Measured lateral earth pressure versus the measured vertical pressure: (a) Wall W-1, (b) Wall B-W, and (c) Wall B-1

Figure 4.18 presents the distribution of the normalized coefficient of lateral earth pressure with depth, *Z*, from measured lateral earth pressures and maximum tensile forces in Walls W-1, B-W, and B-1. **Figure 4.18(a)** shows the profile of the normalized coefficient of lateral earth pressure (K_r/K_a) with depth, *Z*. The coefficient of lateral earth pressures was determined from the measured lateral earth pressures behind the wall facing and the tensile forces in the geogrid. All Walls W-1, B-W, and B-1 had the K_r/K_a ratios calculated based on the measurements from the earth pressure

cells approximately between 1.5 and 4 within the upper half of the wall height as shown in **Figure 4.18(a)**. At the toe of the Walls W-1 and B-1, the K_r/K_a ratios calculated based on the earth pressure cells were close to 1.0. However, the K_r/K_a ratio in wall B-W was about 3.4.

Figure 4.18(a) also shows that the value of K_r/K_a ratio calculated based on the maximum measured tension in the reinforcement (ΔT_{max}) and the maximum measured vertical earth pressure ($\Delta\sigma_{v,\,max}$) was 1.64 and 1.9 for the Wall W-1 and Wall B-W, respectively. In addition, The value K_r/K_a ratio calculated based on the measured tension in the reinforcement behind the wall facing (ΔT) and the measured vertical earth pressures behind the wall facing ($\Delta\sigma_v$) was 1.8 and 3.95 for the Wall W-1 and Wall B-W, respectively. That is to say, the K_r/K_a ratios calculated based on $\Delta T_{\max}$ and $\Delta\sigma v_{,\max}$ was closer to the ratio recommended by FHWA guideline (i.e., K_r/K_a =1.0) compared to the other K_r/K_a ratios.

Figure 4.18(b) also shows that for Walls W-1, B-W, and B-1 subjected to footing loading, the K_r values calculated based on the measurements from the instruments placed within the 2:1 distributed area, are close to the K_o value. Therefore, the lateral earth pressure within the 2:1 distributed area using the following equation:

$$\sigma_h = K_a\gamma Z + \Delta\sigma_h = K_a\gamma Z + K_o\Delta\sigma_v \qquad \textbf{Eq. 4.3}$$

where σ_h = lateral earth pressure, γ = backfill density, Z = depth, $\Delta\sigma_h$ = lateral earth pressure induced by footing loading, K_o = coefficient of at rest earth pressure, and $\Delta\sigma_v$ = vertical earth pressure induced by footing loading.

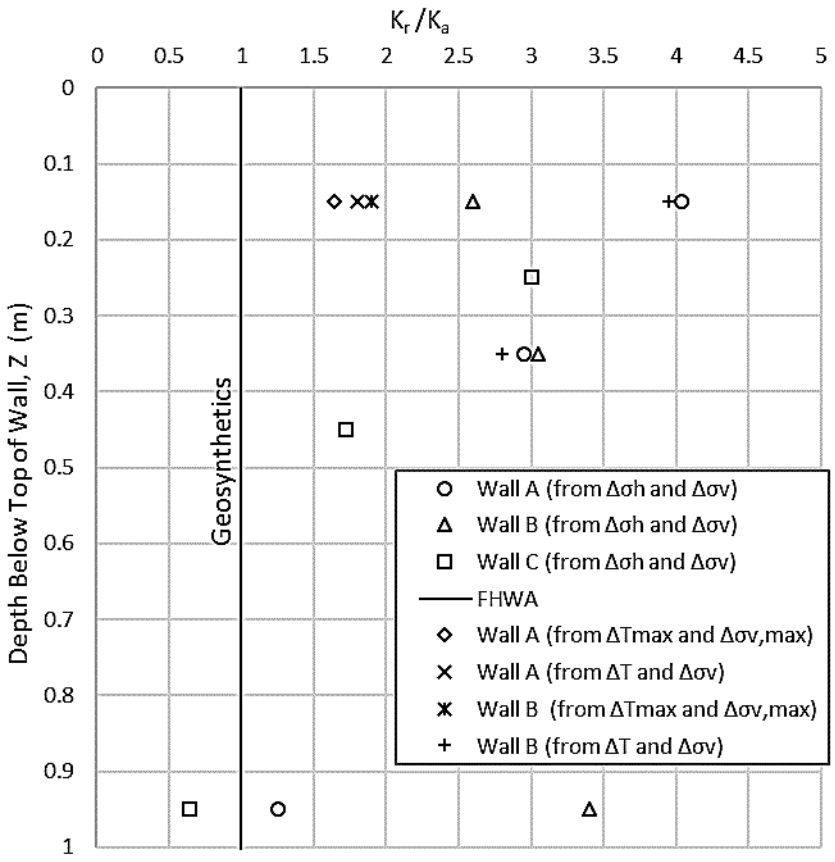

(a)

Figure 4. 18. Distribution of the normalized coefficient of lateral earth pressure ratio with depth from measured lateral earth pressures and maximum tensile forces: (a) using K_a and (b) using K_0

(continued)

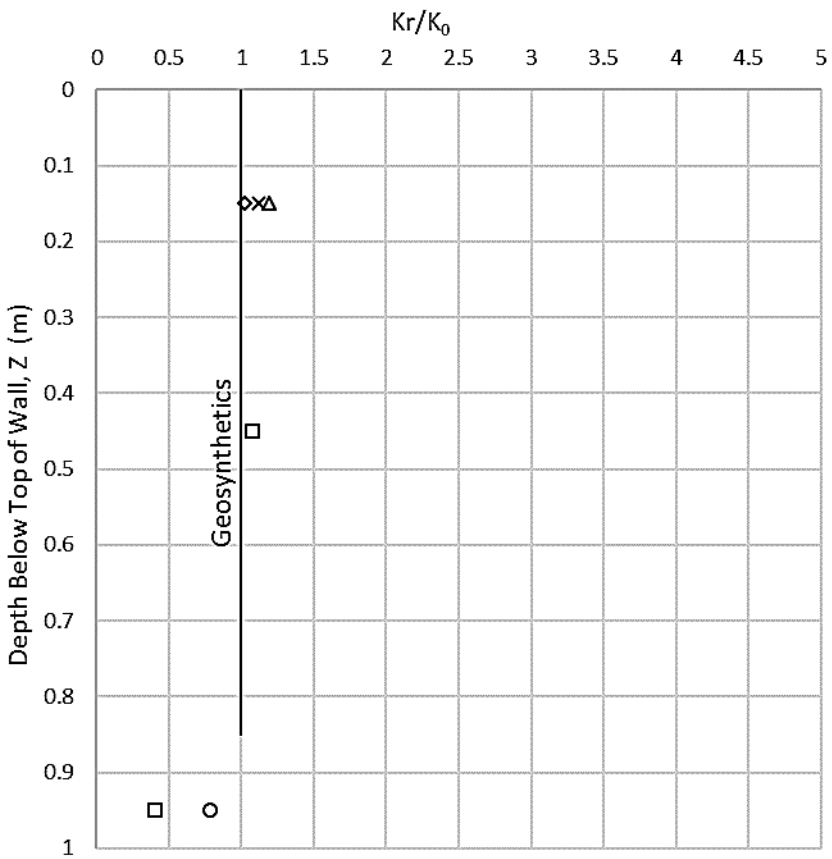

(b)

Figure 4.18. Distribution of the normalized coefficient of lateral earth pressure ratio with depth from measured lateral earth pressures and maximum tensile forces: (a) using K_a and (b) using K_0

4.3.7. Failure mode

The plexiglass allowed the visual observation and photogrammetry of the failure modes of the test walls during construction and loading. **Figure 4.19** shows the slip surfaces and deformed facing in the abutment Walls W-1, B-W, and B-1. In Wall W-1, no obvious failure was observed on the wrapped facing. However, in Walls B-W and B-1 the facing failed at the locations of the maximum

outward displacements. At these locations, because the upper and lower blocks were restrained by geogrids, local bulging occurred in the middle of the geogrid layers. As a result, the blocks at these locations rotated and gaps between blocks developed as shown in **Figure 4.19** for Wall B-W. In Wall B-W, the geogrids also broke close to the mechanical connections. However, in Wall B-1 the blocks were fell down at the location of the maximum outward displacement.

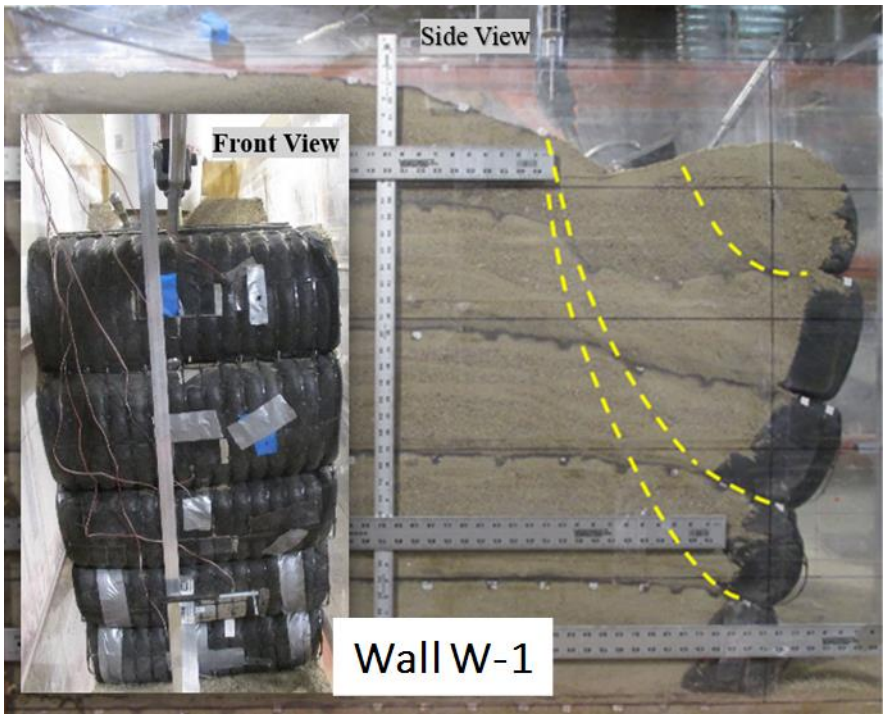

(a)

Figure 4. 19. Slip surfaces and facing deflections: (a) Wall W-1, (b) Wall B-W, and (c) Wall B-1 (continued)

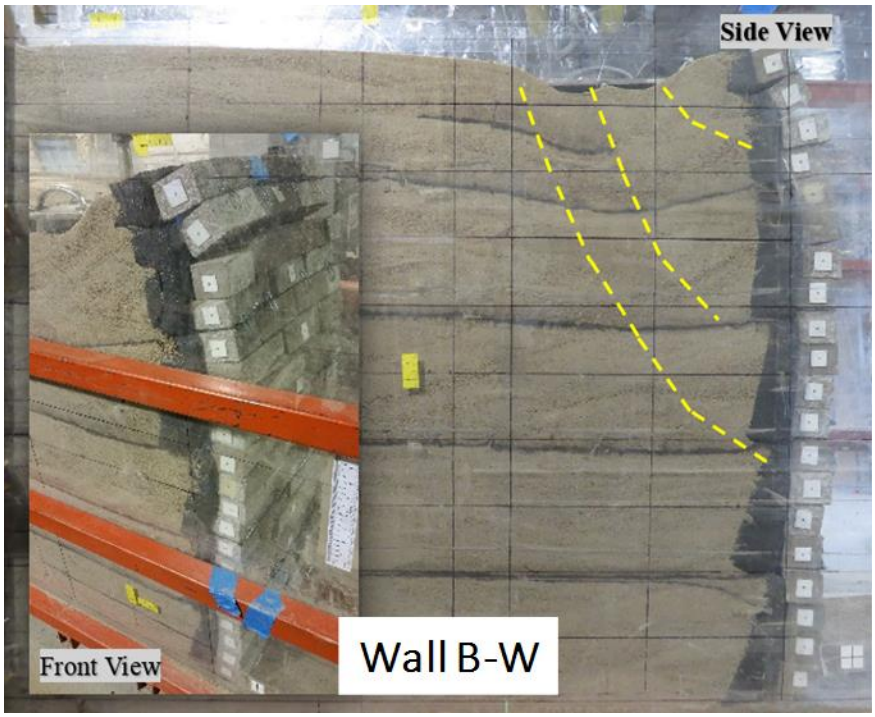

(b)

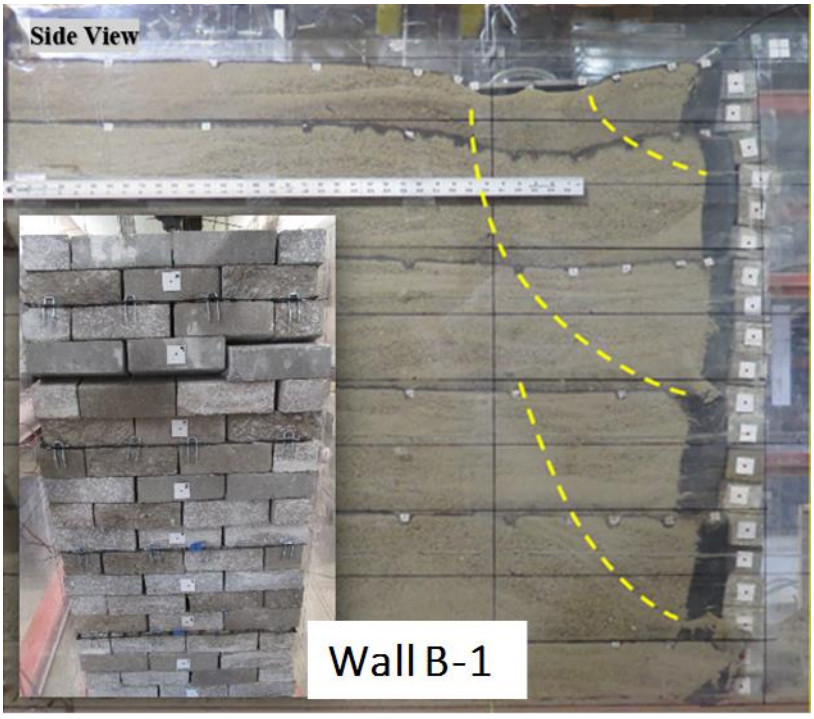

(c)

Figure 4.19. Slip surfaces and facing deflections: (a) Wall W-1, (b) Wall B-W, and

(c) Wall B-1

The observed slip surfaces were marked with dashed lines, which were traced based on the distortion of the colored sand layers and the wall facing. Based on the visual observation, the slip surfaces began from the edge of the footing and developed into the reinforced zone towards the wall facing. Moreover, all of the shallow, middle and deep slip surfaces that were mentioned by Xiao et al. (2016) were observed in these tests. No slip surfaces developed through the toe of the walls. Xiao et al. (2016) found that for the abutment walls with block facing, when the footing was close to the facing (D/H = 0.15, 0.2 and 0.3), the blocks within the upper portion of the wall had obviously relative movement.

4.4. Summary

The objective of this study was to evaluate and compare the performance of the geosynthetic-reinforced retaining (GRR) walls with the wrapped-around and modular block facing subjected to static footing loading under a plane strain condition. To achieve this objective, eight model tests were conducted in the laboratory to examine the effect of the facing stiffness on the pressure-settlement curve, the deflection of the wall, the vertical and lateral pressures, and the failure modes. The following consequences can be summarized based on this chapter:

(1) The modular block facing behaved as relatively rigid facing and reduced the footing settlement as compared with the wrapped-around facing.

(2) The maximum lateral displacements in the wall with the wrapped-around facing was much larger than the walls with modular block facing.

(3) In general, for all the walls the coefficient of lateral earth pressure, K_r, calculated from the measured earth pressures and the tension in geogrid, were between the coefficient of passive (K_p) and at rest (K_o) earth pressures.

(4) For the walls subjected to footing loading, the K_r values calculated based on the measurements from the instruments placed within the 2:1 distributed area, are close to the K_o value.

(5) At failure, the slip surfaces began from the edge of the footing and developed into the reinforced zone toward the wall facing. The shallow, middle and deep slip surfaces were observed in these test walls. No obvious failure was observed on the wrapped facing. However, for the walls with the modular block facing, the failure occurred on the facing.

Chapter 5. Stability and Deflection of GRR Walls Subjected to Footing Loading

5.1. Introduction

Although several studies have been conducted to evaluate the behavior of the GRR walls with flexible facing under self-weight or surcharge, limited studies have been conducted to evaluate the behavior of the GRR walls with different wall facing under footing loading. Different from typical GRR walls, GRR abutment walls are generally subjected to high footing loading that are close to the wall facing. Therefore, not only the stability of the GRR walls but also the bearing capacity and settlement of the bridge footing should be considered in design. Although the GRR abutment walls with flexible facing have been the subject of a few studies, the interaction between the GRR wall and the footing is not well understood. In addition, very few studies have investigated the behavior of the GRR walls with wrapped-around facing. Moreover, so far, there is no solution for determining bearing capacity and settlement of the footing on the GRR walls, and not a proper method to predict deflection of the GRR wall facing induced by footing loadi. For instant, Saghebfar et al. (2017) found a significant difference between the predicted lateral deflection of the facing wall using FHWA method (discussed in Section 2.7.5) and measured lateral deflections underpredicted the. The difference between measurement and theoretical values was more significant during the construction of bridge, however, after open the bridge to traffic (10/6/2015), the difference between the predicted and measured lateral deflections and strains were decreased.

As discussed in Chapter 4, an experimental study has been conducted including the physical models constructed in a test box under a plane strain condition and subjected to static

footing loading. Each model test wall had a dimension of 0.45 m wide, and 1.0 m high. Geogrid layers were used as reinforcement in the walls. The experimental study evaluated the settlement of the footing, the lateral displacements of the facing, the vertical and lateral pressure distributions, the strains and tensile forces along the reinforcement, and the failure surfaces through the GRR abutment fill.

In this chapter, the effect of the footing loading on the global stability of GRR walls with wrapped-around and modular block facing was investigated. The limit equilibrium (i.e., the Bishop modified method and the Spencer method) in the ReSSA program was used to determine the critical slip surfaces and their corresponding factors of safety of the eight reduced-scale experimental models and ten case histories. Then, an analytical study was conducted to develop solutions for the settlement of the footing and the lateral deflection of the GRR walls with wrapped-around and with modular concrete block facing induced by footing loading.

5.2. Limit Equilibrium Method

Limit equilibrium methods have been used for decades to analyze the stability of geosynthetic reinforced slopes and retaining walls. In this study, the limit equilibrium program, ReSSA version 3.0, developed by the ADAMA Engineering, Inc., was used to determine the critical slip surfaces and calculate the factors of safety. ReSSA uses two methods of stability analysis: (1) the Bishop modified method (Bishop, 1955) and (2) the Spencer method (Spencer, 1967). The Bishop method uses circular arc slip surfaces. The Bishop method is a common limit equilibrium method. However, the Bishop method does not satisfy horizontal force limit equilibrium (Leshchinsky and Han, 2004; Han and Leshchinsky, 2010). In ReSSA version 3.0, Bishop's modified method was modified to include reinforcement as a horizontal force intersecting the slip circle (Han and

Leshchinsky, 2010). However, this modified method is consistent with the original developed method by Bishop (1955). The Spencer method is considered rigorous since it explicitly satisfies equilibrium. Spencer (1976) utilized two- and three-part wedge mechanism. The two-part wedge is used to assess the potential for direct sliding along each reinforcement layer. The slip surface divides the walls or slopes into unstable and stable zones (Rahmaninezhad et al., 2018). The rear pullout capacity of reinforcement, its long-term strength, and the soil strength have effects on the mobilization of tension in the reinforcement near the slip circle (Han and Leshchinsky, 2010; Han, 2015; Rahmaninezhad et al., 2018).

5.3. Limit Equilibrium Analysis

The focus of this section is to investigate the effect of footing loading on global stability of GRR walls with wrapped-around and modular block facing. The limit equilibrium methods (i.e., the Bishop modified method and the Spencer method) in the ReSSA program were used to determine critical slip surfaces and their corresponding factors of safety of the model walls and 10 test walls which were described in Chapters 4 and 2, respectively.

5.3.1. Reduced-scale walls subjected to footing loading

GRR model walls with wrapped-around facing

Figure 5.1 presents the calculated factors of safety using the Bishop and Spencer methods versus the applied pressures for Walls W-1, W-2, W-3, and W-4 with wrapped-around facing. The dimensions of these walls were described in **Section 4.2.7** and **Table 4.1**. The comparison between

two methods indicates that the factors of safety evaluated by Spencer's two-part wedge method for all the walls were smaller than those by Bishop's method. Therefore, the two-part wedge failure was more critical than the circular failure in these walls. By applying pressure higher than 191, 152, 100, and 100 kPa in Walls W-1, W-2, W-3, and W-4, the calculated factor of safety using the Bishop method became less than one, as shown in **Figure 5.1**. These pressures can be defined as the ultimate bearing capacity. In other words, the ultimate bearing capacity is the pressure at which the corresponding factor of safety using the Bishop method is one. Moreover, the ultimate bearing capacity identified by the Bishop method had a better agreement with the measured critical footing pressure in these walls than that by the spencer method, as shown in Chapter 4.

Figure 5.1 also indicates that the walls with longer geogrid reinforcement length (Walls W-1 and W-2) had a higher ultimate bearing capacity than the walls with shorter geogrid reinforcement length (Walls W-3 and W-4). In addition, Wall W-1 with a retained fill zone had a higher ultimate bearing capacity than Wall W-2 without a retained fill zone.

Figure 5.2 shows the critical slip surfaces under the ultimate bearing capacity identified by Bishop's and Spencer's methods for the walls with wrapped-around facing. Figure 5.2 also plots the locations of the maximum tensile force lines in walls with large surcharge slabs and inextensible reinforcements proposed by FHWA (Berg et al., 2009) as shown in **Figure 2.1**. The comparison between the Bishop and Spencer methods indicates that the factors of safety calculated by Spencer's two-part wedge method for all the model walls with the wrapped-around facing are smaller than those by Bishop's method. Therefore, the two-part wedge failure could be considered more critical than the circular failure.

Figure 5.2 also shows that the slip surface, identified by the Bishop method, began from

the inner edge of the footing and developed into the reinforced zone towards the walls facing. However, the slip surfaces, identified by the Spencer method, began from the center of the footing toward the upper part of the walls facing. Moreover, the critical slip surfaces identified by the Spencer, Bishop, and FHWA methods agreed well with the observed shallow, middle, and deep slip surfaces in Wall W-1 shown in **Figure 4.19(a)**.

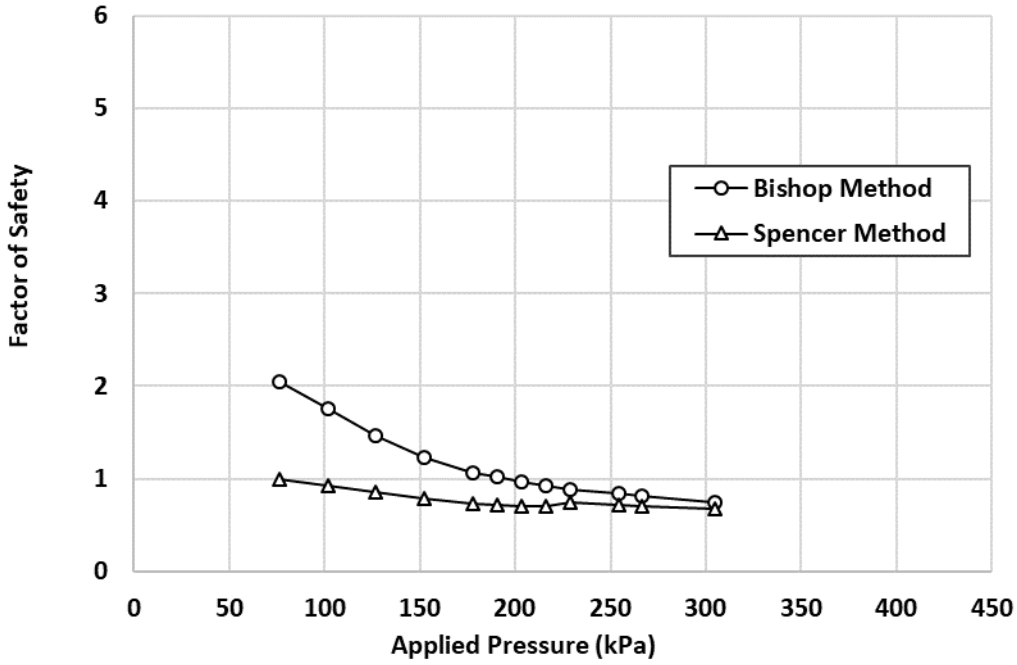

(a)

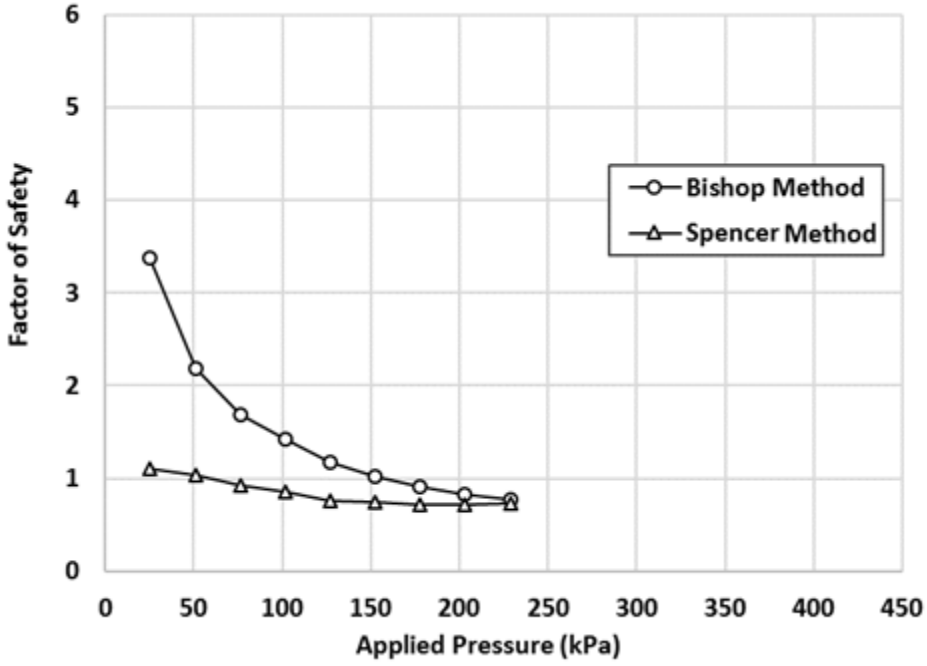

(b)

Figure 5. 1. Factor of Safety versus applied pressure: (a) Wall W-1, (b) Wall W-2, (c) Wall W-3, and (d) Wall W-4 (continued)

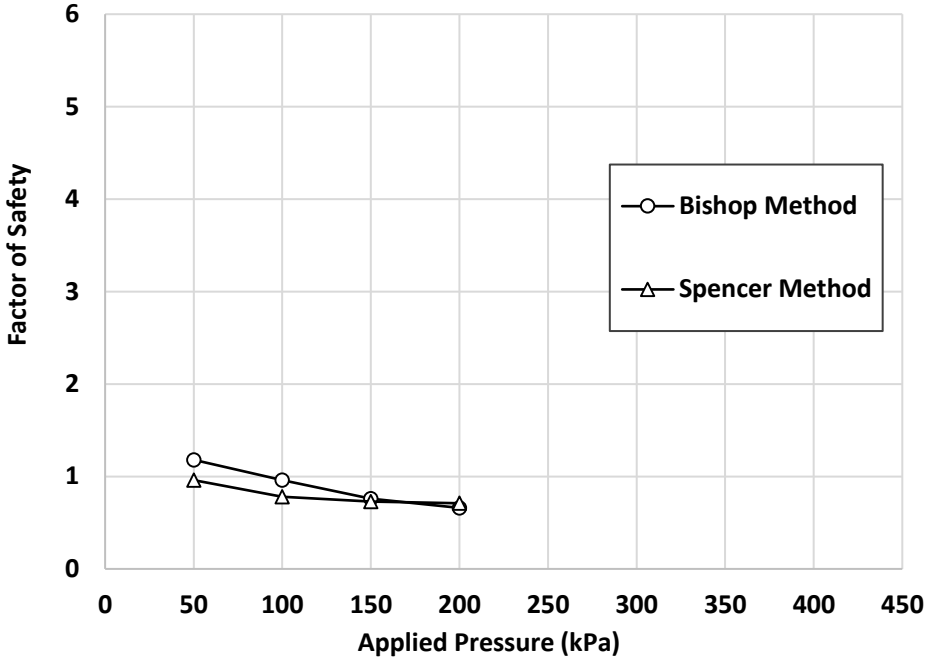

(c)

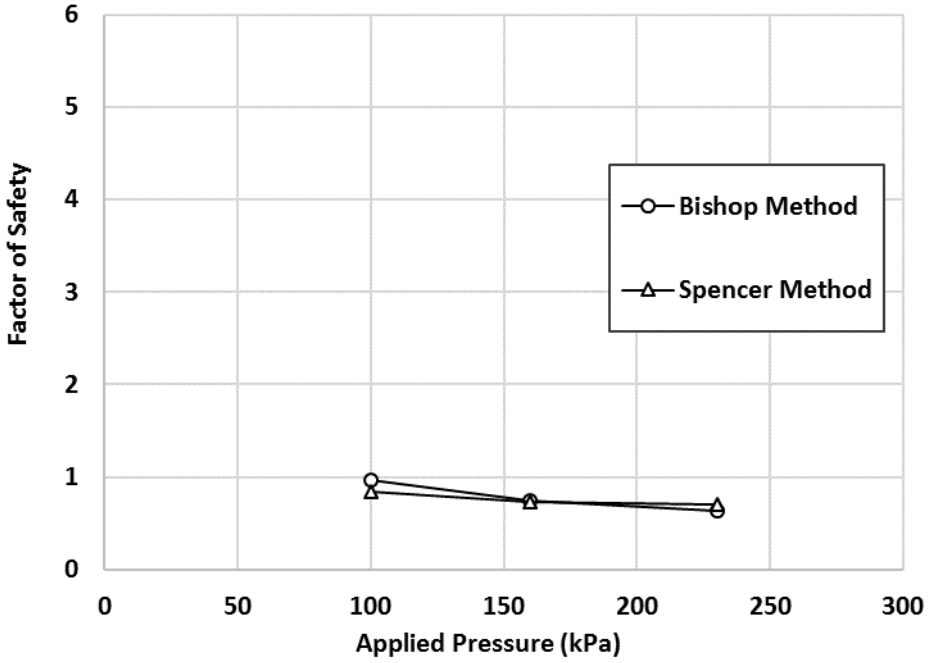

(d)

Figure 5.1. Factor of Safety versus applied pressure: (a) Wall W-1, (b) Wall W-2, (c) Wall W-3, and (d) Wall W-4

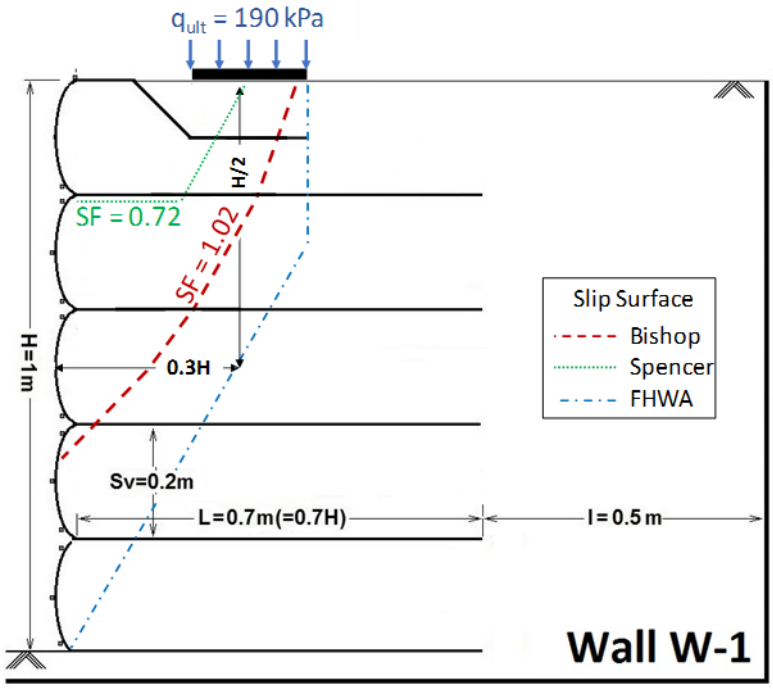

(a)

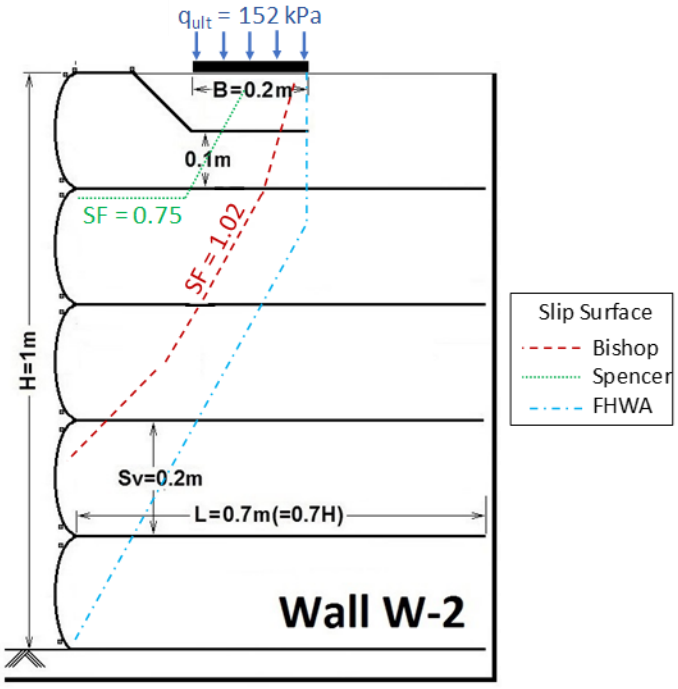

(b)

Figure 5. 2. Slip surfaces and factors of safety for: (a) Wall W-1, (b) Wall W-2, (c) Wall W-3, and (d) Wall W-4 (continued)

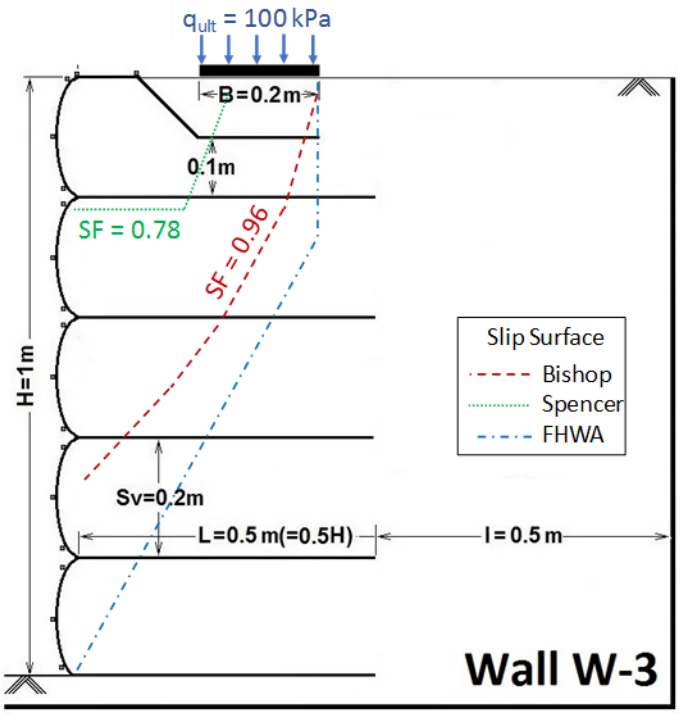

(c)

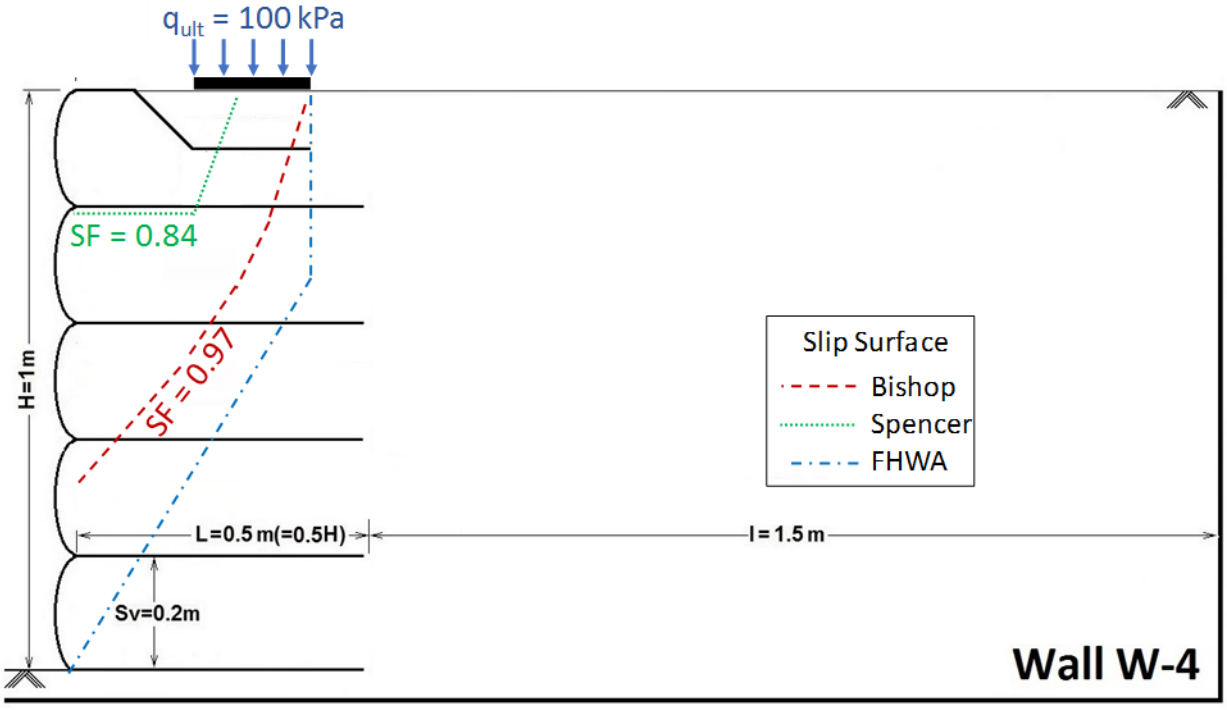

(d)

Figure 5.2. Slip surfaces and factors of safety for: (a) Wall W-1, (b) Wall W-2, (c) Wall W-3, and (d) Wall W-4

GRR model walls with modular block facing

Figure 5.3 presents the calculated factors of safety versus applied pressures using the Bishop and Spencer methods for Walls B-W, B-1, B-2, and B-3 with modular block facing. The dimensions of these walls were described in **Section 4.2.7** and **Table 4.1**. **Figure 5.3** also illustrates that the ultimate bearing capacity for Walls B-W, B-1, B-2, and B-3 were 425, 300, 400, and 200 kPa. The comparison between Walls W-1 and B-W indicates that facing rigidity increased the ultimate bearing capacity by 55%. Moreover, the comparison between Walls B-W and B-1 shows that the layout of geogrids had a significant effect on the magnitude of the ultimate bearing capacity. For instant, the ultimate bearing capacity of Wall B-W with six geogrid layers was approximately 30% higher than Wall B-1 with five geogrid layers. In addition, Wall B-1 with a retained fill zone had a lower ultimate bearing capacity than Wall B-2 without a retained fill zone.

Figure 5.4 shows the critical slip surfaces under the ultimate bearing capacity identified by Bishop's and Spencer's methods for the model walls with modular block facing and the locations of maximum tensile force lines in walls with large surcharge slabs and inextensible reinforcements proposed by FHWA (Berg et al., 2009). Similar to the walls with wrapped-around facing, the comparison between the Bishop and Spencer methods indicates that the factors of safety calculated by Spencer's two-part wedge method for all the model walls with the modular block facing are smaller than those by Bishop's method. Therefore, the two-part wedge failure could be considered more critical than the circular failure.

In Walls B-W, B-1, and B-2, the slip surfaces, identified by both Bishop's and Spencer's methods, began from the inner edge of the footing towards the wall facing, as shown in **Figure 5.4**. In Wall B-3 with a wider footing, the slip surfaces, identified by both Bishop's and Spencer's

methods, began from the middle and inner edge of the footing and developed into the reinforced zone. Moreover, in Walls B-W and B-1, the slip surfaces identified by Spencer, Bishop, and FHWA methods agreed well with the observed shallow, middle and deep slip surfaces shown in **Figure 4.19(b) and (c)**.

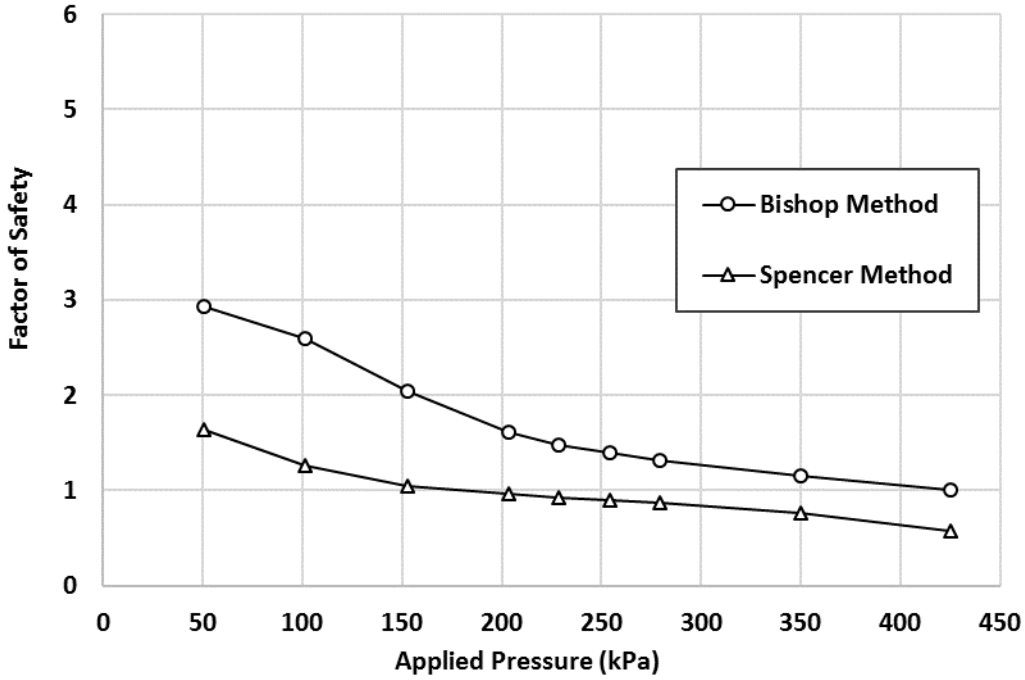

(a)

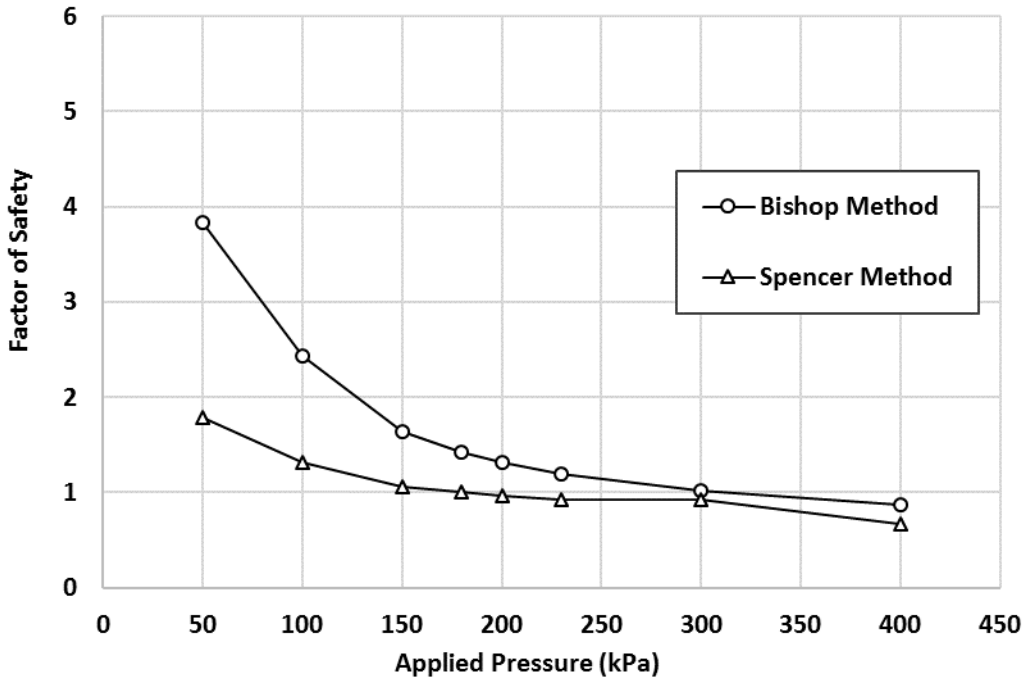

(b)

Figure 5. 3. Factor of Safety versus applied pressure: (a) Wall B-W, (b) Wall B-1, (c) Wall B-2, and (d) Wall B-3 (continued)

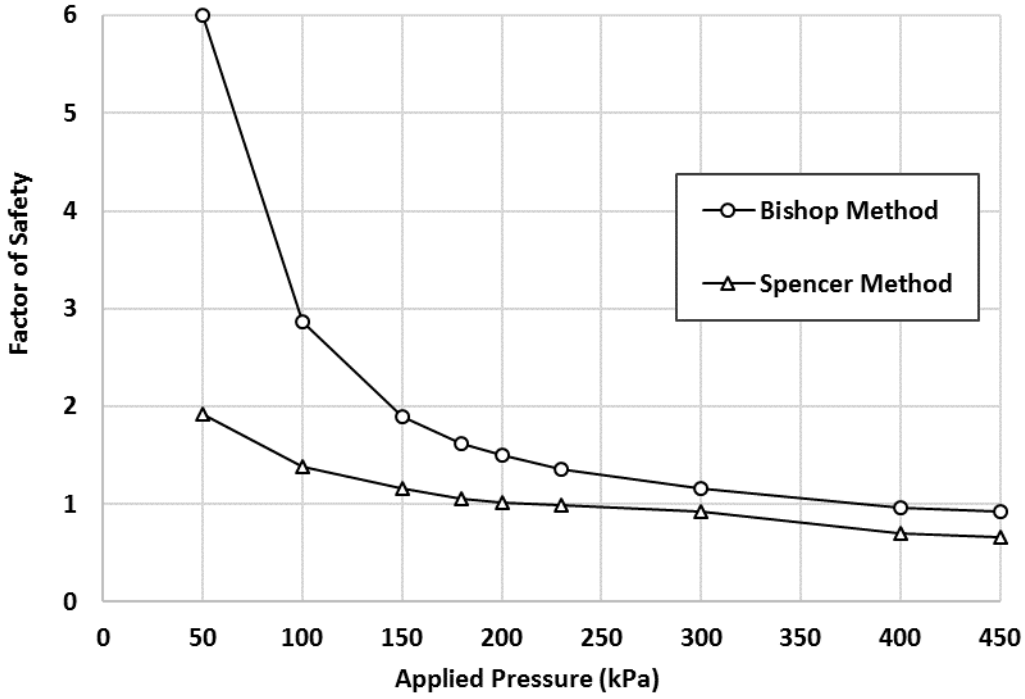

(c)

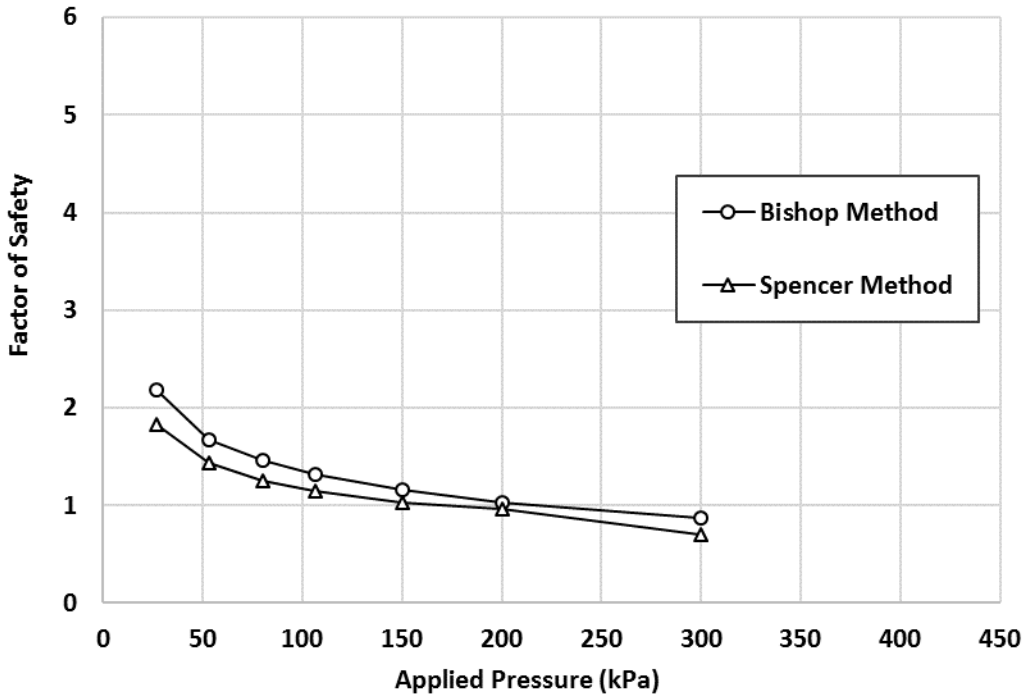

(d)

Figure 5.3. Factor of Safety versus applied pressure: (a) Wall B-W, (b) Wall B-1, (c) Wall B-2, and (d) Wall B-3

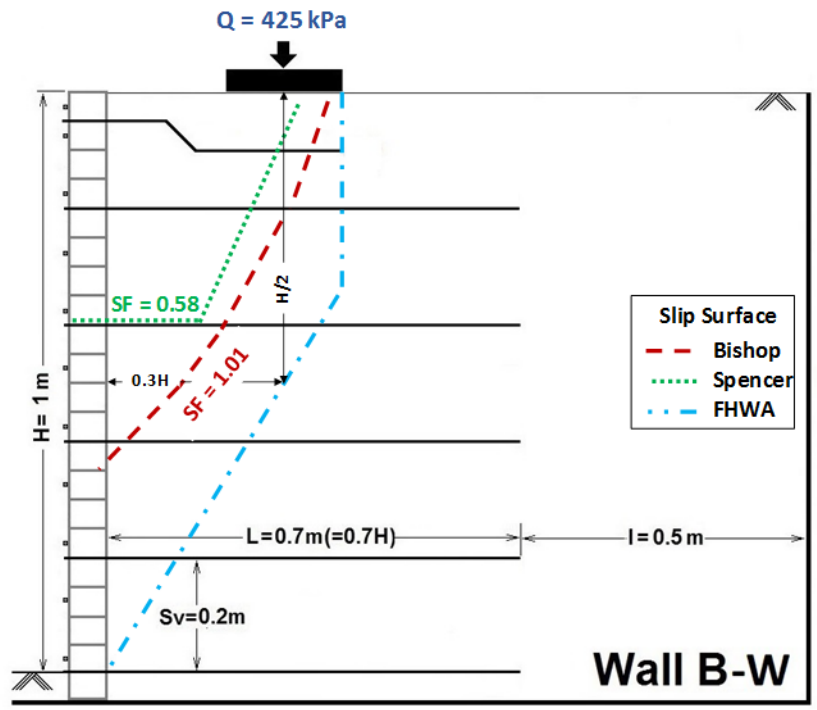

(a)

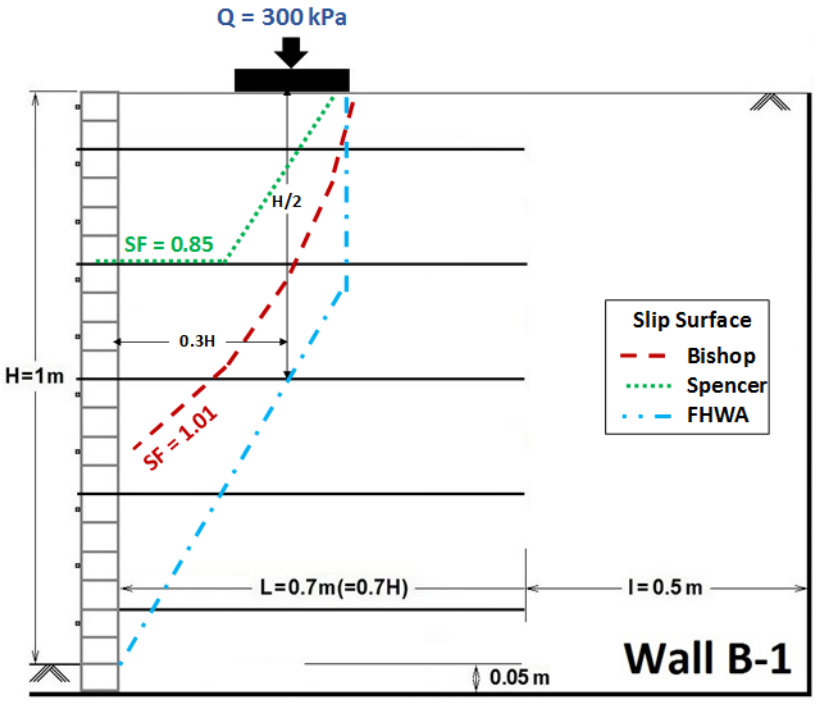

(b)

Figure 5. 4. Slip surfaces and factors of safety: (a) Wall W-1, (b) Wall W-2, (c) Wall W-3, and (d) Wall W-4 (continued)

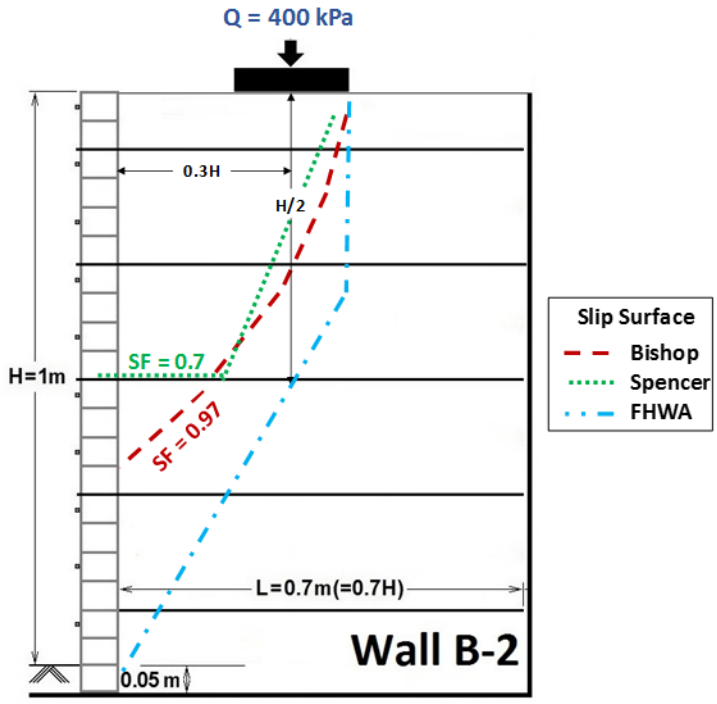

(c)

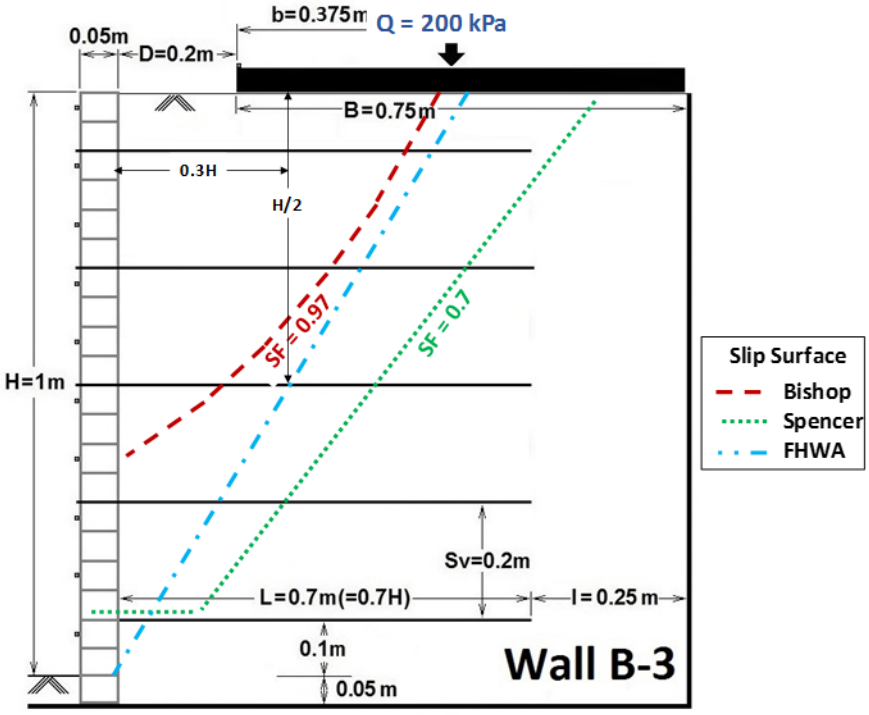

(d)

Figure 5.4. Slip surfaces and factors of safety for: (a) Wall W-1, (b) Wall W-2, (c) Wall W-3, and (d) Wall W-4

Kakrasul (2018)

As discussed in **Section 2.3.2**, Kakrasul (2018) conducted a series of laboratory model tests to investigate the performance of GRR walls constructed with limited fill space subjected to strip footing loading. **Figure 2.4** shows one model wall with the height, H, of 1 m, the vertical spacing between geogrid layers, S_v, of 0.2 m, the offset distance of the footing to the back of the wall facing, D, of 0.05 m, and the geogrid length, L, of 0.5 m. Error! Reference source not found.**2.5 and 2.6** p resent the pressure-settlement curves of the footing on the model wall and the lateral displacements along the height of the wall under the applied footing pressures , respectively.

Figure 5.5 presents the results of the limit equilibrium analysis on the Kakrasul wall in the Kakrasul (2018) study using the Bishop and Spenser methods. The result shows the ultimate bearing capacity was 200 kPa. The comparison between this wall and Wall B-2 (**Section 5.3.1**) indicates that the wall with longer geogrid reinforcement (Wall B-2) had a higher ultimate bearing capacity than the walls with shorter geogrid reinforcement length (Kakrasul's wall). **Figure 5.6** shows the critical slip surfaces identified by Bishop's and Spencer's methods under the ultimate bearing capacity. The slip surfaces began from the inner edge of the footing and developed into the reinforced zone towards the wall facing.

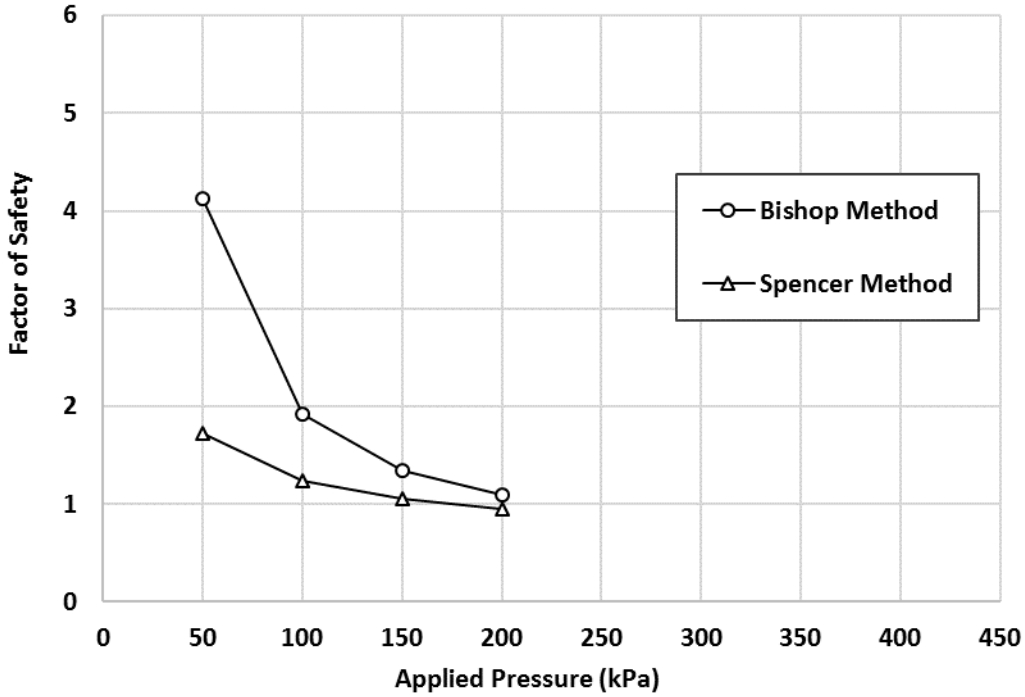

Figure 5.5. Factors of safety versus applied pressure for the wall with limited fill space

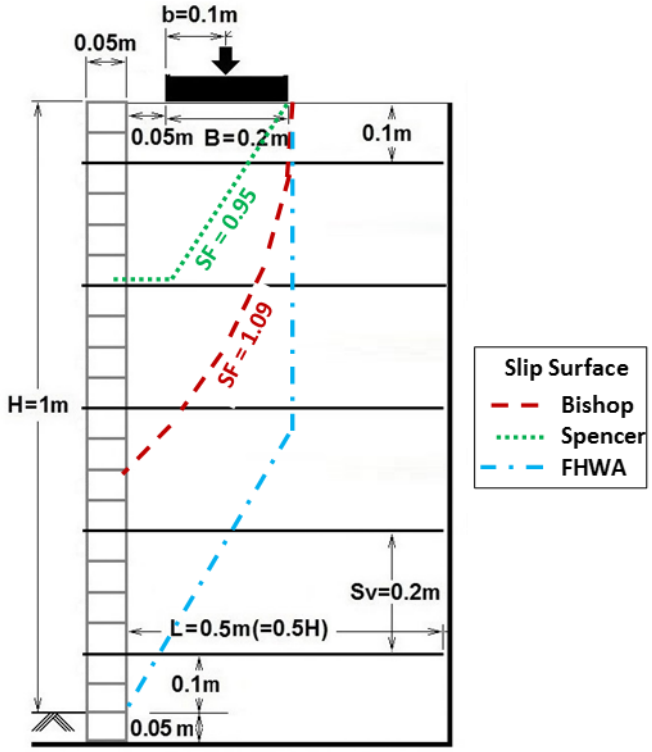

Figure 5.6. Slip surfaces and factors of safety under the ultimate bearing capacity for the wall with limited space (after Kakrasul 2018)

5.3.2. Full-scale model walls subjected to footing loading

Chemie Linz wall

Werner and Resl (1986) evaluated the performance of a 2.4-m-high full-scale field geotextile-reinforced wall with wrapped-around facing under static footing loading, as discussed in **Section 2.4.1**. They exposed the wall to three years of climatic fluctuations and environmental influences until loading in 1984. The geometry, loading scheme, and material properties of the wall are shown in **Figure 2.7**. A polypropylene needle-punched nonwoven geotextile with an ultimate tensile strength of 16 kN/m was used as reinforcement. Moreover, **Figure 5.7** present the critical slip surfaces identified by Bishop's and Spencer's methods and their corresponding factors of safety. Under the applied pressure of 130 kPa, the calculated factors of safety using the Bishop modified method and the Spencer two-part wedge method were 1.03 and 1.08, respectively. Therefore, the applied pressure of 130 kPa can be considered as the ultimate bearing capacity. While the calculated factors of safety are approximately equal, the Spenser method presents a deeper slip surface than the Bishop method. Werner and Resl (1986) reported that the settlement of the footing and the maximum lateral displacement of the wall facing induced under footing loading of 130 kPa were 160 and 110 mm, respectively.

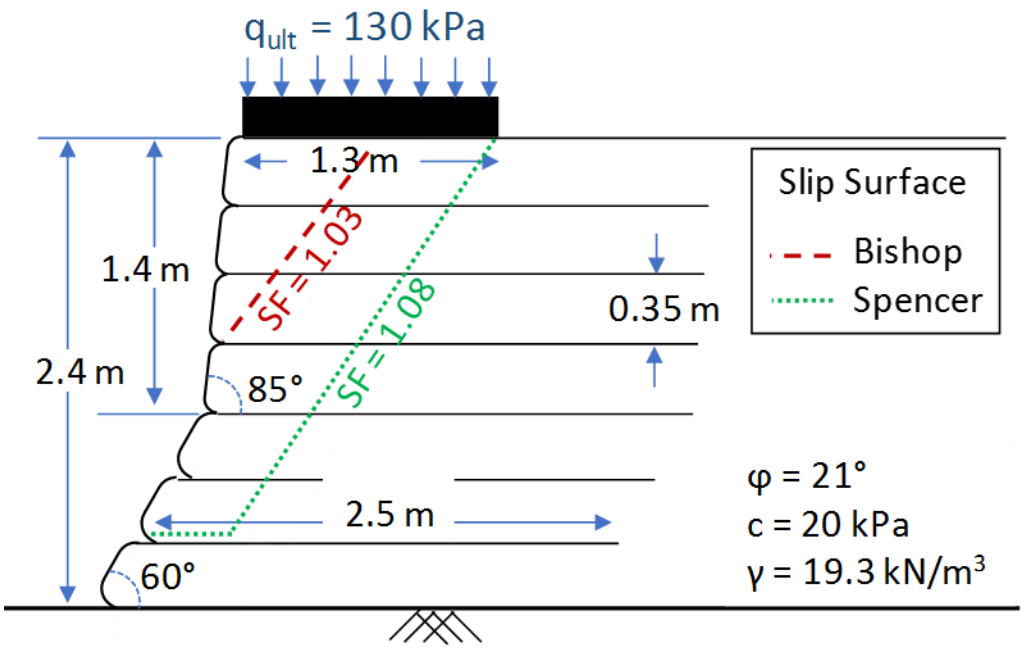

Figure 5.7. Critical slip surfaces and factors of safety for Chemie Linz wall (Werner and Resl, 1986)

Trento Wall

Benigni et al. (1996) evaluated the performance of a 5-m-high test wall, so-called the Trento test wall, with wrapped around facing, under static footing loading, as discussed in **Section 2.4.2**. **Figure 2.8** shows the geometry and loading scheme of the Trento Wall. A geocomposite with the tensile strength of 27 kN/m at 16 percent strain was used as reinforcement. The load was applied by a weight of two 3 m by 3 m wide loading platforms placed on top of the wall. **Figure 5.8** shows the calculated factors of safety using the Bishop and Spenser methods versus the applied load. The results indicate that the ultimate bearing capacity is 450 kPa. **Figure 5.9** shows the critical slip surfaces identified by Bishop's and Spencer's methods and their corresponding factors of safety

under the ultimate bearing capacity. The comparison between the Bishop and Spencer methods indicates similar slip surfaces with similar factors of safety. Benigni et al. (1996) reported that, under the applied pressure of 84 kPa, the settlements of the platform on the top of the wall was 50 mm. Moreover, they reported that the induced maximum lateral displacements for the wall under the applied pressure of 130 kPa was 90 mm.

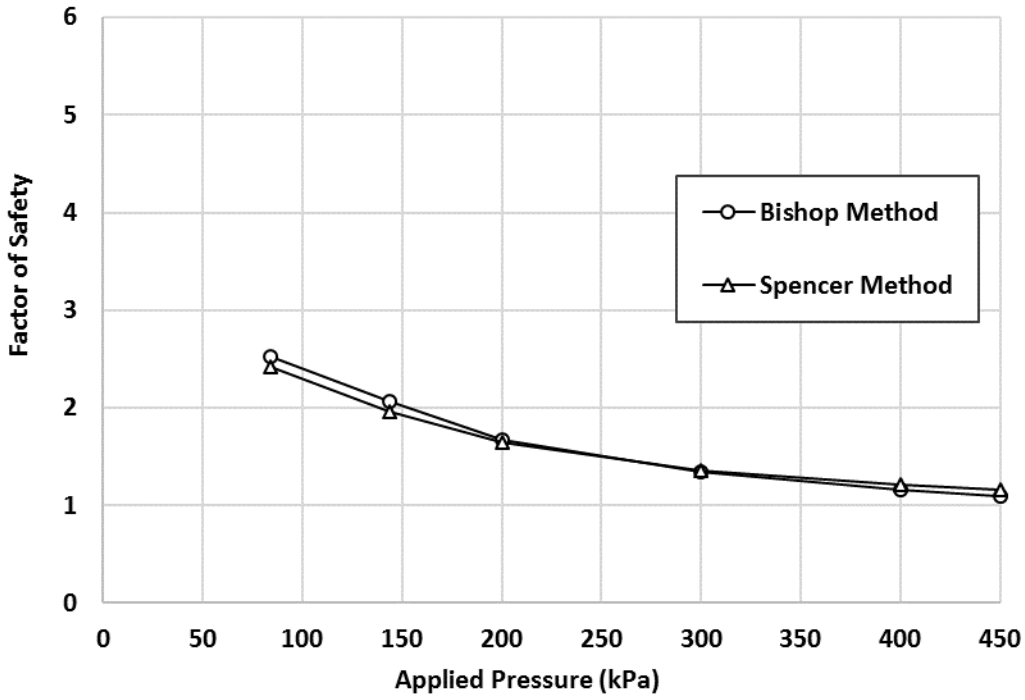

Figure 5.8. Calculated factors of safety versus applied pressure for the Trento wall

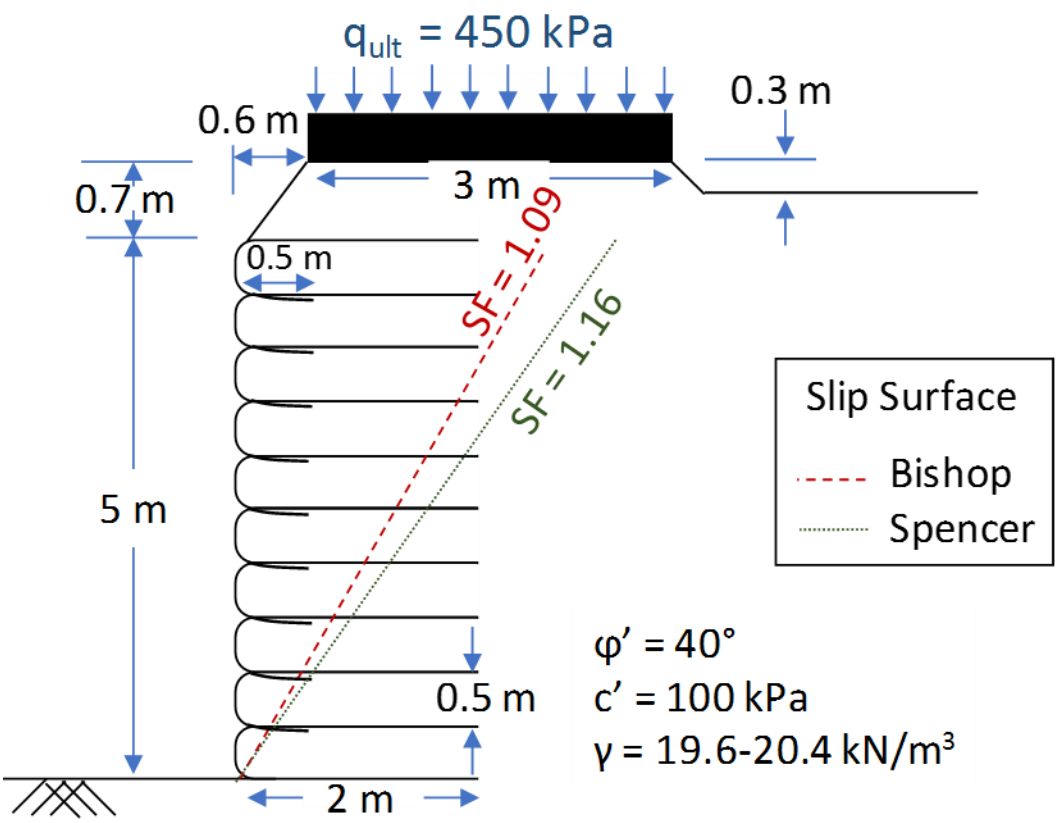

Figure 5.9. Critical slip surfaces and factors of safety under the ultimate bearing capacity in the Trento wall (after Benigni et al. 1996)

Garden test wall

Gotteland et al. (1997) monitored the performance of a 4.35-m-high full-scale test wall to investigate the failure behavior of the geosynthetic-reinforced soil structure as a bridge abutment, as discussed in **Section 2.4.3**. The wall was divided into two parts corresponding to two different wall profiles: the first part reinforced by nonwoven geotextiles (NW) and the second part reinforced by woven geotextiles (W). **Figure 2.9** shows the geometry, loading scheme, and material properties of the wall. The nonwoven and woven geotextiles had tensile strengths of 25

kN/m at 30% strain and 44 kN/m at 15% strain, respectively. **Figure 5.10** shows the calculated factors of safety using the Bishop and Spenser methods for the Garden test wall. The result shows that the ultimate bearing capacity for both walls was 300 kPa. **Figure 5.11** shows the critical slip surfaces identified by Bishop's and Spencer's methods and their corresponding factors of safety, under the ultimate bearing capacity. The results indicate that the factors of safety calculated by Spencer's method for both walls were smaller than those by Bishop's method. Therefore, in this case, the two-part wedge failure could be considered more critical than the circular failure. The critical slip surface identified by the Bishop method in NW wall is deeper than that in W wall. Gotteland et al. (1997) reported that under the applied pressure of 190 kPa, the induced maximum lateral deflections of the wall facing with nonwoven and woven geotextiles were 110 and 90 mm, respectively, as shown in **Figure 2.11**. At the same applied pressure, in the wall NW, the calculated factors of safety using the Bishop method and theSpencer method were 1.37 and 0.99, respectively. However, those in the wall W were 1.26 and 0.93, respectively.

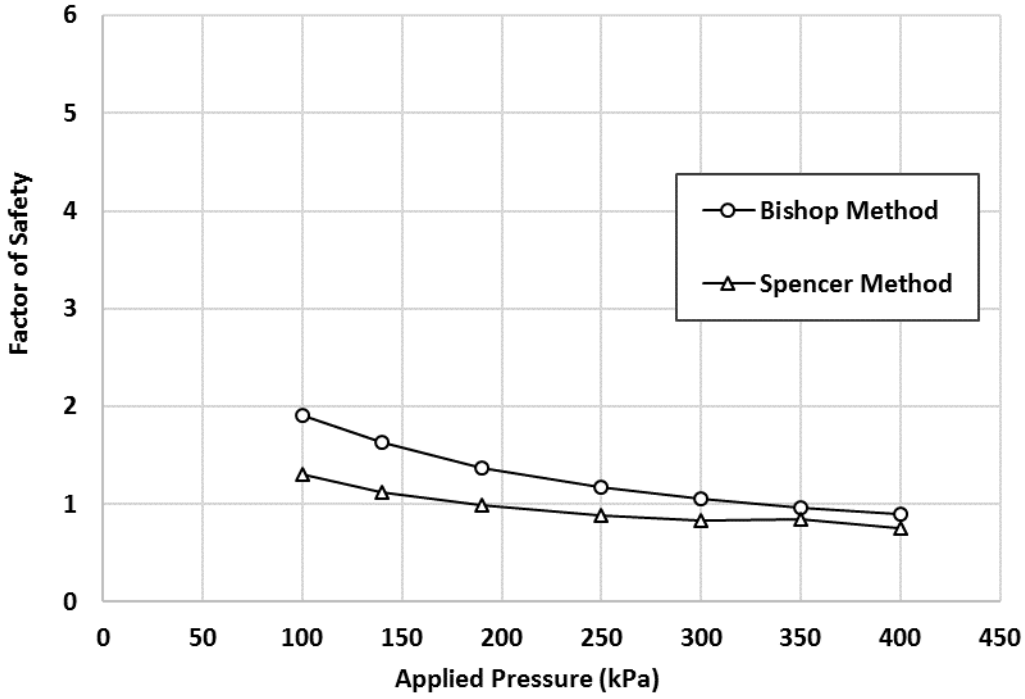

(a)

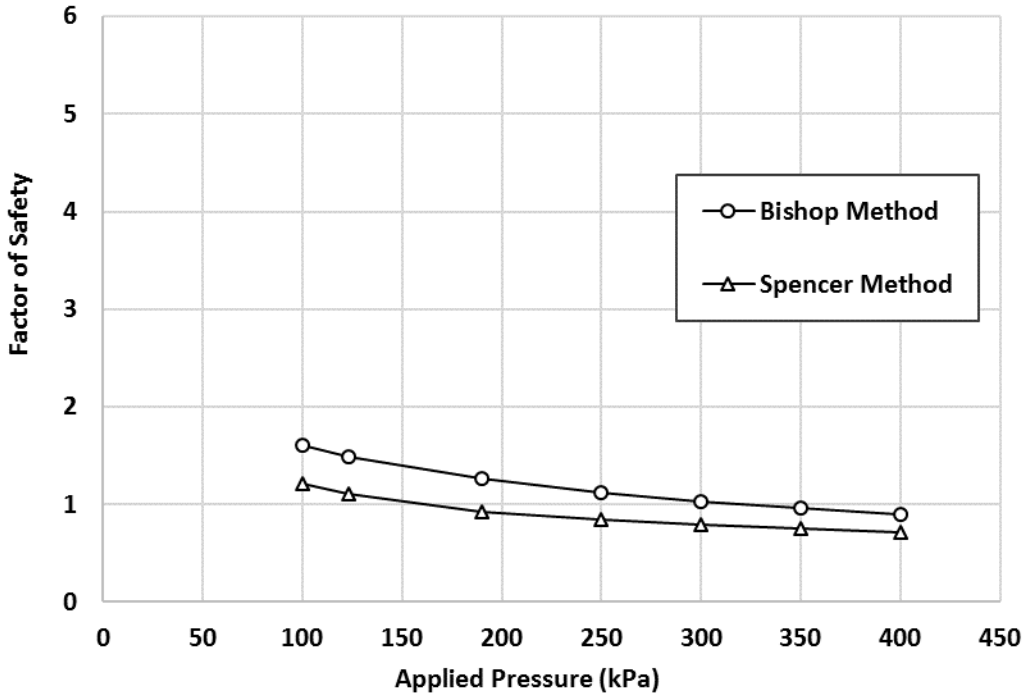

(b)

Figure 5.10. Calculated factors of safety versus applied pressure for: (a) wall with nonwoven geotextile (NW) and (b) wall with woven geotextile (W)

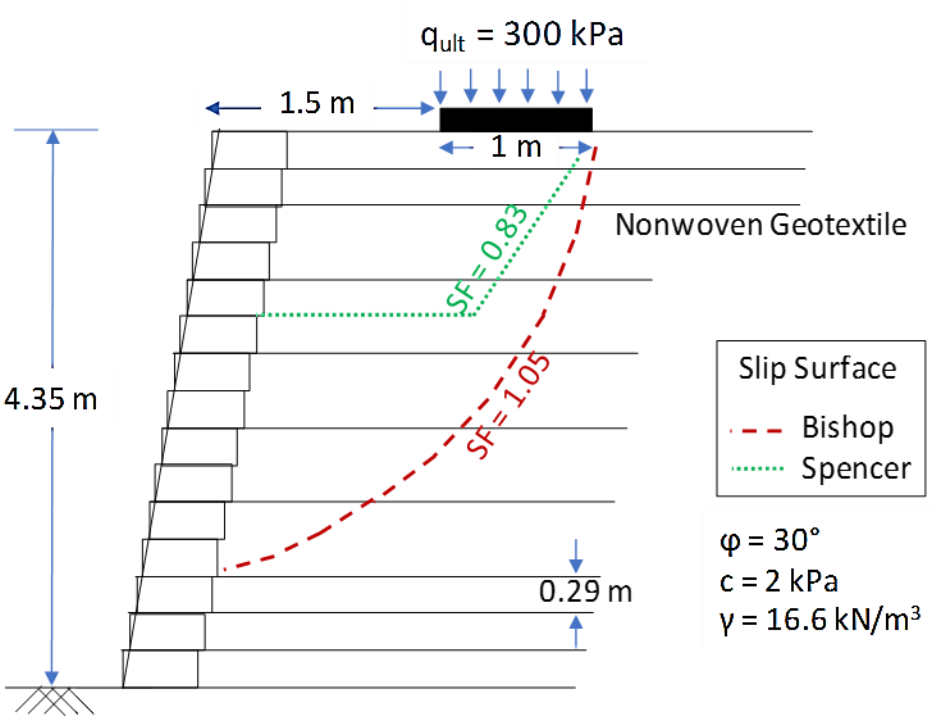

(a)

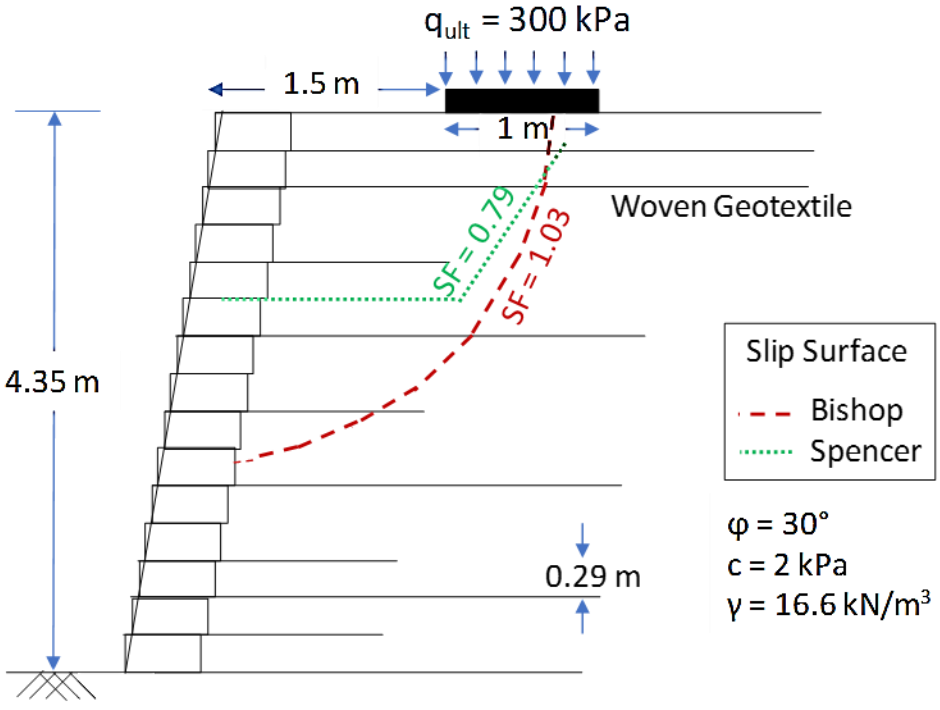

(b)

Figure 5.11. Critical slip surfaces and factors of safety for: (a) wall with nonwoven geotextile (NW) and (b) wall with woven geotextile (W) (after Gotteland et al. 1997)

5.3.2.4. Yoo and Kim (2008)

Yoo and Kim (2008) investigated the performance of a 5-m-high full-scale two-tier geogrid-reinforced retaining wall with modular block facing subjected to various levels of surface loading, as discussed in **Section 2.4.4**. **Figure 2.12** shows the measured lateral displacements along the height of the wall. **Figure 5.12** presents the calculated factor of safety using the Bishop and Spenser methods for this two-tiered wall. The result indicates that the ultimate bearing capacity for both walls is 850 kPa. The factor of safety calculated by Spencer's method was smaller than that by Bishop's method. Therefore, in this case, the two-part wedge failure could be more critical than the circular failure. In addition, the comparison between this wall and the other case histories shows that the tiered wall may allow higher footing pressure than un-tiered walls. **Figure 5.13** shows the critical slip surfaces and their corresponding factors of safety using the Bishop and the Spencer methods, under the ultimate bearing capacity. **Figure 5.13** also shows the critical slip surfaces may occur in the upper tier in this wall.

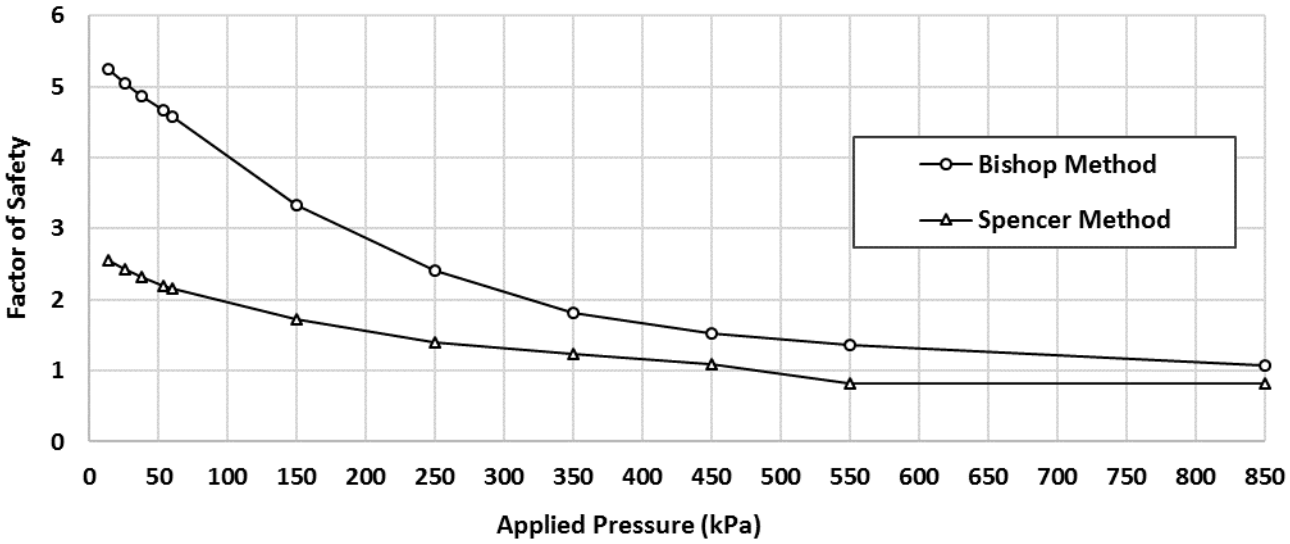

Figure 5. 12. Calculated factors of safety versus applied pressure for the tiered wall

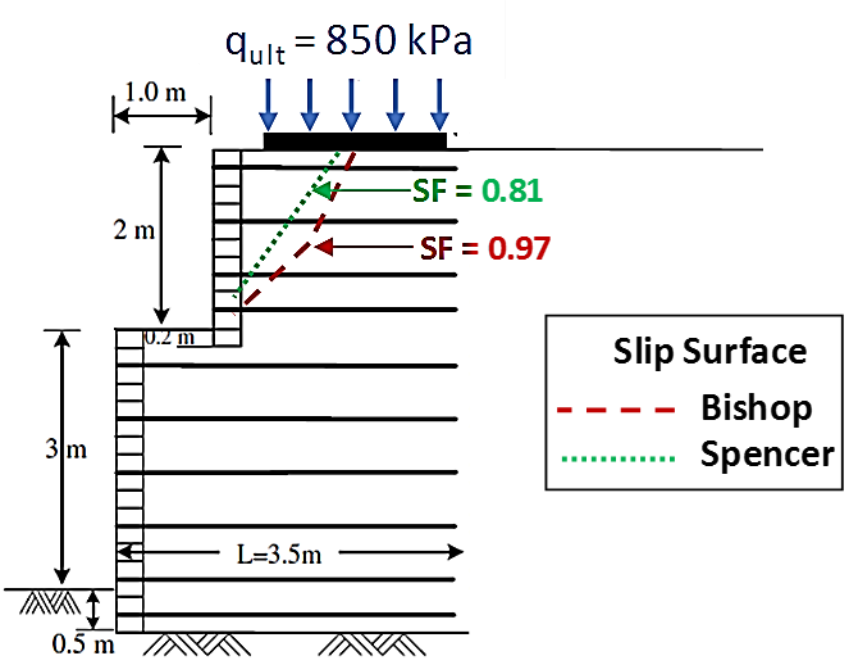

Figure 5.13. Critical Slip surfaces and factors of safety for the tiered wall (after Yoo and Kim 2008)

Ahmadi and Bezuijen (2018)

Ahmadi and Bezuijen (2018) carried out a footing loading test on a full-scale mechanically stabilized earth (MSE) wall with a plywood face, as discussed in **Section 2.4.5**. The full-scale model had a height of 4 m, a width of 4 m, vertical spacing between geogrid layers of 0.5 m, an offset distance of the footing to the back of the wall facing of 0.5 m, and a footing width of 1 m. Error! Reference source not found.**2.14** shows the configuration of the MSE walls. **Figure 2.15** p resents the lateral wall deflection under a strip footing load. **Figure 5.14** shows the calculated factor of safety using the Bishop and Spenser methods for this wall. The result indicates that the ultimate bearing capacity for both walls is 500 kPa. **Figure 5.15** shows the critical slip surfaces identified by Bishop's and Spencer's methods and their corresponding factors of safety under the ultimate bearing capacity. The comparison between the Bishop and Spencer methods indicates similar slip surfaces and factors of safety.

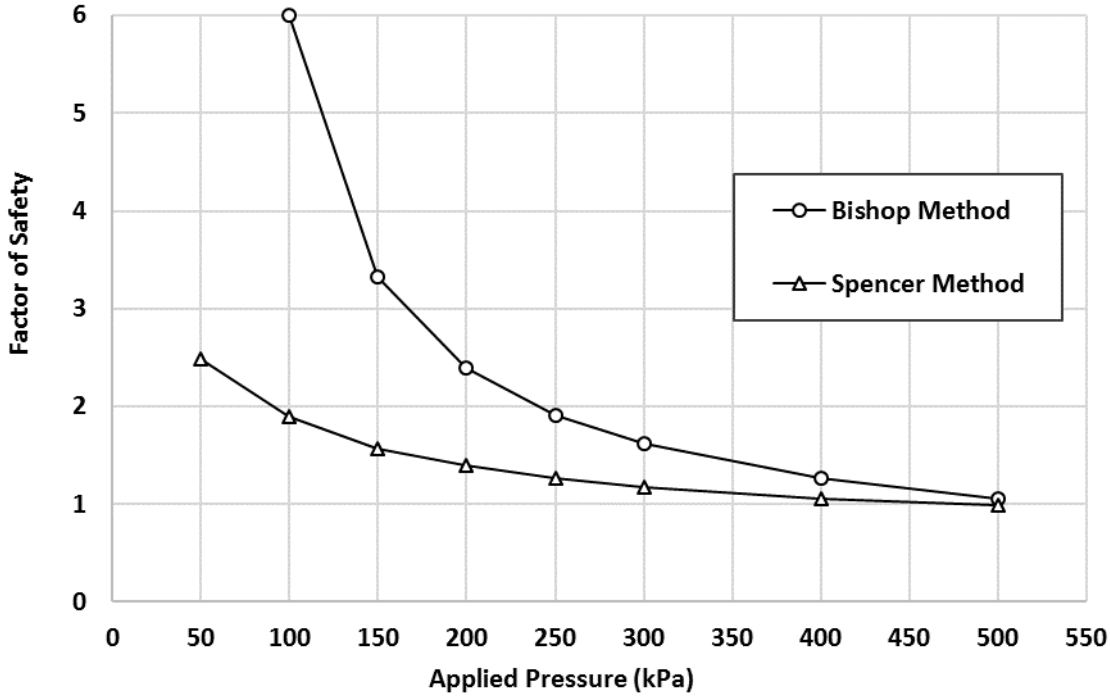

Figure 5. 14. Calculated factors of safety versus applied pressure in MSE wall with a plywood face

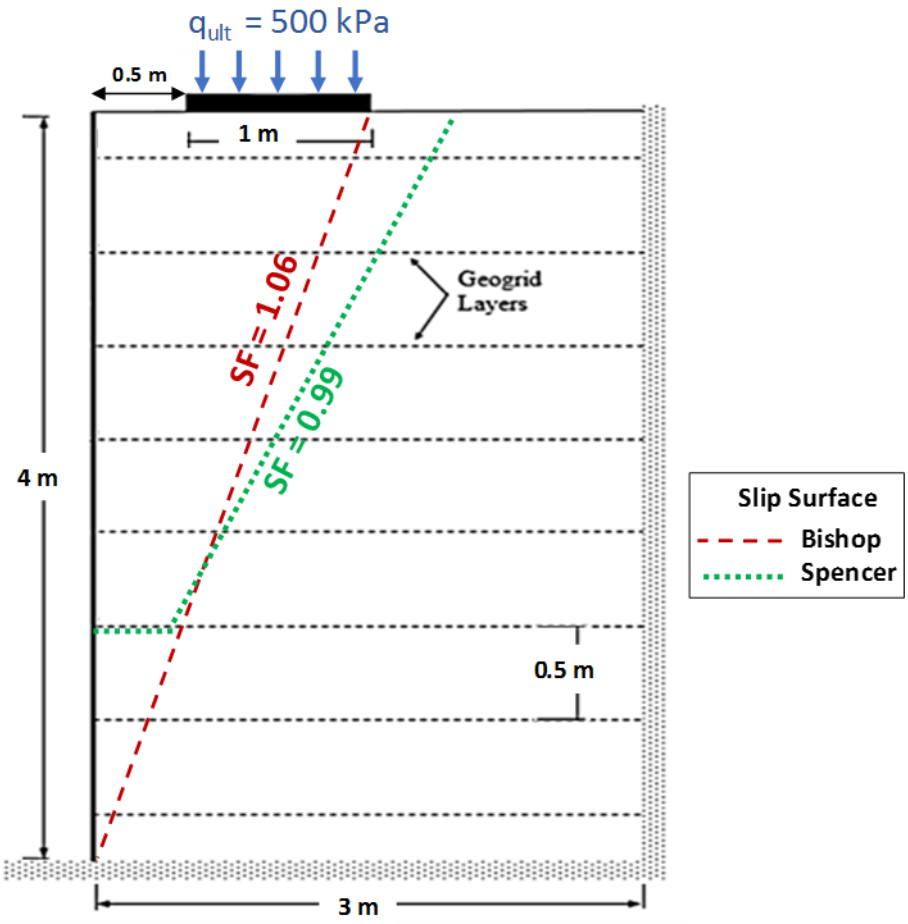

Figure 5.15. Critical slip surfaces and factors of safety in MSE wall with a plywood face (after Ahmadi and Bezuijen 2018)

5.3.3. Field studies on walls subjected to footing loading

Founder/Meadows bridge abutments

Abu-Hejleh et al. (2001) monitored the behavior of geogrid-reinforced segmental retaining walls, which supported the bridge superstructure and the approaching roadway, as discussed in **Section 2.5.1**. **Figure 2.16** shows the cross-section of one of the Founder/Meadows Bridge abutment walls. Three grades of geogrid reinforcement with their ultimate tensile strengths of 157.3, 64.2 and 39.3 kN/m, in accordance with the ASTM D4595 test method, were used in the abutment walls. The vertical spacing between the reinforcement layers was 0.4 m. The average unit weight and dry unit weight of the backfill were 22.1 and 21.0 kN/m^3, respectively. **Figure 2.17** presents the lateral deflections of the facing of the abutment walls. **Figure 5.16** shows the calculated factors of safety using the Bishop and Spenser methods for this wall. The result indicates that the ultimate bearing capacity for both walls is 850 kPa. **Figure 5.17** shows the critical slip surfaces and their corresponding factors of safety using the Bishop and the Spencer methods, under the ultimate bearing capacity. The comparison between the Bishop and Spencer methods indicates similar factors of safety. Moreover, the slip surfaces, identified by both methods, began from the center of the footing and developed into the reinforced zone.

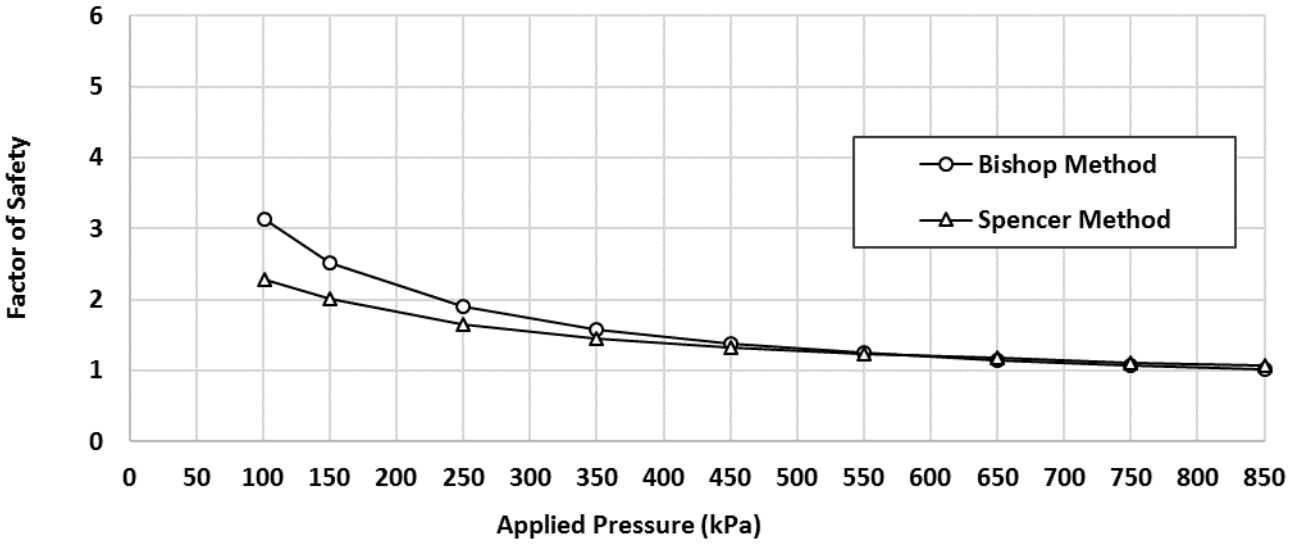

Figure 5. 16. Calculated factors of safety versus applied pressure for Founder/Meadows bridge abutment

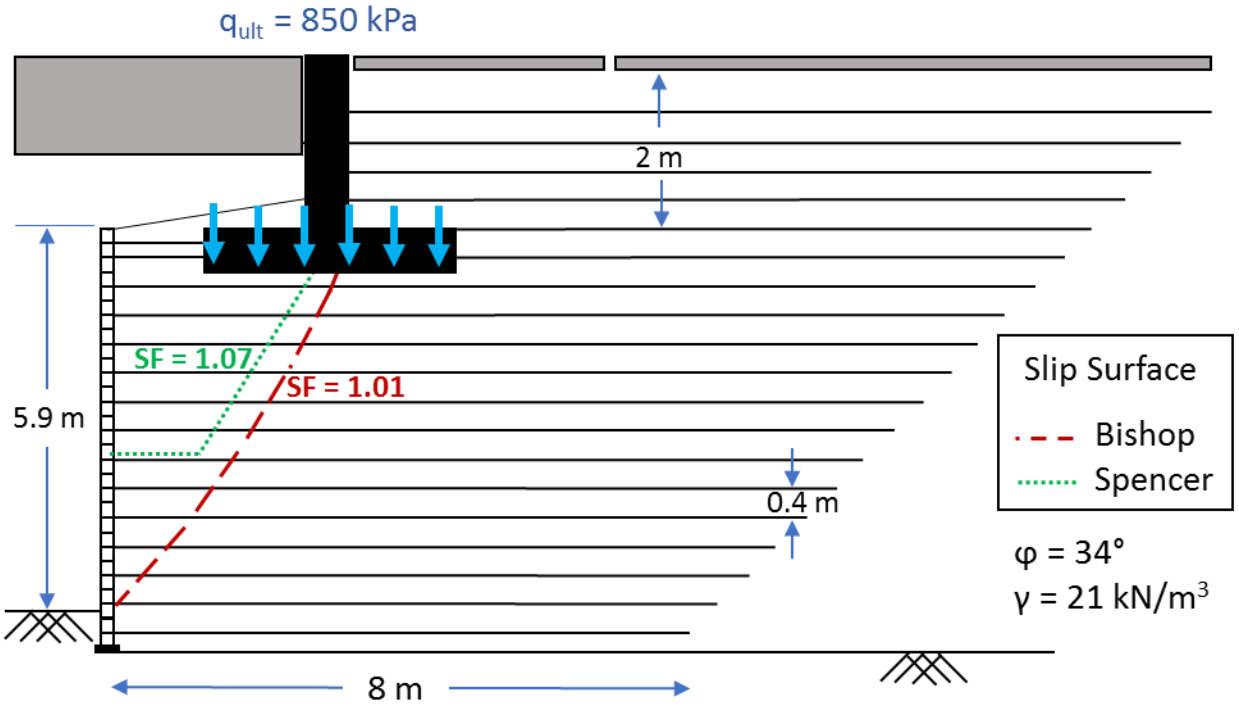

Figure 5.17. Critical slip surfaces for Founder/Meadows bridge abutment (after Abu-Hejleh et al. 2001)

5.3.4. Numerical studies on walls subjected to footing loading

Fakharian and Kashkooli (2018)

Fakharian and Kashkooli (2018) conducted a finite different analysis on the behavior of a reinforced soil abutment wall of a single-span bridge, as discussed in **Section 2.6.7**. **Figure 2.23** shows the abutment wall. Fakharian and Kashkooli (2018) reported the post-cyclic facing lateral deflections, the bridge deck footing settlements, and the seismic behavior of the wall. **Figure 2.24** shows the maximum lateral deflection of the facing at the end of construction. **Figure 2.25** presents the bridge deck footing settlement.

Figure 5.18 shows the calculated factors of safety using the Bishop and Spencer methods for this wall. The result indicates that the ultimate bearing capacity for both walls is 150 kPa. **Figure 5.19** shows the critical slip surfaces and their corresponding factors of safety using the Bishop and the Spencer methods, under the ultimate bearing capacity. The result indicates that the factor of safety calculated by Spencer's method for this wall with the wrapped-around facing was smaller than that by Bishop's method. Therefore, in this case, the two-part wedge failure could be considered more critical than the circular failure. **Figure 5.19** also shows that the slip surfaces identified by both methods began from the outer edge of the footing towards the walls facing.

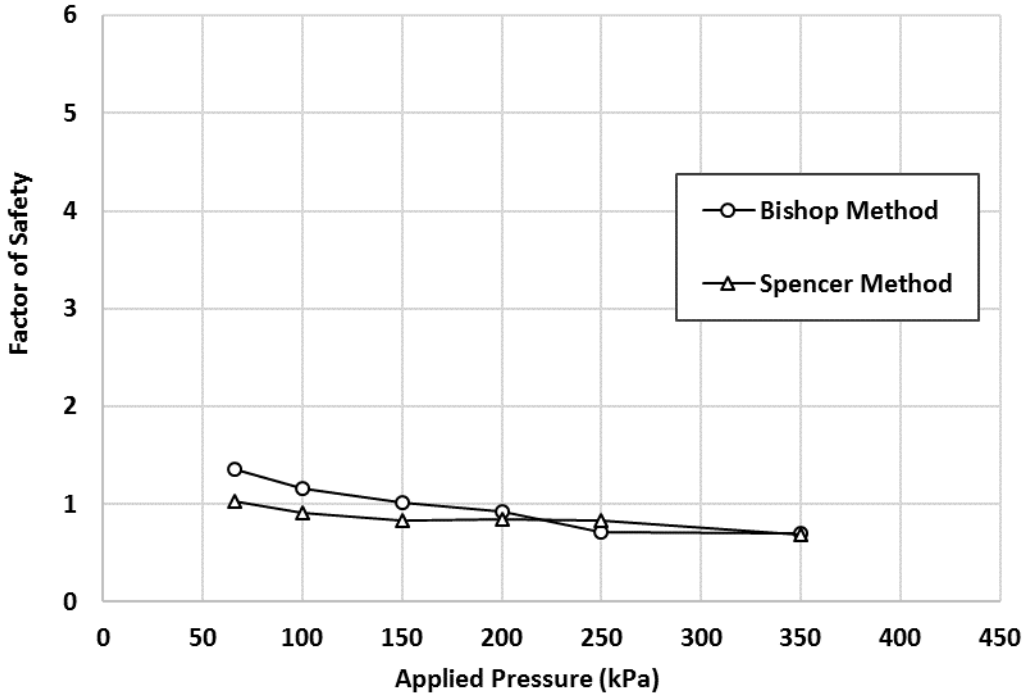

Figure 5.18. Calculated factors of safety versus applied pressure for reinforced soil abutment wall with wrapped-around facing

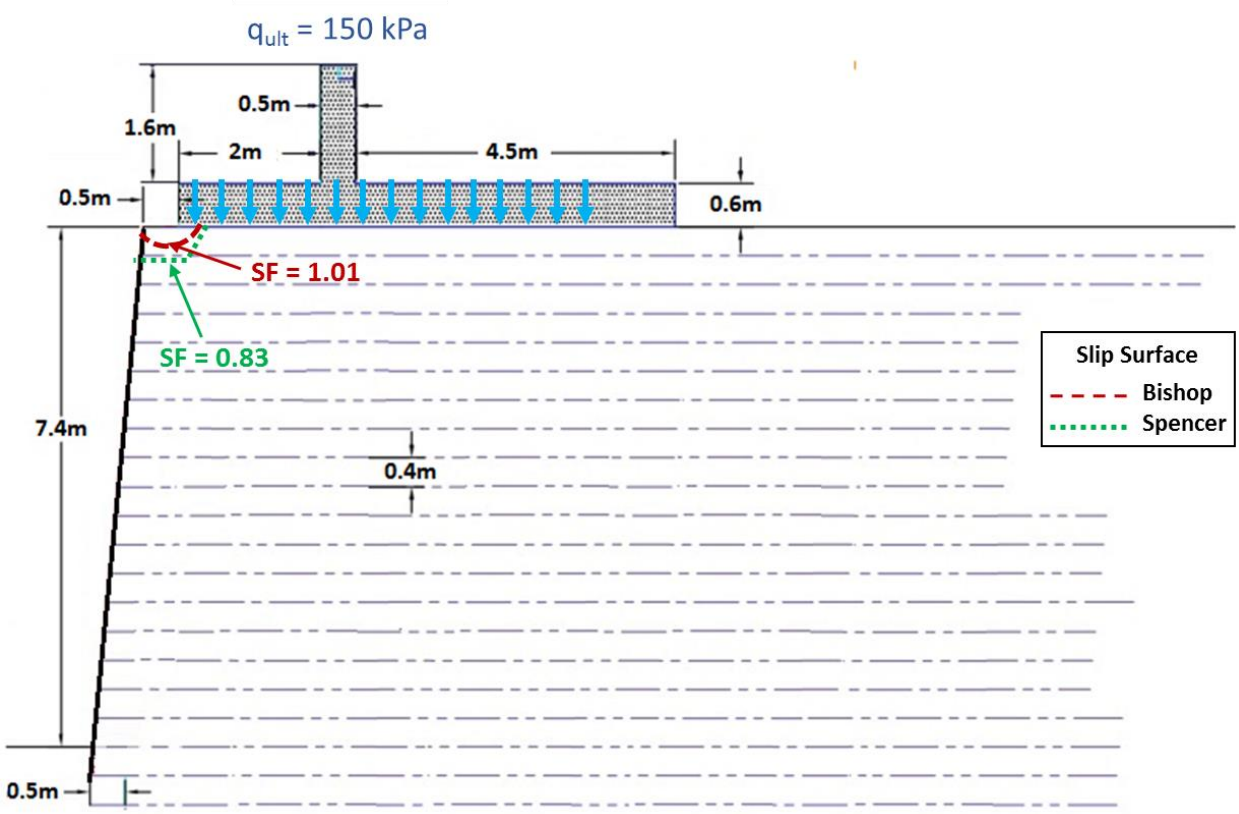

Figure 5.19. Critical slip surfaces and factors of safety for reinforced soil abutment wall with wrapped-around facing (after Fakharian and Kashkooli 2018)

5.4. Prediction of Maximum Lateral Deflection of Facing and Settlement of Footing

This section presents two empirical methods to calculate: (1) the maximum lateral deflection of the GRR wall with flexible facing subjected to the footing loading and (2) the settlement of the footing on the GRR wall. The empirical methods were developed based on eight reduced-scale model tests and ten case histories, which were presented in previous chapters. **Table 5.1** presents the main performance characteristics of these ten case histories, including one reduced-scale experimental study, five full-scale experimental studies, three field studies, and one numerical study on walls subjected to footing loading. The performance characteristics include wall height,

backfill, reinforcement type, reinforcement spacing, facing type, and measured maximum settlement of footing and maximum lateral deflection of wall facing, ultimate bearing capacity, and calculated factor of safety.

Table 5.1. Summary of case studies of with flexible wall facing under footing loading

Case	Wall	Heigth of Wall	Type of Backfill	Type of Reinforcement	Vertical Specing	Type of Facing	Maximum Footing Settlement	Maximum Facing Deflection	Factor of Safety	
									Bishop's Method	Spencer's Method
1	Kakrasul (2018)	1 m	$\phi = 37°$ c = 0kPa $\gamma = 18.9$ kN/m3	Geogrid Tult =19 kN/m @ $\varepsilon = 4\%$	0.2 m	Concrete Blocks	98 mm @ 200 kPa	58 mm @ 200 kPa	0.95 @ 200 kPa	1.09 @ 200kPa
							54 mm @ 150 kPa	29.5 mm @ 150 kPa	1.35 @ 150 kPa	1.05 @ 150 kPa
							32.5 mm @ 100 kPa	15.5 mm @ 100 kPa	1.92 @ 100 kPa	1.24 @ 100 kPa
							16 mm @ 50 kPa	6.5 mm @ 50 kPa	4.13 @ 50 kPa	1.72 @ 50 kPa
2	Chemie Linz wall *Werner and Resl (1986)*	2.4 m	$\phi = 21°$ c = 20 kPa $\gamma = 19.3$ kN/m^3	Nonwoven geotextile T_{ult} =16 kN/m @ $\varepsilon = 80\%$	0.35 m	Wrapped-around	160 mm @ 130 kPa	110 mm @ 130 kPa	1.26 @ 130 kPa	1.08 @ 130 kPa
3	Trento Wall *Benigni et al. (1996)*	5 m	$\phi' = 40°$ c' = 100 kPa γ= 19.6-20.4 kN/m^3	Geocomposite T =27 kN/m @ $\varepsilon = 16\%$	0.5 m	Wrapped-around	50 mm @ 84 kPa	90 mm @ 130 kPa	2.18 @ 130 kPa	2.06 @ 130 kPa
4	Garden wall *Gotteland et al. (1997)*	4.35 m	$\phi = 30°$ c= 2 kPa $\gamma = 16.6$ kN/m^3	Nonwoven Geotextile T =25 kN/m @ $\varepsilon = 30\%$	0.29 m	Concrete Cells	36 mm @ 140 kPa	110 mm @ 190 kPa	1.37 @ 190 kPa	0.99 @ 190 kPa
				Woven Geotextile T =44 kN/m @ $\varepsilon = 15\%$	0.29 m	Concrete Cells	33 mm @ 123 kPa	90 mm @ 190 kPa	1.26 @ 190 kPa	0.93 @ 190 kPa
5	Yoo & Kim (2008)	5 m	$\phi = 35°$-37° c= 5-10 kPa $\gamma = 20$ kN/m^3	Geogrid T_{ult} =55 kN/m @ $\varepsilon = 12.5\%$	0.6 m	Concrete Blocks	-	1.7 mm @ 60.4 kPa	4.57 @ 60.4 kPa	2.15 @ 60.4 kPa
								1.3 mm @ 53.5 kPa	4.67 @ 53.5 kPa	2.19 @ 53.5 kPa

								1.0 mm @ 37.5 kPa	4.87 @ 37.5 kPa	2.32 @ 37.5 kPa
								0.45 @ 25.5 kPa	5.05 @ 25.5 kPa	2.43 @ 25.5 kPa
								0.3 @ 13.5 kPa	5.25 @ 13.5 kPa	2.55 @ 13.5 kPa
6	Ahmadi and Bezuijen (2018)	4 m	$\phi = 39°$ c= 1 kPa $\gamma = 17.3$ kN/m^3	Geogrid T_{ult} =40 kN/m @ $\varepsilon = 6.6\%$	0.5 m	Plywood	-	16.5 mm @ 300 kPa	1.62 @ 300 kPa	1.18 mm @ 300 kPa
								12 mm @ 250 kPa	1.91 @ 250 kPa	1.21 @ 250 kPa
								8.25 mm @ 200 kPa	2.39 @ 200 kPa	1.39 @ 200 kPa
								4.75 mm @ 150 kPa	3.33 @ 150 kPa	1.57 @ 150 kPa
								2 mm @ 100 kPa	6 @ 100 kPa	1.89 @ 100 kPa
								0.5 mm @ 50 kPa	70.6 @ 50 kPa	2.49 @ 50 kPa
7	Founder / Meadows Abutments *Abu-Hejleh et al. (2001)*	5.9 m	$\phi = 34°$ $\gamma = 21$ kN/m^3	HDPE geogrids with T_{ult} =39, 64, & 157 kN/m	0.4 m	Concrete Blocks	-	10 mm @ 101 kPa	2.41 @ 101 kPa	1.42 @ 101 kPa
								15 mm @ 150 kPa	1.96 @ 150 kPa	1.3 @ 150 kPa

8	Lindsey (2018)	3 m	$\phi = 38°$ $\gamma = 20$ kN/m^3	Geotextile T_{ult} =70 and 38 kN/m	0.2 and 0.4 m	Concrete Blocks	-	7.62 mm @ 85 kPa	4.37 @ 85 kPa	2.78 @ 85 kPa
9	Maree Michel GRS-IBS bridge Saghebfar et al. (2017)	5.5 m	$\phi =$ 50.9° $\gamma = 21.3$ kN/m3	Woven Polypropylene Geotextile T_{ult} =80 kN/m @ ε =2%	0.2 m	Concrete Masonry Units	-	2.75 mm @ 110 kPa	5.34 @ 110 kPa	4.5 @ 110 kPa
10	Fakharian & Kashkooli (2018)	9 m	$\phi = 35°$ $\gamma = 22.1$ kN/m3	HDPE geogrids with T_{ult} =42.4 & 56.5 kN/m @ ε =5%	0.4 m	Wrapped-around	-	150 mm @ 65.8 kPa	1.36 @ 65.8 kPa	1.03 @ 65.8 kPa

5.4.1. Method to predict the maximum lateral deflection of GRR wall facing

Figure 5.20 presents the normalized maximum measured lateral facing deflections, induced by the applied pressures from the model tests and case studies versus their corresponding calculated factors of safety using the Bishop method. The results show an exponential relationship between the calculated factors of safety using the Bishop method and the maximum lateral facing deflections for both walls with wrapped-around and modular block facing. The trend line and its corresponding equation is also shown in **Figure 5.20**. Therefore, the maximum lateral deflection of the facing induced by footing loading can be estimated using the following equation:

$$\delta_{max} = 4.1 \times 10^{-4} \times H \times e^{5.5/\mathrm{FS}} \qquad \textbf{Eq. 5.1}$$

where δ_{max} = the maximum lateral deflection of the facing, H = height of the wall, and FS = factor of safety using the Bishop method.

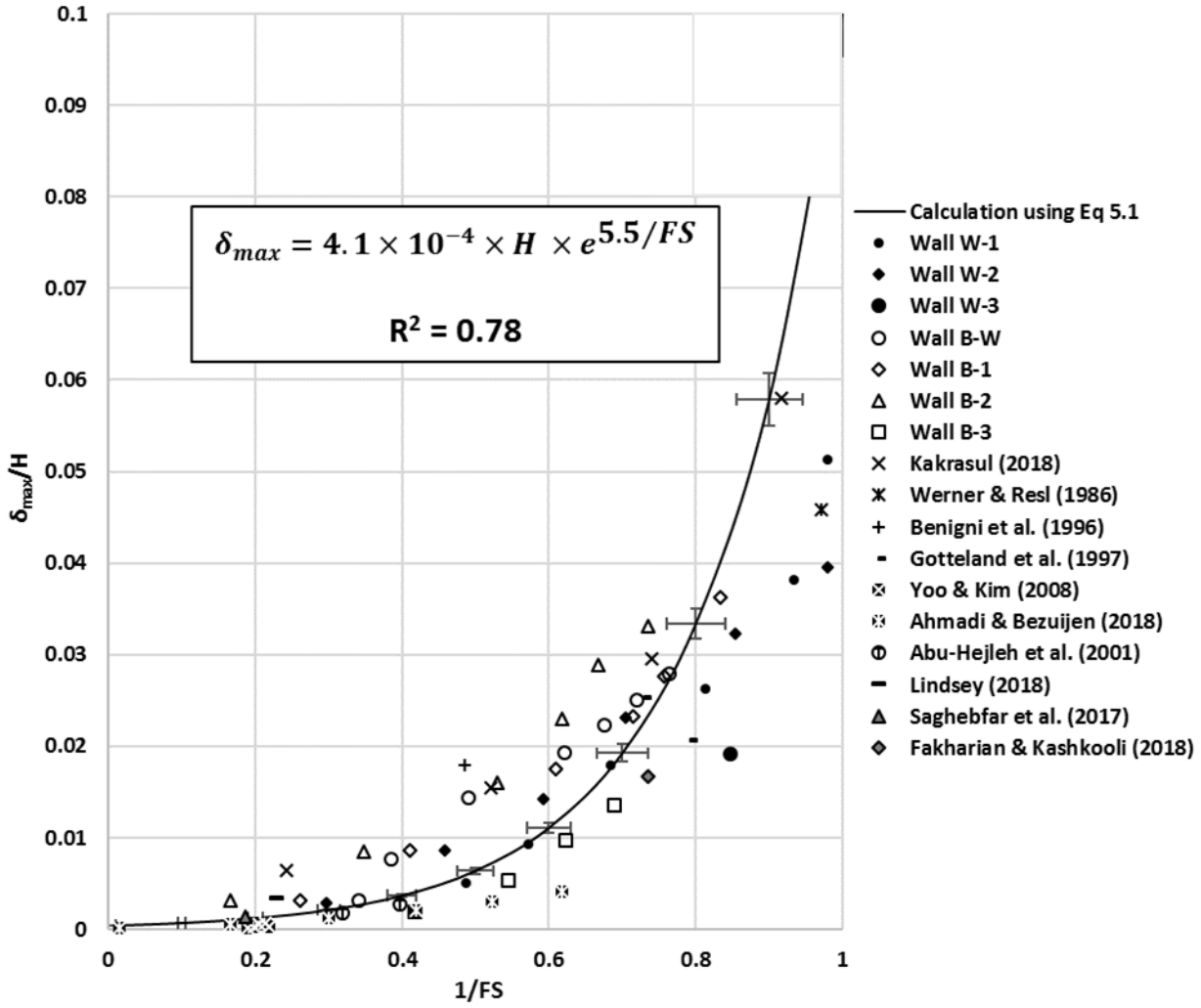

Figure 5.20. Normalized maximum lateral facing deflection versus calculated factor of safety using the Bishop method

5.4.1. Method to predict the settlement of footing above GRR Wall

Figure 5.21 presents the normalized measured settlement values at the center of the footing under the applied pressures from the model tests and case studies versus their corresponding calculated factors of safety using the Bishop method. **Figure 5.21** also show the exponential relationships between the calculated factor of safety using the Bishop method and the settlement of the footing. However, the relationship for the walls with wrapped-around facing is different from that for the walls with modular block facing. **Figure 5.21** presents the trend lines and their corresponding empirical equations. For the walls with wrapped-around facing, the footing settlement can be estimated using the following equation:

$$s = 1.6 \times 10^{-3} \times H \times e^{3.3/\mathrm{FS}} \qquad \textbf{Eq. 5.2}$$

where s = settlement at the center of the footing, H = height of the wall, and FS = factor of safety using the Bishop method. Moreover, for the walls with modular block facing, the footing settlement can be estimated using the following equation:

$$s = 2.1 \times 10^{-3} \times H \times e^{5/\mathrm{FS}} \qquad \textbf{Eq. 5.2}$$

where s = settlement at the center of the footing, H = height of the wall, and FS = factor of safety using the Bishop method.

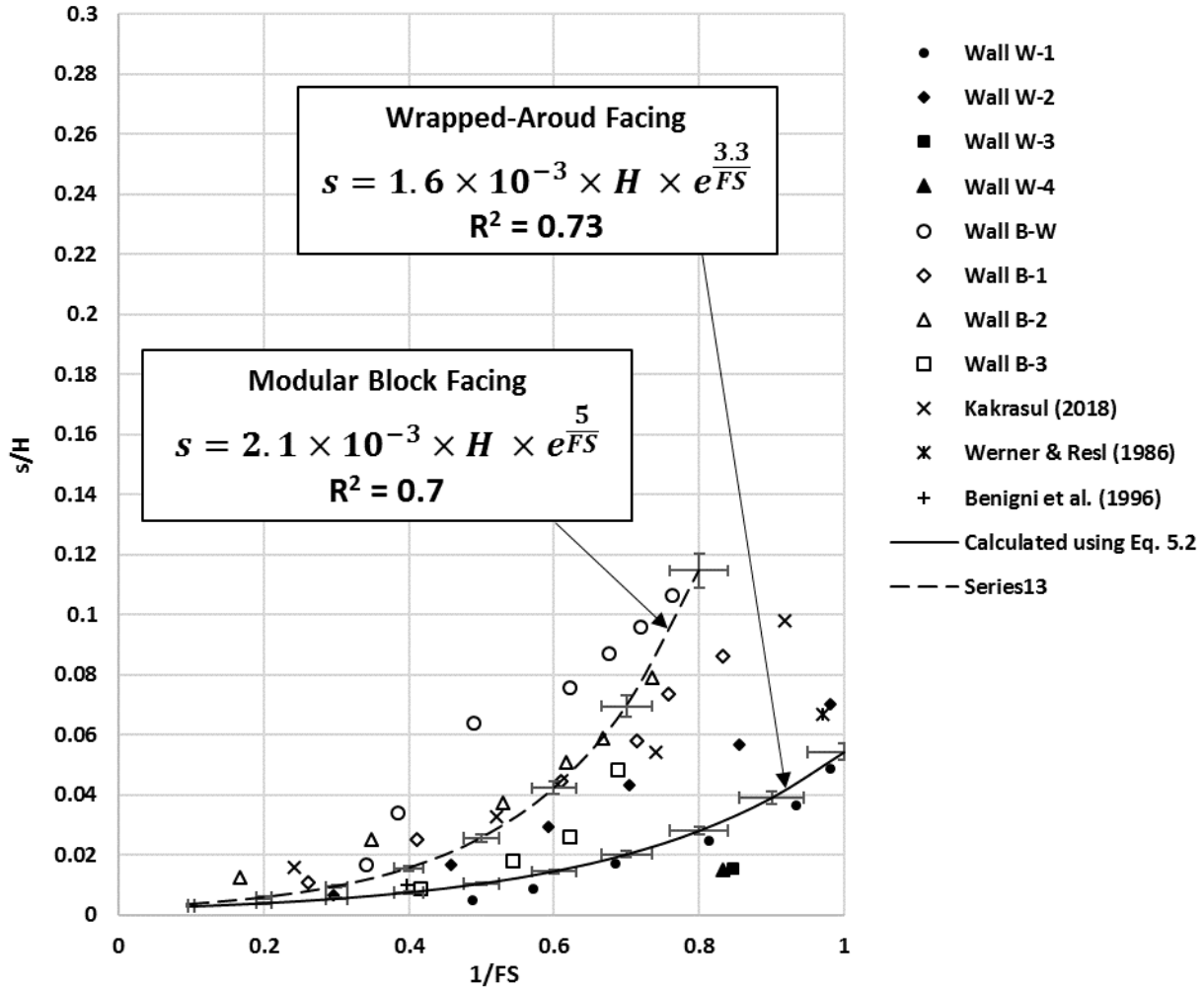

Figure 5. 21. Normalized footing settlement versus calculated factor of safety using the Bishop method

5.5. Summary

The objectives of this study were: (1) to evaluate the effect of footing loading on the global stability of GRR walls with wrapped-around and modular block facing and (2) to develop solutions for predicting the settlement of the footing, and the lateral deflection of the GRR walls with wrapped-around and modular block facing induced by footing loading. The following findings can be summarized based on this chapter:

(1) The comparison between the Bishop and Spencer methods indicates that the factors of safety calculated by Spencer's two-part wedge method for the GRR walls subjected to the footing loading were generally equal or less than those by Bishop's method.
(2) The facing rigidity increased the ultimate bearing capacity by approximately 50%.
(3) Based on the limit equilibrium analyses, the critical slip surfaces identified by Bishop's modified method and Spencer's two-part wedge method were similar to those observed in the walls under footing loading.
(4) Exponential relationships were obtained between the calculated factor of safety using the Bishop method and the maximum lateral facing deflection and the footing settlement of the GRR walls under footing loading.

Chapter 6. Conclusions and Recommendations

This study had four main objectives. The first objective was to evaluate the effects of stiff plates under an airbag on the distributions of vertical stresses, the pullout capacities, and the displacements of the reinforcement in the pullout tests. To achieve this objective, six large-scale pullout tests were conducted, in which the geogrid was placed within the soil mass. The following conclusions and recommendations can be made based on this experimental study:

(1) When the normal stresses were applied by the airbag without stiff plates, the measured maximum vertical pressures in the transverse direction on top of the soil mass occurred in the middle of the pullout box. However, in the case of the airbag with stiff plates, the maximum vertical pressures in the transverse direction were measured near the edges of the box.

(2) When the normal stress was applied by the airbag without any stiff plates, the distribution of the vertical pressures along the centerline in the longitudinal direction on top of the soil mass was relatively uniform, and the measured maximum vertical pressure was higher than that measured by the airbag on the stiff plates. Although the sleeve minimized the effect of the box front face, it still created the distribution of the vertical pressures in front of the box.

(3) The maximum vertical pressure on the bottom of the box under the normal stresses applied by the airbag without stiff plates occurred in the middle of the box.

(4) When the normal stress was applied by the airbag without any stiff plates, the maximum vertical pressures at the level of the reinforcement in the transverse and longitudinal sections were in the middle and close to the front of the box, respectively.

(5) Because of different distributions of the vertical pressures, the pullout resistance of the geogrid under the normal stresses applied by the airbag without any stiff plates was larger than that by the airbag with stiff plates. With the increase of the normal stress, their difference in the pullout resistance increased.

(6) When the normal stress was applied by the airbag without stiff plates, the displacements at the transverse bar of the geogrid were approximately equal. When the stiff plates were used, low vertical pressures in the central zone of the box led to the maximum displacement of the geogrid at that location.

The second objective of this study was to evaluate the combined effects of tension, bending, and friction on the relationship between local and global strains in the geogrid and on the measured local strains from the upper and lower sides of uniaxial geogrid specimens subjected to a tensile force. This study also investigated the effect of the confined pressure induced by the applied normal stress on the calculated calibration factor (CF) using the pullout box. The following conclusions can be made based on this experimental study:

(1) The effect of friction on the strains in the geogrid could not eliminated by averaging the strains measured by the strain gauges on upper and lower sides of the geogrid.

(2) The global strain in the geogrid induced by tension was higher than that induced by tension, bending, and friction.

(3) The calibration factors (CFs) calculated from the strain gauges subjected to tension, bending, and friction were approximately 39% higher than those calculated from the strain gauges subjected to tension only in the test in air.

(4) The diameter of the cylinder had a minor effect on the ratio of the average local strain induced by only tension to the average local strain induced by tension, bending, and friction in the test in air.

(5) In the pullout box tests for evaluating the CF, the normal stress and friction had a significant effect on the calculated CF as compared with that from the test in air.

The third objective of this study was to evaluate and compare the performance of the geosynthetic-reinforced retaining (GRR) walls with the wrapped-around and modular block facing subjected to static footing loading under a plane strain condition. To achieve this objective, eight model tests were conducted in the laboratory to examine the effect of the facing stiffness on the pressure-settlement curve, the deflection of the wall facing, the vertical and lateral pressures, and the failure modes. The following conclusions can be made based on this experimental study:

(1) The modular block facing behaved as relatively rigid facing and reduced the footing settlement as compared with the wrapped-around facing. For the wall with wrapped-around facing under footing loading, the settlement began from the back of the footing, became the maximum value under the footing, and developed into the facing. For the walls with modular block facing, the settlement was nearly symmetric to the centerline of the footing and localized under the footing.

(2) The maximum lateral deflections of the walls with the wrapped-around facing were much larger than the walls with modular block facing.

(3) The measured maximum vertical pressures induced by footing loading in all the walls were higher than the calculated pressures from the Boussinesq and 2:1 methods.

(4) In both wrapped-around and modular block facing walls, the measured lateral earth pressure generally increased with the applied pressure. The measured maximum lateral earth pressure was recorded at the upper 1/3 of the wall with wrapped-around facing but at the mid-height of the wall with modular block facing.

(5) The Boussinesq method suggested by FHWA and AASHTO approximately estimated the lateral earth pressure distribution for the wall with wrapped-around facing. However, this method did not accurately estimate the lateral earth pressure distribution for the wall with modular block facing.

(6) In general, for all the walls, the coefficients of lateral earth pressure, K_r, calculated from the measured earth pressures and the tension in geogrid, were between the coefficients of passive (K_p) and at-rest (K_o) earth pressures.

(7) For the walls subjected to footing loading, the K_r values calculated based on the measurements from the instruments placed within the 2:1 distributed area, are close to the K_o values.

(8) At failure, the slip surfaces began from the edge of the footing and developed into the reinforced zone toward the wall facing. The shallow, middle, and deep slip surfaces were observed in these test walls. No obvious failure was observed on the wrapped facing. However, for the walls with the modular block facing, the failure occurred on the facing.

The last objective of this study was to evaluate the effect of footing loading on the global stability of GRR walls with wrapped-around and modular block facing. The limit equilibrium (i.e., the Bishop modified method and the Spencer method) in the ReSSA program was used to determine the critical slip surfaces and their corresponding factors of safety of the eight reduced-

scale experimental models and ten case histories. Then, an analytical study was conducted to obtain the equations for the settlement of the footing, and the lateral deflection of the GRR walls with wrapped-around and with modular concrete block facing induced by footing loading. The following conclusions can be made based on this study:

(1) The comparison between the Bishop and Spencer methods indicates that the factors of safety calculated by Spencer's two-part wedge method for the GRR walls subjected to footing loading were generally equal or less than those by Bishop's method.

(2) The walls with wrapped-around facing and longer geogrid reinforcement had higher ultimate bearing capacities than those with shorter geogrid reinforcement.

(3) The walls with wrapped-around facing and a retained fill zone had higher ultimate bearing capacities than those without any retained fill zone.

(4) The ultimate bearing capacity of the walls with modular block facing was approximately 50% higher than that with wrapped around facing.

(5) The layout of geogrids had a significant effect on the magnitude of the ultimate bearing capacity.

(6) The walls with modular block facing and retained fill zone had lower ultimate bearing capacities than those without any retained fill zone.

(7) Based on the limit equilibrium analyses, the critical slip surfaces identified by Bishop's modified method and Spencer's two-part wedge method were similar to those observed in the walls under the footing loading.

(8) Exponential relationships were established between the calculated factor of safety, using the Bishop method, and the maximum lateral facing deflection and footing settlement of the GRR walls under the footing loading.

Page left intentionally blank.

REFERENCES

AASHTO, 2012. Section 11: Walls, Abutments, and Piers. AASHTO LRFD Bridge Design Specifications, 6th edition, Customary U.S. Units, AASHTO, Washington, D.C.

Abdelrahman, A. H., Ashmawy, A. K., and Abdelmoniem, M., 2008, "An Apparatus for Direct Shear, Pullout, and Uniaxial Testing of Geogrids," Geotech. Test. J., Vol. 31, No. 6, pp. 470–479, https://doi.org/10.1520/GTJ100761

Abdi, M. R. and Arjomand, M. A., 2011, "Pullout Tests Conducted on Clay Reinforced with Geogrid Encapsulated in Thin Layers of Sand," Geotext. Geomembr., Vol. 29, No. 6, pp. 588–595, https://doi.org/10.1016/j.geotexmem.2011.04.004

Abu-Hejleh, N., Zornberg, J.G., Wang, T., and McMullen, M., 2001. Performance of Geosynthetic-Reinforced Walls Supporting the Founders/Meadows Bridge and Approaching Roadway Structures. Report 2: Assessment of the performance and design of the front GRS walls and recommendations for future GRS abutments.

Adams, M., Nicks, J., Stabile, T., Schlatter, W. and Hartmann, J., 2012. *Geosynthetic reinforced soil integrated bridge system, interim implementation guide* (No. FHWA-HRT-11-026). Federal Highway Administration.

Ahmadi, H. and Bezuijen, A., 2018. Full-scale mechanically stabilized earth (MSE) walls under strip footing load. *Geotextiles and Geomembranes*, *46*(3), pp.297-311.

Alagiyawanna, A. M. N., Sugimoto, M., Sato, S., and Toyota, H., 2001, Influence of Longitudinal and Transverse Members on Geogrid Pullout Behavior during Deformation. Geotext. Geomembr. Vol. 19, No. 8, pp. 483–507, https://doi.org/10. 1016/S0266-1144(01)00020-6

Allen, T.M. and Bathurst, R.J., 2003. Prediction of reinforcement loads in reinforced soil walls (No. Final Research Report,). Washington State Department of Transportation, Report WA-RD

522.2.

ASTM D422-63, 2007, Standard Test Method for Particle-Size Analysis of Soils, ASTM International, West Conshohocken, PA, www.astm.org

ASTM D3080/D3080M, 2011, Standard Test Method for Direct Shear Test of Soils under Consolidated Drained Conditions, ASTM International, West Conshohocken, PA, www.astm.org

ASTM D4253, 2016, Standard Test Methods for Maximum Index Density and Unit Weight of Soils Using a Vibratory Table, *American Society for Testing and Materials*, West Conshohocken, PA, www.astm.org.

ASTM D4254, 2016, Standard Test Methods for Minimum Index Density and Unit Weight of Soils and Calculation of Relative Density, *American Society for Testing and Materials*, West Conshohocken, PA, www.astm.org

ASTM D-4595, 2011. Standard Test Method for Tensile Properties of Geotextiles by the Wide-Width Strip Method, *American Society for Testing and Materials*, West Conshohocken, Pennsylvania, USA. www.astm.org.

ASTM D6706-01, 2013, Standard Test Method for Measuring Geosynthetic Pullout Resistance in Soil, *American Society for Testing and Materials*, West Conshohocken, PA, www.astm.org

ASTM D7181, 2011, Standard Test Method for Consolidated Drained Triaxial Compression Test for Soils, *American Society for Testing and Materials*, West Conshohocken, PA, www.astm.org

Badakhshan, E. and Noorzad, A., 2017. A simplified method for prediction of ultimate bearing capacity of eccentrically loaded foundation on geogrid reinforced sand bed. *Int. J. Geosynthetics and Ground Eng. 3*(2), 14.

Bathurst, R.J., Allen, T.M., and Walters, D.L. 2002. Short-term strain and deformation behavior of geosynthetic walls at working stress conditions. *Geosynthetics International*, 9(5-6): 451-482.

Bathurst, R.J. and Ezzein, F.M., 2015. Geogrid and soil displacement observations during pullout using a transparent granular soil. *Geotechnical Testing Journal*, *38*(5), pp.673-685.

Bathurst, R.J., Vlachopoulos, N., Walters, D.L., Burgess, P.G., and Allen, T.M., 2006. The influence of facing stiffness on the performance of two geosynthetic reinforced soil retaining walls. Canadian Geotech. J. 43(12), 1225-1237.

Bathurst, R.J., Walters, D.L., Allen, T.M., 2002. Short-term strain and deformation behavior of geosynthetic walls at working stress conditions. Geosynthetics Int. 9(5-6), 451-482.

Bathurst, R.J., Walters, D.L., Hatami, K., Allen, T.M., 2001. Full-scale performance testing and numerical modelling of reinforced soil retaining walls. International Symposium on Earth Reinforcement, Fukuoka, Japan.

Benigni, C., Bosco, G., Cazzuffi, D., Col, R.D., 1996. Construction, performance of an experimental largescale wall reinforced with geosynthetics. In: Ochiai, H., Yasufuku, N., Omine, K. (Eds.), *Earth Reinforcement, Vol. 1*. A. A. Balkema Publisher, Rotterdam, pp. 315–320.

Benjamim, C.V.S., Bueno, B.S., Zornberg, J.G., 2007. Field monitoring evaluation of geotextile-reinforced soil-retaining walls. Geosynthetics Int. 14(2), 100-118.

Berg, R., Christopher, B., Samtani, N., 2009. Design and construction of mechanically stabilized earth walls and reinforced soil slopes, vols. 1 & 2. Report No: FHWA-NHI-10–024. FHWA, U.S. Department of Transportation.

Bowles, L.E., 1996. Foundation Analysis and Design. McGraw-Hill.

Christopher, B.R. and Holtz, R.D., 1985. Geotextile Engineering Manual, No. FHWA-TS-86/203.

Ezzein, F.M. and Bathurst, R.J., 2014. A new approach to evaluate soil-geosynthetic interaction using a novel pullout test apparatus and transparent granular soil. *Geotextiles and Geomembranes*, *42*(3), pp.246-255.

Fakharian, K. and Attar, I.H., 2007. Static and seismic numerical modeling of geosynthetic-reinforced soil segmental bridge abutments. Geosynthetics Int. 14(4), 228-243.

Fakharian, K. and Kashkooli, M., 2018. Numerical study of seismic behavior of reinforced soil bridge abutments located on soft clays of Southwest Iran. *Proceedings of the 11th International Conference on Geosynthetics,*

Fannin, R.J. and Hermann, S. 1990. Performance data for a sloped reinforced soil wall. *Canadian Geotechnical Journal*, *27*(5): 676-686.

Ferreira, J.A. and Zornberg, J.G., 2015. A transparent pullout testing device for 3D evaluation of soil–geogrid interaction. *Geotechnical Testing Journal*, *38*(5), pp.686-707.

Gotteland, P., Gourc, J.P. and Villard, P., 1997, February. Geosynthetics reinforced structures as bridge abutments: full scale experimentation and comparison with modelisations. In *Int. Symp. On Mechanically Stabilized Backfill* (pp. 25-34). AA Balkema, Denver, USA.

Han, J., 2015. *Principles and practice of ground improvement*, John Wiley & Sons, Hoboken, New Jersey, USA, ISBN: 978-1-118-25991-7, 432p.

Han, J. and Gabr, M.A. 2002. Numerical analysis of geosynthetic-reinforced and pile-supported earth platforms over soft soil. *Journal of Geotechnical and Geoenvironmental Engineering*, ASCE, 128(1): 44-53.

Han, J. and Leshchinsky, D., 2006. General analytical framework for design of flexible reinforced earth structures. *Journal of geotechnical and geoenvironmental engineering*, *132*(11),

pp.1427-1435.

Helwany, S.M., Wu, J.T., Froessl, B., 2003. GRS bridge abutments—an effective means to alleviate bridge approach settlement. Geotext. Geomembranes 21(3), 177-196.

Hirakawa, D., Kongkitkul, W., Tatsuoka, F. and Uchimura, T. 2003. Time-dependent stress–strain behaviour due to viscous properties of geogrid reinforcement. *Geosynthetics International*, 10(6): 176-199.

Holtz, R.D., Kovacs, W.D., 1981. An introduction to geotechnical engineering. Prentice-Hall, Inc, Englewood Cliffs, New Jersey, 733p.

Holtz, R.D., Lee, W.F., 1998. Geosynthetic reinforced wall analysis phase II: Use of in-soil geosynthetic behavior to predict deformations, Volume 2: Implementation—computer codes and files, No. WA-RD 452.2.

Huang, B. and Bathurst, R.J., 2009. Evaluation of soil-geogrid pullout models using a statistical approach. *Geotechnical Testing Journal*, *32*(6), pp.489-504.

Huang, B., Bathurst, R.J., Hatami, K., 2009. Numerical study of reinforced soil segmental walls using three different constitutive soil models. J. Geotech. Geoenviron. Eng. 135(10), 1486-1498.

Huang, J. and Han, J. 2010. Two-dimensional parametric study of geosynthetic-reinforced column-supported embankments by coupled hydraulic and mechanical modeling. *Computers and Geotechnics*, 37(5): 638-648.

Jayawickrama, P.W., Lawson, W.D., Wood, T.A. and Surles, J.G., 2014. Pullout resistance factors for steel MSE reinforcements embedded in Gravelly backfill. *Journal of Geotechnical and Geoenvironmental Engineering*, *141*(2), p.04014090.

Jiang, Y., Han, J., Parsons, R.L., Brennan, J.J., 2016. Field instrumentation and evaluation of

modular-block MSE walls with secondary geogrid layers. J. Geotech. Geoenviron. Eng. 14 (12), 05016002.

Kakrasul, J.I., Han, J., Rahmaninezhad, S.M., Weldu, M., 2016. Model tests of geosynthetic-reinforced earth walls with limited-space retained fill. 3rd Pan-American Conference on Geosynthetics, 1279-1286.

Kakrasul, J.I., 2018. Geosynthetic reinforced retaining walls with limited fill space under static footing loading. Ph.D. Dissertation, Civil, Environmental and Architectural Engineering Department, The University of Kansas. Lawrence, KS, USA.

Kulhawy, F.H., Mayne, P.H., 1990. Manual on estimating soil properties for foundation design. Report EL-6800 Electric Power Research Institute, EPRI, August.

Lajevardi, S.H., Dias, D. and Racinais, J., 2013. Analysis of soil-welded steel mesh reinforcement interface interaction by pull-out tests. *Geotextiles and geomembranes*, *40*, pp.48-57.

Lawson, W. D., Jayawickrama, P. W., Wood, T. A., and Surles, J. G., 2013. Pullout Resistance Factors for Steel Reinforcements Used in TxDOT MSE Walls. Presented at the *Geo-Congress; Stability and Performance of Slopes and Embankments III*, San Diego, CA, American Society of Civil Engineers, Reston, VA, pp. 44–53.

Lee, K.Z., Wu, J.T., 2004. A synthesis of case histories on GRS bridge-supporting structures with flexible facing. Geotext. Geomembranes 22 (4), 181-204.

Leshchinsky, B., 2014. Limit analysis optimization of design factors for mechanically stabilized earth wall-supported footings. Transportation Infrastructure Geotechnology 1 (2), 111-128.

Leshchinsky, D., Imamoglu, B. and Meehan, C.L. 2010. Exhumed geogrid-reinforced retaining wall. *Journal of Geotechnical and Geoenvironmental Engineering,* ASCE, 136(10): 1311-1323.

Leshchinsky, D. and Marcozzi, G.F., 1990. Bearing capacity of shallow foundations: rigid versus flexible models. *Journal of Geotechnical Engineering*, *116*(11), pp.1750-1756.

Lindsey, E.D., 2015. *Performance observations of geosynthetic reinforced bridge abutments* (Masters of Science Thesis, University of Missouri--Columbia).

Madhav, M.R., Gurung, N. and Iwao, Y., 1998. A theoretical model for the pull-out response of geosynthetic reinforcement. *Geosynthetics International*, *5*(4), pp.399-424.

Maheshwari, P. and Viladkar, M.N. 2009. A mathematical model for beams on geosynthetic reinforced earth beds under strip loading. *Applied Mathematical Modelling*, 33(4): 1803-1814.

Min, Y., Leshchinsky, D., Ling, H.I., Kaliakin, V.N., 1995. Effects of sustained and repeated tensile loads on geogrid embedded in sand. Geotech. Testing J. 18(2), 204-225.

Nayeri, A. and Fakharian, K., 2009. Study on pullout behavior of uniaxial HDPE geogrids under monotonic and cyclic loads. *International Journal of Civil Engineering*, *7*(4), pp.211-223.

Ochiai, H., Yasufuku, N., Yamaji, T., Xu, G.L. and Hirai, T., 1996. Experimental evaluation of reinforcement in geogrid-soil structure. In *Proceedings of the international symposium on earth reinforcement* (pp. 249-254).

Otani, J., Miyamoto, K., Mukunoki, T. and Hirai, T., 2001. Visualization of interaction behavior between soil and reinforcement using X-ray CT. *Landmarks in earth reinforcement*, *1*, pp.117-120.

Palmeira, E.M., 2004. Bearing force mobilisation in pull-out tests on geogrids. *Geotextiles and geomembranes*, *22*(6), pp.481-509.

Palmeira, E.M., 2009. Soil–geosynthetic interaction: modelling and analysis. *Geotextiles and Geomembranes*, *27*(5), pp.368-390.

Patra, S. and Shahu, J.T., 2012. Pasternak model for oblique pullout of inextensible reinforcement. *Journal of Geotechnical and Geoenvironmental Engineering*, *138*(12), pp.1503-1513.

Perkins, S.W. and Cuelho, E.V., 1999. Soil-geosynthetic interface strength and stiffness relationships from pullout tests. *Geosynthetics International*, *6*(5), pp.321-346.

Perkins, S.W. and Lapeyre, J.A. 1997. In-isolation strain measurement of geosynthetics in wide-width strip tension test. *Geosynthetics International*, 4(1): 11-32.

Rahmaninezhad, S.M., Han, J., Kakrasul, J.I., 2018. Effect of Facing Stiffness on Performance of Geosynthetic-Reinforced Retaining Walls Subjected to Footing Loading. 97th Annual Meeting Transportation Research Board, No. 18-04884.

Rahmaninezhad, S.M., Han, J., Kakrasul, J.I., and Weldu, M. 2019. Behavior of geosynthetic-reinforced retaining walls with wrapped-around and modular block facing subjected to footing loading. Submitted to *Geotextiles and Geomembranes.*

Rahmaninezhad, S.M., Han, J., Kakrasul, J.I., and Weldu, M. 2018. Stress distributions and pullout responses of extensile and inextensible reinforcement in soil using different normal loading methods. *Geotechnical Testing Journal 42*(6).

Rahmaninezhad, S.M., Han, J., Weldu, M. and Kakrasul, J.I., 2016. Effects of methods of applying normal stresses in pullout tests on pressure distributions and pullout resistance. In *Vol. 2 of Proc., 3rd Pan-American Conf. on Geosynthetics (GeoAmericas)* (pp. 1308-1315).

Rahmaninezhad, S.M., Yasrobi, S.S. and Eftekharzadeh, S.F., 2009. Effects of compaction in the subgrade of the reinforced sand backfills with geotextile on bearing capacity. *Int. J. Civil Eng.*, *12*, pp.320-328.

Roodi, G.H. and Zornberg, J.G., 2017. Stiffness of soil-geosynthetic composite under small

displacements. II: Experimental evaluation. *Journal of Geotechnical and Geoenvironmental Engineering*, *143*(10), p.04017076.

Sabermahani, M., Ghalandarzadeh, A., Fakher, A., 2009. Experimental study on seismic deformation modes of reinforced-soil walls. Geotext. Geomembranes 27 (2), 121-136.

Saghebfar, M., Abu-Farsakh, M., Ardah, A., Chen, Q. and Fernandez, B.A., 2017. Performance monitoring of geosynthetic reinforced soil integrated bridge system (GRS-IBS) in Louisiana. *Geotextiles and Geomembranes*, *45*(2), pp.34-47.

Sieira, A.C.C., Gerscovich, D.M. and Sayão, A.S., 2009. Displacement and load transfer mechanisms of geogrids under pullout condition. *Geotextiles and Geomembranes*, *27*(4), pp.241-253.

Skinner, G.D., Rowe, R.K., 2005. Design and behaviour of a geosynthetic reinforced retaining wall and bridge abutment on a yielding foundation. *Geotextiles and Geomembranes*, *23*(3), 234-260.

Sugimoto, M., Alagiyawanna, A.M.N. and Kadoguchi, K., 2001. Influence of rigid and flexible face on geogrid pullout tests. *Geotextiles and Geomembranes*, *19*(5), pp.257-277.

Sukmak, K., Sukmak, P., Horpibulsuk, S., Han, J., Shen, S.L. and Arulrajah, A., 2015. Effect of fine content on the pullout resistance mechanism of bearing reinforcement embedded in cohesive–frictional soils. *Geotextiles and Geomembranes*, *43*(2), pp.107-117.

Tatsuoka, F., Tateyama, M., Koseki, J., Yonezawa, T., 2014. Geosynthetic-reinforced soil structures for railways in japan. *Transportation Infrastructure Geotechnology, 1* (1), 3-53.

Tatsuoka, F., Tateyama, M., Uchimura, T., Koseki, J., 1997. Geosynthetic-reinforced soil retaining walls as important permanent structures, 1996–1997 Mercer Lecture. *Geosynthetics Int., 4*(2), 81-136.

Teixeira, S.H., Bueno, B.S. and Zornberg, J.G., 2007. Pullout resistance of individual longitudinal and transverse geogrid ribs. *Journal of geotechnical and geoenvironmental engineering*, *133*(1), pp.37-50.

Tran, V.D.H., Meguid, M.A. and Chouinard, L.E., 2013. A finite–discrete element framework for the 3D modeling of geogrid–soil interaction under pullout loading conditions. *Geotextiles and Geomembranes*, *37*, pp.1-9.

Yoo, C. and Kim, S.B., 2008. Performance of a two-tier geosynthetic reinforced segmental retaining wall under a surcharge load: full-scale load test and 3D finite element analysis. *Geotextiles and Geomembranes*, *26*(6), pp.460-472.

Viswanadham, B.V.S., Razeghi, H.R., Mamaghanian, J., Manikumar, C.H.S.G., 2017. Centrifuge model study on geogrid reinforced soil walls with marginal backfills with and without chimney sand drain. *Geotextiles and Geomembranes*, *45* (5), 430–446.

Wang, Z., Jacobs, F. and Ziegler, M., 2016. Experimental and DEM investigation of geogrid–soil interaction under pullout loads. *Geotextiles and Geomembranes*, *44*(3), pp.230-246.

Warren, K.A., Christopher, B. and Howard, I.L., 2010. Geosynthetic strain gage installation procedures and alternative strain measurement methods for roadway applications. *Geosynthetics International*, 17(6): 403-430.

Wayne, M. H., Han, J., Akins, K. 1998. The design of geosynthetic reinforced foundations. Design and Construction of Retaining Systems. *Geotechnical Special Publication, 76*, 1-18.

Weldu, M.T., Han, J., Rahmaninezhad, S.M., Parsons, R.L. and Kakrasul, J.I., 2015. *Pullout resistance of mechanically stabilized earth wall steel strip reinforcement in uniform aggregate* (No. K-TRAN: KU-14-7). University of Kansas. Dept. of Civil, Environmental, and Architectural Engineering.

Weldu, M.T., Han, J., Rahmaninezhad, S.M., Parsons, R.L., Kakrasul, J.I., Jiang, Y., 2016. Effect of aggregate uniformity on pullout resistance of steel strip reinforcement. *J. Transportation Research Board* 2(2579), 1-7.

Werner, G. and Resl, S., 1986. Stability mechanisms in geotextile reinforced earth-structures. In *III International Conference on Geotextiles, Vienna, Austria* (Vol. 4, pp. 1131-1135).

Wilson-Fahmy, R.F., Koerner, R.M. and Sansone, L.J., 1994. Experimental behavior of polymeric geogrids in pullout. *Journal of geotechnical engineering*, *120*(4), pp.661-677.

Wu, J.T.H., Lee, K.Z.Z., Pham, T., 2000. Allowable bearing pressure of bridge sills on GRS abutments with flexible facing. *J. Geotech. Geoenviron. Eng. 7* (132), 830-841.

Xiao, C., Han, J., Zhang, Z., 2016. Experimental study on performance of geosynthetic-reinforced soil model walls on rigid foundations subjected to static footing loading. *Geotext. Geomembranes 44*(1), 81-94.

Yang, G., Liu, H., Lv, P., Zhang, B., 2012. Geogrid-reinforced lime-treated cohesive soil retaining wall: Case study and implications. *Geotext. Geomembranes 35*, 112-118.

Yang, G., Zhang, B., Lv, P., Zhou, Q., 2009. Behaviour of geogrid reinforced soil retaining wall with concrete-rigid facing. *Geotext. Geomembranes 27*(5), 350-356.

Yasrobi, S.S., Rahmaninezhad, S.M., Eftakharzadeh, S.F., 2009a. Characterization of shallow foundations on loose sand reinforced with geotextile. *2nd Int. Conference on New Developments in Soil Mechanics and Geotechnical Engineering*.

Yasrobi, S.S., Rahmaninezhad, S.M., Eftekharzadeh, S.F., 2009b. Large physical modeling to optimize the geometrical conditions of geotextile in reinforced loose sand. *Geotechnical Special Publication 189*, 53-59.

Yoo, C., Kim, S.B., 2008. Performance of a two-tier geosynthetic reinforced segmental retaining

wall under a surcharge load: full-scale load test and 3D finite element analysis. *Geotext. Geomembranes 26*(6), 460-472.

Zhu, H., Ma, Y., Liu, Y.X., Wang, J., 2008. Application of the geogrid reinforced soil retaining walls for a high slope supporting project. *Geosynthetics in Civil and Environmental Engineering,* 266-270.

Zornberg, J.G., Roodi, G.H. and Gupta, R., 2017. Stiffness of Soil–Geosynthetic Composite under Small Displacements: I. Model Development. *Journal of Geotechnical and Geoenvironmental Engineering*, *143*(10), p.04017075.